Dynamics and Control in Natural and Engineered Multi-Agent Systems

Benjamin Nabet

A Dissertation

Presented to the Faculty

of Princeton University

in Candidacy for the Degree

of Doctor of Philosophy

Recommended for Acceptance

by the Department of

Mechanical and Aerospace Engineering

November, 2009

Abstract

Today there is a rapidly expanding and vibrant community of scientists interested in the phenomenon of collective behavior. Collective behavior holds clues to the evolution of social dynamics in animal or human groups, and also for the development of novel technological solutions, from autonomous swarms of exploratory robots to smart grids that reliably distribute electricity to consumers in a dynamic fashion. In this dissertation we study the dynamics and control of multi-agent systems in both the engineered and the natural setting.

Focusing first on the engineered setting, we derive provable, distributed control laws for stabilizing and changing the shape of a formation of vehicles in the plane using dynamic models of tensegrity structures. Tensegrity models define the desired, controlled, multi-vehicle system dynamics, in which each node of the tensegrity structure maps to a vehicle and each interconnecting strut or cable in the structure maps to a virtual interconnection between vehicles. Our method provides provably well-behaved changes of formation shape over a prescribed time interval. A designed path in shape space is mapped to a path in the parametrized space of tensegrity structures, and the vehicle formation tracks this path with forces derived from the time-varying tensegrity model.

Turning our attention to the natural setting, we then present and study Lagrangian models to investigate the mechanisms of decision-making and leadership in animal groups. We study the motion dynamics of a population that includes "informed" individuals with conflicting preferences and "uninformed" individuals without preferences. This work is the result of an interaction between complex discrete-time models developed by biologists that

produce highly suggestive simulations, and continuous-time models that, though simpler and less suggestive, allow for a thorough investigation of the dynamics in a general context with a complete exploration of parameter space, thus allowing us to uncover unifying principles of motion.

Acknowledgements

First, I would like to thank my advisor Professor Naomi Leonard for giving me the opportunity to work with her, and for her constant support and inspiration. I am particularly grateful for her openness to new ideas and her encouragement to define my own research topics.

I would like to thank the principal readers of this dissertation, Professor Simon Levin and Professor Jeremy Kasdin. Their comments and feedback improved this dissertation immeasurably. My examiners Professor Philip Holmes and Professor Iain Couzin deserve many thanks for their time and interest.

Princeton is a unique academic institution where I had the privilege to meet and work with many great scholars. I thank Professor Simon Levin and Professor Philip Holmes for serving on my thesis committee and taking much of their precious time to discuss my research and provide me with their guidance. I am deeply grateful to Professor Iain Couzin and the members of his research group for their collaboration. The research presented here on collective behavior in animal groups would not have been possible without their contributions and insights. I would also like to acknowledge all my instructors at Princeton University for sharing their knowledge and passion. Thanks also to the many administrators who have helped me navigate my time in Princeton. I am especially grateful to Jessica O'Leary who is a source of constant support for all of us MAE graduate students, and who always has a nice word to say.

Apart from the academics, I also found in Princeton many friends. I want to thank particularly Laurent Pueyo for being no less than the best office mate one could possibly

imagine. *Un grand merci* to my dear friend Arthur Denner, it is a privilege to have you as a friend along with my other "Princeton uncle". I cannot thank you enough for going over every line of this dissertation; your facility with language and your generosity in sharing it with me not only improved the work at hand but also gave me skills that I will carry with me wherever I go.

I cannot thank my family enough; I know it was hard for them to see me leave for the other side of the Atlantic, but they nevertheless gave me their support. *Papa et Maman*, I would never be writing these lines without your love and encouragement, I hope to always be a source of joy and satisfaction for you. I thank my older brother and sister Olivier and Estelle and their families. I also thank my wife's parents Herbert and Ann Berezin for thinking of me as one of their own children.

Finally my last words go to my dear wife Shani, I cannot thank you enough for always being there and riding the ups and downs of the life of a graduate student always with a smile and comforting words. For a long time I wondered what led me to Princeton and not anywhere else in the world, but then I met you and it was all clear.

Contents

Chapter 1

Introduction

1.1 Motivation and Problem Statement

Collective behavior in the human, animal or engineered setting is a fascinating phenomenon. Whether it is behavioral economists trying to understand the decision-making process of market participants and its influence on market prices and returns, or biologists wondering how schooling fishes, flocking birds or swarming ants make rapid collective decisions on where to move or what task to perform in often variable and dangerous environments, or engineers trying to design collaborating teams of robots by emulating mechanisms observed in nature, the attention of many scientists has been captivated by the subject of collective behavior.

Today we are far from the "thought transference" abilities hypothesized by Selous in which a connectivity of individual minds is required to explain how tens of thousands of starlings come together to roost [106]. It is now accepted that individuals in animal groups make their movement decisions on the basis of local cues from both the environment and near neighbors [18], and that through its interactions with other individuals in the group, each individual gains access to information beyond its own cognitive abilities. The transfer of information in this way between group members creates collective behaviors that give the impression to a field observer that there exists a "collective mind" within the group

[17]. That is, through their simple interactions, individuals in a group collectively perform tasks without the need for a centralized control or global blueprint, as though endowed with a collective mind. This capability holds the solution to the decentralized control problem that engineers designing collaborating teams of mobile robots are to solve. The mechanisms through which the capabilities of a group of individuals become greater than the sum of the capabilities of its individual members provides a compelling model for the design of collaborating teams of mobile robots.

Cooperative teams of mobile robots have been deployed on land, sea and air to perform various tasks including searching and sampling both for commercial and for military applications. Recent efforts in cooperative control of groups of robots have focused on emulating collective behaviors observed in animal groups. This new multi-disciplinary effort has been beneficial to biologists and engineers alike. Mathematical techniques commonly used in the engineered setting help reveal fundamental mechanisms of collective behavior in the natural setting, and the mechanisms of animal collective behavior, once deciphered, provide new inspiration for design in engineering.

In this dissertation we study the dynamics and control of both engineered and natural systems. We first derive provable, decentralized control laws for stabilizing and smoothly changing the shape of a group of vehicles in the plane. Tensegrity structures are used to model the controlled multi-vehicle system dynamics, with each node in the tensegrity corresponding to a vehicle and each connecting element of the tensegrity corresponding to a virtual interconnection between a pair of vehicles. Then, turning our attention to the biological setting, we present and study models to investigate the mechanisms of decision-making and leadership in animal groups. We study the motion dynamics of a population that includes two subgroups that are "informed" such that individuals in each subgroup have a preferred direction and one subgroup that is "uninformed" such that individuals in this subgroup do not have a preferred direction of motion. This work is the results of an interaction between two types of models: complex discrete time models developed by biologists that produce highly suggestive simulations, and continuous time models that,

though simple and less suggestive, make it possible to explore the dynamics in a more general context, thus allowing us to uncover unifying principles of motion.

1.2 Survey of Related Work

The literature on topics related to this dissertation is vast, and the survey of related work that we present is therefore necessarily incomplete. Although in this dissertation the first chapters focus on multi-agent systems in the engineered setting while later chapters focus on multi-agent systems in the natural setting, we present our survey of related work in the opposite order. We first summarize research in modeling of aggregation and decision making in animal groups. We then summarize related research in coordinated control of robotic teams. This order is chosen as the research on multi-agent systems in the natural setting has tended to precede and inspire the research on multi-agent systems in the engineered setting.

1.2.1 Aggregation and Decision-making in Animal Groups

Aggregation Modeling: Most animal species live in groups, in the sense defined by Wilson as "any set of organisms, belonging to the same species, that remains together for a period of time, interacting with one another to a distinctly greater degree than with other conspecifics" [81]. The reasons why species have evolved to this social tendency have been extensively studied and are well understood. They include an increased chance of surviving predation, enhanced foraging, conservation of heat and such social benefits as finding a mate. See Chapter 2 in [57] for a full review of the benefits of group formation. The mechanisms of aggregation and cohesiveness of aggregated groups, however, are not as well understood. The modeling and analysis of these phenomena continue to generate considerable interest in the *ethology* community with many problems remaining open. *Self organization theory* has gone a long way in explaining the emergence of group behavior, suggesting that complex large-scale behaviors are the result of simple interactions among individuals in the group [43, 10]. Deriving the precise mechanism by which simple interactions produce complex

behaviors has proven difficult. One of the difficulties stems from the fact that patterns which are posited to emerge from individual behavior are observable only at the level of the population [42]. The observation that the same individual interaction may translate into different group behaviors under the influence of different environments complicates the problem, posing another challenge to uncovering aggregation mechanisms [30].

The dynamics of aggregation in animal groups that have been studied in the ethology literature have been described mainly with two types of models: Eulerian and Lagrangian. Eulerian models, also known as continuum models, describe a group using a continuous density measure. They characterize the behavior of the group by describing the dynamics of *group properties* such as population density or group size. The dynamics of the group properties are usually modeled with a set of partial differential equations. Abstracting to group properties has been a very appealing approach, given the availability of sophisticated mathematical tools to analyze such systems. Gueron and Levin modelled the dynamics of large wildebeest herds using an Eulerian approach [41]. Their model revealed a plausible mechanism for self organization that spontaneously produces front patterns. Front patterns predicted by this model were validated with aerial photos. The Eulerian approach has also been very successful in describing the mechanism of aggregation for dense species such as bacteria or for some insect swarms [37].

The Eulerian approach has its limitations however. It has not proven particularly well suited for modeling aggregation of groups of moderate to low density including some schools of fish and flocks of bird. Also, since in continuum models individual animals are not represented, their social interactions cannot be implemented directly. Many continuum models therefore describe social behavior using a heuristic interpretation of individual-based models or of data collected in observations; the partial differential equations for the group property of interest are formulated so as to include relevant diffusion, convection, and interaction terms. Aiming to avoid building a model based on heuristic interpretation, Grünbaum derived the formulation of a continuum model explicitly from a Lagrangian-type model [38]. This allowed him to directly implement relevant interactions between

individuals in the group.

Lagrangian models describe the group as a collection of discrete individuals interacting with each other and determine the trajectories of individual animals. The rules governing the group's movements are often described with a set of discrete time or continuous time ordinary differential equations incorporating physical laws (e.g., Newton's second law) and social rules (attraction, repulsion and tendency to align). Okubo, in paralleling Newtonian dynamics to diffusion processes in ecological systems, revealed the tendency of individuals to be both attracted to and align with others, but he did not discuss the tendency to move away from individuals that are too close [84]. Aoki's pioneering simulation study of schools of fish proved the relevance of all three aforementioned social rules suggesting that the main tendencies that individual fish adopt are attraction to and alignment with neighbors and repulsion to individuals presenting a risk of collision [3]. While a clear advantage of the Lagrangian approach is that it allows for implementation of specific behavioral rules, limited computing power for many years made it impossible to study those models to their full potential. Simulations of these models could only be performed on groups of few individuals and for short periods of time. With the advent of ever more powerful computers it is now possible to perform simulations on large numbers of individuals and for significant amount of time. Accordingly, Lagrangian models are now capturing more attention [130, 19].

Another advantage of the Lagrangian approach is that the simulated behavior can be visualized and in this way compared with the observed behavior of the natural systems they represent. Grünbaum et al. developed motion analysis hardware and software to precisely track in three dimensions the positions of fishes in small schools of four or eight fishes [39]. The authors used this framework to calibrate the parameters of the alignment force and attraction/repulsion force of their theoretical model [20]. More recently Bellerini et al. performed a large-scale observational study of flocks of starlings, reconstructing groups of up to three thousand birds [4]. The results of their field study supported the notion, assumed in most theoretical models, of a zone of repulsion around each individual. However, their

study suggested that interactions between individuals depend on "topological" distances (how many "birds away") rather than on metric distances as many models assume.

Information and Decision Making: Although animal groups are known to utilize social information [57], little is known about the mechanisms underlying decision-making and information transfer in groups, this despite the growing interest in collective phenomena in biology, engineering and psychology. Currently, research is being done to understand how animals use the behavior of other group members to make accurate decisions.

It has been shown that some animals species migrating in groups (especially birds), are born with genetic information of migratory directions [44]. In a classic field experiment, Perdeck displaced juvenile and adult starlings 800km in an airplane flight [92, 23]. It was shown that the juvenile starlings continued to migrate in the same direction that they had flown prior to displacement, whereas the adults compensated for the displacement by taking a different direction. However this type of genetic information of migratory direction has not been found in many species. Another type of elaborate mechanism used by individuals to make decisions is the famous waggle-dance that honeybees have been observed to use in recruiting members to visit food sources [66]. However such elaborate mechanisms are not observed in most groups of fish or birds [57]. For many species, it has been shown that only a few individuals with pertinent information, such as the knowledge of a migration route, of a source of food or of the efficient behavior to adopt, are necessary to successfully guide the group. Further, in many species, it is not possible to identify which individuals have information and whether it is reliable or not. In a controlled experiment, Reebs trained golden shiners to expect food at a given time and given location in the tank and showed that when introduced to a shoal of untrained golden shiners, the trained shiners were able to direct the shoal to the food source [96] without causing it to split. With a different controlled experiment involving guppy shoal, Swaney et al. showed further that familiar and well trained demonstrators were more efficient than unfamiliar and poorly trained demonstrator in guiding the shoal to a food source [119].

Animal groups may be constituted with informed individuals with conflicting informa-

tion. Convergence to a common decision such as direction of travel or other activity is described with the notion of *consensus*. In a recent paper, Couzin et al. revealed plausible mechanisms for decision making and leadership by using a discrete simulation of particles moving in the plane [19]. In this simulation, each particle represents an individual animal and the motion of each individual is influenced by the state of its neighbors (e.g., relative position and relative heading). Within this group, there are two subgroups of informed individuals and one subgroup of naive individuals; each subgroup of informed individuals has a preferred direction of motion that it can use along with the information on its neighbors to make decisions. It is shown that information can be transferred within groups even when there is no signaling, no identification of the informed individuals, and no evaluation of others' information. It was also observed that with two informed subgroups of equal population, the direction of group motion depends on the degree to which the preferred directions differ. For small disagreement, the group follows the average preferred direction of all informed individuals, while for large disagreement the group selects one of the two preferred directions. This model is more thoroughly studied in Chapter 4. Recent research has also suggested that *quorum response* may be a particular mechanism for such decision making. A quorum like behavior means that the probability of an individual performing a certain action increases dramatically when seeing a threshold number of other individuals performing this action. It has been shown to be relevant to decision-making in fish [132, 118], honeybees [104], ants [94] or cockroaches [2].

1.2.2 Coordination under Decentralized Control in Groups of Robots

The apparent effortlessness with which coordination under decentralized control emerges in natural systems, as reported in the previous section, has motivated engineers to seek to emulate such systems for the design of collaborative teams of robots. Two key parameters govern the possibility of achieving coordination under decentralized control in engineered multi-agent systems: sensing and inter-vehicle communication. Unlike their biological couterparts which can use their senses, refined through evolution, to take cues from the environement

and neighbors, robots have more limited sensing and communication technologies at their disposal. Our survey provides an overview of existing research on two types of coordination under decentralized control: first on consensus and synchronization, then on formation control.

Consensus and synchronization: Interest in the phenomenon of consensus and synchronization appeared in the computer science community during the 1980s. Bertsekas and Tsitsiklis designed models of distributed asynchronous computation in order to create efficient methods for parallel computating, strategies of distributed optimization, and distributed signal processing [128, 5, 127]. An important building block of all these methods is the "agreement algorithm" in which agents (e.g. signal processing units, computation units) reach consensus on a common value through each agent forming convex combinations of its current value and those of its neighbors. Reynolds in his 1987 seminal paper used such an "agreement algorithm" to propose a simple model of flocking, his motivation being to create computer animations realistically representing the motion of a flock of birds [97].

In the 1990s Viscek et al. demonstrated the relevance of Reynolds' work to particle physics by proposing a Lagrangian, discrete-time linear model to investigate the emergence of self-ordered motion in multi-particle systems with biologically motivated interactions [129]. In the Viscek model individuals traveling at constant speed head in the average direction of motion of their neighbors. The model presented in this now classic paper, which is actually a special case of the flocking model developed by Reynolds [97], catalyzed research efforts in the physics community around the topic of consensus dynamics. Toner and Tu developed an Eulerian model of flocking dynamics describing a large class of microscopic rules, including the ones utilized in the Viscek paper [125, 126]. Other studies of collective motion of self-propelled particles that are related to the Viscek model include [36, 35]. Savkin later implemented the Viscek model on groups of autonomous robots [102].

The behavior predicted by the Viscek model was explained theoretically by Jadbabaie et al. who treated it as a switched linear system and applied tools from algebraic graph theory and matrix analysis [48]. They were able to prove for a coordinated group of agents

behaving according to the "nearest neighbor" rules of the Viscek model, convergence to a common direction of travel under constraints on the switching times. Their worked sparked tremendous interest in the control theory community. Recognizing the relevance of graph theory, Olfati-Saber and Murray used "balanced graphs" to address the average-consensus problem [87] and produced an algorithm that is valid for multi-agent networks with fixed or switching topologies, with or without time-delays. Moreau extended the results in [48] and presented sufficient conditions on the communication topology that guarantee consensus, deriving them by supplementing the tools from graph theory with tools from systems-theory [74]. Moreau studied both discrete-time and continuous-time consensus models and presented sufficient conditions under which the equilibrium corresponding to all individual agents' converging to a common state value is uniformly exponentially stable. Moreau showed that the common value to which the agents converge depends on the initial condition. A key, non-intuitive result that Moreau demonstrated was that a more complete communication topology does not necessarily translate into a faster convergence and in some extreme cases may even cause loss of convergence. However, when the common state space shared by the agents is non-Euclidean and/or the dynamics of the agents are nonlinear, the results in Moreau [74] are only local. Scardovi et al. generalized Moreau's result to nonlinear dynamics on non-Euclidean space [103]. They studied the behavior of a network of N agents that each evolves on the circle $\mathcal{S}^1$, also known as the problem of consensus on the N-torus, and proposed an algorithm that achieves synchronization or balancing under mild connectedness assumptions on the communication graph. The convergence results proven in [103] are global.

The problem of consensus on the N-torus has been studied by many scientists in various contexts including biology [135], chemistry [59] and neuroscience [113] to understand and model periodic phenomena. The formulation of the problem of consensus on the N-torus used in many of these works was first presented by Kuramoto in his 1984 study of "chemical oscillations" [60]. The Kuramoto model describes the evolution in time of a group of coupled-phase oscillators with global interactions. Many variations of the Kuramoto model

have been studied. See [115, 1] for reviews of these variations. The Kuramoto model has recently played a critical role in our context of collective motion. Justh and Krishnaprasad developed a motion model in which vehicles travel at constant speed and are controlled by steering their direction of travel [49, 50]. This framework was successfully used by Sepulchre et al. to stabilize circular and parallel collective motion [108]. Extensions of these results assuming only limited communications between the steered particles were presented by the same authors in [107]. In the formulation of the steering control laws used in [108, 107] the coupling between particles is based on the Kuramoto model. In Chapters 5 and 6 of this dissertation, the particle models used to study leadership and decision-making are similar to the cooperative models used in [49, 50, 108, 107] with coupling between agents based on the Kuramoto model.

Formation Control: Also within the domain of decentralized control is the problem of formation control which is central to Chapters 2 and 3 of this dissertation. In the context of formation control, vehicle interactions are driven by the task they are required to perform. For example, for the design of mobile sensors carrying out collective sampling or searching tasks, the configuration of the group can be critical. Controlling the geometry and resolution of the vehicle formation, also referred to collectively as the "shape" of the formation, offers important advantages to performance and efficiency of data gathering and processing. Depending on the field being surveyed, smaller or larger formations might be more efficient and certain shapes of the group might be preferable for estimating field parameters such as gradients or higher-order derivatives from noisy measurements made by the mobile sensors. Ögren et al. presented a stable control strategy for groups of vehicles to move and reconfigure cooperatively to perform gradient climbing missions [83]. In this work optimal shapes were designed to minimize error. Zhang and Leonard, taking the results from Ögren et al. a step further, presented an algorithm for level set tracking where the shape of the group was dynamically controlled so as to minimize the least mean square error in gradient estimates of a scalar field [139, 140]. Shape control can be significant in other vehicle network tasks as well, for example, when vehicles need to coordinate their activity

in order to escort, carry or otherwise interact with objects in their environment.

The earliest work on formation control, which can be dated back at least to the 1960's, involved one dimensional strings of inter-connected vehicles. Motivated by the development of a high speed ground transport system, Levine and Athans presented an optimal linear feedback control law regulating the position and velocity of a densely packed string of high speed vehicles [65]. Other related work on the control of strings of vehicles includes [91, 70].

A method particularly relevant to the work presented in Chapters 2 and 3 that has proven successful in designing distributed control laws of multi-vehicle formations has involved the use of *artificial potential functions* [98, 85]. Initially, potentials were used solely to prevent collisions in the vehicle network. Wang used repulsive potential functions to reduce the possibility of collisions with other robots and obstacles but in this work, potentials were not used to achieve a desired formation [131]. In a related work, Khosla and Volpe used potentials to design the workspace of a manipulator; regions in the workspace to be avoided by the manipulator were modelled by repulsive potentials (energy peaks), and the regions into which the manipulator is to move were modelled by an attractive potential (energy valleys) [56].

Research on multi-robot path coordination using artificial potentials appeared later with Warren [133]. In this work, the planning of multi-robot paths is performed by mapping the real space of the robots into a configuration-space-time, with appropriate potential fields applied throughout in order to influence the paths of the robots. Leonard and Fiorelli presented a different framework for coordinated and distributed control of a multi-vehicle system using artificial potentials [63]. They supplemented the artificial potentials by introducing "virtual leaders" which are moving reference points to which vehicles respond much as they respond to other neighbors. These virtual leaders are used in the methodology to eliminate undesirable equilibria created by the artificial potentials and to manipulate the group behavior (e.g., translation and rotation of the formation). In this dissertation we map the vehicle formation to a virtual tensegrity structure and design the potentials in this structure in order to drive the shape of the formation.

Research on formation control has also drawn inspiration and tools from graph theory, which, as we have already discussed, has proven useful in the context of consensus and synchronization. Tabuada et al. modelled formations using formation graphs, i.e., graphs whose nodes represent the individual vehicle kinematics and whose edges represent the inter-vehicle constraints to be satisfied [120]. Fax and Murray described the interactions between vehicles using results on graph Laplacians [27]. They derived a Nyquist-like stability criterion for vehicle formation from the eigenvalues of the Laplacian matrix. Olfati-Saber and Murray utilized the notion of graph rigidity to study and manipulate (i.e., join or split) multi-vehicle formations [86]. Also inspired by the notion of graph rigidity, Eren et al. presented a systematic method of maintaining rigidity for a vehicle formation when a vehicle is lost [26]. Their method descibes how to minimally rearrange the connectivity of the formation while maintaining rigidity. Tensegrity structures studied in Chapter 2 can be treated as undirected graphs, and the stress matrix defined in equation (2.3) can be viewed as a weighted pseudo Laplacian.

1.3 Thesis Overview

Motivated by the resurgence of interest in group motion by engineers as well as biologists, this dissertation offers contributions to the analysis of control and dynamics of multi-agent systems in the engineered and natural settings. The dissertation is divided in two parts. In Chapters 2 and 3 we focus on the engineering setting and develop a mathematical framework to generate control laws that stabilize any desired group shape in the plane and allow for continuous reconfiguration of the group shape. In Chapters 4 through 6 where we focus on the natural setting, we develop and analyze mathematical models for leadership and decision making in the context of animal group motion. Some of the developments of this dissertation have been previously published or submitted for publication in archival journals. See [78, 80, 72]. Conference papers in which earlier versions of the results appeared include [77, 79]. Results presented in Chapters 4 and 6 have not yet appeared elsewhere.

In Chapter 2 we design control laws that drive vehicle formations into shapes with

forces that can be represented as those internal to tensegrity structures. We first give a brief history of the field of tensegrities and present existing methods for designing tensegrity structures. We then motivate the use of tensegrity structures for solving the problem of formation control. We go on to present two possible models for the forces of a tensegrity structure: Connelly's model [12] and an augmented version of it that we construct. For each model, the relationship between the parameters of the model and the equilibrium structure is formulated. We then present a smooth method for choosing the parameters of the augmented model in a way that makes an arbitrary shape stable. Stability of the desired shape is proven using the linearization of the controlled system. We illustrate the results with examples of the computation of the parameters and a discussion on the number of links between the nodes of a tensegrity that are necessary to realize a desired shape.

In Chapter 3 we again use the map between vehicles in a formation and nodes in a tensegrity structure to derive a control law for vehicles in a formation that enables a well-behaved reconfiguration between arbitrary planar shapes. The new control law, designed to make nodes follow a smooth path in the space of stable tensegrities, is defined as a smooth parameterization by time of the control law for stabilization of planar shapes that is presented in Chapter 2. Tools from the nonlinear systems theory literature are utilized to prove that the trajectory of the formation, in shape space, is close to the prescribed path and that it converges to the desired final shape. We then present numerical simulations of the time-varying control law and discuss its performance.

In Chapter 4 we investigate mechanisms of leadership and decision making in animal groups such as schools of fish or flocks of birds through the simulation and analysis of a discrete-time individual-based (i.e. Lagrangian) model developed by Couzin et al. in [19]. We consider a heterogeneous group of both informed individuals with conflicting preferences and uninformed individuals, i.e, individuals without preferences. We consider two variations of the discrete-time model presented in [19], one where the informed individuals have a fixed preferred direction of travel and another where the preference is a destination, referred to as a target. For each variation of this model we investigate the role of uninformed individuals

in the decision-making process highlighting both the drawbacks and the benefits of having uninformed individuals in the group.

In Chapter 5, we analyze a continuous-time model of a multi-agent system. This model is motivated by the simulation study in [19] also treated in Chapter 4, on the dynamics of leadership and decision making in animal group motion. In this model, each individual moves at constant speed in the plane and adjusts its heading in response to relative headings of others in the population. The population includes three subgroups - two "informed" subgroups in which individuals have a preferred direction of motion and one "uninformed" subgroup in which individuals do not have a preferred direction of motion. We present the model first in its general form and prove that it can be reduced to a three-dimensional system using a time-scale reduction argument. We then study the full phase space dynamics of the reduced model in a particular case, computing equilibria and proving stability and bifurcations. We conclude the chapter with an investigation of several extensions of the model to test its robustness through numerical simulations.

In Chapter 6, we derive and study the dynamics of a low-dimensional, deterministic, coordinated control system. This model, motivated by the observed deviations between the qualitative behavior of the discrete-time model presented in [19] and that of the continuous-time model presented in Chapter 5, relaxes two of that model's simplifying assumptions. We present the model first in its general form and prove that it can be reduced to a three-dimensional system using a time-scale reduction argument. However, unlike the model presented in Chapter 5 which has only one invariant manifold the model presented in this chapter has several, each characterized by a set of interaction gains between the different subgroups. For each invariant manifold, we determine whether they are attractive or not and for the manifolds that are attractive, we also describe the stable and unstable equilibria of the corresponding reduced model and interpret the stable motions in the context of animal group motion. We conclude the chapter by an extension of the model investigated numerically to test its robustness.

We conclude in Chapter 7 with a summary of the contributions of this dissertation and

suggest possible future lines of research motivated by the presented work.

Chapter 2

Shape Control and Tensegrity Structures

The tasks a mobile sensor network may need to perform include gradient climbing [83, 9], boundary tracking [139, 140] and surveillance [136]. For a network carrying out such sampling or searching tasks, efficient feedback and coordinated control over the formation of the sensors is critical. Depending on the field that is being surveyed, as well as the task that is being performed, certain shapes and sizes of the group are preferable. For a mobile sensor network moving through a time-varying environment, an ideal coordinated control design should enable the network to reconfigure itself in response to real time measurements. We seek in this chapter to present a method to systematically design control laws which use dynamic models of tensegrity structures to stabilize any desired planar shape, shape referring, in our case, to the scale and geometry of the group, i.e. the way the individual vehicles are arranged relative to one another rather than where the group is or how it is oriented. This work has appeared in [77, 78].

2.1 Background on Tensegrity Structures

2.1.1 Origins of Tensegrities

A number of people participated in the creation of the field of tensegrity structures, and, as with many other fields, the question of "paternity" of the concept is a little controversial. In 1948, the artist Kenneth Snelson built the first tensegrity structure while studying in North Carolina at Black Mountain College (Figure 2.1). Inspired by this original structure, Buckminster Fuller coined the word *tensegrity* by joining the two words *tension* and *integrity*. He also gave the first definition of a tensegrity, as "a structural-relationship principle in which structural shape is guaranteed by the finitely closed comprehensively continuous, tensional behaviors of the system and not by the discontinuous and exclusively local compressional member behaviors"[101]. In the late 1950's D.G. Emmerich, apparently unaware of the earlier works by Snelson and Fuller, built several "self-tensioning structures." He observed that these structures could be maintained in equilibrium with no external action applied and with all the cables in tension [24]. Emmerich is considered to be the pioneer of experimental work on tensegrity structures.

In the 1950's and 1960's, the early years of the field, tensegrity structures were viewed mainly as artistic sculptures. At the same time however, Snelson, Fuller, Emmerich, and others began to move beyond the aesthetic dimension and made some scientific observations; their work on tensegrities remained mostly empirical, and no rigorous analysis was performed [112, 32]. In 1976 Pugh wrote a book setting out practical rules for building tensegrity structures, constituting the first attempt to formalize earlier studies [95] . It was not until the 1980's, with the work of mathematicians such as Connelly, Roth and Whiteley, that rigorous analysis of tensegrities started to appear. Their work yielded important results in the theory of tensegrity frameworks, introducing the notions of prestress stability and super stability, as well as static, infinitesimal, first and second-order stability, and contributing to significant discoveries in the field of rigid graphs [12, 14, 13, 15, 100]. Around the same time, Motro, among others [75, 76], initiated research that focused on the

Figure 2.1: The plywood X-Piece built by Kenneth Snelson in 1948. It is considered to be the first prestressed tensegrity ever built.

dynamics of tensegrity structures. They were able to determine the dynamic characteristics of a tensegrity prototype by applying a harmonic excitation on one node and measuring the dynamic response of the other nodes. Mathematicians such as Oppenheim and Williams took the study of these dynamics further. They proved closed-form analytical solutions for the vibrations and damping of simple tensegrity structures [134, 88]. During the 1990's these structures caught the attention of the control theory community, among them Skelton and Sultan, who went on to develop the concept of controllable tensegrity structures [111, 117, 116]. Inspired by this concept of controllable structures, civil and aerospace engineers began, in more recent years, to use tensegrity structures for the construction of deployable domes, bridges, space constructions, and morphing wings, drawn by the aesthetic appeal of these constructions as well as by their structural properties [73, 122, 33]. In biology, some scholars argue that tensegrity is a fundamental element of the building architecture of life [137, 47].

2.1.2 Analysis and Design Methods for Tensegrity Structures.

A major obstacle in the production of systematic design methods for tensegrity structures has been the determination of the equilibrium configuration, i.e. the geometrical configuration, given a set of nodes and edges, at which the shape of the structure is maintained with no outside force. This problem, known as the form-finding problem, has been a significant focus in tensegrity literature. Snelson, Fuller and Emmerich used a trial and error geometric approach to find a large number of possible equilibrium configurations. These configurations, consisting almost exclusively of regular convex polyhedra, were classified by Pugh [95].

Other scientists took a more formal approach to develop form-finding methods for tensegrity structures. Tibert and Pellegrino classified these methods in two families, the kinematical methods and the statical methods, and analyzed them to find each one's advantages and limitations [123, 122]. Their analysis revealed that some of the methods were equivalent. Among the statical methods, the Energy method developed by Connelly has been a great inspiration to our work. In the remainder of this section we summarize some of Connelly's key findings [12, 13, 14, 15].

In his 1999 paper, Connelly observed: "there are many inequivalent, but related definitions of rigidity and/or stability" [13]. Indeed his main contribution to the field has been to rigorously define as well as relate the different types of both rigidity and stability for tensegrity frameworks. A key step in defining and relating these different stability and rigidity notions is to define and exploit a potential energy for a tensegrity structure. Following Connelly's notations, let a configuration of N points in a d dimensional space be described by

$$\mathbf{q} = \begin{pmatrix} \vec{q}_1 & \cdots & \vec{q}_N \end{pmatrix}.$$

A tensegrity framework $G(\mathbf{q})$ is a signed graph $(V; E_-, E_0, E_+)$, where V is the set of nodes in the structure, E_- is the set of cables, E_0 is the set of bars, E_+ is the set of struts and $\mathbf{q} \in \mathbb{R}^{dN}$ is the characterization of the tensegrity structure in absolute space such that each $\vec{q}_i \in \mathbb{R}^d$ corresponds to a vertex of G.

Tensegrities with the same shape and edges should be viewed as identical. Shape refers to the way the nodes are arranged relative to one another regardless of where the structure is or how it is oriented. Thus, a given shape can be associated with an equivalence class containing an infinite number of absolute position vectors. As we defined in [78], let $\vec{q}_c = (1/N)\sum_{i=1}^{N}\vec{q}_i$ be the center of mass of the tensegrity. For two configurations $\mathbf{q}^1 \in \mathbb{R}^{dN}$ and $\mathbf{q}^2 \in \mathbb{R}^{dN}$, we define the equivalence relation $\mathcal{R}$ as

$$\mathbf{q}^1\mathcal{R}\mathbf{q}^2 \Longleftrightarrow \exists(R,\vec{t}) \in SE(d) \text{ and}$$
$$\mathbf{q}^2 = (\mathbf{q}^1 \text{ after rigid rotation about } \vec{q}_c^{\,1} \text{ by } R \text{ and translation by } \vec{t}).$$

An element of $SE(d)$ is a rigid motion and so any two configurations in the same equivalence class $\mathcal{R}$ have the same shape. We can therefore identify a given shape with the equivalence class $[\mathbf{q}^e] = \{\mathbf{q} \in \mathbb{R}^{dN} \mid \mathbf{q}^e\mathcal{R}\mathbf{q}\}$, where $\mathbf{q}^e$ is a representative configuration with the given shape. The class $[\mathbf{q}^e]$ can be identified with $SE(d)$. We note that the ordering of the nodes in the placement matters to classify shapes since two configurations $\mathbf{q}^1$ and $\mathbf{q}^2$ representing the same geometric shape but with nodes permuted will not be in the same equivalence class.

The edges in E_- correspond to cables, the edges in E_0 to bars, and the edges in E_+ to struts. Cables are always in tension, struts are always in compression, and bars can bear both tension and compression. In addition, physical constraints are assumed on the edges: cables cannot increase in length, struts cannot decrease in length, and bars cannot change length. For each $1 \le i \le N$ and $1 \le j \le N$, we define ω_{ij} to be the stress of the edge ij linking node i and j. This parameter is assumed to be symmetric i.e., $\omega_{ij} = \omega_{ji}$, and in the case that node i and j are not connected, we have $\omega_{ij} = 0$. This collection of stresses is denoted as one vector $\boldsymbol{\omega} \in \mathbb{R}^{\frac{N(N-1)}{2}}$; in the case that $\boldsymbol{\omega}$ has all components non-zero, the connection topology of the graph is complete. A stress $\boldsymbol{\omega}$ on a tensegrity framework is a *proper self stress* if the following three conditions are satisfied [15]:

1. $\omega_{ij} \ge 0$ for cables i.e. $ij \in E_-$

2. $\omega_{ij} \le 0$ for struts i.e. $ij \in E_+$

3. $\sum_{j=1}^{N} \omega_{ij}(\mathbf{q}_j - \mathbf{q}_i) = 0 \ \forall i \in \ \{1, \cdots, N\}$.

A tensegrity is said to be *prestress stable* if it has a strict proper self stress (i.e., a proper self stress with all inequalities strict) such that a certain energy function has a local minimum at the given configuration [15]. Connelly defines a potential energy and states sufficient conditions on the defined potential for prestress stability [12]. Given a stress $\boldsymbol{\omega}$, we have

$$V(\mathbf{q}) = \frac{1}{2} \sum_{i=1}^{N} \sum_{j=i+1}^{N} \omega_{ij} \|\vec{q}_j - \vec{q}_i\|^2 \tag{2.1}$$

where $\vec{q}_i \in \mathbb{R}^d$ is the position vector of node i, $\mathbf{x} = (x_1, \ldots, x_N)^T$, $\mathbf{y} = (y_1, \ldots, y_N)^T$, $\mathbf{z} = (z_1, \ldots, z_N)^T$ and $\mathbf{q} = \begin{pmatrix} \mathbf{x} \\ \mathbf{y} \\ \mathbf{z} \end{pmatrix}$. (From now on we write $\sum_{i<j}$ to represent $\sum_{i=1}^{N} \sum_{j=i+1}^{N}$.) From the Energy Principle, if such a potential has a local minimum at $\mathbf{q}^e$ which is isolated up to rigid transformation, then the tensegrity framework $G(\mathbf{q}^e)$ is prestress stable [12, 13].

In order to make the search for critical points of the potential $V(\mathbf{q})$ more systematic [77, 78], the potential (2.1) is rewritten as the following quadratic form:

$$V(\mathbf{q}) = \frac{1}{2} \mathbf{q}^T (\Omega \otimes I_3) \mathbf{q}, \tag{2.2}$$

where I_3 is the 3×3 identity matrix, $\Omega \otimes I_3$ is the $3N \times 3N$ block diagonal matrix $\begin{pmatrix} \Omega & 0 & 0 \\ 0 & \Omega & 0 \\ 0 & 0 & \Omega \end{pmatrix}$ and the elements of Ω are given by

$$\Omega_{ij} = \begin{cases} \sum_{j=1}^{N} \omega_{ij} & \text{if } i = j \\ -\omega_{ij} & \text{if } i \neq j. \end{cases} \tag{2.3}$$

This matrix Ω introduced by Connelly in [12] is called the *stress matrix*. The stress matrix is an $N \times N$ symmetric matrix, and the N-dimensional vector $\mathbf{1} = \begin{pmatrix} 1 & \ldots & 1 \end{pmatrix}^T$ is in the kernel of Ω . As mentioned earlier, a sufficient condition for the tensegrity framework to be prestress stable in a configuration $\mathbf{q}^e$ is that the quadratic form $V(\mathbf{q})$ have a local minimum

at $\mathbf{q}^e$. The positive definiteness of $V(\mathbf{q})$ is directly related to that of Ω, but we cannot expect strict positive definiteness as we already noted that $\mathbf{1} \in \ker(\Omega)$. In addition, the necessary condition that ω be a proper self stress can be rewritten as

$$(\Omega \otimes I_3)\mathbf{q}^e = 0. \tag{2.4}$$

This means that the kernel of Ω should be at least $d+1$ dimensional to make $\mathbf{q}^e$ a prestress stable configuration.

Connelly defined a stronger type of prestress stability called *super stability* which requires prestress stability with the additional condition that Ω be positive semidefinite with maximal rank, i.e. $\text{rank}(\Omega) = N - d - 1$. Hence, to design a super stable tensegrity framework, one must find a set of stresses such that $\Omega \geq 0$ and $\dim(\ker(\Omega)) = d+1$. Connelly was able with this characterization to create and analyze super stable tensegrity frameworks in the shape of any strictly convex polygons. We will use this characterization in Section 2.3 and adapt them to our setting and motivating application.

2.2 Tensegrity Structures and the Shape Control Problem

Our goal to design control laws that drive vehicle formation into shapes with forces that can be represented as those internal to tensegrity structures is motivated by the already existing use of tensegrity structures as controllable structures [111, 116, 117]. Skelton and his collaborators who developed the concept of controllable tensegrity structures [111] promoted them as a "new class of smart structures." They argued that tensegrity structures present promising opportunities for control design, with the edges "simultaneously perform-[ing] the functions of strength, sensing, actuating and feedback control." In addition, tensegrity structures are deployable as Tibert has shown [122], meaning that they are capable of large displacements, making them attractive for modeling a reconfigurable mobile sensor network. These large displacements, as Skelton argued, can be achieved, moreover, with little change in the potential energy of the structure [110]. This observation from Skelton and his collaborators is justified by the fact that shape changes of tensegrity structures are achieved by

changing the equilibrium of the structure, thus removing the need of control energy to hold the new shape against the previous equilibrium. It suggests that a reconfigurable mobile sensor network controlled with forces that can be represented as those internal to a tensegrity structures would be energy efficient. It was further shown that the prestress nature of tensegrity structures is critical in maintaining the shape in the presence of external forces [109].

We define a one-to-one mapping between the mobile sensor network and a tensegrity structure as follows [77, 78]: each node of the tensegrity structure is identified with one vehicle of the network and the edges of the structure correspond to communications and directions of forces between the vehicles. If an edge is a cable, the force is attractive; if the edge is a strut, the force is repulsive. The magnitude of the forces depends on the tensegrity structure parameters as well as the relative distance between the vehicles associated with the edge. This mapping implies that each vehicle is modeled as a point mass with double integrator dynamics. The point-mass model may appear somewhat simplistic as it seems to ignore the challenges of controlling the detailed dynamics of each of the individual vehicles. However, in practical experiments such as AOSN (Autonomous Ocean Sampling Network), involving design and implementation of coordinated control for a network of autonomous underwater vehicles deployed in the ocean, decoupling the design of the coordinating control strategy from the lower-level, individual-based trajectory tracking control has proven to be possible and also critical [29]. We thus focus our efforts on the coordinated trajectory design problem of a group of point masses with double-integrator dynamics.

As we described in the previous section, the form-finding problem has been a major focus of the tensegrity literature. In order to solve our shape control problem, we essentially have to solve a "reverse engineering" problem, i.e., determine a set of edges and a model for the forces that realizes any desired shape. Connelly has proven a conjecture that provides a means to systematically design stable planar tensegrities in the shape of any strictly convex polygon [12]. Connelly's result is valid however only if physical constraints on the edges of the tensegrity framework are assumed. In our virtual setting, these constraints associated

with physical struts and cables have to be relaxed. The restrictions that cables do not increase in length and struts do not decrease in length, cannot be imposed as constraints on the distances between pairs of vehicles that are not physically connected. For the same reason, it is not possible for us to use bars in the tensegrity framework we design. As we will show, this requires us to modify Connelly's model by augmenting it. The augmented model is used to stabilize tensegrities of any arbitrary planar shape and is not limited to strictly convex polygons. However, in comparison to Connelly's results, our systematic method produces a tensegrity framework with often a greater number of edges required. The issue of the number of edges required to realize a given shape is further discussed in Section 2.5.

2.3 Mathematical Models for the Dynamics of a Tensegrity

In this section we describe two possible models for the forces of a tensegrity structure in the plane, Connelly's and our augmented version of it. For each of these models we determine the equations of motion and the potential of the structure as well as the equilibrium condition, i.e., the relationship between the choice of cables, struts and parameters for the corresponding model and its equilibria. We described this first in [77, 78]. In Connelly's model, presented in Section 2.1.2, the edges are modeled as linear springs with zero rest length. Cables have a positive spring constant while struts have a negative one [12, 14]. Hence, as we noted in Section 2.1.2, shape control cannot be achieved with this model in the constraint free approach we are considering. In the absence of the cable and strut constraints, Connelly's model does not yield an isolated equilibrium but a continuum of equilibria, allowing for arbitrary stretching and shrinking of a tensegrity in the plane. To isolate planar tensegrities without assuming any constraints on the distances between the agents, it is necessary to modify the model. We propose a second model built as an augmented version of Connelly's model. In this model the edges are modeled as springs with finite, nonzero rest length. Cables are always longer than their rest length, i.e., in tension; struts are always shorter than their rest length, i.e., in compression.

2.3.1 Connelly's Model

This model for the forces of a tensegrity is derived from Connelly's potential energy defined in Section 2.1.2 specialized in the plane. The force $\vec{f}_{i\to j} \in \mathbb{R}^2$ applied to node j as a result of the presence of node i is derived from the defined potential (2.2) and is given by

$$\vec{f}_{i\to j} = \omega_{ij}(\vec{q}_i - \vec{q}_j) = -\vec{f}_{j\to i}. \tag{2.5}$$

Using the force model (2.5), we derive the equations of motion for each node of the tensegrity. We introduce in the system a linear damping of the form $-\nu\dot{\vec{q}}_n$, where $\nu > 0$ is the damping coefficient. The equations of motion for the nodes of the tensegrity structure in a Cartesian planar reference frame are computed from Hamilton's equations as

$$\begin{cases} \dot{x}_i = p_i^x \\ \dot{y}_i = p_i^y \\ \dot{p}_i^x = -\nu p_i^x - \dfrac{\partial V}{\partial x_i} \\ \dot{p}_i^y = -\nu p_i^y - \dfrac{\partial V}{\partial y_i} \end{cases} \quad \forall i \in \{1, ..., N\}, \tag{2.6}$$

where $V(\mathbf{q}) = \mathbf{q}^T(\Omega \otimes I_2)\mathbf{q}$ and, where (p_i^x, p_i^y) are the momenta of the i^{th} unit mass particle, respectively, in the x- and the y-directions. From now on the following notations will be used: $\mathbf{q} = (\mathbf{x}, \mathbf{y}) \in Q = (\mathbb{R}^2)^N$ is an element in the configuration space and $\mathbf{z} = (\mathbf{q}, \mathbf{p}) = (\mathbf{x}, \mathbf{y}, \mathbf{p}^x, \mathbf{p}^y) \in T^*Q = (\mathbb{R}^4)^N$ is an element in the cotangent bundle, where $\mathbf{p}^x = (p_1^x, ..., p_N^x)$ and $\mathbf{p}^y = (p_1^y, ..., p_N^y)$.

Our goal is to solve for and stabilize the tensegrity structure such that a desired shape $[\mathbf{q}^e]$ is a stable equilibrium of the system. This requires solving for the stresses ω_{ij}. In the case where $\omega_{ij} = 0$ is computed for some ij, it is interpreted that nodes i and j are not connected. $\mathbf{z}^e$ is an equilibrium of (2.6) if and only if $\mathbf{p}^x = \mathbf{p}^y = \mathbf{0}$ and $\mathbf{q}^e = (\mathbf{x}^e, \mathbf{y}^e)$ is a critical point of the potential $V(\mathbf{q})$. Since the potential $V(\mathbf{q})$ only depends on the relative positions of nodes, then $\mathbf{q}^e$ is an equilibrium shape of (2.6) if and only if every $\mathbf{q} \in [\mathbf{q}^e]$ is an equilibrium shape of (2.6). Let $[\mathbf{z}^e] = ([\mathbf{q}^e], \mathbf{0}, \mathbf{0})$, it follows that $\mathbf{z}^e$ is an equilibrium of (2.6) if and only if every $\mathbf{z}^e \in [\mathbf{z}^e]$ is an equilibrium of (2.6).

Using the expression of the potential from (2.2) we derive a simple relationship between the choice of stresses ω_{ij} and the equilibria of the model. The critical points of (2.2) and hence the equilibrium shapes of (2.6) are given by

$$\mathbf{q}^T(\Omega \otimes I_2) = 0. \tag{2.7}$$

Since the stress matrix is symmetric, a placement $\mathbf{q}^e = (\mathbf{x}^e, \mathbf{y}^e)$ is a critical point of the potential $V(\mathbf{q})$ if and only if $\mathbf{x}^e$ and $\mathbf{y}^e$ are in the kernel of Ω. We note that, assuming $\omega_{ij} \geq 0$ for cables and $\omega_{ij} \leq 0$ for struts, (2.7) fulfills the last condition to make $\boldsymbol{\omega}$ a proper self stress. Recall that $\mathbf{1}$ is in the kernel of Ω. Assuming that the nodes are not all in a line, $\mathbf{x}^e, \mathbf{y}^e$ and $\mathbf{1}$ are linearly independent. We can conclude that with this model a combination of cables and struts can generate an equilibrium shape if and only if $\text{rank}(\Omega) \leq N - 3$. We assume from now on that $N \geq 4$. By choosing the stresses of the edges of the structure so that $\text{rank}(\Omega) = N - 3$, the kernel of the stress matrix Ω is exactly three dimensional, and we can prescribe the shape of the equilibrium. We note that choosing the parameters ω_{ij} such that $\Omega \geq 0$ makes $[\mathbf{q}^e]$ a super stable tensegrity structure.

However, in our constraint free approach, this model does not prescribe the size of the equilibrium configuration. Indeed if $\ker(\Omega) = \text{span}\{\mathbf{x}^e, \mathbf{y}^e, \mathbf{1}\}$ then $[\mathbf{q}^e] = [(\alpha\mathbf{x}^e, \beta\mathbf{y}^e)]$ is also an equilibrium shape $\forall \alpha, \beta \in \mathbb{R}$. For real tensegrities this is not a problem because the cable and strut constraints are incompatible with the shapes $[\mathbf{q}^e] = [(\alpha\mathbf{x}^e, \beta\mathbf{y}^e)]$ for $(\alpha, \beta) \neq (1, 1)$. In the virtual setting, however, where the same constraints cannot be imposed, we get a continuum of equilibria, which is not desirable. For example, if the prescribed shape for the tensegrity is a square, it will be the case that not only all squares but also all rectangles will be equilibria.

In order to use tensegrity structures in our virtual setting, we need to modify this model to isolate the equilibrium. In the next section we exploit the simple equation (2.7), derived using the linear model (2.5), that determines the geometry of the tensegrity as a function of the parameters ω_{ij}. We propose an augmented model for the forces along edges that isolates a shape, fixing both geometry and size.

2.3.2 Augmented Model

Modeling the edges as springs with zero rest length yielded, in the absence of physical constraints on the edges, a continuum of equilibria for the system (2.6), fixing only the geometry of the structure but not its size. To isolate the equilibrium of the size of the desired shape, we augment Connelly's model and make the edges linear springs with finite, nonzero rest length. In this augmented model, cables are always longer than their rest length, i.e., in tension, and struts are always shorter than their rest length i.e. in compression. For two nodes i, j we define

$$\vec{f}_{i\to j} = \alpha_{ij}\omega_{ij}\frac{r_{ij} - l_{ij}}{r_{ij}}(\vec{q}_i - \vec{q}_j) = -\vec{f}_{j\to i}. \tag{2.8}$$

Here $r_{ij} = \|\vec{q}_i - \vec{q}_j\|$ is the relative distance between nodes i and j, l_{ij} is the rest length of the spring that models the edge ij, ω_{ij} is the spring constant/stress from model (2.5), and α_{ij} is a scalar parameter that fixes the spring constant of model (2.8) for the edge ij. With these forces, the potential of a tensegrity framework is given by

$$\tilde{V}(\mathbf{q}) = \frac{1}{2}\sum_{i<j}\alpha_{ij}\omega_{ij}(r_{ij} - l_{ij})^2. \tag{2.9}$$

With the same damping used in (2.6), the equations of motion are

$$\begin{cases} \dot{x}_i = p_i^x \\ \dot{y}_i = p_i^y \\ \dot{p}_i^x = -\nu p_i^x - \sum_{j=1}^{N}\tilde{\omega}_{ij}(x_i - x_j) \quad \forall i \in \{1, ..., N\}, \\ \dot{p}_i^y = -\nu p_i^y - \sum_{j=1}^{N}\tilde{\omega}_{ij}(y_i - y_j) \end{cases} \tag{2.10}$$

where $\widetilde{\omega}_{ij}$ is given by

$$\widetilde{\omega}_{ij}(\mathbf{x}, \mathbf{y}) = \alpha_{ij}\omega_{ij}(1 - \frac{l_{ij}}{r_{ij}}). \tag{2.11}$$

Our goal again is to solve for and stabilize the tensegrity structure such that $[\mathbf{q}^e]$ is an equilibrium shape of the system (2.10), i.e., to find the relationship between the choice of parameters α_{ij}, l_{ij} and ω_{ij} and the equilibrium shapes of the system (2.10). As in the

previous model, since $\tilde{V}(\mathbf{q})$ only depends on the relative position of nodes, then $\mathbf{q}^e$ is an equilibrium shape of (2.10) if and only if every $\mathbf{q} \in [\mathbf{q}^e]$ is an equilibrium shape of (2.10). We likewise define $[\mathbf{z}^e] = ([\mathbf{q}^e], \mathbf{0}, \mathbf{0})$. Then $\mathbf{z}^e$ is an equilibrium of (2.10) if and only if every $\mathbf{z} \in [\mathbf{z}^e]$ is an equilibrium of (2.10). As for model (2.6), $\mathbf{z}^e$ is an equilibrium of (2.10) if and only if $\mathbf{p}^x = \mathbf{p}^y = \mathbf{0}$ and $\mathbf{q}^e = (\mathbf{x}^e, \mathbf{y}^e)$ is a critical point of the potential $\tilde{V}(\mathbf{q})$. The critical points of $\tilde{V}(\mathbf{q})$ are given by

$$\sum_{j=1}^{N} \alpha_{ij}\omega_{ij}(\vec{q}_j - \vec{q}_i)(1 - \frac{l_{ij}}{r_{ij}}) = 0, \;\; i = 1, \ldots, N. \tag{2.12}$$

From (2.12), an analogue of the stress matrix Ω is constructed. The new stress matrix is not a constant matrix and depends on the relative distances between pairs of nodes. The entries of the new stress matrix are given by

$$\widetilde{\Omega}_{ij}(\mathbf{x}, \mathbf{y}) = \begin{cases} \sum\limits_{j=1}^{N} \widetilde{\omega}_{ij}(\mathbf{x}, \mathbf{y}) & \text{if } i = j \\ -\widetilde{\omega}_{ij}(\mathbf{x}, \mathbf{y}) & \text{if } i \neq j \end{cases}$$

where $\tilde{\omega}_{ij}$, the stress of the edge ij (now state dependent), is defined by (2.11). The vector $\mathbf{1}$ is also in the kernel of $\widetilde{\Omega}$, $\forall\ (\mathbf{x}, \mathbf{y}) \in \mathbb{R}^{2N}$.

This new state dependent stress matrix is now used to characterize the equilibria of (2.10). To make a shape $[\mathbf{q}^e]$ a critical point of the potential, we need to pick (if possible) the parameters α_{ij}, l_{ij} and ω_{ij} so that for all $\mathbf{q} = (\mathbf{x}, \mathbf{y}) \in [\mathbf{q}^e]$,

$$\begin{aligned} \widetilde{\Omega}(\mathbf{x}, \mathbf{y})\mathbf{x} &= 0 \\ \widetilde{\Omega}(\mathbf{x}, \mathbf{y})\mathbf{y} &= 0. \end{aligned} \tag{2.13}$$

We show in the next section that it is possible to choose the parameters α_{ij}, l_{ij} and ω_{ij} such that equation (2.13) is solved and that $[\mathbf{z}^e] = ([\mathbf{q}^e], \mathbf{0}, \mathbf{0})$ is an isolated exponentially stable equilibrium set of (2.10).

2.4 Stabilization for a Desired Group Geometry

Our goal is to solve for and stabilize the tensegrity structure so that $[\mathbf{z}^e] = ([\mathbf{q}^e], \mathbf{0}, \mathbf{0})$ is a stable equilibrium set of (2.10) making $[\mathbf{q}^e]$ a stable shape of the tensegrity framework.

This requires us to find the parameters α_{ij}, l_{ij} and ω_{ij} that solve (2.13). We present in this section a systematic method to choose the parameters α_{ij}, l_{ij} and ω_{ij} to solve (2.13). Further, we prove that this choice of parameters makes $[\mathbf{z}^e] = ([\mathbf{q}^e], \mathbf{0}, \mathbf{0})$ an isolated locally exponentially stable equilibrium set of (2.10). These developments have been described in [77, 78].

2.4.1 Smooth Parameterization of the Model

For any desired group shape $[\mathbf{q}^e]$, we explain how to choose the parameters α_{ij}, l_{ij} and ω_{ij} to make $[\mathbf{q}^e]$ an isolated equilibrium shape of the system. As a first step we choose the parameters α_{ij} and l_{ij} for all i, j so that $\widetilde{\Omega}(\mathbf{x}^e, \mathbf{y}^e) = \Omega$. In order to make $\widetilde{\omega}_{ij}(\mathbf{x}^e, \mathbf{y}^e) = \omega_{ij}$, we choose α_{ij}, l_{ij} such that $\alpha_{ij}(1 - \frac{l_{ij}}{r^e_{ij}}) = 1$. This last equation is solved by picking

$$\begin{aligned} \alpha_{ij} &= \frac{\pi}{\arctan \omega_{ij}} \\ l_{ij} &= r^e_{ij} \left(1 - \frac{1}{\pi} \arctan \omega_{ij}\right). \end{aligned} \tag{2.14}$$

In the case where edge ij is a strut, then $\omega_{ij} < 0$, and equation (2.14) makes $\alpha_{ij} < 0$ and $l_{ij} > r^e_{ij}$. This is consistent with the assumption that a strut is modeled as a linear spring, with a positive spring constant $\alpha_{ij}\omega_{ij} > 0$, shorter than its rest length. In the case that edge ij is a cable, then $\omega_{ij} > 0$, and equation (2.14) makes $\alpha_{ij} > 0$ and $l_{ij} < r^e_{ij}$. This is consistent with the assumption that a cable is modeled as a linear spring, with a positive spring constant $\alpha_{ij}\omega_{ij} > 0$, longer than its rest length. The choice of l_{ij} and α_{ij} is not unique, but rather was chosen to make the vector field (2.10) a C^∞ map of ω_{ij} and r^e_{ij}. This result is critical in the next chapter to prove that the time varying control law that changes the shape of the formation from any initial shape to any final desired shape is well behaved.

We now show that the parameters ω_{ij} can be found independently of parameters α_{ij} and l_{ij}, such that $\ker(\Omega) = \text{span}\{\mathbf{x}^e, \mathbf{y}^e, \mathbf{1}\}$ and the nonzero eigenvalues of Ω are all strictly positive. This makes the equilibrium shape $[\mathbf{q}^e] = (\mathbf{x}^e, \mathbf{y}^e)$ an isolated minimum of the potential $\tilde{V}(\mathbf{q})$, i.e., our choices ensure that we have the right combination of struts and

cables to make $[\mathbf{q}^e]$ a stable equilibrium shape. The stress matrix Ω is symmetric; hence it has only real eigenvalues and can be diagonalized using an orthonormal basis. As mentioned previously, assuming that all the nodes are not in a line, then $\mathbf{x}^e, \mathbf{y}^e$ and $\mathbf{1}$ are linearly independent. We complete these three vectors with $N-3$ others and obtain a basis of $\mathbb{R}^N$. Then applying the Gram-Schmidt procedure to those vectors yields an orthonormal basis $(\mathbf{v}_1, \ldots, \mathbf{v}_N)$ for $\mathbb{R}^N$ that satisfies

$$\text{span}\{\mathbf{v}_1, \mathbf{v}_2, \mathbf{v}_3\} = \text{span}\{\mathbf{x}^e, \mathbf{y}^e, \mathbf{1}\}.$$

We now define the $N \times N$ diagonal matrix D with diagonal elements $(0, 0, 0, d_4, \ldots, d_N)$, where $d_i > 0 \; \forall i$, and the orthonormal $N \times N$ matrix $\Lambda = \begin{pmatrix} \mathbf{v}_1 & \cdots & \mathbf{v}_N \end{pmatrix}$. The matrix computed as $\Lambda D \Lambda^T$, is symmetric positive semi-definite with its kernel equal to $\text{span}\{\mathbf{x}^e, \mathbf{y}^e, \mathbf{1}\}$. Setting $\Omega = \Lambda D \Lambda^T$ determines values of stresses ω_{ij} that make the desired shape $[\mathbf{q}^e]$ a tensegrity structure. The choice of eigenvalues D and eigenvectors Λ for the stress matrix is not unique. In Section 2.5.2 we investigate, through an example, how the choice of D and Λ influences the resulting interconnection topology that is needed to achieve the desired shape.

We now prove that this choice of parameters makes $[\mathbf{z}^e]$ an isolated equilibrium set of (2.10).

Theorem 2.4.1 *Choosing the parameters α_{ij}, l_{ij} and ω_{ij} to solve (2.13) makes $[\mathbf{z}^e] = ([\mathbf{q}^e], \mathbf{0}, \mathbf{0})$ an isolated equilibrium set of (2.10).*

Proof: In order to prove this result, we show that $[\mathbf{q}^e]$ is an isolated critical point of $\tilde{V}(\mathbf{q})$ by proving that the second variation of $\tilde{V}(\mathbf{q})$, evaluated at $[\mathbf{q}^e]$ is a positive definite matrix except in the symmetry directions $SE(2)$. As we pointed out earlier, the potential $\tilde{V}(\mathbf{q})$ only depends on the relative distances between nodes. This implies that $\tilde{V}(\mathbf{q})$ and also the Lagrangian of the system are invariant under the action of the Lie group $SE(2)$ on the configuration space Q. With these symmetries, critical points of $\tilde{V}(\mathbf{q})$ are only isolated modulo $SE(2)$ transformation making $\delta^2 V(\mathbf{q}^e)$ not definite in these directions. The matrix

$\delta^2\tilde{V}(\mathbf{q}^e)$ is given by

$$\delta^2\tilde{V}(\mathbf{q}^e) = \begin{pmatrix} \Omega + L_{\omega x}(\mathbf{q}^e) & L_{\omega xy}(\mathbf{q}^e) \\ L_{\omega xy}(\mathbf{q}^e) & \Omega + L_{\omega y}(\mathbf{q}^e) \end{pmatrix} \tag{2.15}$$

where Ω is the stress matrix derived in equation (2.3) and the ijth element of each bloc matrix is

$$L_{\omega x}(i,j) = \begin{cases} -\alpha_{ij}\omega_{ij}\frac{(x_i-x_j)^2 l_{ij}}{r_{ij}^3} & \text{if } i \neq j \\ \sum\limits_{j=1, j\neq i}^{N} \alpha_{ij}\omega_{ij}\frac{(x_i-x_j)^2 l_{ij}}{r_{ij}^3} & \text{if } i = j \end{cases}$$

$$L_{\omega y}(i,j) = \begin{cases} -\alpha_{ij}\omega_{ij}\frac{(y_i-y_j)^2 l_{ij}}{r_{ij}^3} & \text{if } i \neq j \\ \sum\limits_{j=1, j\neq i}^{N} \alpha_{ij}\omega_{ij}\frac{(y_i-y_j)^2 l_{ij}}{r_{ij}^3} & \text{if } i = j \end{cases}$$

and

$$L_{\omega xy}(i,j) = \begin{cases} -\alpha_{ij}\omega_{ij}\frac{(x_i-x_j)(y_i-y_j) l_{ij}}{r_{ij}^3} & \text{if } i \neq j \\ \sum\limits_{j=1, j\neq i}^{N} \alpha_{ij}\omega_{ij}\frac{(x_i-x_j)(y_i-y_j) l_{ij}}{r_{ij}^3} & \text{if } i = j. \end{cases}$$

Lemma 2.4.2 *$\delta^2 V(\mathbf{q}^e)$ is a positive semi-definite matrix.*

Proof: We write $\delta^2 V(\mathbf{q}^e)$ as

$$\delta^2 V(\mathbf{q}^e) = M_1 + M_2 = \begin{pmatrix} \Omega & 0_N \\ 0_N & \Omega \end{pmatrix} + \begin{pmatrix} L_{\omega x} & L_{\omega xy} \\ L_{\omega xy} & L_{\omega y} \end{pmatrix}.$$

Recall that Ω is designed to be positive semi-definite, hence $M_1 \geq 0$. We then show that M_2 is positive semi-definite. By direct computation,

$$\begin{pmatrix} \mathbf{q}_x^T & \mathbf{q}_y^T \end{pmatrix} \begin{pmatrix} L_{\omega x} & L_{\omega xy} \\ L_{\omega xy} & L_{\omega y} \end{pmatrix} \begin{pmatrix} \mathbf{q}_x \\ \mathbf{q}_y \end{pmatrix} = \mathbf{q}_x^T L_{\omega x}\mathbf{q}_x + \mathbf{q}_y^T L_{\omega y}\mathbf{q}_y + 2\mathbf{q}_x^T L_{\omega xy}\mathbf{q}_y, \tag{2.16}$$

where $\mathbf{q}_x = (q_{x_1} \cdots q_{x_N})^T \in \mathbb{R}^N$, and $\mathbf{q}_y = (q_{y_1} \cdots q_{y_N})^T \in \mathbb{R}^N$. Each term of the sum can

be rewritten as

$$\begin{aligned}
\mathbf{q}_x^T L_{\omega x}\mathbf{q}_x &= \sum_{i=1}^{N}\sum_{j=1,j\neq i}^{N} q_{x_i}\frac{\alpha_{ij}\omega_{ij}(x_i-x_j)^2 l_{ij}}{r_{ij}^3}(q_{x_i}-q_{x_j}) \\
&= \sum_{i<j}\frac{\alpha_{ij}\omega_{ij}(x_i-x_j)^2 l_{ij}}{r_{ij}^3}(q_{x_i}-q_{x_j})^2, \\
\mathbf{q}_y^T L_{\omega y}\mathbf{q}_y &= \sum_{i=1}^{N}\sum_{j=1,j\neq i}^{N} q_{y_i}\frac{\alpha_{ij}\omega_{ij}(y_i-y_j)^2 l_{ij}}{r_{ij}^3}(q_{y_i}-q_{y_j}) \\
&= \sum_{i<j}\frac{\alpha_{ij}\omega_{ij}(y_i-y_j)^2 l_{ij}}{r_{ij}^3}(q_{y_i}-q_{y_j})^2, \\
\mathbf{q}_x^T L_{\omega xy}\mathbf{q}_y &= \sum_{i=1}^{N}\sum_{j=1,j\neq i}^{N} q_{x_i}\frac{\alpha_{ij}\omega_{ij}(x_i-x_j)(y_i-y_j) l_{ij}}{r_{ij}^3}(q_{y_i}-q_{y_j}) \\
&= \sum_{i<j}\frac{\alpha_{ij}\omega_{ij}(x_i-x_j)(y_i-y_j) l_{ij}}{r_{ij}^3}(q_{y_i}-q_{y_j})(q_{x_i}-q_{x_j}).
\end{aligned}$$

(2.16) can now be factored as

$$\mathbf{q}_x^T L_{\omega x}\mathbf{q}_x+\mathbf{q}_y^T L_{\omega y}\mathbf{q}_y+2\mathbf{q}_x^T L_{\omega xy}\mathbf{q}_y = \sum_{i<j}\frac{\alpha_{ij}\omega_{ij} l_{ij}}{r_{ij}^3}\Big((y_i-y_j)(q_{y_i}-q_{y_j})+(x_i-x_j)(q_{x_i}-q_{x_j})\Big)^2 \geq 0. \tag{2.17}$$

Equation (2.17) concludes the proof that $M_2 \geq 0$, and hence $\delta^2 V(\mathbf{q}^e) \geq 0$ $\square$

Lemma 2.4.3 *The kernel of $\delta^2 V(\mathbf{q}^e)$ is equal to*

$$\textit{span}\left\{\begin{pmatrix}\mathbf{1}\\ \mathbf{0}\end{pmatrix}, \begin{pmatrix}\mathbf{0}\\ \mathbf{1}\end{pmatrix}, \begin{pmatrix}-\mathbf{y}^e\\ \mathbf{x}^e\end{pmatrix}\right\}.$$

Proof: We write again $\delta^2 V(\mathbf{q}^e)$ as

$$\delta^2 V(\mathbf{q}^e) = M_1 + M_2 = \begin{pmatrix}\Omega & 0_N\\ 0_N & \Omega\end{pmatrix} + \begin{pmatrix}L_{\omega x} & L_{\omega xy}\\ L_{\omega xy} & L_{\omega y}\end{pmatrix}.$$

By Lemma 2.4.2, M_1 and M_2 are symmetric, positive semi-definite matrices, hence

$$\mathbf{q} \in \ker(\delta^2 V(\mathbf{q}^e)) \Longleftrightarrow \mathbf{q} \in \ker(M_1) \text{ and } \mathbf{q} \in \ker(M_2). \tag{2.18}$$

By design, $\ker(M_1) = \text{span}\{\mathbf{w}_1, \mathbf{w}_2, \mathbf{w}_3\}$; by direct computation, we check $\text{span}\{\mathbf{w}_1, \mathbf{w}_2, \mathbf{w}_3\} \in \ker(M_2)$. Using (2.18), we conclude that the kernel of $\delta^2 V(\mathbf{q}^e)$ is exactly spanned by $\{\mathbf{w}_1, \mathbf{w}_2, \mathbf{w}_3\}$. $\square$

We can now conclude the proof of the theorem by combining these two lemmas. By Lemma 2.4.3, the three linearly independent eigenvectors for the three zero eigenvalues are $\left\{ \begin{pmatrix} \mathbf{1} \\ \mathbf{0} \end{pmatrix}, \begin{pmatrix} \mathbf{0} \\ \mathbf{1} \end{pmatrix}, \begin{pmatrix} -\mathbf{y}^e \\ \mathbf{x}^e \end{pmatrix} \right\}$. These vectors correspond respectively to symmetries of translation along the x-axis and the y-axis and of rotation about the origin. In addition, Lemma 2.4.2 guarantees that all other eigenvalues of $\delta^2 V(\mathbf{q}^e)$ are strictly positive. Combining Lemma 2.4.2 and Lemma 2.4.3 concludes the proof of the theorem. $\square$

2.4.2 Stability Analysis

We now present the proof of the local exponential stability for the isolated equilibrium set $[\mathbf{z}^e]$ using the linearization of (2.10).

Theorem 2.4.4 $[\mathbf{z}^e] = ([\mathbf{q}^e], \mathbf{0}, \mathbf{0})$ *is a locally exponentially stable equilibrium set of (2.10).*

Proof: We prove local exponential stability for the isolated equilibrium set $[\mathbf{z}^e]$ using the linearization of (2.10). The Jacobian of (2.10) evaluated at $\mathbf{z}^e = (\mathbf{x}^e, \mathbf{y}^e, \mathbf{0}, \mathbf{0})$ is given by

$$\mathrm{D}g(\mathbf{z}^e) = \begin{pmatrix} 0_{2n} & I_{2n} \\ -\delta^2 V(\mathbf{q}^e) & -\nu I_{2n} \end{pmatrix}. \tag{2.19}$$

We show that this matrix is negative semi-definite and that the three zero eigenvalues correspond to the symmetry directions $SE(2)$. The linearization $\mathrm{D}g(\mathbf{z}^e)$ can be written as

$$\mathrm{D}g(\mathbf{z}^e) = \begin{pmatrix} \frac{1}{\nu}\delta^2 V(\mathbf{q}^e) & I_{2n} \\ -\delta^2 V(\mathbf{q}^e) & -\nu I_{2n} \end{pmatrix} + \begin{pmatrix} -\frac{1}{\nu}\delta^2 V(\mathbf{q}^e) & 0_{2n} \\ 0_{2n} & 0_{2n} \end{pmatrix} = B_1 + B_2.$$

By Lemma 2.4.2, B_2 is negative semi definite. To show that B_1 is also negative semi definite, we proceed to two changes of basis represented by the following two invertible matrices:

$$P_1 = \begin{pmatrix} \frac{1}{\nu} I_{2n} & \frac{1}{\nu} I_{2n} \\ 0_{2n} & I_{2n} \end{pmatrix}$$

$$P_2 = \begin{pmatrix} 0_{2n} & I_{2n} \\ I_{2n} & \frac{1}{\nu}\delta^2 V(\mathbf{q}^e)\left(\frac{1}{\nu}\delta^2 V(\mathbf{q}^e) - \nu I_{2n}\right)^{-1} \end{pmatrix}.$$

The representation of B_1 in the new basis is computed as

$$P_2^{-1}P_1^{-1}B_1P_1P_2 = \begin{pmatrix} \frac{1}{\nu}\delta^2 V(\mathbf{q}^e) - \nu I_{2n} & 0_{2n} \\ 0_{2n} & 0_{2n} \end{pmatrix}.$$

This matrix is negative semi definite $\forall \nu > \sqrt{\lambda_{max}(\delta^2 V(\mathbf{q}^e))}$, where $\lambda_{max}\left(\delta^2 V(\mathbf{q}^e)\right)$ is the largest eigenvalue of $\delta^2 V(\mathbf{q}^e)$. We now show by direct computation that the zero eigenvalues correspond to the $SE(2)$ symmetries.

$$\begin{pmatrix} \mathbf{0}_{2n} & I_{2n} \\ -\delta^2 V(\mathbf{q}^e) & -\nu I_{2n} \end{pmatrix} \begin{pmatrix} \mathbf{x} \\ \mathbf{y} \\ \mathbf{p}_x \\ \mathbf{p}_y \end{pmatrix} = \begin{pmatrix} \mathbf{0} \\ \mathbf{0} \\ \mathbf{0} \\ \mathbf{0} \end{pmatrix}$$

if and only if

$$\begin{pmatrix} \mathbf{p}_x \\ \mathbf{p}_y \\ -\delta^2 V(\mathbf{q}^e) \begin{pmatrix} \mathbf{x} \\ \mathbf{y} \end{pmatrix} - \nu I_{2n} \begin{pmatrix} \mathbf{p}_x \\ \mathbf{p}_y \end{pmatrix} \end{pmatrix} = \begin{pmatrix} \mathbf{0} \\ \mathbf{0} \\ \mathbf{0} \\ \mathbf{0} \end{pmatrix}$$

if and only if

$$\begin{pmatrix} \mathbf{x} \\ \mathbf{y} \\ \mathbf{p}_x \\ \mathbf{p}_y \end{pmatrix} \in \text{span}\{ \begin{pmatrix} \mathbf{1} \\ \mathbf{0} \\ \mathbf{0} \\ \mathbf{0} \end{pmatrix}, \begin{pmatrix} \mathbf{0} \\ \mathbf{1} \\ \mathbf{0} \\ \mathbf{0} \end{pmatrix}, \begin{pmatrix} -\mathbf{y}^e \\ \mathbf{x}^e \\ \mathbf{0} \\ \mathbf{0} \end{pmatrix} \}.$$

These three vectors correspond respectively to symmetries of translation along the x-axis and the y-axis and of rotation about the origin. $\square$

Local asymptotic stability can also be proven using the total energy of the system as a Lyapunov function. In the next chapter we utilize the exponential stability result for the equilibrium set $[\mathbf{z}^e] = ([\mathbf{q}^e], \mathbf{0}, \mathbf{0})$ to construct a well behaved time-dependent control law that enables the tensegrity to reconfigure itself between arbitrary planar shapes.

2.5 Examples and Simulations

In this section, we illustrate with examples the computation of the stress matrix and parameters α_{ij}, l_{ij} using the method developed in Section 2.4.1. We first look at Snelson's X tensegrity which is one of the simplest and most studied "super stable" tensegrity frameworks and show Matlab simulation results for the stabilization of its equilibrium shape. We next present a five node tensegrity structure and show how the freedom in the choice of the stress matrix Ω can be used to affect the resulting interconnection topologies.

2.5.1 Snelson's X Tensegrity Framework

Snelson's X tensegrity framework is one of the simplest tensegrities, it is the main component of the plywood X piece, the first 3 dimensional tensegrity structure built by Snelson in 1948 (Figure 2.1). For this tensegrity framework (Figure 2.2), a representative configuration of the desired shape is

$$\mathbf{q}^e = \begin{pmatrix} \mathbf{x}^e \\ \mathbf{y}^e \end{pmatrix} = \begin{pmatrix} 0 & 1 & 1 & 0 \\ 0 & 0 & 1 & 1 \end{pmatrix}.$$

Following the procedure describe in Section 2.4.1 with $D = \text{diag}\begin{pmatrix} 0 & 0 & 0 & 4 \end{pmatrix}$, we find the following, well known, expression for the stress matrix [12, 14, 123]:

$$\Omega = \begin{pmatrix} 1 & -1 & 1 & -1 \\ -1 & 1 & -1 & 1 \\ 1 & -1 & 1 & -1 \\ -1 & 1 & -1 & 1 \end{pmatrix}. \tag{2.20}$$

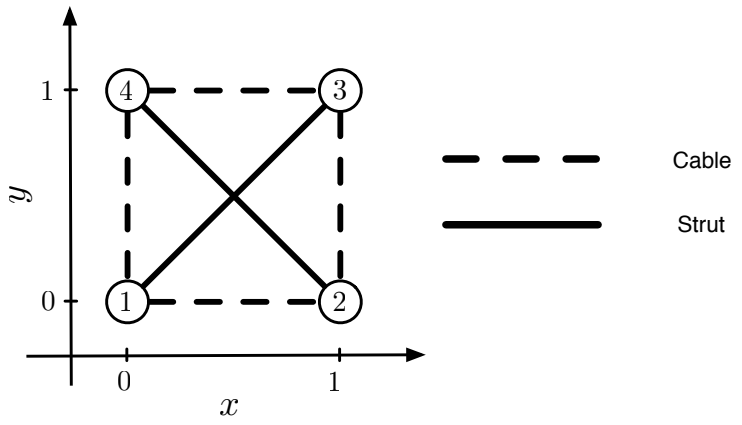

Figure 2.2: Snelson's X tensegrity framework, consists of four nodes (denoted by circles) in a square formation. A continuous network of cable form the edge of the square while a discontinuous network of struts connects across each diagonal of the square. The labels on the nodes define the ordering.

The computed values for the parameters α_{ij} and l_{ij} are

$$\alpha = \begin{pmatrix} 0 & 4 & -4 & 4 \\ 4 & 0 & 4 & -4 \\ -4 & 4 & 0 & -4 \\ 4 & -4 & 4 & 0 \end{pmatrix}$$
$$l = \begin{pmatrix} 0 & \frac{3}{4} & \frac{5\sqrt{2}}{4} & \frac{3}{4} \\ \frac{3}{4} & 0 & \frac{3}{4} & \frac{5\sqrt{2}}{4} \\ \frac{5\sqrt{2}}{4} & \frac{3}{4} & 0 & \frac{3}{4} \\ \frac{3}{4} & \frac{5\sqrt{2}}{4} & \frac{3}{4} & 0 \end{pmatrix}, \tag{2.21}$$

where the ij-th entry of α (respectively l) corresponds to α_{ij} (respectively l_{ij}). The corresponding tensegrity framework is graphed in Figure 2.2; it consists of four nodes (denoted by circles) in a square formation, a continuous network of cable on the edge of the square and a discontinuous network of struts connecting across each diagonal of the square.

Having computed all the parameters of the system (2.10), we now show a Matlab simulation for the controlled network of $N = 4$ vehicles with the parameters ω_{ij}, α_{ij} and l_{ij} values given by (2.20) and (2.21). The damping coefficient is set to $\nu = 1$, and the simulation of

the system is run from $t = 0s$ to $t = 20s$. The initial conditions are given by

$$\begin{pmatrix} x_1(0) & x_2(0) & x_3(0) & x_4(0) \\ y_1(0) & y_2(0) & y_3(0) & y_4(0) \\ \dot{x}_1(0) & \dot{x}_2(0) & \dot{x}_3(0) & \dot{x}_4(0) \\ \dot{y}_1(0) & \dot{y}_2(0) & \dot{y}_3(0) & \dot{y}_4(0) \end{pmatrix} = \begin{pmatrix} -1 & 2 & 0 & -2 \\ -1 & 1 & 2 & 1 \\ 1 & -2 & 3 & 0 \\ \frac{1}{2} & 0 & 2 & -1 \end{pmatrix},$$

where x_i, y_i have units of m and $\dot{x}_i, \dot{y}_i$ have units of m/s. Figure 2.3 shows plots of the positions for each of the four networked vehicles and Figure 2.4 shows plots of the velocities for each of the four networked vehicles, after some oscillations, convergence to a fixed shape is obvious. In Figure 2.5 snapshots of the tensegrity network are plotted at $t = 0$s, 0.25s, 2s and at $t = 20$. The prescribed shape $[\mathbf{q}^e]$ is indeed reached by the vehicle network but the structure is both translated and rotated from $\mathbf{q}^e$. This is due to the initial conditions and the changing linear and angular momentum of the system. It highlights the fact that we are only controlling the shape of the formation but not its position or orientation in absolute space.

2.5.2 A Five Vehicle Network Example

We now illustrate with a five node tensegrity network example the effect of the choices of eigenvalues D and eigenvector Λ of the stress matrix Ω on the resulting interconnection topology of the tensegrity realizing the desired shape. This study is reported in [77, 78]. It is known that stable tensegrity structures with N nodes require at least $2N - 2$ edges [14]. Connelly has proven a result that provides a means to systematically design stable planar tensegrities in the shape of any strictly convex polygon [12]. His method is designed to yield tensegrity structures with minimal number of edges. Our method allows us to generate tensegrity structures of any shape, convex or non-convex, but often yields interconnection topologies with number of edges greater than the proven lower bound. However, as we illustrate, it is possible in our method to use the freedom of choice in the eigenvalues and eigenvectors of the stress matrix to reduce the number of edges.

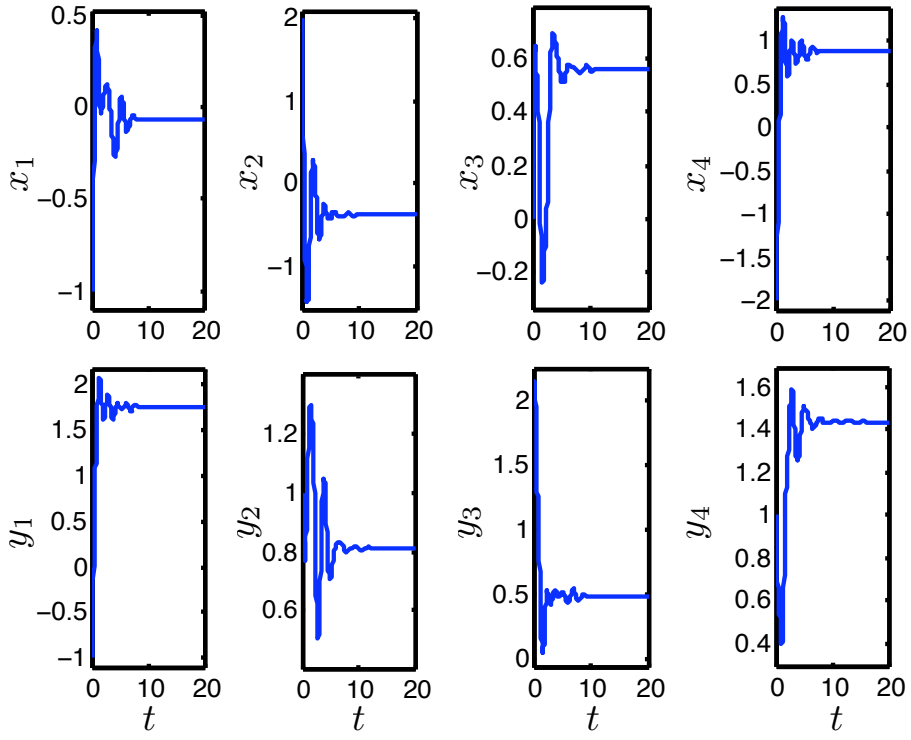

Figure 2.3: Plots of both cartesian coordinates for each networked vehicle controlled to the X tensegrity framework; convergence to a stable configuration is obvious.

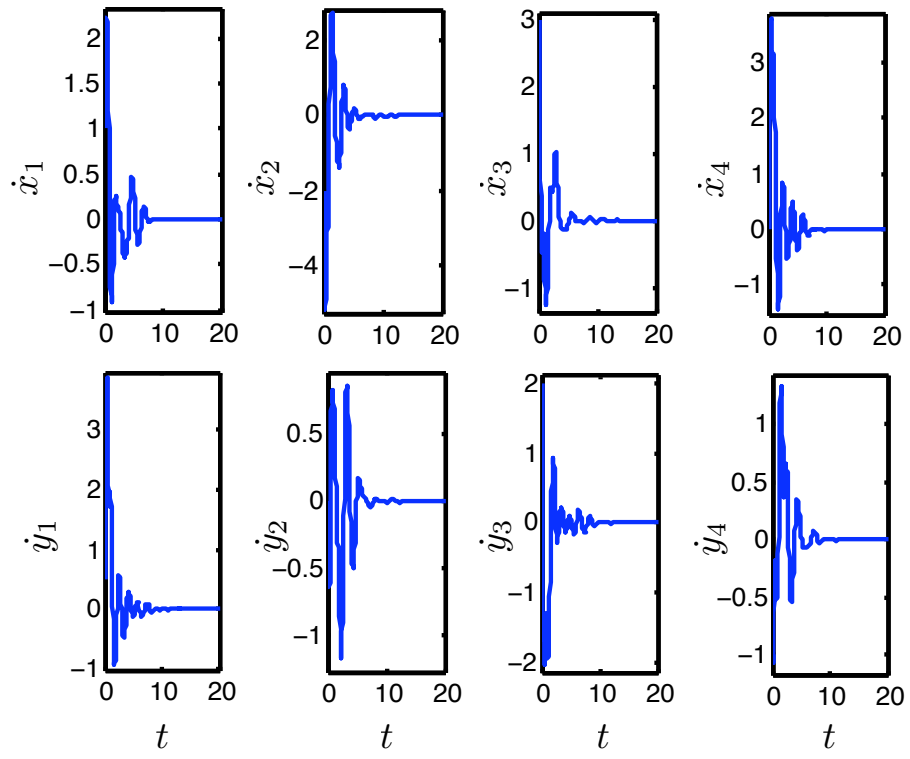

Figure 2.4: Plots of both cartesian velocities for each networked vehicle controlled to the X tensegrity framework; convergence to a static configuration is obvious.

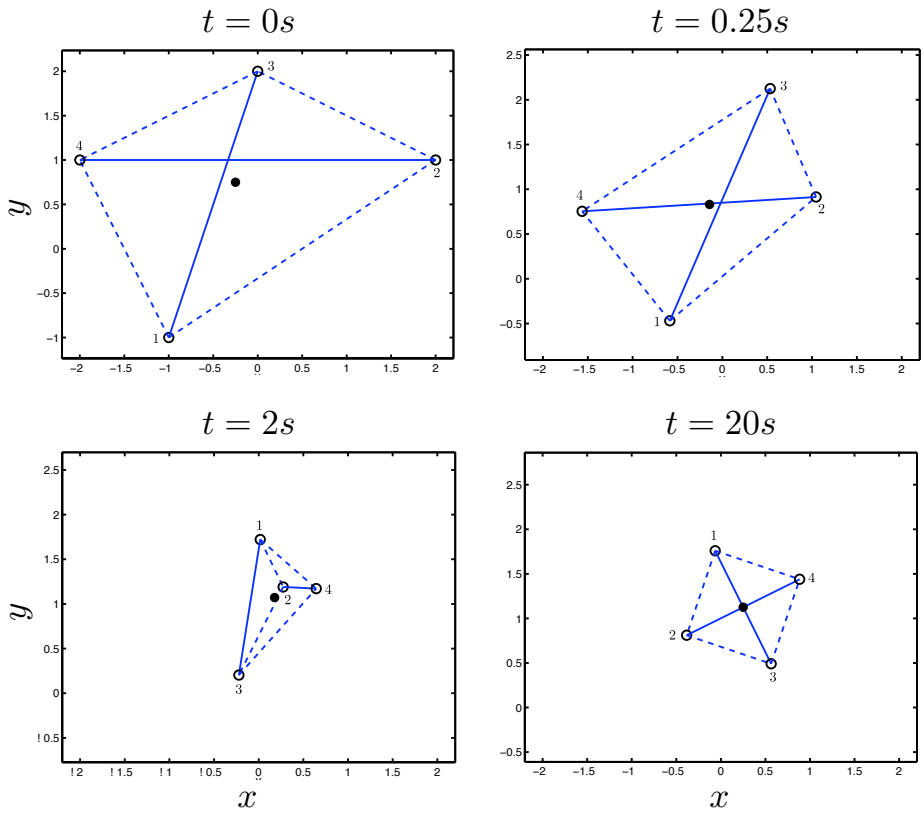

Figure 2.5: Snapshots of the tensegrity network at $t = 0$s, 0.25s, 2s and at $t = 20$. The prescribed shape $[\mathbf{q}^e]$ is indeed reached by the vehicle network but the structure is both translated and rotated from $\mathbf{q}^e$, highlighting that we are only controlling the shape of the formation but not its position and orientation in absolute space. The black dot represent the center of mass of the formation for each snapshot.

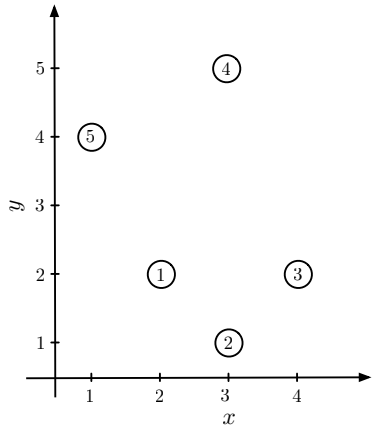

Figure 2.6: Five node configuration given by $\mathbf{x}^e = (2,3,4,3,1), \mathbf{y}^e = (2,1,2,5,4)$. The labels on the nodes define the ordering.

We consider the shape represented by the configuration

$$\mathbf{q}^e = \begin{pmatrix} \mathbf{x}^e \\ \mathbf{y}^e \end{pmatrix} = \begin{pmatrix} 2 & 3 & 4 & 3 & 1 \\ 2 & 1 & 2 & 5 & 4 \end{pmatrix} \tag{2.22}$$

and plotted in Figure 2.6. Following the method from Section 2.3.2 we take $D_1 = \mathrm{diag}(0,0,0,1,1)$ and

$$\Lambda_1 = \begin{pmatrix} \frac{\sqrt{5}}{5} & -\frac{3}{\sqrt{130}} & -\frac{\sqrt{182}}{39} & -\frac{\sqrt{518}}{222} & \frac{10\sqrt{74}}{111} \\ \frac{\sqrt{5}}{5} & \frac{2}{\sqrt{130}} & -\frac{\sqrt{182}}{26} & -\frac{\sqrt{518}}{37} & -\frac{3\sqrt{74}}{74} \\ \frac{\sqrt{5}}{5} & \frac{7}{\sqrt{130}} & -\frac{\sqrt{182}}{273} & \frac{43\sqrt{518}}{1554} & -\frac{2\sqrt{74}}{111} \\ \frac{\sqrt{5}}{5} & \frac{2}{\sqrt{130}} & -\frac{31\sqrt{182}}{546} & -\frac{13\sqrt{518}}{777} & \frac{5\sqrt{74}}{222} \\ \frac{\sqrt{5}}{5} & \frac{-8}{\sqrt{130}} & \frac{2\sqrt{182}}{182} & \frac{3\sqrt{518}}{259} & -\frac{2\sqrt{74}}{37} \end{pmatrix},$$

where the columns of Λ_1 constitute a basis of orthonormal eigenvectors obtained with the Gram-Schmidt procedure. The stress matrix $\Omega_1 = \Lambda_1 D_1 \Lambda_1^T$ is given by

$$\Omega_1 = \begin{pmatrix} \frac{11}{18} & -\frac{1}{3} & -\frac{1}{18} & \frac{1}{9} & -\frac{1}{3} \\ -\frac{1}{3} & \frac{1}{2} & -\frac{1}{3} & \frac{1}{6} & 0 \\ -\frac{1}{18} & -\frac{1}{3} & \frac{53}{126} & -\frac{17}{63} & -\frac{5}{21} \\ \frac{1}{9} & \frac{1}{6} & -\frac{17}{63} & \frac{23}{126} & -\frac{4}{21} \\ -\frac{1}{3} & 0 & \frac{5}{21} & -\frac{4}{21} & \frac{2}{7} \end{pmatrix}. \tag{2.23}$$

The tensegrity structure corresponding to this stress matrix, plotted in Figure 2.7(a) has an interconnection topology requiring 9 edges. To reduce the number of edges, we manipulate our choice of D and Λ so that $\Omega = \Lambda D \Lambda^T$ has entries identically equal to zero. Consider, for example, setting $D_2 = \text{diag}\begin{pmatrix} 0 & 0 & 0 & \frac{60}{253} & \frac{30}{253} \end{pmatrix}$ and

$$\Lambda_2 = \begin{pmatrix} 0 & 0 & \frac{\sqrt{14}}{6} & \frac{\sqrt{2}}{3} & -\frac{\sqrt{14}}{6} \\ \frac{1}{\sqrt{42}} & -\frac{2}{\sqrt{21}} & \frac{\sqrt{14}}{7} & -\frac{\sqrt{2}}{2} & 0 \\ \frac{4}{\sqrt{42}} & -\frac{2}{\sqrt{21}} & \frac{\sqrt{14}}{42} & \frac{\sqrt{2}}{3} & \frac{5\sqrt{14}}{42} \\ \frac{5}{\sqrt{42}} & \frac{2}{\sqrt{21}} & -\frac{\sqrt{14}}{21} & -\frac{\sqrt{2}}{6} & -\frac{2\sqrt{14}}{21} \\ 0 & \frac{3}{\sqrt{21}} & \frac{\sqrt{14}}{7} & 0 & \frac{\sqrt{14}}{7} \end{pmatrix}.$$

We compute the stress matrix:

$$\Omega_2 = \begin{pmatrix} \frac{25}{253} & -\frac{20}{253} & \frac{5}{253} & 0 & -\frac{10}{253} \\ -\frac{20}{253} & \frac{30}{253} & -\frac{20}{253} & \frac{10}{253} & 0 \\ \frac{5}{253} & -\frac{20}{253} & \frac{135}{1771} & -\frac{80}{1771} & \frac{50}{1771} \\ 0 & \frac{10}{253} & -\frac{80}{1771} & \frac{50}{1771} & -\frac{40}{1771} \\ -\frac{10}{253} & 0 & \frac{50}{1771} & -\frac{40}{1771} & \frac{60}{1771} \end{pmatrix}. \tag{2.24}$$

The tensegrity corresponding to this stress matrix, plotted in Figure 2.7(b) has an inter-

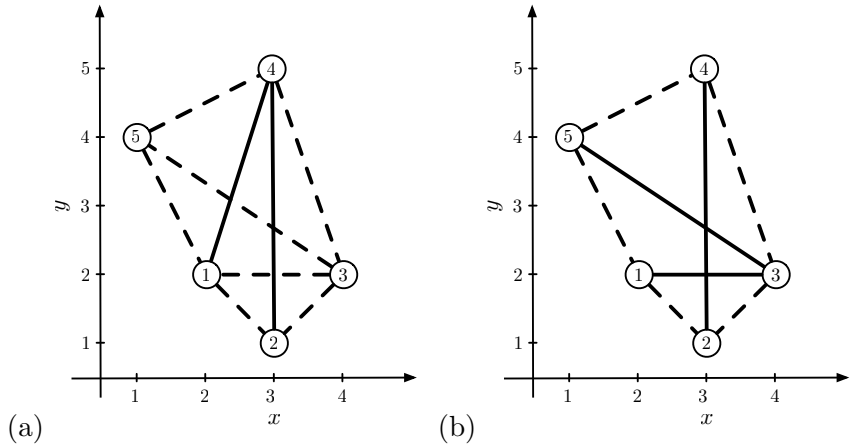

Figure 2.7: Tensegrity structures generated from the stress matrices (a) Ω_1, (b) Ω_2. Solid lines are struts and dashed lines are cables

connection topology requiring only $8 = 2 \times 5 - 2$ edges. The number of edges cannot be

reduced further since we have reached the lower bound proven in [14]. We note that not only the number of edges required is different between the tensegrities realized by Ω_1 and Ω_2 but also the nature of the edges. While both tensegrities have a continuous network of cables around, the tensegrity realized by Ω_1 has inside a discontinuous network of cables and strut and the tensegrity realized by Ω_2 has inside a discontinuous network of only struts. Tensegrities with a continuous network of cables around and a discontinuous network of struts is a common outcome of the method designed by Connelly in [14].

As the number of nodes increases, it becomes harder to systematically find a combination of eigenvalues and eigenvectors that yields a tensegrity with the minimum number of edges. However, as the above example illustrates, it may be possible to manipulate the choices of D and Λ to reduce the number of connections in a tensegrity derived using our method.

Our approach has significant advantages because it is systematic and smooth. We exploit these features in the next chapter, where we define a smooth parameterization (by time) of the control law (2.10), creating a systematic framework for smooth reconfiguration of tensegrity structures between arbitrary planar shapes.

Chapter 3

Group Reconfiguration and Tensegrity Structure

In the previous chapter, we created a framework to stabilize arbitrary planar formations by mapping vehicles of a network to nodes of a tensegrity structure and controlling the vehicles with the forces induced by the tensegrity's edges, modeled by (2.8). In this chapter, we take this result a step further and present a new control law for the nodes that enables a well-behaved reconfiguration between arbitrary planar shapes. The control law is designed to make the nodes follow a smooth path, in shape space, of stable tensegrities. This new control law is defined as a smooth parameterization over time of the control law for stabilization of planar tensegrities presented in the previous chapter, given by (2.10). In Section 3.1 we present the construction of the parameterized control law. In Section 3.2 we study the resulting controlled time-varying dynamical system and prove that the system is well behaved, i.e., that the trajectory stays close, in shape space, to the prescribed path and that it converges to the final shape. In Section 3.3 we present a numerical example of the implementation of the control law and discuss its performance. This work has appeared in [78].

3.1 Control Law for Shape Reconfiguration

Using the same notations as in Chapter 2, we define a desired starting shape $[\mathbf{q}_0^e]$ and a desired ending shape $[\mathbf{q}_f^e]$, each with the same number of nodes. Our goal is to design a control law that smoothly takes the structure from the shape $[\mathbf{q}_0^e]$ to the shape $[\mathbf{q}_f^e]$ over a given time interval. The proposed control law is constructed in two steps. First, we design in shape space a smooth path $[\mathbf{q}^e](t)$ such that $[\mathbf{q}^e](0) = [\mathbf{q}_0^e]$ and $[\mathbf{q}^e](\tau) = [\mathbf{q}_f^e]$, where τ is a parameter to be chosen that determines the speed of the reconfiguration. Second we develop a method to deduce the variations of parameters $\alpha_{ij}(t), l_{ij}(t)$ and $\omega_{ij}(t)$ that are necessary to make the tensegrity follow the planned path $[\mathbf{q}^e](t)$ in shape space. The smooth evolution of the parameters defines a smoothly time-varying control law.

3.1.1 Path Design in Shape Space

In this section, we design a smooth path of tensegrity shapes such that, given any initial and final shapes $[\mathbf{q}_0^e]$ and $[\mathbf{q}_f^e]$, $[\mathbf{q}^e](0) = [\mathbf{q}_0^e]$ and $[\mathbf{q}^e](\tau) = [\mathbf{q}_f^e]$. To do so, we first need to pair each node of the initial shape with a node of the final shape and thus determine which place each node will take in the final shape. The pairing of nodes between the initial shape and final shape is not unique. For our motivating application, that of a vehicle network, depending on the environment in which the network operates and the optimization objectives of the reconfiguration, one pairing may be preferable over another. The path we design here in order to define the control law is the simplest possible. We assume that the vehicles are moving free of any external force from the environment and that there are no obstacles. Further, with an eye toward preventing collisions between vehicles and minimizing the energy input to vehicles, we set the following two conditions: first, the planned trajectories of two distinct nodes must not intersect and second, the planned total distance travelled by all the nodes should be minimized. Meeting these two conditions in the planned trajectories, however, does not guarantee that in an actual vehicle network there will be no collisions between the vehicles and that the total consumption of energy by all the vehicles through the reconfiguration will be minimized. As we observe in the simulation

presented in Section 2.5, the linear and angular momenta of the controlled system for stabilization of a given shape (2.10) are not conserved, and for this reason, the center of mass and the orientation of the vehicle network may change during the reconfiguration. These deviations in absolute space from the planned path may cause the chosen pairing to exceed the minimum energy consumption and/or may create situations in which collisions between vehicles occur. However, simulations like the one presented in Section 3.3 suggest good performance for a "slow enough" reconfiguration (i.e., one with a "large enough" τ) using the control law designed in this section.

In the simple path we propose, each vehicle travels on a straight line [78]. The advantage of using the straight line solution is that choosing the pairing with minimal total distance covered by the vehicles automatically guarantees that no crossing will occur between the planned trajectories. However, in the case of a perturbed environment or with obstacles in the field, tracking such a path is almost always not optimal or not feasible. For example, in the context of underwater vehicles operating in the ocean, as considered in [64], the vehicles may be subject to currents. If the current acts in the opposite direction of the trajectory of one vehicle, this vehicle could be significantly slowed down and/or may be unable to track the prescribed (straight-line) trajectory; under either circumstance the reconfiguration would be compromised. In the context of a unsteady field, Inanc et al. developed a method to choose an optimal path using Lagrangian Coherent Structures [46]. In the context of a field with obstacles, Erdmann and Lozano-Perez proposed a solution to choose an optimal path in two steps [25]. First, paths that avoid collisions with static obstacles are planned for each robot, then the speed of each robot is adjusted to prevent collisions between the vehicles. Although we focus on straight line paths here, our approach can be adapted to accommodate other kinds of planned paths.

To plan a path, we select representative configurations $\mathbf{q}_0 \in [\mathbf{q}_0^e]$ and $\mathbf{q}_f \in [\mathbf{q}_f^e]$ in such a way as to minimize

$$d_{0\to f} = \sum_{i=1}^{N} \|\vec{q}_{0i} - \vec{q}_{fi}\|. \tag{3.1}$$

This is done by computing $d_{0\to f}$ for all possible node pairings and shape orientations (with

$\mathbf{q}_0, \mathbf{q}_f$ having the same centroid) and choosing the node pairing and shape orientations that yields the smallest $d_{0\to f}$. This choice, which minimizes the planned total distance travelled by all the vehicles, also ensures that no planned trajectories intersect.

Lemma 3.1.1 *A pairing, such that the trajectories of two nodes cross, does not minimize $d_{0\to f}$, the total distance travelled by all the nodes.*

Proof: Consider any two nodes i, j of the initial configuration $\mathbf{q}_0$ and suppose that they are paired with two nodes i', j' of the final configuration $\mathbf{q}_f$. There are two possible pairings: either i is paired with i' and j is paired with j' or i is paired with j' and j is paired with i', as plotted in Figure 3.1. For the intersecting trajectories (dotted lines), the total distance travelled by the nodes is equal to $b_1+b_2+b_3+b_4$. For the non-intersecting trajectories (solid lines), the total distance travelled by the nodes is equal to $a_1 + a_2 < b_1 + b_2 + b_3 + b_4$, this from the triangle inequality. Hence a chosen pairing of nodes with intersecting trajectories of any pair of nodes does not minimize $d_{0\to f}$. $\square$

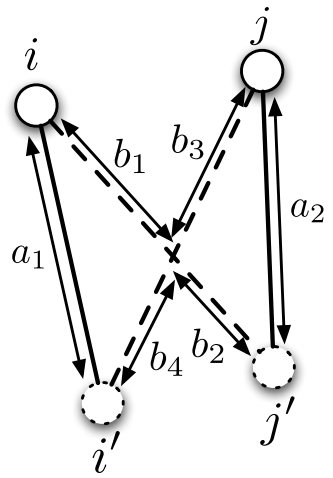

Figure 3.1: Two possible pairings between two starting nodes i, j and two ending nodes i', j'. For the intersecting trajectories (dotted lines) the total distance travelled by the nodes is equal to $b_1+b_2+b_3+b_4$. For the non-intersecting trajectories (solid lines) the total distance travelled by the nodes is equal to $a_1 + a_2 < b_1 + b_2 + b_3 + b_4$.

Given initial and final configurations $\mathbf{q}_0$ and $\mathbf{q}_f$ minimizing (3.1), we design a smooth

path of tensegrities $\mathbf{q}^e(t) = (\mathbf{x}^e(t), \mathbf{y}^e(t))$ using the following linear interpolation [78]:

$$\begin{aligned} \mathbf{q}^e(t) &= \frac{t}{\tau}\mathbf{q}_f + \left(1 - \frac{t}{\tau}\right)\mathbf{q}_0, \quad t \in [0, \tau] \\ \mathbf{q}^e(t) &= \mathbf{q}_f, \quad t > \tau. \end{aligned} \tag{3.2}$$

The parameter τ has units of time and allows for tuning of the tensegrity's reconfiguration speed. The greater τ is, the slower the tensegrity reconfigures itself.

The linear interpolation given by (3.2), defines a smooth path of shapes between two arbitrary shapes $[\mathbf{q}_0^e]$ and $[\mathbf{q}_f^e]$. We now use our map from shapes to tensegrities to define a control law that will track this or any other planned smooth path. The design of the reconfiguration using a path of stable tensegrities is motivated by the robustness properties of stable tensegrity structures mentioned in the previous chapter and explained in [109].

3.1.2 Parameterized Control Law

In this section we define a smooth parameterization (over time) of the dynamics of a tensegrity structure (2.10) such that the tensegrity follows a smooth path in shape space $[\mathbf{q}^e](t)$, for example the straight-line path given by (3.2). This control law was presented earlier in [78]. The control law we present does not require a straight-line path, but only a smooth path $[\mathbf{q}^e](t)$ such that $[\mathbf{q}^e](0) = [\mathbf{q}_0^e]$ and $[\mathbf{q}^e](\tau) = [\mathbf{q}_f^e]$. The simulations presented in Section 3.3 use the path given by (3.2) to illustrate the method. The parameterization of the controlled system (2.10) which we now consider is given by

$$\begin{cases} \dot{x}_i = p_i^x \\ \dot{y}_i = p_i^y \\ \dot{p}_i^x = -\nu p_i^x - \displaystyle\sum_{j=1}^{N} \alpha_{ij}(t)\omega_{ij}(t)\left(1 - \frac{l_{ij}(t)}{r_{ij}(t)}\right)(x_i - x_j) \quad i = 1, \ldots, N, \\ \dot{p}_i^y = -\nu p_i^y - \displaystyle\sum_{j=1}^{N} \alpha_{ij}(t)\omega_{ij}(t)\left(1 - \frac{l_{ij}(t)}{r_{ij}(t)}\right)(y_i - y_j), \end{cases} \tag{3.3}$$

where the parameters $\alpha_{ij}(t), l_{ij}(t)$ and $\omega_{ij}(t)$ are to be chosen so that at each time t, $[\mathbf{z}^e](t) = ([\mathbf{q}^e](t), \mathbf{0}, \mathbf{0})$ is an exponentially stable equilibrium set of (3.3). This choice of parameters

thus creates a manifold of stable tensegrities along the path $[\mathbf{q}^e](t)$. As a first step to making the solution of the controlled system follow the path $[\mathbf{q}^e](t)$, we define the appropriate variation of the parameters $\alpha_{ij}(t), l_{ij}(t)$ and $\omega_{ij}(t)$ so that at each instant t, $[\mathbf{q}^e](t)$ is an exponentially stable equilibrium shape of the controlled system (3.3). Given that the system (3.3) is nonlinear with time-varying inputs, we use results from Lawrence and Rugh [62] to show that the non-autonomous system (3.3) is well behaved. By well behaved, we mean that the quantity $\|[\mathbf{q}](t) - [\mathbf{q}^e](t)\|$ is bounded during the trajectory and that $[\mathbf{q}](t)$ converges to the final shape $[\mathbf{q}^e_f]$ as $t \to \infty$. To ensure that at each instant t, $[\mathbf{q}^e](t)$ is an exponentially stable shape of (3.3), we follow a procedure similar to the one developed in Section 2.4.1. We choose the parameters $\alpha_{ij}(t), l_{ij}(t)$ and $\omega_{ij}(t)$ so that

$$\begin{aligned}
&\begin{pmatrix} \tilde{\Omega}(t, \mathbf{x}^e(t), \mathbf{y}^e(t)) & 0 \\ 0 & \tilde{\Omega}(t, \mathbf{x}^e(t), \mathbf{y}^e(t)) \end{pmatrix} \begin{pmatrix} \mathbf{x}^e(t) \\ \mathbf{y}^e(t) \end{pmatrix} = 0, \quad t \in [0, \tau] \\
&\begin{pmatrix} \tilde{\Omega}(t, \mathbf{x}^e(\tau), \mathbf{y}^e(\tau)) & 0 \\ 0 & \tilde{\Omega}(t, \mathbf{x}^e(\tau), \mathbf{y}^e(\tau)) \end{pmatrix} \begin{pmatrix} \mathbf{x}^e(\tau) \\ \mathbf{y}^e(\tau) \end{pmatrix} = 0, \quad t > \tau,
\end{aligned} \tag{3.4}$$

where the explicit dependence of $\tilde{\Omega}$ in t comes from its dependence on the parameters $\alpha_{ij}(t), l_{ij}(t)$ and $\omega_{ij}(t)$. As with equation (2.13) in Section 2.4.1, equation (3.4) is solved in two steps. First we choose the parameters $\alpha_{ij}(t), l_{ij}(t)$ for all i, j so that $\tilde{\Omega}(t, \mathbf{x}^e(t), \mathbf{y}^e(t)) = \Omega(t)$. This last equation is solved by choosing

$$\begin{aligned}
\alpha_{ij}(t) &= \frac{\pi}{\arctan\left(\omega_{ij}(t)\right)} \\
l_{ij}(t) &= r^e_{ij}(t)\left(1 - \frac{1}{\pi}\arctan\left(\omega_{ij}(t)\right)\right),
\end{aligned} \tag{3.5}$$

where $r^e_{ij}(t) = \|\vec{q}^e_i(t) - \vec{q}^e_j(t)\|$ is the relative distance between node i and node j at time t along the planned path in shape space $[\mathbf{q}^e](t)$. The parameters $\omega_{ij}(t)$ are then computed as in Section 2.4.1 using the identity

$$\Omega(t) = \Lambda(t) D \Lambda(t)^T, \tag{3.6}$$

where $D = \text{diag}\begin{pmatrix} 0 & 0 & 0 & d_4 & \cdots & d_N \end{pmatrix}$, $d_i > 0$, $i = 4, \ldots, N$ and the columns of $\Lambda(t)$ constitute a basis of orthonormal eigenvectors obtained by the Gram-Schmidt procedure

on the N linearly independent vectors $\mathbf{x}^e(t), \mathbf{y}^e(t), \mathbf{1}, \mathbf{w}_4(t), \cdots, \mathbf{w}_N(t)$. This choice makes $[\mathbf{q}^e](t)$ a parameterized (over t) family of exponentially stable equilibrium shapes for the system (3.3). We now use results from Lawrence and Rugh [62] to show that the nonlinear system with time-varying control inputs (3.3) is well behaved as defined above.

3.2 Boundedness and Convergence

In this section we prove that with the parameters $\alpha_{ij}(t), l_{ij}(t)$ and $\omega_{ij}(t)$ solving (3.5) and (3.6), the controlled system (3.3) is well behaved. In other words we prove that under the time-varying controlled system (3.3), the reconfiguring tensegrity remains close, in shape space, to the prescribed shape path $[\mathbf{q}^e](t)$ (i.e., $\|[\mathbf{q}](t) - [\mathbf{q}^e](t)\|$ bounded) and that it converges to the final prescribed shape $[\mathbf{q}^e_f]$ (i.e., $[\mathbf{q}](t) \to [\mathbf{q}^e_f]$ as $t \to \infty$). These developments have been described in [78]. We prove these results for the time-varying controlled system (3.3) by using the main theorem in Lawrence and Rugh [62] for nonlinear systems with slowly varying inputs. The argument of the proof of this theorem is that solutions of a nonlinear system with a manifold of exponentially stable equilibria parameterized by constant inputs remains close to the manifold if the initial condition is "close" to that manifold and the inputs "slowly" vary. Similar results have been proven in [51, 53], although the assumptions on the vector field are not exactly identical and the methods used to prove the respective theorems differ. Kelemen [51] investigated stability of the manifold using the linearization of the system and the Gronwall-Bellman inequality, while Khalil and Kokotovic [53] used a Lyapunov function type approach to prove their stability result. The stability theorem we are using from Lawrence and Rugh [62] is also proven with a Lyapunov function type approach. Borrowing the notations from [62], the following setting is considered: a system described by

$$\dot{\mathbf{z}}(t) = f(\mathbf{z}(t), \mathbf{u}(t)), \;\; \mathbf{z}(0) = \mathbf{z}_0, \quad t \geq 0, \tag{3.7}$$

where $\mathbf{z}(t) \in \mathbb{R}^{4N}$ is the state vector, $\mathbf{u}(t) = (\alpha_{ij}(t), l_{ij}(t), \omega_{ij}(t), r^e_{ij}(t))$ is the time-varying input vector, and f is the vector field given by (3.3). For such system, Lawrence and Rugh proved the following result [62]:

Theorem 3.2.1 *Suppose the system (3.7) satisfies*

H1 $f : \mathbb{R}^{4N} \times \mathbb{R}^m \mapsto \mathbb{R}^{4N}$ *is twice differentiable,*

H2 there is a bounded, open set $\Gamma \subset \mathbb{R}^m$ *and a continuously differentiable function* $\mathbf{z} : \Gamma \mapsto \mathbb{R}^{4N}$ *such that for each constant input value* $\mathbf{u} \in \Gamma$, $f(\mathbf{z}(\mathbf{u}), \mathbf{u}) = 0$,

H3 there is a $\lambda > 0$ *such that for each* $\mathbf{u} \in \Gamma$, *the eigenvalues of* $(\partial f/\partial \mathbf{z})(\mathbf{z}(\mathbf{u}), \mathbf{u})$ *have real parts no greater than* $-\lambda$.

Then there is a $\rho^* > 0$ *such that given any* $\rho \in [0, \rho^*]$ *and* $T > 0$, *there exist* $\delta_1(\rho), \delta_2(\rho, T) > 0$ *for which the following property holds. If a continuously differentiable input* $\mathbf{u}(t)$ *satisfies* $\mathbf{u}(t) \in \Gamma, t \geq t_0$,

$$\|\mathbf{z}_0 - \mathbf{z}(\mathbf{u}(t_0))\| < \delta_1$$

and

$$\frac{1}{T}\int_t^{t+T} \|\dot{\mathbf{u}}(\sigma)\| d\sigma < \delta_2, \quad t \geq t_0,$$

then the corresponding solution of (3.7) satisfies

$$\|\mathbf{z}(t) - \mathbf{z}(\mathbf{u}(t))\| < \rho, \quad t \geq t_0.$$

To apply Theorem 3.2.1 to our system, we first show that all three conditions H1-H3 are satisfied.

We prove that the vector field (3.3) satisfies H1 using the smoothness of $f(\mathbf{z}(.), \mathbf{u}(.))$ as a function of $\Omega(.)$ and $\mathbf{r}^e(.)$ as noted in Section 2.4.1 and showing that $\Omega(t)$ and $\mathbf{r}^e(t)$ are smooth functions of t. Assuming $[\mathbf{q}^e](t)$ is a smooth path of tensegrities in shape space between the starting and ending shapes $[\mathbf{q}_0^e]$ and $[\mathbf{q}_f^e]$ (e.g., the path $[\mathbf{q}^e](t)$ given by the linear interpolation (3.2)), $\mathbf{r}^e(t)$ is a smooth function of t. The time-varying stress matrix $\Omega(t)$ is computed as

$$\Omega(t) = \Lambda(t) D \Lambda(t)^T,$$

where D is a constant diagonal matrix and the columns of $\Lambda(t)$ constitute an orthonormal basis of $\mathbb{R}^N$ obtained through a Gram-Schmidt procedure on the N linearly independent

vectors $\mathbf{x}^e(t), \mathbf{y}^e(t), \mathbf{1}, \mathbf{w}_4(t), \cdots, \mathbf{w}_N(t)$. The vectors obtained from a Gram-Schmidt procedure consist of linear combinations of the original set of linearly independent vectors; hence $\Lambda(t)$ and consequently $\Omega(t)$ are smooth functions of t. In Section 2.4.1 we noted that the choice for the parameters α_{ij} and l_{ij} given by

$$\alpha_{ij} = \frac{\pi}{\arctan \omega_{ij}}$$
$$l_{ij} = r^e_{ij}\left(1 - \frac{1}{\pi}\arctan \omega_{ij}\right)$$

is such that the vector field (2.10) is a smooth map of ω_{ij} and r^e_{ij}. This shows that the vector field $f(\mathbf{z}(.), \mathbf{u}(.))$ is a smooth function of $\Omega(t)$ and $\mathbf{r}^e(t)$, concluding the proof that the system (3.3) satisfies H1 being C^∞ and hence C^2 differentiable in $t, \Omega(t)$ and $\mathbf{r}^e(t)$.

Using the results from Section 2.4.2, we now prove that (3.3) satisfies both H2 and H3. From Theorems 2.4.1 and 2.4.4 we know that choosing the parameters α_{ij}, l_{ij} and ω_{ij} satisfying (2.13) makes $[\mathbf{z}^e]$ an isolated exponentially stable equilibrium set of (2.10). Hence choosing $\alpha_{ij}(t), l_{ij}(t)$ and $\omega_{ij}(t)$ satisfying (3.4) for every t makes $[\mathbf{z}^e](t)$ a parameterized (by $\Omega(t)$ and $\mathbf{r}^e(t)$) exponentially stable equilibrium set of (3.3), concluding the proof that (3.3) satisfies both H2 and H3.

Theorem 3.2.1 guarantees that if we start "close enough" to the shape $[\mathbf{q}^e_i]$ (i.e., $\|[\mathbf{z}_0] - [\mathbf{z}^e_0]\| < \delta_1$) and the reconfiguration is not "too fast" (i.e τ is large enough such that $\frac{1}{T}\int_t^{t+T} \|\dot{\mathbf{u}}(\sigma)\| d\sigma < \delta_2$), then the solution of (3.3) satisfies $\|[\mathbf{z}](t) - [\mathbf{z}^e](t)\| < \rho$. This proves that the reconfiguration is well behaved with $\|[\mathbf{q}](t) - [\mathbf{q}^e](t)\|$ bounded and $[\mathbf{z}](t) \to [\mathbf{z}^e_f] = \begin{pmatrix} [\mathbf{q}^e_f] \\ \mathbf{0} \end{pmatrix}$ as $t \to \infty$. We next explore the performance of this control law with a simulated example.

3.3 Examples and Simulations

In this section we present simulation results for the reconfiguration control law given by (3.3). With an example involving six nodes, we investigate the effect of the choice of τ on the "shape error" and on the total distance travelled by the vehicles through the reconfiguration.

Shape error $e(t)$ is measured as

$$e(t) = \sqrt{\sum_{i=1}^{N} (d_{iG}(t) - d^e_{iG}(t))^2}, \tag{3.8}$$

where $d_{iG}(t)$ is the observed distance between the ith node and the center of mass of the tensegrity at time t and $d^e_{iG}(t)$ is the planned distance between the ith node and the center of mass of the tensegrity at time t.

Looking at snapshots of the reconfiguration for different times allows us to interpret the physical meaning of shape error. We consider as an example the reconfiguration of a six-vehicle formation from initial shape $[\mathbf{q}^e_0]$ to final shape $[\mathbf{q}^e_f]$, represented respectively by the configurations $\mathbf{q}_0, \mathbf{q}_f$, given by

$$\mathbf{q}_0 = \begin{pmatrix} -1 & 1 & 2 & 1 & -1 & -2 \\ -2 & -2 & 0 & 2 & 2 & 0 \end{pmatrix}$$

$$\mathbf{q}_f = \begin{pmatrix} -2 & 2 & 0 & \frac{1}{2} & 0 & -\frac{1}{2} \\ -\frac{3}{2} & -\frac{3}{2} & -\frac{1}{2} & \frac{1}{2} & \frac{5}{2} & \frac{1}{2} \end{pmatrix},$$

where the coordinates are expressed in meters. Figure 3.2 shows the planned initial shape, final shape and planned intermediary shapes as prescribed by (3.2) for $t = \frac{\tau}{3}$ and $t = \frac{2\tau}{3}$. We note that the final shape is non-convex. In the context of a mobile sensor network, this reconfiguration corresponds to having the network that is sampling the environment shift from lower resolution in a larger space to higher resolution in a smaller space.

Figure 3.3 shows the evolution of the mean total distance travelled by the six nodes calculated over four thousand runs as a function of τ, for values of τ between .1s and 16s with increment of .1s. Each run has an initial condition randomly picked from a normal distribution with mean $[\mathbf{z}^e_0] = \begin{pmatrix} [\mathbf{q}^e_0] \\ \mathbf{0} \end{pmatrix}$ and variance 0.1. For increasing τ in the range from 0 to 3s, the total distance decreases dramatically from about 30m to about 12m. For $\tau > 3$s, as τ increases, the total distance converges to an asymptote. This is lower bounded by the total distance travelled in the linear designed path given by (3.2), represented in Figure 3.3 by the solid white line. The planned distance for this path is calculated as 8.58m.

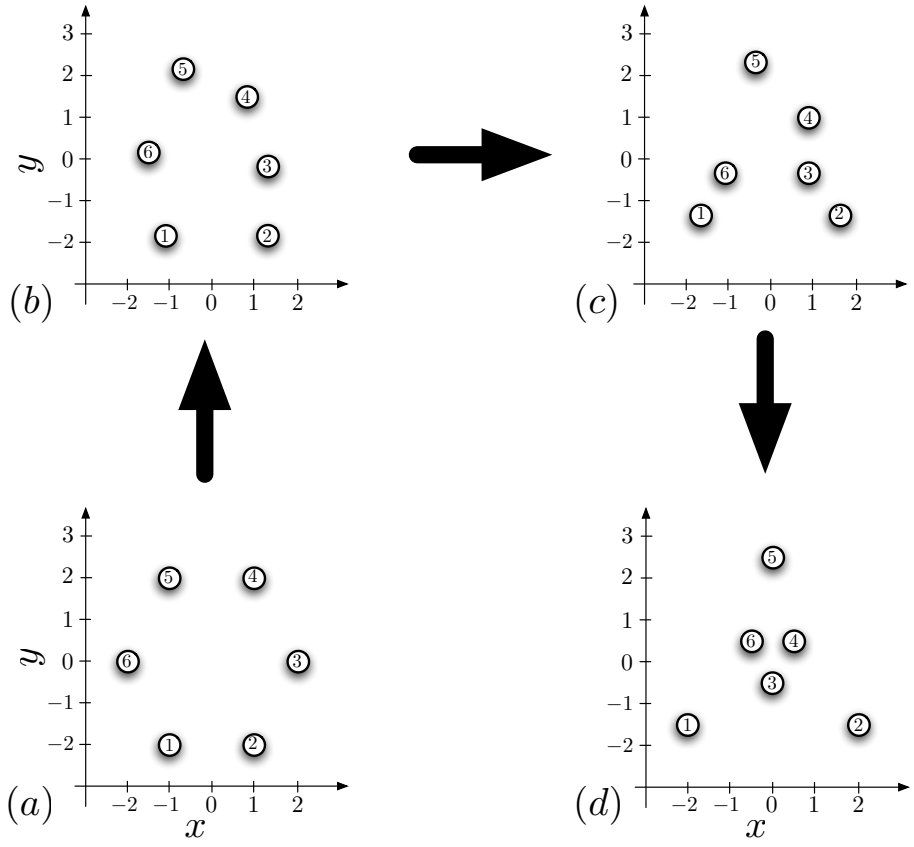

Figure 3.2: Plot of the the studied six vehicle formation along the planned path at (a) $t = 0$, (b) $t = \frac{\tau}{3}$, (c) $t = \frac{2\tau}{3}$ and (d) $t = \tau$. The final configuration is non-convex. In the context of a mobile sensor network, this reconfiguration can be interpreted as having the network sampling the environment from a lower to a higher resolution.

Figure 3.4 shows the evolution of the mean minimum distance between all pair of nodes calculated over four thousand runs as a function of τ, for values of τ between .1s and 16s with increment of .1. For increasing τ in the range from 0 to 4s, the minimum distance between pairs of nodes increases dramatically from about .2m to about .9m. As τ increases for $\tau > 4$s, the minimum distance converges to an asymptote. This is upper bounded by the minimum distance between pairs of nodes along the linear designed path given by (3.2), represented by a solid white line in Figure 3.4. The minimum distance between pairs of nodes is calculated as 1m.

In Figures 3.5 and 3.6 we give for different values of τ ($\tau = .1s,\ .8s,\ 1.8s$ and $10s$) a plot of the shape error $e(t)$, and snapshots of the six vehicle network at four meaningful instants: at the beginning of the reconfiguration, at the first two peaks of the $e(t)$ curve and when $e(t)$ becomes permanently smaller than 10^{-2}m. (Note that the $e(t)$ graphs do not all have the same scale.) Looking at the graph of $e(t)$ for the cases $\tau = .1$s and $\tau = 10$s we observe a difference of one order of magnitude. The case where $\tau = .1$s corresponds to the extreme case where the final configuration is prescribed with no intermediate points on the path. This is tantamount to requiring the system to stabilize to the shape $[\mathbf{q}_f^e]$ given the initial condition $\mathbf{q}_0^e$ as in Section 2.4. In the snapshots of the system at the peaks of shape error for the case $\tau = .1$s, the peaks can be interpreted either as the system's being too slow to react to the input (in the case of the first peak) or as an overshoot (in the case of the second peak). As τ increases, the structure follows the planned path more smoothly. In the case where $\tau = 10$s, the structure follow the prescribed path very smoothly. We also note that independently of the choice of τ, the structure at its final configuration is rotated, due to changing angular momentum in the system. This highlights the fact that we are controlling only the shape of the structure but not its position or orientation in absolute space. These simulations show that with τ sufficiently large, the distance covered by the nodes is minimized and no collisions occur.

In Chapter 2, we presented and proved a systematic methodology to create decentralized control laws for the stabilization of multi-vehicle formations of arbitrary planar shape. In

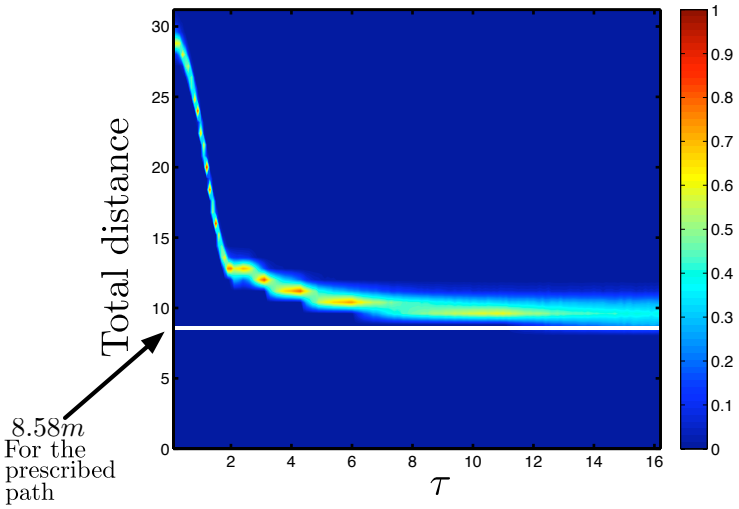

Figure 3.3: Normalized probability distribution (proportion of maximum) of the total distance travelled by the six nodes calculated over four thousand runs as a function of τ, for values of τ between .1s and 16s with increment of .1. The greater τ is (i.e., the slower the network is prescribed to reconfigure itself), the least distance is travelled by the five vehicles. The lower bound is given by the total distance travelled for the linear designed path (solid white line which gives 8.58m).

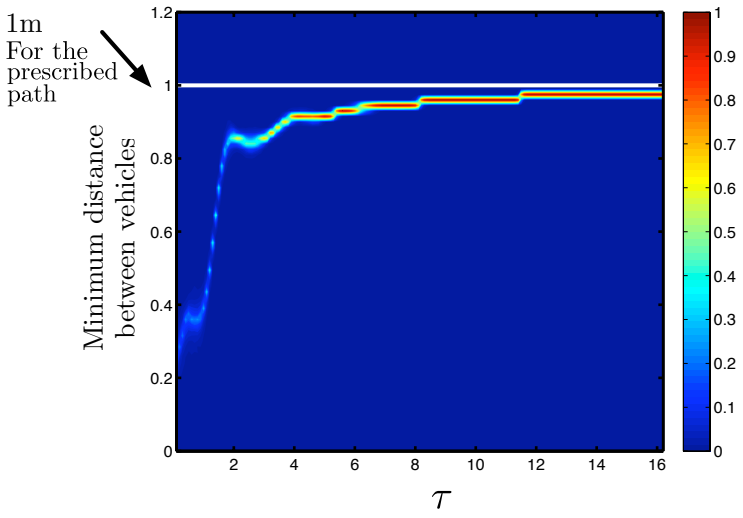

Figure 3.4: Normalized probability distribution (proportion of maximum) of the minimum distance between all pair of nodes calculated over four thousand runs as a function of τ, for values of τ between .1s and 16s with increment of .1. The greater τ is (i.e., the slower the network is prescribed to reconfigure itself), the greater the distance between pairs of vehicles. The upper bound shown is given by minimum distance between all pairs of nodes for the linear designed path (solid white line which gives 1m).

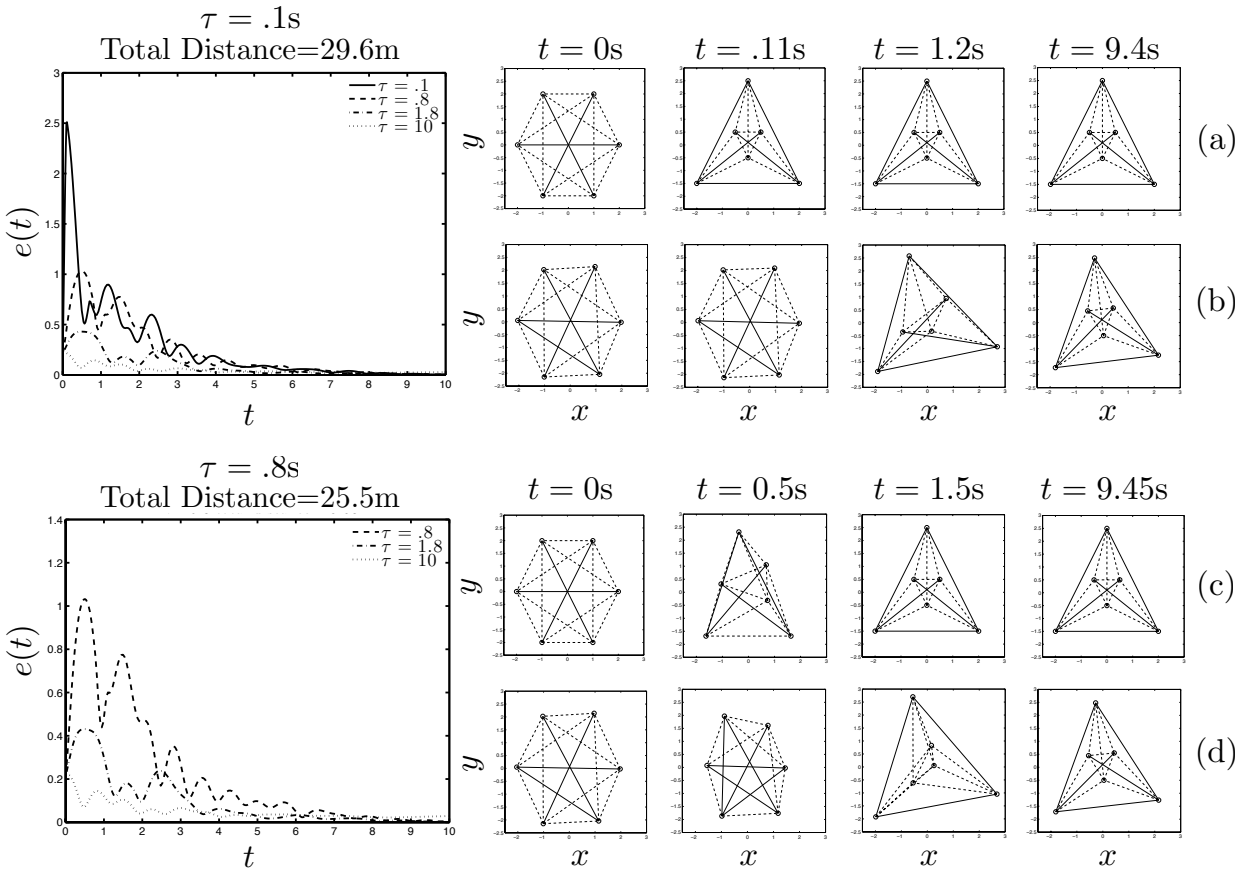

Figure 3.5: For $\tau = 0.1\text{s}, .8\text{s}$, shape error is plotted as a function of time. (a)-(c) give snapshots of the six vehicle network along the prescribed path $\mathbf{q}^e(t)$ respectively for $\tau = 0.1\text{s}, .8\text{s}$. (b)-(d) give snapshots of the actual six vehicle network at the beginning of the reconfiguration, at the first two peak of the $e(t)$ curve and when the shape error becomes permanently smaller than 10^{-2}m respectively for $\tau = 0.1\text{s}, .8\text{s}$.

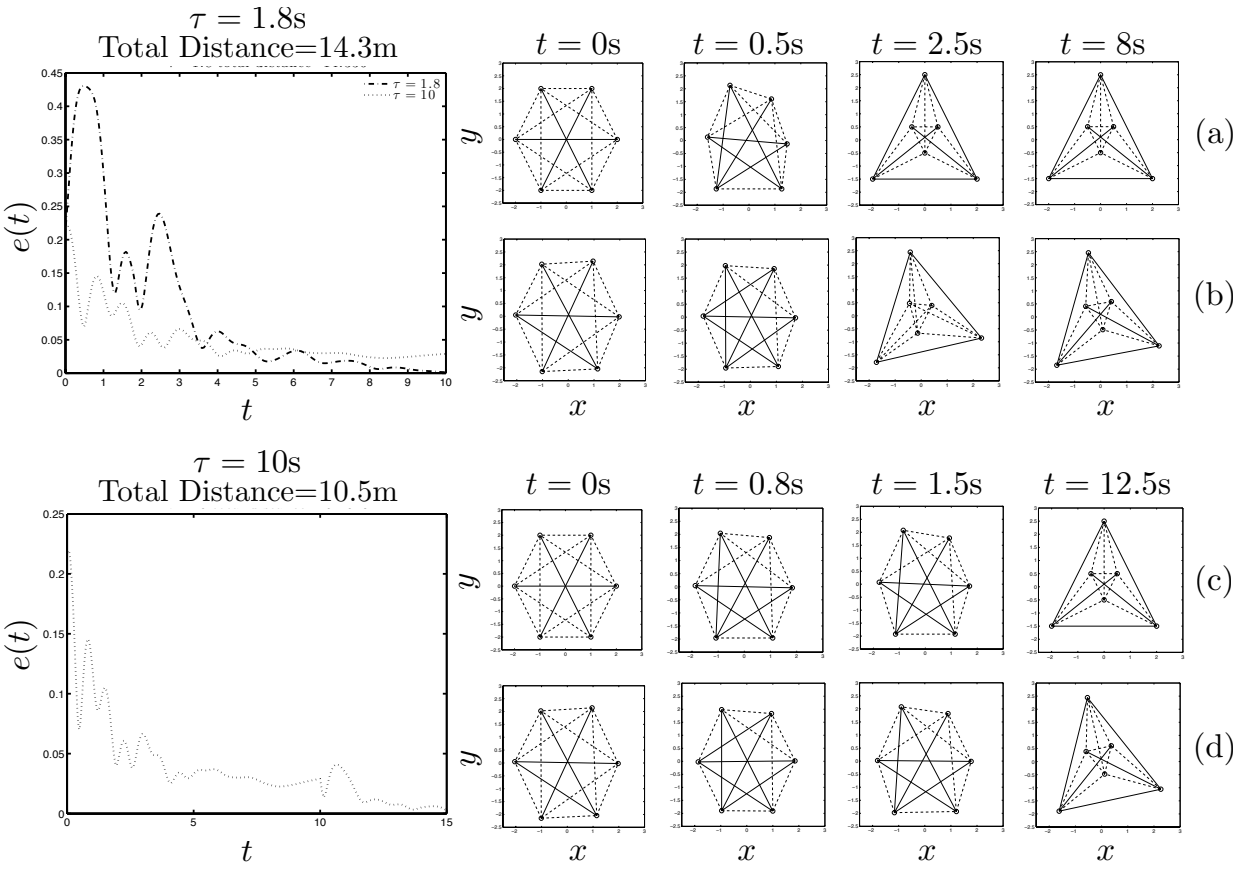

Figure 3.6: For $\tau = 1.8$s and 10s, shape error is plotted as a function of time. (a)-(c) give snapshots of the six vehicle network along the prescribed path $\mathbf{q}^e(t)$ respectively for $\tau = 1.8$s and 10s. (b)-(d) give snapshots of the actual six vehicle network at the beginning of the reconfiguration, at the first two peak of the shape error curve and when the shape error becomes permanently smaller than 10^{-2}m respectively for $\tau = 1.8$s and 10s. As τ increases, the shape error decreases and the network follows the prescribed path $\mathbf{q}^e(t)$ more closely.

this chapter we extended the proven framework to control changes of formation shape over a given time interval. In the subsequent chapters of this dissertation we will turn our attention to the dynamics of decision making in groups. The problem of interest is the following: given a group of individuals, by which mechanisms if any can they agree on a direction of travel even when some individuals have conflicting preferences. We look at this problem in a natural setting and build and/or study models with the motivation of understanding the key mechanisms. The goal is to set the foundation for a mutually beneficial interaction between biology and engineering such that analysis tools derived to study collective robotic behavior are used to test plausible mechanisms of decision making in animal groups, and, in return, the understanding of such phenomenon provides inspiration for new control strategies for engineered cooperative multi-agent systems.

Chapter 4

Collective Decision Making: Discrete Time Models

In the remaining chapters of this dissertation, we turn our attention to group dynamics in the context of natural systems. We investigate mechanisms of leadership and decision making in animal groups such as schools of fish or flocks of birds through the simulation and analysis of discrete- and continuous-time individual-based (i.e. Lagrangian) models. More specifically we consider a heterogeneous group of both informed individuals with conflicting preferences and uninformed individuals, i.e, individuals without preferences. We assume that there is no explicit signaling and that group members cannot recognize which individuals are informed and how accurate the information is. This conservative assumption makes this research relevant to species where it is not reasonable to assume sophisticated cognitive abilities. For example groups of migrating fish, birds or insects can be so crowded as to limit significantly the range over which neighbors can be detected, making the hypothesis of sophisticated communication abilities unlikely.

For such a collective, we address the following leadership and consensus decision-making problems: how can information be transferred and how can a consensus be reached in the group? This research has been conducted with both complex stochastic discrete times models and simplified deterministic continuous-time models. The former gives highly suggestive

simulations, whereas the latter allows a deeper investigation of the microscopic reasons for the macroscopic behaviors observed and a more complete exploration of parameter space. In this chapter we present a discrete-time model developed by Couzin et al. in [19] and present a new investigation of this model focusing on the role of uninformed individuals in the decision-making process within a heterogeneous group. We highlight both the drawbacks and the benefits of having uninformed individuals in the group. In Section 4.1 we present two variations of the discrete-time model used in [19]. In one variation, the informed individuals have a fixed preferred direction of travel; in the other variation, the preference is a destination, referred to as a target. We then summarize the results in Couzin et al. [19]. In Section 4.2 we investigate the influence of the uninformed individuals in the model with preferred direction. In Section 4.3 we investigate the influence of uninformed individuals in the model with targets.

4.1 Discrete-time Model from Couzin et al. [19]

4.1.1 The Model

The discrete-time model from [19] considers a group of N individuals, each modeled as a particle moving in the plane at constant speed s_i, $i = 1, \ldots, N$. At time t, each individual is characterized by a position vector $\mathbf{c}_i(t)$ and a velocity vector $\mathbf{v}_i(t)$. The velocity $\mathbf{v}_i(t)$ is applied to the i-th particle between time $t - \Delta t$ and time t. At each time step, the individuals in the group update their direction of travel depending on social interactions with local neighbors and, when applicable, on a preferred direction of travel. The population is divided into three subgroups, two informed and one uninformed. Let $\mathcal{N}_i$, $i = 1, 2, 3$ be, respectively, the set of indices in $\{1, \cdots, N\}$ corresponding to individuals in the first and second informed subgroups and in the uninformed subgroup. Each individual in the first and second subgroups has a preferred direction of travel (where the preference represents, for example, knowledge of the direction to a food source or of a migration route) and can use that preference along with information it has on its neighbors to make decisions.

The preferred direction is denoted with a unit vector $\mathbf{g}_i$ $i \in \mathcal{N}_1, \mathcal{N}_2$. In the variation of the model in which informed individuals have a fixed preferred direction of travel, $\mathbf{g}_i$ is a constant vector pointing in the respective preferred direction of each informed subgroup. In the variation in which informed individuals have a fixed target, $\mathbf{g}_i$ is updated at every time step so as to point in the direction from the informed individual's current position to the position of its target.

Individuals in the group interact with other group members according to the following rules (see Figure 4.1):

1. Maintain a minimum distance α with others by turning away from neighbors within that range.

2. If no neighbors are within a distance α, move towards and align with any other individuals within a local interaction range of $\beta > \alpha$.

Formally, individual agent i, for $i = 1, \ldots, N$ computes a direction of travel $\mathbf{d}_i^{\mathrm{SOC}}(t + \Delta t)$ to be followed between times t and $t + \Delta t$ in accordance with social interactions. $\mathbf{d}_i^{\mathrm{SOC}}(t)$ evolves according to the following discrete-time dynamics:

$$\begin{aligned} \mathbf{d}_i'(t + \Delta t) &= -\sum_{j \in \alpha_i} \frac{\mathbf{c}_j(t) - \mathbf{c}_i(t)}{\|\mathbf{c}_j(t) - \mathbf{c}_i(t)\|} + \left(\sum_{j \in \beta_i} \frac{\mathbf{c}_j(t) - \mathbf{c}_i(t)}{\|\mathbf{c}_j(t) - \mathbf{c}_i(t)\|} + \frac{\mathbf{v}_j(t)}{\|\mathbf{v}_j(t)\|} \right) (1 - \chi_{\alpha_i}) \\ \mathbf{d}_i^{\mathrm{SOC}}(t + \Delta t) &= \frac{\mathbf{d}_i'(t + \Delta t)}{\|\mathbf{d}_i'(t + \Delta t)\|}, \end{aligned} \tag{4.1}$$

where α_i denotes the subset of indices in $\{1, \cdots, N\}$ corresponding to the individuals in the zone of repulsion of individual i, where β_i denotes the subset of indices in $\{1, \cdots, N\}$ corresponding to the individuals in the zone of attraction/alignment of individual i, and where χ_{α_i} is an indicator function taking the value 0 if the set α_i is empty and the value of 1 otherwise.

Individuals in the first and second informed subgroups have a preferred direction of travel that they balance with the social influence $\mathbf{d}_i^{\mathrm{SOC}}(t)$. Informed individual i determines its net desired direction of motion as $\mathbf{d}_i^{\mathrm{SOC}}(t + \Delta t) + \omega \mathbf{g}_i$, where $\omega \geq 0$ is a constant gain (referred to as "assertiveness") that weights the attention paid to the preferred direction

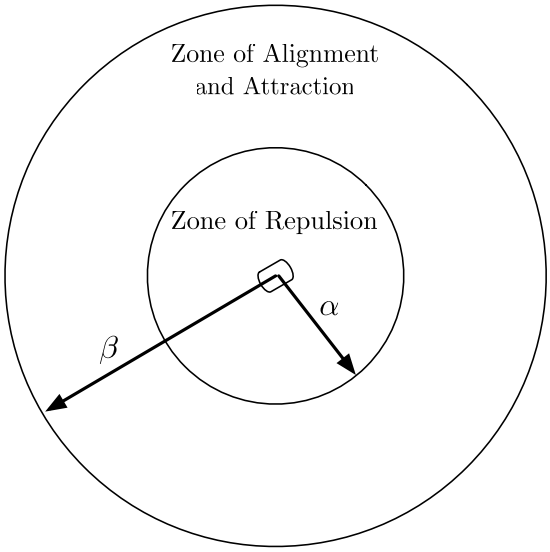

Figure 4.1: Zone of interaction of an individual in the simulation. Individuals turn away from neighbors within a distance α or move towards and align with neighbors within a distance β.

versus attention paid to neighbors. If ω is large, informed individuals desire to move at each time step predominantly in their preferred direction/destination. If ω is small, informed individuals desire, at each time step, to predominantly move toward and align with their neighbors. Combining the influences of social interactions and, when applicable, attraction to a preferred direction, the dynamics of the computed direction of travel of all the individuals in the group between times t and $t + \Delta t$ are given by the following set of discrete-time equations:

$$\begin{aligned}
\mathbf{d}_i(t+\Delta t) &= \frac{\mathbf{d}_i^{\mathrm{SOC}}(t+\Delta t) + \omega \mathbf{g}_1}{\|\mathbf{d}_i^{\mathrm{SOC}}(t+\Delta t) + \omega \mathbf{g}_1\|} + X_i \quad i \in \mathcal{N}_1 \\
\mathbf{d}_i(t+\Delta t) &= \frac{\mathbf{d}_i^{\mathrm{SOC}}(t+\Delta t) + \omega \mathbf{g}_2}{\|\mathbf{d}_i^{\mathrm{SOC}}(t+\Delta t) + \omega \mathbf{g}_2\|} + X_i \quad i \in \mathcal{N}_2 \\
\mathbf{d}_i(t+\Delta t) &= \mathbf{d}_i^{\mathrm{SOC}}(t+\Delta t) + X_i \quad i \in \mathcal{N}_3,
\end{aligned} \tag{4.2}$$

where X_i is a random angle taken from a circular-wrapped gaussian distribution centered on zero and with a standard deviation $\sigma = 0.01$rad.

Individuals use their calculated desired direction of travel $\mathbf{d}_i(t + \Delta t)$ to adapt their actual direction of travel. They are constrained, however, by a maximum turning rate Ω

such that the maximum change in direction of travel between t and $t + \Delta t$ is $\Omega\Delta t$. For an individual moving at a speed of s_i, if the angle between the velocity vector $\mathbf{v}_i(t)$ at time t and the calculated direction of travel $\mathbf{d}_i(t + \Delta t)$ between time t and time $t + \Delta t$ is smaller than $\Omega\Delta t$, then $\mathbf{v}_i(t + \Delta t)$ is equal to $s_i\mathbf{d}_i(t + \Delta t)$; otherwise $\mathbf{v}_i(t + \Delta t)$ is equal to $\mathbf{v}_i(t)$ rotated by $\Omega\Delta t$ towards $\mathbf{d}_i(t + \Delta t)$. The discrete-time dynamics of the individuals in the group can then be written as

$$\begin{aligned}
\mathbf{v}_i(t + \Delta t) &= \begin{cases} s_i\mathbf{d}_i(t + \Delta t) & \text{if } |\mathrm{mod}(\theta_d - \theta_v, 2\pi) - \pi| \leq \Omega\Delta t \\ \mathbf{v}_i(t)R\left(\mathrm{sgn}(\mathrm{mod}(\theta_d - \theta_v, 2\pi) - \pi)\Omega\Delta t\right) & \text{otherwise,} \end{cases} \\
\mathbf{c}_i(t + \Delta t) &= \mathbf{c}_i(t) + \mathbf{v}_i(t + \Delta t)\Delta t,
\end{aligned} \tag{4.3}$$

where θ_v (respectively θ_d) is the oriented principal value of the angle between $\mathbf{v}_i(t)$ and the rightward unit vector i.e., the angle θ_v between $\mathbf{v}_i(t)$ and the rightward unit vector such that $\theta_v \in [-\pi, \pi)$ (respectively between $\mathbf{d}_i(t+\Delta t)$ and a rightward unit vector), the function $\mathrm{mod}(x, 2\pi)$ is defined as $x - 2\pi n$ with $n = \mathrm{floor}(\frac{x}{2\pi})$, the function sgn is defined as

$$\mathrm{sgn}(x) = \begin{cases} 1 & \text{if } x > 0 \\ -1 & \text{if } x < 0 \\ 0 & \text{if } x = 0, \end{cases}$$

and $R(\theta)$ is the 2×2 rotation matrix given by

$$R(\theta) = \begin{pmatrix} \cos\theta & -\sin\theta \\ \sin\theta & \cos\theta \end{pmatrix}.$$

In some of the simulations presented in [19], a "forgetting factor" feedback was introduced by making the weight ω of the attraction to the preferred direction state dependent. More specifically, if at a given time step, informed individuals find themselves moving in a "similar" direction to their preferred direction (within $\pm$ 20 deg), the weight ω is increased by ω_{inc} up to a maximum value ω_{max}; otherwise it is decreased by ω_{dec} up to 0. In the simulations presented in this chapter, no "forgetting factor" feedback is considered. However, similar feedback terms are considered in the extensions for the analytical models presented in Chapters 5 and 6.

4.1.2 Summary of the Results in Couzin et al. [19]

Using the model described above considering informed individuals with fixed preferred directions, Couzin et al. addressed the following two questions: how can information be transferred within a group without signaling or individual recognition and how can consensus decisions be made by groups containing individuals with conflicting preferences. They demonstrated plausible mechanisms for information to flow within a group, assuming limited cognitive abilities for the group members. This work also revealed that leadership can emerge from the differences in preference of members when individuals, informed or uninformed, respond spontaneously to those individuals that have information although without necessarily recognizing them as such.

The first question was investigated by considering a group with one informed subgroup and one uninformed subgroup. The authors showed that for a given group size, the accuracy of group motion increases asymptotically as the proportion of informed individuals increases, accuracy being measured as the normalized angular deviation of group direction around the preferred direction $\mathbf{g}$. They noticed furthermore that the larger the group, the smaller the proportion of informed individuals needed to be to achieve any given level of accuracy. These simulations also showed that higher values of ω yield greater accuracy but at the cost of increasing the probability of group fragmentation.

The second question was investigated by considering a group containing two informed subgroups with conflicting preferences and one uninformed subgroup. Simulations showed that with two informed subgroups of equal population, the direction of group motion depends on the degree to which the preferred directions differ. For disagreements below a certain threshold, the group follows the average preferred direction of all informed individuals, while for disagreements greater than the threshold, the group selects with equal probability one of the two preferred directions. When introducing the "forgetting factor" feedback described above, the same transition from averaging the preferred directions to collectively selecting one preferred direction occurs, although the threshold is smaller. One remarkable feature of these simulations is that the informed individuals are not aware of

how many individuals share their preferred direction and whether or not they are in the majority. Moreover, when one informed subgroup has a population greater than the other, even if only by one extra individual, the group is nevertheless able to sense this. For disagreements greater than the threshold, the group selects with almost probability one the preferred direction of the informed subgroup in the majority rather than randomly selecting either of the preferred directions.

This model produces highly suggestive simulation results but contains many degrees of freedom. In order to isolate biologically plausible mechanisms for the decision-making behavior observed in [19] when there are two informed subgroups with conflicting information, we proposed and analyzed in [80] a continuous-time model making several simplifying assumptions. First, rather than considering interaction zones as in (4.1), we assumed an all-to-all communication topology, meaning that every individual senses every other individual in the group and adjusts its own direction of travel accordingly. Second, we removed the "forgetting factor" feedback term considered in some simulations in [19] by not allowing informed individuals to update the strength of their attraction to their preferred direction. Finally we ignored the presence of uninformed individuals. This model and its analysis are presented in detail in Chapter 5 of this dissertation. Notably, the continuous-time model produced some but not all of the behaviors observed in [19], suggesting that some of the simplifying assumptions made may be responsible for the collective behavior observed in [19]. Driven by the analysis of the continuous-time model, we reexamine, in the remainder of this chapter, the simulation from [19], focusing on the subtle and nontrivial role of uninformed individuals in achieving consensus decisions. We first explore the role of naive individuals in the case where informed individuals have a fixed preferred direction of travel. We then consider the case where informed individuals have a fixed target.

4.2 Influence of Naive Individuals in the Direction Model

In the context of animal foraging or migration, it has been shown that in many cases only a few individuals have pertinent information of where to travel [96, 119, 31, 105]. Simulations

of the model presented in the previous section from [19] revealed plausible mechanisms for information transfer and leadership in such groups, further assuming limited cognitive abilities of individual group members. However these observations raise the following question: *why would an informed individual team up with naive individuals?* In other word, if an individual has information about a food source, what, if any, is the gain from traveling along with naive individuals. In this chapter, we argue that naive individuals can in fact increase the accuracy of decision making and reduce the probability of fragmentation in a group containing individuals with conflicting preferences. We also show that when the number of naive individuals is too large, these trends are reversed. In this section, we focus our investigation on the influence of naive individuals in the case where the informed individuals have a fixed preferred direction of travel. This setting is well suited for modeling animal migration for example, where the desired destinations are "infinitely" far away.

In order to reveal the role of naive individuals, we run a suite of simulations. We consider groups containing two informed subgroups with equal populations $N_1 = N_2 = 5$, an equal level of assertiveness ω varying between .1 and .4 with increments of .1 and respective preferred directions of 0 and $\bar{\theta}_2$, with $\bar{\theta}_2$ varying between 0 and 180 deg with increments of 5 degrees. We include one naive subgroup with population N_3 varying between 0 and 100 with increments of 10. For each set of values for the parameters $(N_3, \omega, \bar{\theta}_2)$, we simulate the motion of the group for 25,000 time steps and check if the group fragmented or not. In the cases where the group has not fragmented, we record the direction followed by the group. We simulate each set of parameters enough times to get 3000 non-fragmented replicates. With these simulations we compute for each level of assertiveness ω, the normalized probability distribution of group fragmentation (proportion of maximum number of fragmented simulations for a given set of parameters). Figures 4.2-4.5 represent respectively for $\omega = .1, .2, .3$ and .4 the normalized probability distributions of group fragmentation for $\bar{\theta}_2 \in [90, 180]$ and $N_3 \in [0, 100]$. We also reproduced bifurcation plots (not shown) similar to the ones presented in Figure 3 of [19], for each set of values for ω, N_3. These plots show the normalized probability distribution (proportion of maximum) of group direction as a

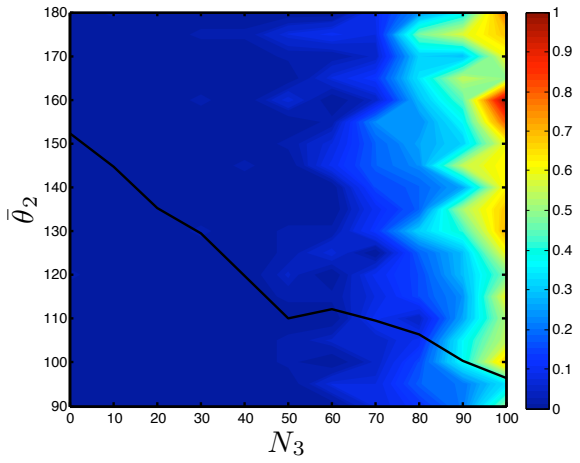

Figure 4.2: Color scale shows normalized probability distribution (proportion of maximum) of group fragmentation for a group containing $N_1 = 5$ informed individuals with preferred direction of 0 degrees, $N_2 = 5$ informed individuals with preferred direction $\bar{\theta}_2 \in [0, 180]$, and $N_3 \in [0, 100]$ naive individuals with no preferred direction. The informed individuals in each subgroup have the same level of assertiveness $\omega = .1$. The plot of the bifurcation angle as a function of N_3 is superimposed in black. For this level of assertiveness, introducing small numbers of naive individuals in the group does not reduce the level of group fragmentation. On the other hand, adding more than 70 naive individuals to the group causes the probability of group fragmentation to start increasing. As the number of naive individuals is increased, the bifurcation angle drops from about 152 degrees to about 97 degrees.

function of $\bar{\theta}_2$ for a group containing $N_1 = 5$ informed individuals with preferred direction of 0 degrees, $N_2 = N_1 = 5$ informed individuals with preferred direction $\bar{\theta}_2 \in [0, 180]$, and N_3 naive individuals with no preferred direction. An example of such a plot is given in Figure 4.7(a). They are referred to as bifurcation plots since they represent the possible steady state behavior as the bifurcation parameter $\bar{\theta}_2$ (the difference between the preferred directions of the two informed subgroups) is varied. Using these bifurcation plots, we then record the bifurcation angle $\bar{\theta}_2$ at the bifurcation point, i.e., when the group switches from following the average of the preferred directions to collectively selecting one of the preferred directions. For each value of ω considered (.1,.2,.3 and .4 respectively on Figures 4.2, 4.3, 4.4 and 4.5), the plot of the bifurcation angle as a function of N_3 is superimposed in black on the plot of the normalized probability distribution of group fragmentations.

The value of each bifurcation point is obtained using a topological skeleton of the cor-

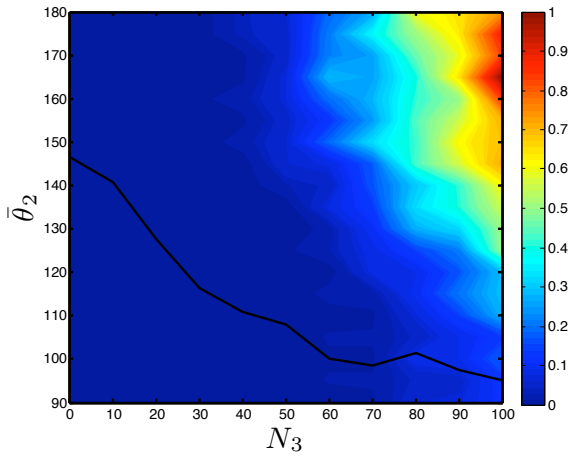

Figure 4.3: Color scale shows normalized probability distribution (proportion of maximum) of group fragmentation for a group containing $N_1 = 5$ informed individuals with preferred direction of 0 degrees, $N_2 = 5$ informed individuals with preferred direction $\bar{\theta}_2 \in [0, 180]$, and $N_3 \in [0, 100]$ naive individuals with no preferred direction. The informed individuals in each subgroup have the same level of assertiveness $\omega = .2$. The plot of the bifurcation angle as a function of N_3 is superimposed in black. For this level of assertiveness, introducing small numbers of naive individuals in the group does not reduce the level of group fragmentation. On the other hand adding more than 60 naive individuals to the group causes the probability of group fragmentation to start increasing. As the number of naive individuals is increased, the bifurcation angle drops from about 148 degrees to about 96 degrees.

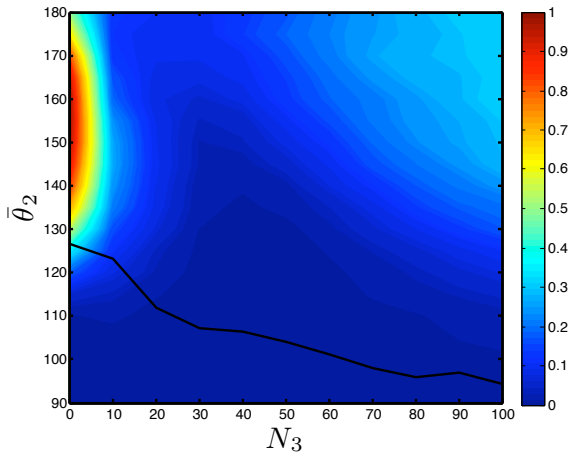

Figure 4.4: Color scale shows normalized probability distribution (proportion of maximum) of group fragmentation for a group containing $N_1 = 5$ informed individuals with preferred direction of 0 degrees, $N_2 = N_1 = 5$ informed individuals with preferred direction $\bar{\theta}_2 \in [0, 180]$, and $N_3 \in [0, 100]$ naive individuals with no preferred direction. The informed individuals in each subgroup have the same level of assertiveness $\omega = .3$. The plot of the bifurcation angle as a function of N_3 is superimposed in black. For this level of assertiveness, introducing naive individuals to the group initially reduces the level of group fragmentation ($N_3 \in [0, 40]$). However adding more than 40 naive individuals to the group causes the probability of group fragmentation to start increasing. As the number of naive individuals is increased, the bifurcation angle drops from about 127 degrees to about 95 degrees.

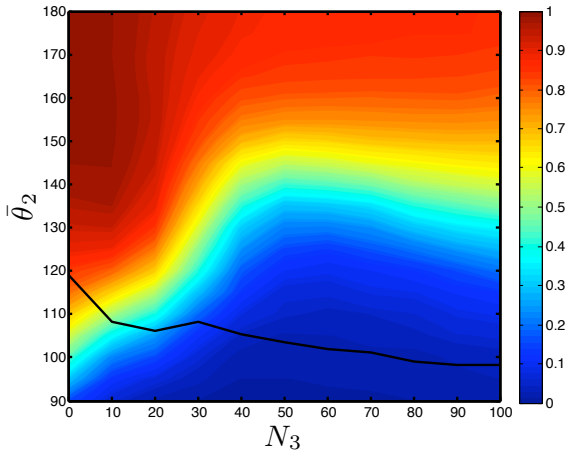

Figure 4.5: Color scale shows normalized probability distribution (proportion of maximum) of group fragmentation for a group containing $N_1 = 5$ informed individuals with preferred direction of 0 degrees, $N_2 = 5$ informed individuals with preferred direction $\bar{\theta}_2 \in [0, 180]$, and $N_3 \in [0, 100]$ naive individuals with no preferred direction. The informed individuals in each subgroup have the same level of assertiveness $\omega = .4$. The plot of the bifurcation angle as a function of N_3 is superimposed in black. For this level of assertiveness, introducing naive individuals to the group initially reduces the level of group fragmentation ($N_3 \in [0, 40]$). However adding more than 40 naive individuals to the group causes the probability of group fragmentation to starts increasing. As the number of naive individuals is increased, the bifurcation angle drops from about 120 degrees to about 100 degrees.

Figure 4.6: Example of a simple shape and its skeleton. The black line is the topological skeleton of the light blue shape; it is equidistant to the boundary of the blue shape.

responding bifurcation plot obtained from the data (Figure 4.7). Figure 4.7(a) shows the bifurcation plot for $\omega = .4$ and $N_3 = 80$, its corresponding topological skeleton is shown in Figure 4.7(b). A topological skeleton of a shape is a "thin" version of that shape that is equidistant to its boundaries. For example a bar with a finite thickness would have a topological skeleton made of a line going through the middle of it as represented in Figure 4.6. We use topological skeletons as they preserve topological properties of a shape while emphasizing them. The skeleton images used to measure the bifurcation points were generated using Matlab. For each skeleton image, we identify the pixel at which the bifurcation occurs and deduce the corresponding bifurcation value for $\bar{\theta}_2$. For example in Figure 4.7 (b), the bifurcation occurs at the pixel $X : 523$ $Y : 527$, hence the bifurcation value for $\bar{\theta}_2$ is given by $\frac{523}{926}180 \simeq 102$deg, where 926 is the width in pixels of the bifurcation plot.

In Figures 4.2-4.5, we observe that depending on the level of assertiveness assumed for the informed individuals in the group, adding naive individuals has a different effect on the probability of group fragmentation. For low levels of assertiveness for the informed individuals, ($\omega = .1$ or .2, Figures 4.2, 4.3), introducing "few" naive individuals in the group (N_3 less than 60) does not affect the probability of group fragmentation. However adding more than 60 naive individuals to the group causes the probability of group fragmentation to increase. For higher levels of assertiveness for the informed individuals, ($\omega = .3$ or .4, Figures 4.4, 4.5), introducing "few" naive individuals in the group (less than 40) reduces the probability of group fragmentation. However adding more than 40 naive individuals to the group reverses the trend and the probability of group fragmentation starts to increase.

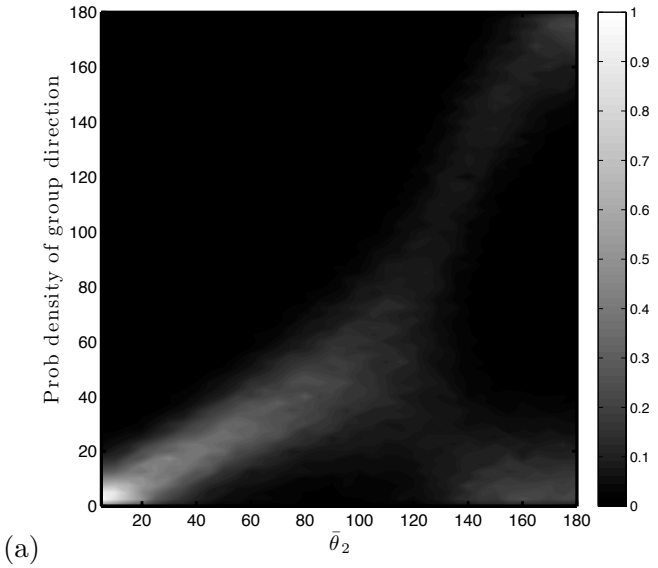

(a)

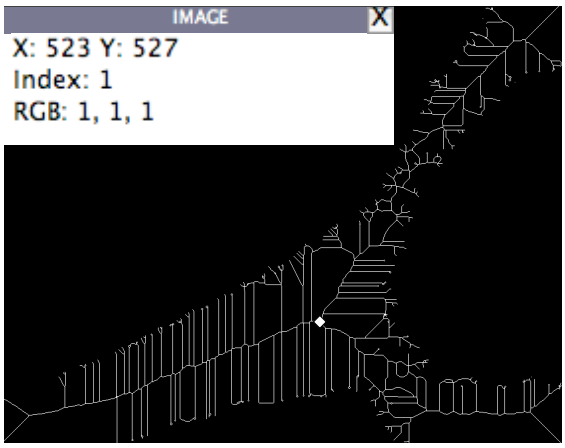

(b)

Figure 4.7: (a) Color scales shows normalized probability distribution (proportion of maximum) of group direction for a group containing $N_1 = 5$ informed individuals with preferred direction of 0 degrees, $N_2 = 5$ informed individuals with preferred direction $\bar{\theta}_2 \in [0, 180]$, and $N_3 = 80$ naive individuals with no preferred direction. The informed individuals in each subgroup have the same level of assertiveness $\omega = .4$. For $\bar{\theta}_2$ smaller than a certain threshold (between 100 and 110 degrees) the group follows the average of the preferred directions, while for $\bar{\theta}_2$ greater than the threshold the group selects one of the preferred directions with equal probability. (b) Processed version of the bifurcation plot in (a) with skeletonization. With this processed image, it is possible to identify more precisely the bifurcation point in pixels (here $X : 523$ $Y : 527$). Using the width of the processed image (here 926 pixels) we compute the bifurcation angle (threshold) $\bar{\theta}_2$ as $\frac{523}{926}180 \simeq 102$deg.

This suggests that for groups with fairly assertive informed individuals with conflicting preferences, naive individuals can help the group remain cohesive. When there are very large numbers of naive individuals, they can increase the probability of group fragmentation.

For all levels of assertiveness, we observe (Figures 4.2-4.5) that the bifurcation angle is a decreasing function of the number of naive individuals N_3, i.e., adding naive individuals moves the bifurcation point to the left. This means that the more naive individuals that join the group, the smaller the disagreement between the informed individuals needs to be to have the group switch from following the average of the preferred directions to collectively selecting one of the preferred directions. In other words, having naive individuals in a group increases the sensitivity of decision making in a group containing informed individuals with conflicting preferences. This trend is observed for all levels of assertiveness for the informed individuals but is more dramatic for lower levels of assertiveness. For $\omega = .1$ the bifurcation angle dropped from about 152 deg to about 97 deg while for $\omega = .4$ the bifurcation angle only dropped from about 120 deg to about 100 deg. This suggests that informed individuals that are less confident derive a greater benefit from associating and sharing their information with naive individuals than more confident informed individuals do.

The simulations presented in this section suggest two things. First naive individuals, in some circumstances, can help keep a group cohesive but, when in too great numbers, cause the group to fragment. Second, adding naive individuals to a group increases the sensitivity of decision making by increasing the size of the region of parameter space in which the group selects one of the preferred directions rather than follow the average of the preferred directions. In order to show that improving the sensitivity of decision making also improves its accuracy, we turn our attention from the the case where the informed individuals have a preferred direction to the case where they have a fixed target.

These two cases are in fact intimately related. As we explained in Section 4.1, informed individuals having a fixed target is equivalent to their having a changing preferred direction pointing towards the target. As shown in Figure 4.8, depending on the location of the agents relative to the targets, the difference of preferred direction between the two informed

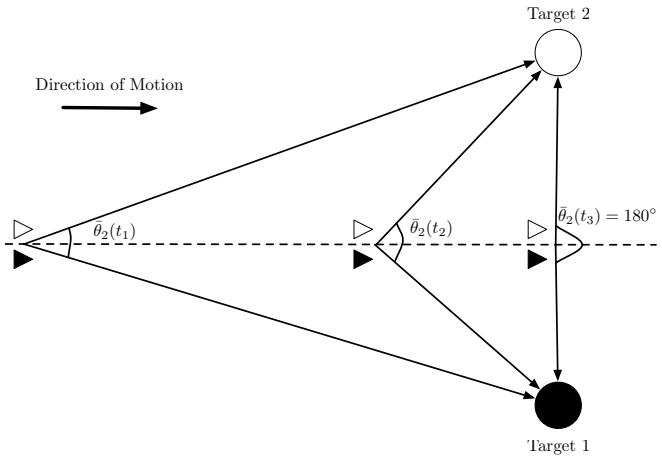

Figure 4.8: Informed individuals with fixed targets traveling in space. Black triangles represent one informed individual traveling along the dotted line at different times with the black disk as its fixed target. White triangles represent a different informed individual traveling along the dotted line at different times with the white disk as its fixed target. As the group moves along the dotted horizontal line the difference between the preferred directions $\bar{\theta}_2(t)$ continuously increases until reaching 180 degrees when the group is located on the line connecting the two targets.

subgroups $\bar{\theta}_2(t)$ changes. For example, if the group moves along the horizontal line between the targets (horizontal dotted line in Figure 4.8), $\bar{\theta}_2(t)$ continuously increases until reaching 180 degrees when the group is located on the line connecting the two targets. Assuming further that the agents are moving "slowly", the model with fixed preferred directions can be viewed as a "fast" time scale of the model with targets. This means that as the group gets closer to the targets, it will undergo the bifurcation investigated in the present section for the direction model.

An increased sensitivity of decision making for the model with fixed preferred directions implies that, for the model with fixed targets, the group will choose its target from further away. In the next section we investigate numerically the influence of naive individuals on the model with fixed targets. We show that adding naive individuals increases the accuracy of decision making and helps reduce the probability of group fragmentation. We also show that these trends are reversed when too many naive individuals are added.

4.3 Influence of Naive Individuals in the Target Model

We now focus our investigation on the influence of naive individuals in the case where the informed individuals have a fixed target. This setting is well suited for modeling animal foraging, for example, where desired destinations are a finite distance away. In order to reveal the role of the naive individuals, we run a suite of simulations. We consider groups containing two informed subgroups of unequal numbers with $N_1 = 6$ and $N_2 = 5$ but with equal levels of assertiveness ω varying from .1 to .4 by increments of .1, along with one naive subgroup with population N_3 varying between 0 and 100 by increments of 5. For such a group, reaching the target of the first informed subgroup constitutes the more accurate decision. For all simulations, the group starts randomly distributed (according to a uniform distribution) in a disk centered at the point $(0, 0)$ in the plane with a radius of $\frac{1}{2}\sqrt{N}$; the individuals in the first subgroup have a fixed target located at $(2300, -1000)$, and the individuals in the second informed subgroup have a fixed target located at $(2300, 1000)$. The targets are chosen such that the difference in preferred direction between two informed informed individuals located at the point $(0, 0)$, at the beginning of the simulation is approximately 47 degrees. Given the restriction on the initial conditions given above, this choice guarantees that the group will go through the bifurcation that we described in the previous section (i.e., when the difference in preferred direction is 100-150 degrees depending on the parameter values). For each set of values of the parameters (N_3, ω), we simulate the motion of the group for 100,000 time steps and check whether it reached a target or not and record which target was reached. We simulate each set of parameters enough times to get 1,000 replicates where the group reaches a target. With these simulations we compute, for all levels of assertiveness $\omega \in [.1, .4]$ and for all values of $N_3 \in [0, 100]$, the probability of group fragmentation, the probability of the group's reaching the target of the first informed subgroup (referred to as the "majority target"), and the probability, given that the group has not fragmented, of the group's reaching the target of the second informed subgroup (referred to as the "minority target"). Figures 4.9-4.11 represent for $\omega = .1, .2, .3$ and .4 the evolution, as a function of N_3, of the probability of group fragmentation, the probability of

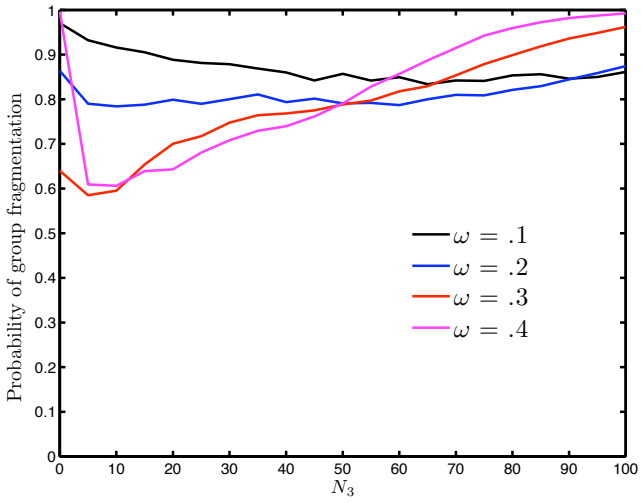

Figure 4.9: Probability of group fragmentation as a function of N_3 for $\omega = .1, .2, .3$ and .4. For low levels of assertiveness of the informed individuals, $\omega = .1$ or .2, introducing "few" naive individuals in the group (less than 60) slightly reduces the probability of group fragmentation, but adding "too many" naive individuals (more than 60) to the group reverses this trend. For high level of assertiveness of the informed individuals, $\omega = .4$, introducing "few" naive individuals in the group (less than 10) dramatically reduces the probability of group fragmentation but adding more than 10 naive individuals reverses this trend. Informed individuals with a level of assertiveness $\omega = .3$, seem never to benefit from associating with naive individuals.

reaching the majority target and the probability of reaching the minority target given that the group has not fragmented.

In Figure 4.9 we observe that the effect of adding naive individuals on the probability of group fragmentation depends on the level of assertiveness assumed for the informed individuals. For low levels of assertiveness of the informed individuals ($\omega = .1$ or .2), introducing "few" naive individuals in the group (less than 60) slightly reduces the probability of group fragmentation (from 97 percent to 82 percent for $\omega = .1$ and from 86 percent to 78 percent for $\omega = .2$). However, adding "too many" naive individuals in the group (more than 60) causes this trend to be reversed. For high levels of assertiveness of the informed individuals ($\omega = .4$), introducing "few" naive individuals in the group (less than 10) dramatically reduces the probability of group fragmentation (from almost 100 percent to about 60 per-

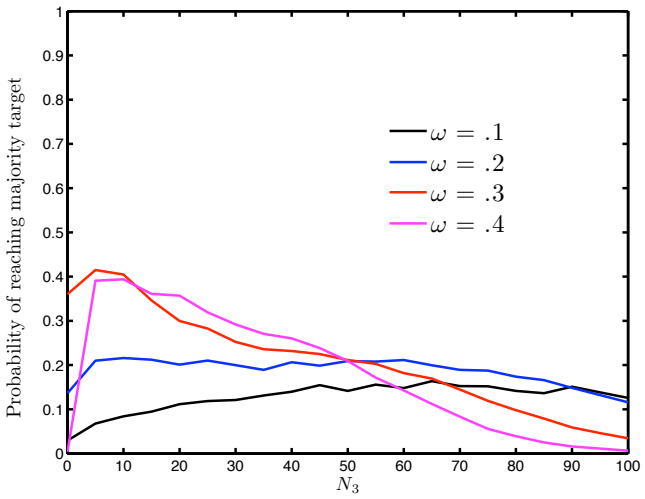

Figure 4.10: Probability of reaching the majority target overall as a function of N_3 for $\omega = .1, .2, .3$ and .4. For low levels of assertiveness of the informed individuals, $\omega = .1$ or .2, introducing "few" naive individuals in the group (less than 60) slightly increases the probability of reaching the majority target but adding "too many" naive individuals (more than 60) to the group causes this trend to be reversed. For high level of assertiveness of the informed individuals, $\omega = .4$, introducing "few" naive individuals in the group (less than 10) dramatically increases the probability of group fragmentation but adding more than 10 naive individuals causes this trend to be reversed. Informed individuals with a level of assertiveness of $\omega = .3$, seem never to benefit from associating with naive individuals.

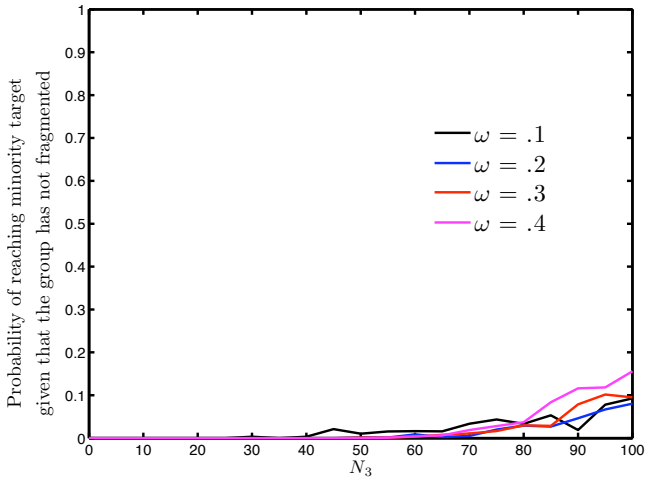

Figure 4.11: Probability of reaching the minority target, given that the group has not fragmented, as a function of N_3 for $\omega = .1, .2, .3$ and $.4$. For all level of assertiveness, adding "too many" naive individuals in the group (more than 60) causes the group to start making mistakes i.e., going to the minority target. We note that the higher the level of assertiveness the more likely the group will be to select the wrong target.

cent). However, adding more than 10 naive individuals causes this trend to be reversed with the probability of group fragmentation returning to nearly 100 percent when over 90 naive individuals are added. These results suggest that it is beneficial for informed individuals to associate with some naive individuals, as they help the group to remain cohesive. When informed individuals associate with "too many" naive individuals, however, the benefit is lost. It is interesting to note that more assertive individuals derive greater benefit from mixing with naive individuals than do less assertive informed individuals. However, more assertive individuals lose this relative benefit much more quickly when they associate with too many naive individuals. The effect of adding naive individuals in the case where $\omega = .3$ is harder to understand because even with no naive individual in the mix, the group already has a "low" rate of fragmentation (a little above 60 percent), and adding naive individuals causes the probability of group fragmentation almost exclusively to increase. It seems as though informed individuals with this level of assertiveness derive almost no benefit from their association with naive individuals.

In Figure 4.10 we observe that the variations of the probability of group fragmentation described in the previous paragraph translates into variations of the probability of the group's reaching the majority target. For "low" levels of assertiveness ($\omega = .1$ or $.2$), introducing "few" naive individuals in the group (less than 60) slightly increases the probability of reaching the majority target (from 4 percent to 16 percent for $\omega = .1$ and from 14 percent to 22 percent for $\omega = .2$). This trend is reversed, however, when "too many" naive individuals (more than 60) are added to the group. For high levels of assertiveness of the informed individuals ($\omega = .4$), introducing "few" naive individuals in the group (less than 10) dramatically increases the probability of reaching the majority target (from almost 0 percent to about 40 percent). However adding more than 10 naive individuals causes this trend to be reversed, with the probability of reaching the majority target decreasing again to nearly 0 percent when more than 90 naive individuals are added. These observations further support the idea that informed individuals benefit from associating with some naive individuals, since it increases the accuracy of decision making, but that associating with too many naive individuals diminishes this benefit. The plot for $\omega = .3$ also suggests that by this measure some informed individuals derive no benefit in associating with naive individuals.

In Figure 4.11 we observe that for all levels of assertiveness, adding "too many" naive individuals in the group (more than 60) causes the group to start making mistakes, i.e., going to the minority target. We note moreover that the higher the level of assertiveness the more likely the group will be to select the wrong target. With one hundred naive individuals in the group, if the informed individuals have a low level of assertiveness ($\omega = .1$), then the group will choose the "wrong" target about 8 percent of the time, whereas if the level of assertiveness of the informed individuals is high ($\omega = .4$), then the group will choose the "wrong" target as often as 18 percent of the time. This trend is consistent with our earlier observation that more assertive informed individuals are more strongly penalized by associating with "too many" naive individuals.

Our numerical investigation of the subtle role of naive individuals in the decision-making process within a heterogeneous group using the discrete-time model developed by Couzin

et al. [19] has highlighted possible drawbacks and benefits for informed individuals in associating with naive individuals. In both settings, with informed individuals having a fixed preferred direction and informed individuals having a fixed target, simulations suggest that informed individuals benefit from associating with some naive individuals, as they help the group remain cohesive and increase the sensitivity and accuracy of the decision making. When informed individuals associate with too many naive individuals, however, the benefits vanish. In these simulations, we also encountered phenomena that are hard to explain. For informed individuals with a certain level of assertiveness, there seemed to be no benefit in associating with naive individuals, only drawbacks. This observation highlights the point made at the beginning of this chapter: although the discrete-time model produces highly suggestive simulations, it is sometime hard to understand in detail the microscopic reasons for the macroscopic behavior observed. In the next two chapters of this dissertation, we turn our attention to simplified deterministic continuous-time models which allow for a deeper investigation of the behavior produced and a more complete exploration of parameter space.

Chapter 5

Collective Decision Making: A Simple Analytical Model

In this chapter, we derive and study the dynamics of a low-dimensional, deterministic, coordinated control system designed as an interacting approximation of the individual-based model investigated in Chapter 4. In Section 5.1, we present the model and its reduction using a time-scale separation argument. In Section 5.2 we study the full phase-space dynamics of the reduced model by computing equilibria and proving stability and bifurcations. In Section 5.3 we consider several extensions of the model to test its robustness. The material in this chapter has previously appeared in [79, 80]. The same model with certain kinds of heterogeneity was studied with an equation-free approach in [72].

5.1 Model and Reduction

The continuous-time model we present here is an interactive partner to the discrete-time model described in Chapter 4. The discrete-time model, first presented by Couzin et al. in [19], contains many degrees of freedom and produces highly suggestive simulation results. It is difficult, however, to use this model to prove particular mechanisms, define unifying principles, and explore all possible behaviors. The continuous-time model that we propose

and study here in a particular case is represented by a set of ordinary differential equations. A clear advantage of using ordinary differential equations is that it makes available to us sophisticated tools from the nonlinear dynamical system literature. It is then possible to study the global phase-space for the proposed simple model by computing equilibria and proving stability and bifurcations.

In order to formulate our continuous-time model, we make several simplifying assumptions from the model presented in [19] and in Chapter 4. First, our model describes the dynamics of the heading angles for all individuals in the population independent of their positions. Second, an all-to-all communication topology is assumed, meaning that every individual senses every other individuals in the population, so as to be able to adjust its own steering rate. Third, we remove the "forgetting factor" feedback term by not allowing informed individuals to update the strength of their attraction to their preferred direction. Finally, for the purpose of the global phase-space analysis, we ignore the presence of naive individuals (i.e. individuals without a preferred direction of travel) when describing the phase-space dynamics of the reduced model. These simplifications from the original discrete-time model yield a model that produces qualitative behaviors some of which, but not all, are observed in [19]. The observed deviations then draw our attention to a small number of assumptions that are potentially responsible for the behavior in [19]. Our exploration of the role of the naive individuals in the decision-making process, for example, as presented in Chapter 4, was motivated by the deviation between [80] and the result published in [19]. It is in this sense that we describe the continuous-time model presented here as an interacting partner to the discrete-time model of [19] and Chapter 4. In Chapter 6, we derive and analyze a similar model but relax the all-to-all coupling assumption and consider the presence of naive individuals. This model produces qualitative behaviors closer, although not identical, to the ones observed in [19] and in Chapter 4.

5.1.1 Particle Model

In this model, we consider a population of N interacting individuals, each described as a unit mass Newtonian particle moving in the plane at constant speed and controlled by its steering rate. The steering rate evolves though time under the influence of inter-particle measurements and, when applicable, information represented by a preferred direction of travel. Preferred directions of travel can, for example, represent knowledge of a migration route or of the direction to a known good source of food or resource. The model assumes an all-to-all communication topology in the group. In the natural setting, this all-to-all coupling assumption may be reasonably well justified for tightly clustered groups. For large swarms of insects or for microscopic organisms, however, this assumption is no longer realistic. It is for this reason that, in the next chapter, we relax this assumption and consider a model where the strength of the coupling between individuals is time-varying, yielding non-complete communication topologies.

The population is divided into three subgroups: two subgroups of informed individuals with N_1 and N_2 agents, respectively, and one subgroup of naive (uninformed) individuals with N_3 agents such that $N_1 + N_2 + N_3 = N$. We define $\mathcal{N}_1$ and $\mathcal{N}_2$, respectively as the subsets of indices in $\{1, \ldots, N\}$ corresponding to individuals in the informed subgroups 1 and 2, and $\mathcal{N}_3$ as the remaining subset of indices corresponding to the naive individuals. The cardinality of each subset $\mathcal{N}_k$ is N_k, $k = 1, 2, 3$. Agents in the informed subgroup i have a preferred direction of travel $\bar{\theta}_i$, for $i = 1, 2$.

We denote as θ_j the instantaneous heading direction of individual j, where θ_j is allowed to take any value in the circle S^1. Let $\vec{r}_j \in \mathbb{R}^2$ be the position in the plane of the j^{th} individual moving at constant speed V_0, then the instantaneous velocity vector $\vec{V}_j = \frac{d\vec{r}_j}{dt}$ is given by

$$\vec{V}_j = (V_0 \cos\theta_j, V_0 \sin\theta_j), \quad j = 1, \ldots, N.$$

The model we define consists of a set of differential equations describing the dynamics of these instantaneous heading directions θ_j. The dynamics are modeled with steering terms

that depend on relative heading angles, as

$$\begin{aligned}
\dot{\theta}_j &= \sin\left(\bar{\theta}_1 - \theta_j\right) + \frac{K}{N}\sum_{l=1}^{N}\sin\left(\theta_l - \theta_j\right), \quad j \in \mathcal{N}_1 \\
\dot{\theta}_j &= \sin\left(\bar{\theta}_2 - \theta_j\right) + \frac{K}{N}\sum_{l=1}^{N}\sin\left(\theta_l - \theta_j\right), \quad j \in \mathcal{N}_2 \\
\dot{\theta}_j &= \frac{K}{N}\sum_{l=1}^{N}\sin\left(\theta_l - \theta_j\right), \quad j \in \mathcal{N}_3\,,
\end{aligned} \tag{5.1}$$

where the parameter $K > 0$ weights the attention paid to other individuals versus the preferred direction. This assumption is related to the assumption of all-to-all communication topology and may be well justified for tightly clustered groups. This model was first presented in [79, 80].

The form of the coupling used in (5.1) is taken from the Kuramoto model for populations of coupled oscillators [60]. As we already emphasized in Chapter 1, the use of similar models in engineered and natural systems is not a coincidence. The very efficient and robust mechanisms refined through evolution and natural selection that are used by natural systems to move and achieve consensus decisions provide compelling inspiration for design of engineered systems, and the tools available for analysis of engineered systems have in turn proven useful for modeling and predicting natural phenomena. The Kuramoto model is a perfect example of this interaction between biology and engineering [1]. The Kuramoto model, which has been used to model natural phenomena in neuroscience [113], chemistry [59] and biology [135], has been studied using sophisticated tools from dynamical systems theory [115], while it has also provided inspiration to Sepulchre et al., to successfully stabilize circular and parallel collective motion of a group of agents [108, 107]. Mirollo and Strogatz used the Kuramoto model to model a group of coupled spins in a random magnetic field [71]. The coupled spin model is similar to our model but without subgroups of individuals with common preferences; rather, each individual oscillator has a randomly assigned "pinning" angle $\bar{\theta}_j$ such that the pinning angles are uniformly distributed around the circle. The authors proved that their system exhibits a jump bifurcation and hysteresis as K is varied. Our model also exhibits interesting bifurcations as the parameter K is varied as we explore

in Section 5.2.2.

5.1.2 Time Scale Reduction

The model (5.1) is challenging to study. It is an N-dimensional system and the "preferred direction" terms of the dynamics break the symmetries exploited to study the original Kuramoto model (see e.g. [115]). Simulations of the model (5.1) shown in Figure 5.1 suggest however that there are two time-scales in the dynamics. At first, during an initial transient time, the heading angles of the individuals in each subgroup synchronize. Then the three average subgroup directions slowly drift to reach a steady state. This means that there exists a set of "few" variables that can describe the long term dynamics of the model (5.1). Motivated by these observations, we formalize this time-scale separation by defining a new set of independent variables that allows us to distinguish between slow and fast variables.

Let ψ_1, ψ_2 and ψ_3 denote the average headings of the three subgroups; we choose them as the slow variables since they characterize the direction of travel of the three subgroups. The average headings ψ_1, ψ_2 and ψ_3 are defined from the parameter p_k, known as the complex order parameter in the coupled oscillator literature. The parameter $p_k \in \mathbb{C}$ is computed as the average of the phasors on the unit circle; its expression is given by

$$p_k = \rho_k e^{i\psi_k} = \frac{1}{N_k} \sum_{l \in \mathcal{N}_k} e^{i\theta_l}, \quad k = 1, 2, 3. \tag{5.2}$$

The argument of p_k, $\arg(p_k) = \psi_k$ corresponds to the average direction of the individuals in the k-th subgroup. The modulus of p_k, $|p_k| = \rho_k$ with values in the interval $[0, 1]$, provides a measure of synchrony among the phases. In particular, $\rho_k = 1$ if all individuals in $\mathcal{N}_k$ are heading in the same direction (synchronized headings) and $\rho_k = 0$ if individuals in $\mathcal{N}_k$ head in directions such that the average velocity of the group is zero. To represent the fast dynamics, we define as in [80] the following variables $\alpha_j \in \mathbb{C}$

$$\alpha_j = e^{i\left(N_k\theta_j - \sum\limits_{l \in \mathcal{N}_k} \theta_l\right)}, \quad j \in \mathcal{N}_k. \tag{5.3}$$

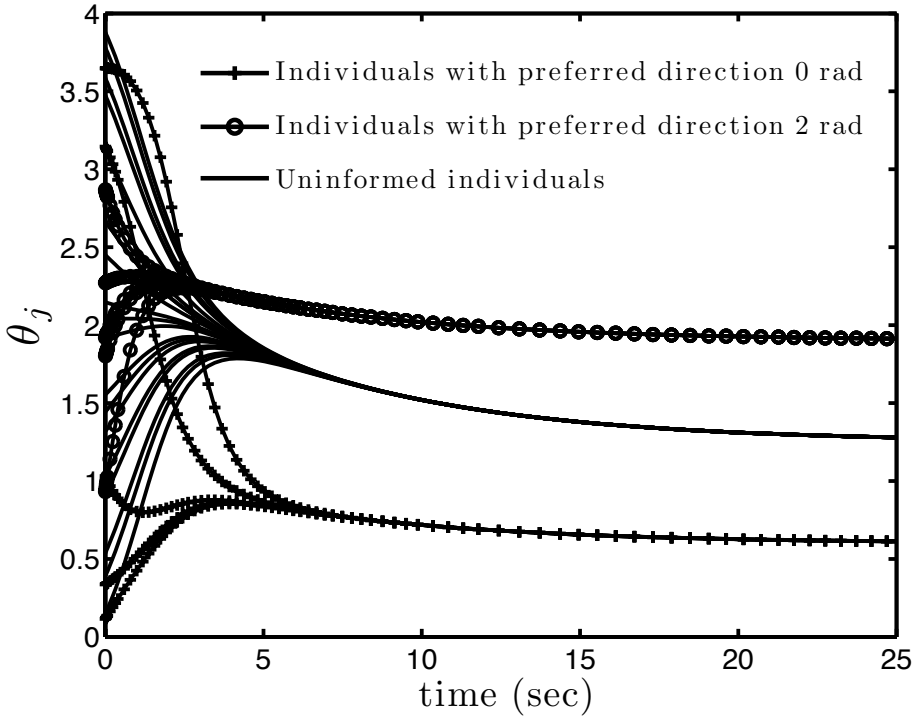

Figure 5.1: Phase angle of each individual in the group versus time for model (5.1) with $K = 1$. For this simulation there are five individuals with preferred direction 0 rad, five individuals with preferred direction 2 rad and twenty individuals with no preferred direction. Two time-scales in the dynamics can be observed. During a short initial transient time, the heading angles of the individuals in each subgroup synchronize. Then the three average subgroup directions change slowly to their steady state values.

Each variable α_j provides a measure of how "close" the heading of individual $j \in \mathcal{N}_k$ is to ψ_k, the average direction of the subgroup k. When all the individuals in the kth subgroup have the same heading, we have $\alpha_j = 1, \quad \forall j \in \mathcal{N}_k$. We denote $\boldsymbol{\theta} = (\theta_1, \ldots, \theta_N) \in T^N$ and $\boldsymbol{\alpha}^k = \left(\alpha_{j_{(k,1)}}, \ldots, \alpha_{j_{(k,N_k-1)}}\right) \in \mathbb{C}^{N_k-1}$, where $\mathcal{N}_k = \left\{j_{(k,1)}, \ldots, j_{(k,N_k)}\right\}$, and consider change of variables $\boldsymbol{\theta} \mapsto \left\{\boldsymbol{\alpha}^1, \boldsymbol{\alpha}^2, \boldsymbol{\alpha}^3, \psi_1, \psi_2, \psi_3\right\}$. The system (5.1) can be rewritten in the new set of coordinates as

$$\begin{aligned} \dot{\alpha}_{j_{(k,i)}} &= i\alpha_{j_{(k,i)}} \left(N_k \dot{\theta}_i - \sum_{l \in \mathcal{N}_k} \dot{\theta}_l \right), \quad i \in 1, \cdots, N_k - 1, \qquad k = 1, 2, 3 \\ \dot{\psi}_k &= \frac{1}{\rho_k N_k} \sum_{l \in \mathcal{N}_k} \dot{\theta}_l \cos(\psi_k - \theta_l), \qquad k = 1, 2, 3 \end{aligned} \tag{5.4}$$

Following the calculations in [115, 80], we rewrite the coupled multi-agent system dynamics (5.4) as

$$
\begin{aligned}
\dot{\alpha}_j &= iN_1\alpha_j\Big(\left(\sin\left(\bar{\theta}_1-\theta_j\right)-\rho_1\sin\left(\bar{\theta}_1-\psi_1\right)\right)+\frac{KN_1}{N}\rho_1\sin\left(\psi_1-\theta_j\right) \\
&\quad+\sum_{k=2,3}\frac{KN_k}{N}\rho_k\left(\sin\left(\psi_k-\theta_j\right)-\rho_1\sin\left(\psi_k-\psi_1\right)\right)\Big), \qquad j\in\mathcal{N}_1,\ j\neq j_{(1,N_1)} \\
\dot{\alpha}_j &= iN_2\alpha_j\Big(\left(\sin\left(\bar{\theta}_2-\theta_j\right)-\rho_2\sin\left(\bar{\theta}_2-\psi_2\right)\right)+\frac{KN_2}{N}\rho_2\sin\left(\psi_2-\theta_j\right) \\
&\quad+\sum_{k=1,3}\frac{KN_k}{N}\rho_k\left(\sin\left(\psi_k-\theta_j\right)-\rho_2\sin\left(\psi_k-\psi_2\right)\right)\Big), \qquad j\in\mathcal{N}_2,\ j\neq j_{(2,N_2)} \\
\dot{\alpha}_j &= iN_1\alpha_j\Big(\frac{KN_3}{N}\rho_3\sin\left(\psi_3-\theta_j\right) \\
&\quad+\sum_{k=2,3}\frac{KN_k}{N}\rho_k\left(\sin\left(\psi_k-\theta_j\right)-\rho_3\sin\left(\psi_k-\psi_3\right)\right)\Big), \qquad j\in\mathcal{N}_3,\ j\neq j_{(3,N_3)} \\
\dot{\psi}_1 &= \frac{1}{\rho_1}\sum_{j\in\mathcal{N}_1}\left(\frac{1}{N_1}\sin\left(\bar{\theta}_1-\theta_j\right)+\frac{K}{N}\left(\sum_{k=1}^{3}\frac{N_k}{N_1}\rho_k\sin\left(\psi_k-\theta_j\right)\right)\right)\cos\left(\psi_1-\theta_j\right) \\
\dot{\psi}_2 &= \frac{1}{\rho_2}\sum_{j\in\mathcal{N}_2}\left(\frac{1}{N_2}\sin\left(\bar{\theta}_2-\theta_j\right)+\frac{K}{N}\left(\sum_{k=1}^{3}\frac{N_k}{N_2}\rho_k\sin\left(\psi_k-\theta_j\right)\right)\right)\cos\left(\psi_2-\theta_j\right) \\
\dot{\psi}_3 &= \frac{1}{\rho_3}\sum_{j\in\mathcal{N}_3}\left(\frac{K}{N}\left(\sum_{k=1}^{3}\frac{N_k}{N_3}\rho_k\sin\left(\psi_k-\theta_j\right)\right)\right)\cos\left(\psi_3-\theta_j\right)
\end{aligned}
\tag{5.5}
$$

for $\rho_k\neq 0$, $k=1,2,3$.

The solution $\alpha_j=1$ for $j\in\mathcal{N}_k$, $k=1,2,3$, (or equivalently $\theta_j=\psi_k$, $j\in\mathcal{N}_k$, $k=1,2,3$,) is an isolated solution of $\dot{\alpha}_j=0$, $j\in\mathcal{N}_k$, $j\neq j_{(k,N_k)}$ $k=1,2,3$. For this solution $\rho_k=1$, $k=1,2,3$. In other words, $\theta_j=\psi_k$, $j\in\mathcal{N}_k$, $k=1,2,3$ is an invariant manifold of the system (5.5); we call this manifold $\mathcal{M}$. Physically this means that if we start with all individuals synchronized within their respective subgroup (i.e., $\theta_j=\psi_k$, $j\in\mathcal{N}_k$, $k=1,2,3$), they will remain so for all time.

Lemma 5.1.1 *The change of variables $\boldsymbol{\theta}\mapsto(\boldsymbol{\alpha}^1,\psi_1,\boldsymbol{\alpha}^2,\psi_2,\boldsymbol{\alpha}^3,\psi_3)$ is well defined near the invariant manifold $\mathcal{M}$.*

Proof: We write $(\boldsymbol{\alpha}^1,\psi_1,\boldsymbol{\alpha}^2,\psi_2,\boldsymbol{\alpha}^3,\psi_3)=F(\boldsymbol{\theta})$ and prove that F is locally invertible near

$\mathcal{M}$. On $\mathcal{M}$, we have

$$\left.\frac{\partial \alpha_{j_{(k,l)}}}{\partial \theta_m}\right|_{\mathcal{M}} = \begin{cases} -i & \text{if } m \in \mathcal{N}_k,\ m \neq j_{(k,l)} \\ (N_k - 1)i & \text{if } m = j_{(k,l)} \\ 0 & \text{otherwise} \end{cases} \tag{5.6}$$

$$\left.\frac{\partial \psi_k}{\partial \theta_m}\right|_{\mathcal{M}} = \begin{cases} \frac{1}{N_k} & \text{if } m \in \mathcal{N}_k \\ 0 & \text{otherwise.} \end{cases}$$

Using (5.6), the Jacobian of F evaluated on $\mathcal{M}$ can be written as

$$\left.\frac{dF}{d\boldsymbol{\theta}}\right|_{\mathcal{M}} = \operatorname{diag}(A_k),$$

where

$$A_k = \begin{pmatrix} (N_k-1)i & -i & \cdots & \cdots & -i \\ -i & \ddots & \ddots & -i & \vdots \\ \vdots & \ddots & \ddots & \ddots & \vdots \\ -i & \cdots & -i & (N_k-1)i & -i \\ \frac{1}{N_k} & \cdots & \cdots & \cdots & \frac{1}{N_k} \end{pmatrix} \in \mathbb{R}^{N_k \times N_k}, k = 1, 2, 3.$$

Each A_k is invertible with

$$A_k^{-1} = \begin{pmatrix} -\frac{i}{N_k} & 0 & \cdots & 0 & 1 \\ 0 & \ddots & \ddots & \vdots & \vdots \\ \vdots & \ddots & \ddots & 0 & \vdots \\ 0 & \cdots & 0 & -\frac{i}{N_k} & \vdots \\ \frac{i}{N_k} & \cdots & \cdots & \frac{i}{N_k} & 1 \end{pmatrix} \in \mathbb{R}^{N_k \times N_k}, \tag{5.7}$$

hence $\left.\frac{dF}{d\boldsymbol{\theta}}\right|_{\mathcal{M}}$ is also invertible. This concludes the proof that $F : \boldsymbol{\theta} \mapsto (\boldsymbol{\alpha}^1, \psi_1, \boldsymbol{\alpha}^2, \psi_2, \boldsymbol{\alpha}^3, \psi_3)$ is locally invertible in a neighborhood of $\mathcal{M}$. Hence the change of variables from $\boldsymbol{\theta} \mapsto (\boldsymbol{\alpha}^1, \psi_1, \boldsymbol{\alpha}^2, \psi_2, \boldsymbol{\alpha}^3, \psi_3)$ is well defined near $\mathcal{M}$. □

In order to prove the time-scale reduction, we rewrite the model (5.5) in the form of a singular perturbation model, decomposing it into a boundary layer (fast) model and a reduced (slow) model. We suppose $K \geq N >> 1$ and let $\epsilon = 1/K$. We assume further that N_1 and N_2 are such that $1/N_1$, $1/N_2$, N_1/N, N_2/N are not as small as ϵ. For example, if

$K = N = 100, N_1 = N_2 = 10, N_3 = 80$, then $\epsilon = 0.01$ but $1/N_1 = 1/N_2 = N_1/N = N_2/N = 0.1 = \sqrt{\epsilon}$. Given these assumptions the coupled multi-agent system dynamics (5.5) become

$$\begin{aligned}
\epsilon\dot{\alpha}_j &= iN_1\alpha_j\Big(\epsilon\left(\sin\left(\bar{\theta}_1-\theta_j\right)-\rho_1\sin\left(\bar{\theta}_1-\psi_1\right)\right)+\frac{N_1}{N}\rho_1\sin\left(\psi_1-\theta_j\right) \\
&\quad +\sum_{k=2,3}\frac{N_k}{N}\rho_k\left(\sin\left(\psi_k-\theta_j\right)-\rho_1\sin\left(\psi_k-\psi_1\right)\right)\Big) \qquad (5.8)\\
&=: g_j^1\left(\boldsymbol{\alpha}^1,\boldsymbol{\alpha}^2,\boldsymbol{\alpha}^3,\psi_1,\psi_2,\psi_3,\epsilon\right), \quad j\in\mathcal{N}_1,\ j\neq j_{(1,N_1)} \\
\epsilon\dot{\alpha}_j &= iN_2\alpha_j\Big(\epsilon\left(\sin\left(\bar{\theta}_2-\theta_j\right)-\rho_2\sin\left(\bar{\theta}_2-\psi_2\right)\right)+\frac{N_2}{N}\rho_2\sin\left(\psi_2-\theta_j\right) \\
&\quad +\sum_{k=1,3}\frac{N_k}{N}\rho_k\left(\sin\left(\psi_k-\theta_j\right)-\rho_2\sin\left(\psi_k-\psi_2\right)\right)\Big) \qquad (5.9)\\
&=: g_j^2\left(\boldsymbol{\alpha}^1,\boldsymbol{\alpha}^2,\boldsymbol{\alpha}^3,\psi_1,\psi_2,\psi_3,\epsilon\right), \quad j\in\mathcal{N}_2,\ j\neq j_{(2,N_2)} \\
\epsilon\dot{\alpha}_j &= iN_1\alpha_j\Big(\frac{N_3}{N}\rho_3\sin\left(\psi_3-\theta_j\right) \\
&\quad +\sum_{k=2,3}\frac{N_k}{N}\rho_k\left(\sin\left(\psi_k-\theta_j\right)-\rho_3\sin\left(\psi_k-\psi_3\right)\right)\Big) \qquad (5.10)\\
&=: g_j^3\left(\boldsymbol{\alpha}^1,\boldsymbol{\alpha}^2,\boldsymbol{\alpha}^3,\psi_1,\psi_2,\psi_3,\epsilon\right), \quad j\in\mathcal{N}_3,\ j\neq j_{(3,N_3)} \\
\dot{\psi}_1 &= \frac{1}{\rho_1}\sum_{j\in\mathcal{N}_1}\left(\frac{1}{N_1}\sin\left(\bar{\theta}_1-\theta_j\right)+\frac{K}{N}\sum_{k=1}^{3}\frac{N_k}{N_1}\rho_k\sin\left(\psi_k-\theta_j\right)\right)\cos\left(\psi_1-\theta_j\right) \qquad (5.11)\\
&=: f_1\left(\boldsymbol{\alpha}^1,\boldsymbol{\alpha}^2,\boldsymbol{\alpha}^3,\psi_1,\psi_2,\psi_3,\epsilon\right) \\
\dot{\psi}_2 &= \frac{1}{\rho_2}\sum_{j\in\mathcal{N}_2}\left(\frac{1}{N_2}\sin\left(\bar{\theta}_2-\theta_j\right)+\frac{K}{N}\sum_{k=1}^{3}\frac{N_k}{N_2}\rho_k\sin\left(\psi_k-\theta_j\right)\right)\cos\left(\psi_2-\theta_j\right) \qquad (5.12)\\
&=: f_2\left(\boldsymbol{\alpha}^1,\boldsymbol{\alpha}^2,\boldsymbol{\alpha}^3,\psi_1,\psi_2,\psi_3,\epsilon\right) \\
\dot{\psi}_3 &= \frac{1}{\rho_3}\sum_{j\in\mathcal{N}_3}\left(\frac{K}{N}\left(\sum_{k=1}^{3}\frac{N_k}{N_3}\rho_k\sin\left(\psi_k-\theta_j\right)\right)\right)\cos\left(\psi_3-\theta_j\right) \qquad (5.13)\\
&=: f_3\left(\boldsymbol{\alpha}^1,\boldsymbol{\alpha}^2,\boldsymbol{\alpha}^3,\psi_1,\psi_2,\psi_3,\epsilon\right)
\end{aligned}$$

for $\rho_k \neq 0$, $k = 1, 2, 3$.

With $\epsilon << 1$, the model (5.8)-(5.13) is in the form of a singular perturbation model (as described in [54]). The $N-3$ dimensional boundary layer (fast) model is represented by (5.8)-(5.10) and the 3 dimensional reduced (slow) model is represented by (5.11)-(5.13). The reduced dynamics on the invariant manifold $\mathcal{M}$ are then given by

$$\dot{\psi}_k = f_k\left(\boldsymbol{\alpha}^1=\mathbf{1},\boldsymbol{\alpha}^2=\mathbf{1},\boldsymbol{\alpha}^3=\mathbf{1},\psi_1,\psi_2,\psi_3,0\right), \quad k=1,2,3,$$

where $\mathbf{1} = (1, \ldots, 1)$, which can be written as

$$\begin{aligned}
\dot{\psi}_1 &= \sin\left(\bar{\theta}_1 - \psi_1\right) + \frac{K}{N} N_2 \sin\left(\psi_2 - \psi_1\right) + \frac{K}{N} N_3 \sin\left(\psi_3 - \psi_1\right) \\
\dot{\psi}_2 &= \sin\left(\bar{\theta}_2 - \psi_2\right) + \frac{K}{N} N_1 \sin\left(\psi_1 - \psi_2\right) + \frac{K}{N} N_3 \sin\left(\psi_3 - \psi_2\right) \\
\dot{\psi}_3 &= \frac{K}{N} N_1 \sin\left(\psi_1 - \psi_3\right) + \frac{K}{N} N_2 \sin\left(\psi_2 - \psi_3\right) \ .
\end{aligned} \tag{5.14}$$

Theorem 5.1.2 *Assuming $N_1 = N_2$ and $N_3 = 0$, the invariant manifold $\mathcal{M}$ is attractive.*

Given the attractiveness of the invariant manifold, singular perturbation theory (see e.g. [54]) then guarantees that solutions to the unreduced dynamics stay close to solutions of the reduced system.

Proof of Theorem 5.1.2: Assuming $N_1 = N_2$ and $N_3 = 0$, we show that the invariant manifold $\mathcal{M}$ is attractive by proving that it is a locally exponentially stable manifold of the boundary layer dynamics

$$\frac{d\alpha_j}{dt} = g_j(\boldsymbol{\alpha}^1, \boldsymbol{\alpha}^2, \psi_1, \psi_2, 0), \quad j \in \mathcal{N}_k,\ j \neq j_{(k,N_k)},\ k = 1, 2, \tag{5.15}$$

uniformly in ψ_1, ψ_2.

The boundary layer dynamics can be written as

$$\begin{aligned}
\dot{\alpha}_j = i N_1 \alpha_j \Bigg(&-\frac{N_1}{N} \rho_1 \sin(\psi_1 - \theta_j) + \frac{N_2}{N} \rho_2 \Big(\sin(\psi_2 - \theta_j) - \rho_1 \sin(\psi_2 - \psi_1) \Big) \\
&+ \frac{N_3}{N} \rho_3 \Big(\sin(\psi_3 - \theta_j) - \rho_1 \sin(\psi_3 - \psi_1) \Big) \Bigg), \quad j \in \mathcal{N}_1, j \neq j_{(1,N_1)} \\
\dot{\alpha}_j = i N_2 \alpha_j \Bigg(&-\frac{N_2}{N} \rho_2 \sin(\psi_2 - \theta_j) + \frac{N_1}{N} \rho_1 \Big(\sin(\psi_1 - \theta_j) - \rho_2 \sin(\psi_1 - \psi_2) \Big) \\
&+ \frac{N_3}{N} \rho_3 \Big(\sin(\psi_3 - \theta_j) - \rho_2 \sin(\psi_3 - \psi_2) \Big) \Bigg), \quad j \in \mathcal{N}_2, j \neq j_{(2,N_2)}.
\end{aligned}$$

The linearization of the boundary layer model is given by

$$\begin{aligned}
\left.\frac{\partial \dot{\alpha}_j}{\partial \alpha_m}\right|_{\mathcal{M}} = -i \frac{N_k}{N} \Bigg(&\left.\frac{\partial \theta_j}{\partial \alpha_m}\right|_{\mathcal{M}} \Big(N_k + \sum_{l \neq k} N_l \cos(\psi_l - \psi_k) \Big) + \left.\frac{\partial \rho_k}{\partial \alpha_m}\right|_{\mathcal{M}} \sum_{l \neq k} N_l \sin(\psi_l - \psi_k) \Bigg), \\
&j \in \mathcal{N}_k,\ j \neq j_{(k,N_k)},\ k = 1, 2, 3,\ m \in \{1, \ldots, N\} \setminus \{j_{(1,N_1)}, j_{(2,N_2)}\}.
\end{aligned} \tag{5.16}$$

Using equation (5.7), the values for $\frac{\partial \theta_j}{\partial \alpha_m}\Big|_{\mathcal{M}}$ can be read as

$$\frac{\partial \theta_j}{\partial \alpha_m}\Big|_{\mathcal{M}} = \begin{cases} -\frac{i}{N_k} & \text{if } m = j, \\ 0 & \text{otherwise.} \end{cases} \tag{5.17}$$

Taking partial derivatives with respect to α_m of equation (5.2) yields

$$\frac{\partial \rho_k}{\partial \alpha_m} e^{i\psi_k} + \rho_k i \frac{\partial \psi_k}{\partial \alpha_m} e^{i\psi_k} = \frac{i}{N_k} \sum_{j \in \mathcal{N}_k} \frac{\partial \theta_j}{\partial \alpha_m} e^{i\theta_j}. \tag{5.18}$$

Evaluating (5.18) on $\mathcal{M}$ and using equation (5.7) gives

$$\frac{\partial \rho_k}{\partial \alpha_m}\Big|_{\mathcal{M}} = \frac{i}{N_k} \sum_j \frac{\partial \theta_j}{\partial \alpha_m}\Big|_{\mathcal{M}} = 0. \tag{5.19}$$

Plugging equation (5.17) and (5.19) into (5.16), the Jacobian can be rewritten as a diagonal matrix J with

$$J_{jj} = -\frac{1}{N}\Big(N_k + \sum_{l \neq k} N_l \cos(\psi_l - \psi_k)\Big), \quad j \in \mathcal{N}_k, j \neq j_{(k,N_k)}, k = 1, 2.$$

When $N_1 = N_2$ the eigenvalues of J are strictly negative, thus concluding the proof that $\mathcal{M}$ is a locally exponentially stable manifold of (5.15) uniformly in ψ_1, ψ_2. Hence $\mathcal{M}$, the invariant manifold of (5.1) defined by $\theta_j = \psi_k$, $j \in \mathcal{N}_k$, $k = 1, 2$, is attractive. □

The solution of the boundary layer (fast) dynamics corresponds to synchronization of all particle headings in subgroup k to a common heading ψ_k, for $k = 1, 2, 3$. These common headings then follow the reduced (slow) model (5.14). This reduced model is one in which all the agents in each subgroup (informed subgroups 1 and 2 and naive subgroup 3) behave as a single entity and the inter-subgroup coupling term is weighted by the corresponding subgroup population size as well as the bifurcation parameter K. This grouping of identical individuals is consistent with the spatial clustering observed in the simulations from [19]. In the next section, we present a full phase-space dynamics analysis of the reduced model (5.14) assuming $N_1 = N_2$ and $N_3 = 0$, and in so doing show the different stable and unstable motions, and investigate bifurcations in the $K, \bar{\theta}_2$ parameters. Extension to the cases $N_1 \neq N_2$ and $N_3 \neq 0$ will be considered numerically in Section 5.3. The extension to the case $N_3 \neq 0$ is developed more formally in Chapter 6.

5.2 Phase Space Dynamics of the Reduced Model

In the case $N_1 = N_2$ and $N_3 = 0$, the system (5.14) becomes

$$\begin{aligned} \dot{\psi}_1 &= \sin\left(\bar{\theta}_1 - \psi_1\right) + \frac{K}{2}\sin\left(\psi_2 - \psi_1\right) \\ \dot{\psi}_2 &= \sin\left(\bar{\theta}_2 - \psi_2\right) + \frac{K}{2}\sin\left(\psi_1 - \psi_2\right). \end{aligned} \tag{5.20}$$

Without loss of generality we set $\bar{\theta}_1 = 0$ and consider the two bifurcation parameters, $K \geq 0$ and $\bar{\theta}_2 \in (0, \pi]$. The case $\bar{\theta}_2 = 0$, which corresponds to having all informed individuals identical, is ignored. In this case there is no disagreement, and it can be shown that the groups travel in the direction $\bar{\theta}_1 = \bar{\theta}_2 = 0$.

We note that in the studied special case (i.e., $N_1 = N_2$ and $N_3 = 0$), the reduced model is a gradient system. The dynamics are gradient such that

$$\dot{\psi}_k = -\frac{\partial V}{\partial \psi_k},$$

where V is given by

$$V\left(\psi_1, \psi_2\right) = -\cos(\bar{\theta}_1 - \psi_1) - \cos\left(\bar{\theta}_2 - \psi_2\right) - \frac{K}{2}\cos\left(\psi_2 - \psi_1\right).$$

Thus, LaSalle's Invariance Principle guarantees that all solutions converge to the set of critical points of $V\left(\psi_1, \psi_2\right)$ and that there are no periodic solutions.

5.2.1 Equilibria of the Reduced System (5.20)

We compute the equilibria of the system (5.20) but note that, except for specific values of the parameters $K, \bar{\theta}_2$, we cannot find closed form expressions for all of them. For each equilibrium we nevertheless describe how its value and stability changes as the bifurcation parameters K and $\bar{\theta}_2$ vary. We call an equilibrium *synchronized* if $\psi_1 = \psi_2 \bmod 2\pi$ and *anti-synchronized* if $\psi_1 - \psi_2 = \pi \bmod 2\pi$. The equilibria are given by

$$\begin{aligned} -\sin\psi_1 + \frac{K}{2}\sin\left(\psi_2 - \psi_1\right) &= 0 \\ \sin\left(\bar{\theta}_2 - \psi_2\right) + \frac{K}{2}\sin\left(\psi_1 - \psi_2\right) &= 0. \end{aligned}$$

There are two sets of solutions, the first set given by

$$\psi_1 = \pi - \bar{\theta}_2 + \psi_2$$
$$\sin\left(\psi_2 - \bar{\theta}_2\right) = \frac{K}{2}\sin\bar{\theta}_2, \tag{5.21}$$

and the second set given by

$$\psi_1 = \bar{\theta}_2 - \psi_2 \tag{5.22}$$
$$\sin\left(\bar{\theta}_2 - \psi_2\right) = \frac{K}{2}\sin\left(2\psi_2 - \bar{\theta}_2\right)\ . \tag{5.23}$$

In the first set of solutions, equation (5.21) has two solutions: $\psi_2 = \bar{\theta}_2 + \arcsin\left(\frac{K}{2}\sin\bar{\theta}_2\right)$ and $\psi_2 = \bar{\theta}_2 + \pi - \arcsin\left(\frac{K}{2}\sin\bar{\theta}_2\right)$. These two solutions exist if and only if $|\frac{K}{2}\sin\bar{\theta}_2| \leq 1$.

Lemma 5.2.1 *If $|\frac{K}{2}\sin\bar{\theta}_2| < 1$, then the two equilibria $\boldsymbol{\psi}_{S1} = (\psi_1, \psi_2)_{S1}$ and $\boldsymbol{\psi}_{S2} = (\psi_1, \psi_2)_{S2}$ satisfying (5.21) and given by*

$$\boldsymbol{\psi}_{S1} = \left(\pi + \arcsin\left(\frac{K}{2}\sin\bar{\theta}_2\right), \bar{\theta}_2 + \arcsin\left(\frac{K}{2}\sin\bar{\theta}_2\right)\right), \tag{5.24}$$
$$\boldsymbol{\psi}_{S2} = \left(-\arcsin\left(\frac{K}{2}\sin\bar{\theta}_2\right), \pi + \bar{\theta}_2 - \arcsin\left(\frac{K}{2}\sin\bar{\theta}_2\right)\right), \tag{5.25}$$

are saddle points $\forall K > 0$ and $\forall\bar{\theta}_2 \in [0, \pi]$. If $\frac{K}{2}\sin\bar{\theta}_2 = 1$, then $\boldsymbol{\psi}_{S1} = \boldsymbol{\psi}_{S2}$. In this case, if also $K > 0$ and $\bar{\theta}_2 \in \left(0, \frac{\pi}{2}\right) \cup \left(\frac{\pi}{2}, \pi\right)$, then $\boldsymbol{\psi}_{S1} = \boldsymbol{\psi}_{S2}$ is unstable with one zero eigenvalue and one positive real eigenvalue. If $\bar{\theta}_2 = \frac{\pi}{2}$ (and $K = 2$), then both eigenvalues are zero.

Proof: The proof of Lemma 5.2.1 can be found in Appendix A.

Figure 5.2 shows the equilibrium $\boldsymbol{\psi}_{S1}$ for $K = 1, 2, 4$ and $\bar{\theta}_2 = 0.1, \frac{\pi}{2}, \pi$. For this equilibrium, the relative heading of the two informed subgroups is constant, and equal to $\bar{\theta}_2 - \pi$. As $\bar{\theta}_2$ goes from 0 to π, the equilibrium goes from being anti-synchronized, with each subgroup traveling opposite to its preferred direction, to being synchronized in the preferred direction of the second informed subgroup.

Figure 5.3 shows the equilibrium $\boldsymbol{\psi}_{S2}$ for $K = 1, 2, 4$ and $\bar{\theta}_2 = .1, \frac{\pi}{2}, \pi$. For this equilibrium, the relative heading of the two informed subgroups is constant, and equal to $\bar{\theta}_2 + \pi$. As $\bar{\theta}_2$ goes from 0 to π, the equilibrium goes from being anti-synchronized, with each subgroup

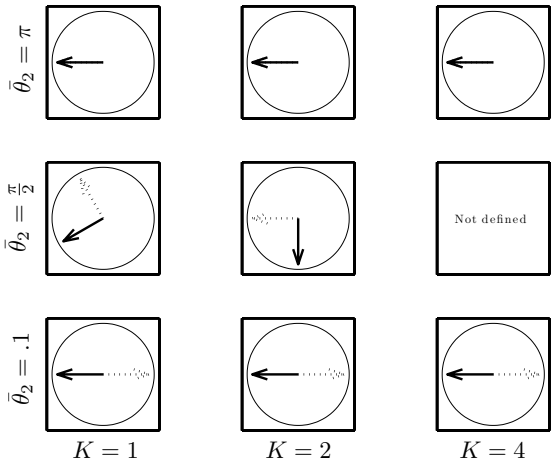

Figure 5.2: Unit circle picture of the equilibrium $\boldsymbol{\psi}_{S1}$ for $K = 1, 2, 4$ and $\bar{\theta}_2 = .1, \frac{\pi}{2}, \pi$. The solid vector represents ψ_1, the average heading of the first informed subgroup, and the dashed vector represents ψ_2, the average heading of the second subgroup. The zero degree reference corresponds to a vector pointing to the right with angles increasing in the counter-clockwise direction.

traveling towards its preferred direction, to being synchronized in the preferred direction of the first informed subgroup.

For the equilibria from the second set of solutions given by equations (5.22)-(5.23) we make a change of variables $(\psi_1, \psi_2) \mapsto (\rho, \Psi)$ where $\rho \in [0, 1]$ and $\Psi \in S^1$ are defined by

$$\rho e^{i\Psi} = \frac{1}{2}\left(e^{i\psi_1} + e^{i\psi_2}\right) = \cos\left(\frac{\psi_1 - \psi_2}{2}\right) e^{i(\psi_1+\psi_2)/2} \tag{5.26}$$

$$= \cos\left(\frac{\bar{\theta}_2}{2} - \psi_2\right)\left(\cos\frac{\bar{\theta}_2}{2} + i\sin\frac{\bar{\theta}_2}{2}\right). \tag{5.27}$$

Equation (5.27) is obtained by combining equations (5.22) and (5.26). For $\bar{\theta}_2 \in (0, \pi]$, $\psi_1 = \bar{\theta}_2 - \psi_2$ implies that $\Psi = \frac{\bar{\theta}_2}{2}$ or $\Psi = \frac{\bar{\theta}_2}{2} + \pi$. We further rewrite (5.23) as

$$\sin\frac{\bar{\theta}_2}{2}\cos\left(\frac{\bar{\theta}_2}{2} - \psi_2\right) + \cos\frac{\bar{\theta}_2}{2}\sin\left(\frac{\bar{\theta}_2}{2} - \psi_2\right) + K\sin\left(\frac{\bar{\theta}_2}{2} - \psi_2\right)\cos\left(\frac{\bar{\theta}_2}{2} - \psi_2\right) = 0. \tag{5.28}$$

For $\Psi = \frac{\bar{\theta}_2}{2}$, (5.27) implies that $\cos\left(\frac{\bar{\theta}_2}{2} - \psi_2\right) = \rho$ and $\sin\left(\frac{\bar{\theta}_2}{2} - \psi_2\right) = \pm\sqrt{1-\rho^2}$. Accordingly, (5.28) implies that ρ satisfies

$$\rho\sin\frac{\bar{\theta}_2}{2} + \sqrt{1-\rho^2}\cos\frac{\bar{\theta}_2}{2} + K\rho\sqrt{1-\rho^2} = 0 \tag{5.29}$$

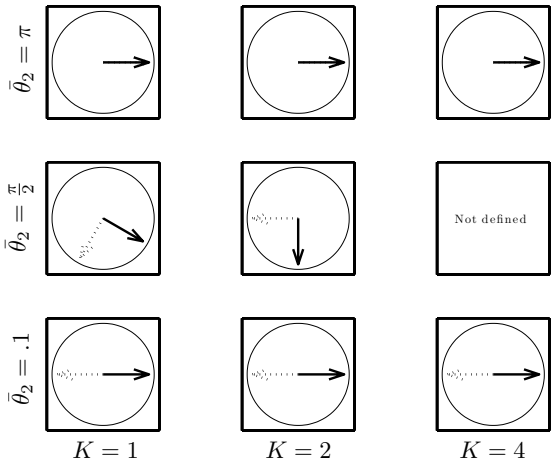

Figure 5.3: Picture of the equilibrium $\boldsymbol{\psi}_{S2}$ for $K = 1, 2, 4$ and $\bar{\theta}_2 = .1, \frac{\pi}{2}, \pi$.

or

$$\rho \sin \frac{\bar{\theta}_2}{2} - \sqrt{1-\rho^2} \cos \frac{\bar{\theta}_2}{2} - K\rho\sqrt{1-\rho^2} = 0. \tag{5.30}$$

For $\Psi = \frac{\bar{\theta}_2}{2} + \pi$, (5.27) implies that $\cos\left(\frac{\bar{\theta}_2}{2} - \psi_2\right) = -\rho$ and $\sin\left(\frac{\bar{\theta}_2}{2} - \psi_2\right) = \pm\sqrt{1-\rho^2}$. Accordingly, (5.28) implies that ρ satisfies

$$-\rho \sin \frac{\bar{\theta}_2}{2} + \sqrt{1-\rho^2} \cos \frac{\bar{\theta}_2}{2} - K\rho\sqrt{1-\rho^2} = 0 \tag{5.31}$$

or

$$-\rho \sin \frac{\bar{\theta}_2}{2} - \sqrt{1-\rho^2} \cos \frac{\bar{\theta}_2}{2} + K\rho\sqrt{1-\rho^2} = 0. \tag{5.32}$$

We now consider equations (5.29)-(5.32) individually and determine the existence and nature of the equilibria that they yield. We ignore for now the case $\bar{\theta}_2 = \pi$; it will be studied separately, in Section 5.2.2. For all solutions of equations (5.29), (5.30), (5.31) and (5.32), as K gets increasingly large, $K\rho\sqrt{1-\rho^2}$ must approach zero. This means that as $K \to \infty$, $\rho \to 0$ or $\rho \to 1$. Thus, for very large values of K all the equilibria will be either *synchronized* ($\rho \to 1$) or *anti-synchronized* ($\rho \to 0$). For finite values of K, the coupling term competes with the attraction to the preferred direction, and the equilibria are often neither fully synchronized nor fully anti-synchronized. We call an equilibrium *K-almost synchronized* (*K-almost anti-synchronized*) if the corresponding equilibrium in the case $K \gg 1$ is

synchronized (anti-synchronized). K-almost synchronization occurs at $\Psi \frac{\bar{\theta}_2}{2}$ and $\Psi = \frac{\bar{\theta}_2}{2} + \pi$ which represent a compromise between the two preferred directions. We now look at the solution of equations (5.29)-(5.32) and study the yielded equilibria.

Equation (5.29) does not have any solution for $(\rho, \bar{\theta}_2) \in [0,1] \times (0, \pi)$ since all of the terms on the left hand side of the equation are strictly positive.

Equation (5.30) has one solution for $(\rho, \bar{\theta}_2) \in [0,1] \times (0, \pi)$; we call the corresponding equilibrium $\boldsymbol{\psi}_{sync1} := (\psi_1, \psi_2)_{sync1}$. This equilibrium is K-almost synchronized, with K-almost synchronization occurring at $\Psi = \frac{\bar{\theta}_2}{2}$

Lemma 5.2.2 *The equilibrium $\boldsymbol{\psi}_{sync1}$ is a stable node for all $\left(K, \bar{\theta}_2\right) \in [0, \infty) \times (0, \pi)$.*

Proof: The proof of Lemma 5.2.2 can be found in Appendix A.

Figure 5.4 shows the equilibrium ψ_{sync1} for $K = 1, 4, 100$ and $\bar{\theta}_2 = .1, \frac{\pi}{2}, 3.1$. For all $\bar{\theta}_2$ fixed, as K increases, the equilibrium becomes synchronized at $\frac{\bar{\theta}_2}{2}$. This motion in the average of the preferred directions is stable for $\left(K, \bar{\theta}_2\right) \in [0, \infty) \times (0, \pi)$ and corresponds to having all individuals compromising between their desire to stay with the group and to follow their preferred direction.

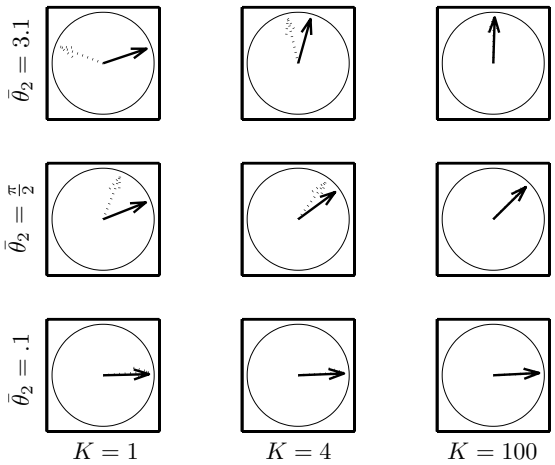

Figure 5.4: Picture of the equilibrium $\boldsymbol{\psi}_{sync1}$ for $K = 1, 4, 100$ and $\bar{\theta}_2 = 0.1, \frac{\pi}{2}, 3.1$.

Equation (5.31) has one solution for $(\rho, \bar{\theta}_2) \in [0,1] \times (0, \pi)$; we call the corresponding equilibrium $\boldsymbol{\psi}_{antisync1} := (\psi_1, \psi_2)_{antisync1}$. This equilibrium is K-almost anti-synchronized.

Lemma 5.2.3 *The equilibrium $\boldsymbol{\psi}_{antisync1}$ is unstable for all $\left(K, \bar{\theta}_2\right) \in [0, \infty) \times (0, \pi)$.*

Proof: The proof of Lemma 5.2.3 can be found in Appendix A.

Figure 5.5 shows the equilibrium $\psi_{antisync1}$ for $K = 1, 4, 100$ and $\bar{\theta}_2 = .1, \frac{\pi}{2}, 3.1$. For all $\bar{\theta}_2$ fixed, as K increases, the equilibrium becomes anti-synchronized. This motion of the two informed subgroups is unstable for $\left(K, \bar{\theta}_2\right) \in [0, \infty) \times (0, \pi)$.

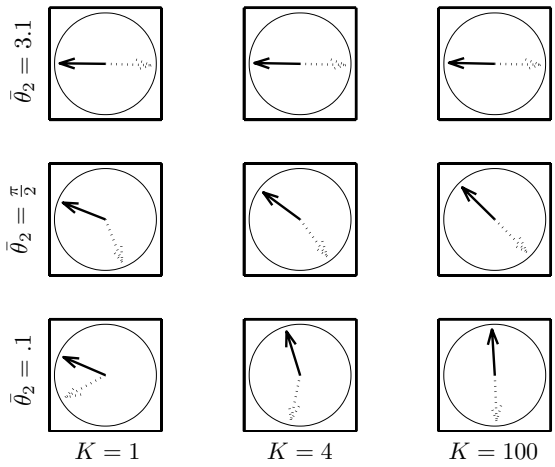

Figure 5.5: Picture of the equilibrium $\boldsymbol{\psi}_{antisync1}$ for $K = 1, 4, 100$ and $\bar{\theta}_2 = 0.1, \frac{\pi}{2}, 3.1$.

Equation (5.32) has between zero and two solutions for $(\rho, \bar{\theta}) \in [0, 1] \times (0, \pi)$. The equilibria emerging from (5.32), when they exist, are called $\boldsymbol{\psi}_{sync2} := (\psi_1, \psi_2)_{sync2}$ and $\boldsymbol{\psi}_{antisync2} := (\psi_1, \psi_2)_{antisync2}$.

Lemma 5.2.4 *Equation (5.32) has two solutions $(\rho_{antisync2}, \rho_{sync2})$ when $K > K_1 = \left(\cos\left(\frac{\bar{\theta}_2}{2}\right)^{\frac{2}{3}} + \sin\left(\frac{\bar{\theta}_2}{2}\right)^{\frac{2}{3}}\right)^{\frac{3}{2}}$ such that*

$$0 < \rho_{antisync2} < \sqrt{1 - \left(\frac{\sin\frac{\bar{\theta}_2}{2}}{K}\right)^{\frac{2}{3}}} < \rho_{sync2} < \sqrt{1 - \left(\frac{\sin\frac{\bar{\theta}_2}{2}}{K}\right)^{2}} < 1. \tag{5.33}$$

Proof: We pose $K' = K/\sin\frac{\bar{\theta}_2}{2}$, which is valid for $\bar{\theta}_2 \in (0, \pi)$. Equation (5.32) becomes

$$\rho \sin\frac{\bar{\theta}_2}{2} + \sqrt{1-\rho^2}\cos\frac{\bar{\theta}_2}{2} - K' \sin\frac{\bar{\theta}_2}{2}\rho\sqrt{1-\rho^2} = 0,$$

which can be rewritten as

$$\rho\left(\frac{1}{\sqrt{1-\rho^2}}-K'\right)=-\cot\frac{\bar{\theta}_2}{2}. \tag{5.34}$$

The solutions of (5.32) exist when the function $g(\rho)=\rho\left(\frac{1}{\sqrt{1-\rho^2}}-K'\right)$ intersects the constant $y=-\cot\frac{\bar{\theta}_2}{2}<0$. The function $g(\rho)$ goes to zero when $\rho\to 0$, approaches $+\infty$ when $\rho\to 1$, and reaches its minimum of $-K'(\rho^*)^3$ at $\rho^*=\sqrt{1-\frac{1}{K'^{2/3}}}$. Equation (5.32) has two solutions $(\rho_{antisync2},\rho_{sync2})$ flanking ρ^* if and only if $g(\rho^*)<-\cot\left(\frac{\bar{\theta}_2}{2}\right)$; this last inequality is satisfied if and only if

$$K>K_1=\left(\cos\left(\frac{\bar{\theta}_2}{2}\right)^{\frac{2}{3}}+\sin\left(\frac{\bar{\theta}_2}{2}\right)^{\frac{2}{3}}\right)^{\frac{3}{2}}. \tag{5.35}$$

The two solutions $(\rho_{antisync2},\rho_{sync2})$ have to be smaller than the zero of the function $g(\rho)$ given by $\sqrt{1-\left(\frac{\sin\frac{\bar{\theta}_2}{2}}{K}\right)^2}<1$. This concludes the proof that equation (5.32) has two solutions $(\rho_{antisync2},\rho_{sync2})$ when $K>K_1=\left(\cos\left(\frac{\bar{\theta}_2}{2}\right)^{\frac{2}{3}}+\sin\left(\frac{\bar{\theta}_2}{2}\right)^{\frac{2}{3}}\right)^{\frac{3}{2}}$ such that

$$0<\rho_{antisync2}<\sqrt{1-\left(\frac{\sin\frac{\bar{\theta}_2}{2}}{K}\right)^{\frac{2}{3}}}<\rho_{sync2}<\sqrt{1-\left(\frac{\sin\frac{\bar{\theta}_2}{2}}{K}\right)^2}<1. \qquad \square$$

We note that given the form of $g(\rho)$, $\rho_{antisync2}$ (ρ_{sync2}) is a decreasing (increasing) function of K, making the equilibrium $\boldsymbol{\psi}_{antisync2}$ ($\boldsymbol{\psi}_{sync2}$) K-almost anti-synchronized (K-almost synchronized).

Lemma 5.2.5 *The equilibrium $\boldsymbol{\psi}_{sync2}$ is unstable for all $(K,\bar{\theta}_2)\in[K_1,\infty)\times(0,\frac{\pi}{2})\cup[K_0,\infty)\times(\frac{\pi}{2},\pi)$ and stable for all $(K,\bar{\theta}_2)\in[K_1,K_0)\times(\frac{\pi}{2},\pi)$, where $\left(\cos\left(\frac{\bar{\theta}_2}{2}\right)^{\frac{2}{3}}+\sin\left(\frac{\bar{\theta}_2}{2}\right)^{\frac{2}{3}}\right)^{\frac{3}{2}}=K_1<K_0=\frac{2}{\sin\theta_2}$.*

Lemma 5.2.6 *The equilibrium $\boldsymbol{\psi}_{antisync2}$ is unstable for all $(K,\bar{\theta}_2)\in[K_1,\infty)\times(0,\pi)$.*

Proof: The proof of Lemmas 5.2.5 and 5.2.6 can be found in Appendix A.

Figure 5.6 shows the equilibrium ψ_{sync2} for $K=1,4,100$ and $\bar{\theta}_2=.1,\frac{\pi}{2},3.1$. For all $\bar{\theta}_2$, as K increases, the equilibrium becomes synchronized at $\frac{\bar{\theta}_2}{2}+\pi$. This motion does not exist

for all values of $(K, \bar{\theta}_2)$ and is stable only for some range of values of K. It corresponds to having all individuals going in the opposite direction from the average preferred direction. Even when this equilibrium is stable, its region of attraction is much smaller than the region of attraction for ψ_{sync1}.

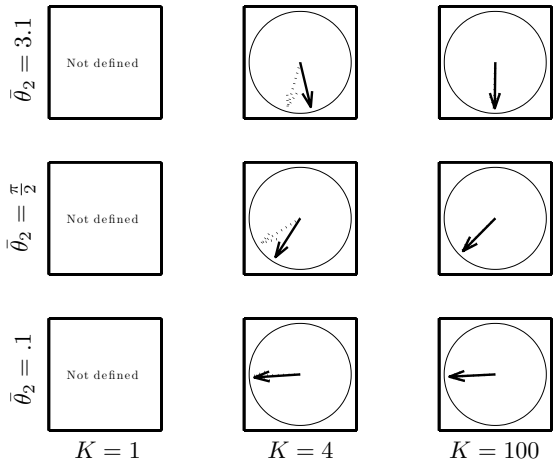

Figure 5.6: Picture of the equilibrium $\boldsymbol{\psi}_{sync2}$ for $K = 1, 4, 100$ and $\bar{\theta}_2 = .1, \frac{\pi}{2}, 3.1$.

Figure 5.7 shows the equilibrium $\psi_{antisync2}$ for $K = 1, 4, 100$ and $\bar{\theta}_2 = .1, \frac{\pi}{2}, 3.1$. For all $\bar{\theta}_2$, as K increases, the equilibrium becomes anti-synchronized. This motion of the two informed subgroups is always unstable.

Figure 5.8 summarizes the evolution of equilibria from the second set showing two bifurcation diagrams in the cases (a) $\bar{\theta}_2 = 1$ rad and (b) $\bar{\theta}_2 = 2$ rad with bifurcation parameter K. The synchrony measure ρ as defined by (5.26) is plotted as a function of K for all equilibria in the second set of solutions. There are two equilibria $\boldsymbol{\psi}_{sync2}$ and $\boldsymbol{\psi}_{antisync2}$ that do not exist for low enough values of K (i.e. for $K < \left(\cos\left(\frac{\bar{\theta}_2}{2}\right)^{\frac{2}{3}} + \sin\left(\frac{\bar{\theta}_2}{2}\right)^{\frac{2}{3}}\right)^{\frac{3}{2}}$); these two equilibria emerge from equation (5.32). Comparing Figures 5.8(a) and (b), we also note that the stability of one of these two equilibria changes as a function of K and $\bar{\theta}_2$, indicating the presence of bifurcations. The other two equilibria, $\boldsymbol{\psi}_{sync1}$ and $\boldsymbol{\psi}_{antisync1}$, are defined for all values of K, and their stability type does not change. The stable node is $\boldsymbol{\psi}_{sync1}$ and becomes synchronized as K increases, i.e., $\rho \to 1$ as $K \to \infty$. The unstable

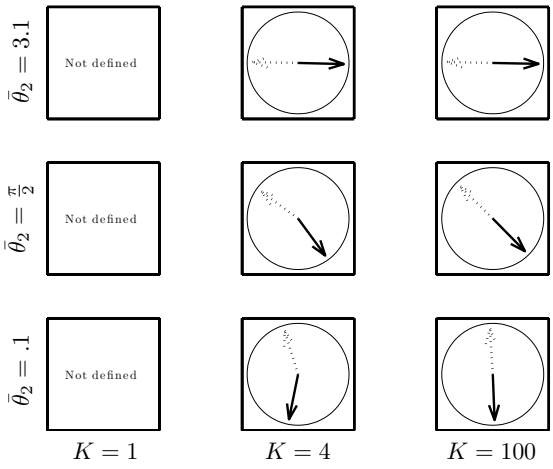

Figure 5.7: Picture of the equilibrium $\boldsymbol{\psi}_{antisync2}$ for $K = 1, 4, 100$ and $\bar{\theta}_2 = 0.1, \frac{\pi}{2}, 3.1$.

node is $\boldsymbol{\psi}_{antisync1}$ and becomes anti-synchronized as K increases, i.e., $\rho \to 0$ as $K \to \infty$. Consistent with the prediction above, as K increases, ρ approaches 0 or 1 for the two other equilibria as well. We now look at bifurcations in both parameters $K, \bar{\theta}_2$ and interpret them in the context of animal group motion.

5.2.2 Bifurcations in the Reduced Model (5.20)

As we observed in the previous section, the system exhibits different bifurcations as the two parameters K and $\bar{\theta}_2$ are varied. The two equilibria $\boldsymbol{\psi}_{S1}$ and $\boldsymbol{\psi}_{S2}$ are defined if and only if $|\frac{K}{2}\sin\bar{\theta}_2| \leq 1$, the equilibria $\boldsymbol{\psi}_{sync2}$ and $\boldsymbol{\psi}_{antisync2}$ are defined only for some values of $(K, \bar{\theta}_2)$, and the stability type of $\boldsymbol{\psi}_{sync2}$ changes as a function of K and $\bar{\theta}_2$. In all of these bifurcations the only equilibrium that becomes stable is $\boldsymbol{\psi}_{sync2}$. It corresponds to the group going in the direction opposite to the average of the preferred directions. From a biological point of view, this equilibrium is inefficient since the group heads in a direction as divergent as possible from both preferred directions. The bifurcation analysis shows that to stabilize this inefficient behavior we need to have $\bar{\theta}_2 > \frac{\pi}{2}$ and $K \in [K_1, K_0]$, where $K_1 = \left(\cos\left(\frac{\bar{\theta}_2}{2}\right)^{\frac{2}{3}} + \sin\left(\frac{\bar{\theta}_2}{2}\right)^{\frac{2}{3}}\right)^{\frac{3}{2}} < \frac{2}{\sin\theta_2} = K_0$. We focus our bifurcation analysis on the three following cases: first we consider $K = 2$ fixed and perform the bifurcation analysis

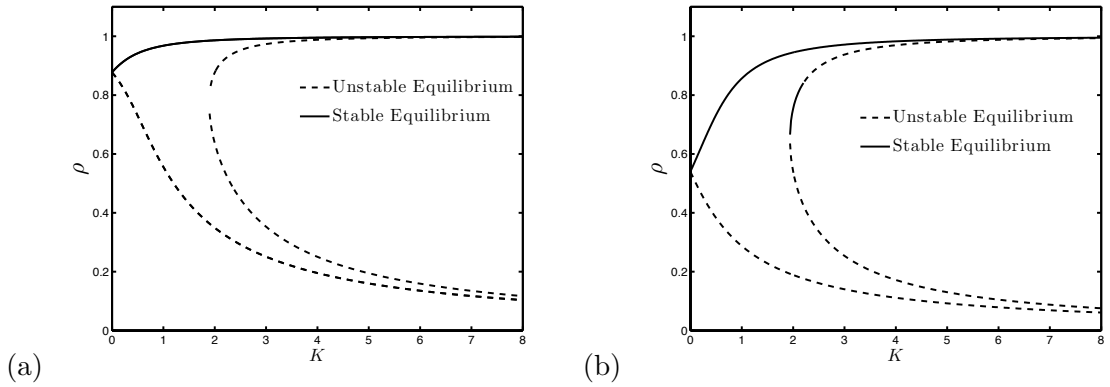

Figure 5.8: Bifurcation diagrams in cases (a) $\bar{\theta}_2 = 1$ rad and (b) $\bar{\theta}_2 = 2$ rad. The bifurcation parameter is K and ρ is plotted as a function of K for all equilibria in the second set of solutions. We note that two equilibria $\boldsymbol{\psi}_{sync2}$ and $\boldsymbol{\psi}_{antisync2}$ do not exist for low values of K. Stability of these same two equilibria changes type between (a) and (b), indicating the presence of bifurcations.

varying $\bar{\theta}_2$. Second, we consider $\bar{\theta}_2 > \frac{\pi}{2}$ fixed, and perform the bifurcation analysis varying K. Finally we consider the extreme case with $\bar{\theta}_2 = \pi$ and perform the bifurcation analysis varying K. In this last case we show that for values of K smaller than a threshold, each subgroup follows its own preferred direction but for larger values of K, the stable motion is synchronized in the average of the preferred directions.

Bifurcations in the $\left(\bar{\theta}_2, \psi_i\right)$ Plane with $K = 2$ Fixed

We set $K = 2$ and study the bifurcations in the $\left(\bar{\theta}_2, \psi_i\right)$ plane. The system (5.20) dynamics become

$$\dot{\psi}_1 = -\sin\psi_1 + \sin\left(\psi_2 - \psi_1\right)$$
$$\dot{\psi}_2 = \sin\left(\bar{\theta}_2 - \psi_2\right) - \sin\left(\psi_2 - \psi_1\right).$$

In this case the strength of each subgroup's attraction towards its preferred direction is equal to the strength of its tendency to align with the other subgroup. For this system it is possible to find closed form expressions of all equilibria. There are a total of six equilibria, given by

1. $\boldsymbol{\psi}_{sync1} = \left(\frac{1}{3}\bar{\theta}_2, \frac{2}{3}\bar{\theta}_2\right)$.

   By Lemma 5.2.2, the equilibrium $\boldsymbol{\psi}_{sync1}$ is a *stable node* for $\bar{\theta}_2 \in (0, \pi)$.

2. $\boldsymbol{\psi}_{sync2} = \left(\frac{1}{3}\bar{\theta}_2 - \frac{2\pi}{3}, \frac{2}{3}\bar{\theta}_2 + \frac{2\pi}{3}\right)$.

   By a check of the Jacobian, the equilibrium $\boldsymbol{\psi}_{sync2}$ is an *unstable node* for $\bar{\theta}_2 \in (0, \frac{\pi}{2})$ and a *stable node* for $\bar{\theta}_2 \in (\frac{\pi}{2}, \pi)$.

3. $\boldsymbol{\psi}_{antisync1} = \left(\frac{1}{3}\bar{\theta}_2 - \frac{4\pi}{3}, \frac{2}{3}\bar{\theta}_2 + \frac{4\pi}{3}\right)$.

   By Lemma 5.2.3, the equilibrium $\boldsymbol{\psi}_{antisync1}$ is an *unstable node* for $\bar{\theta}_2 \in (0, \pi)$.

4. $\boldsymbol{\psi}_{antisync2} = \left(\bar{\theta}_2 - \pi, \pi\right)$.

   By a check of the Jacobian, the equilibrium $\boldsymbol{\psi}_{antisync2}$ is a *saddle point* for $\bar{\theta}_2 \in (0, \frac{\pi}{2}) \cup (\frac{\pi}{2}, \pi)$.

5. $\boldsymbol{\psi}_{S1} = \left(\bar{\theta}_2 + \pi, 2\bar{\theta}_2\right)$.

   By Lemma 5.2.1, the equilibrium $\boldsymbol{\psi}_{S1}$ is a *saddle point* for all $\bar{\theta}_2 \in (0, \frac{\pi}{2}) \cup (\frac{\pi}{2}, \pi)$.

6. $\boldsymbol{\psi}_{S2} = \left(-\bar{\theta}_2, \pi\right)$.

   By Lemma 5.2.1, the equilibrium $\boldsymbol{\psi}_{S2}$ is a *saddle point* for all $\bar{\theta}_2 \in (0, \frac{\pi}{2}) \cup (\frac{\pi}{2}, \pi)$.

Figure 5.9 shows the bifurcation diagram in the $\left(\bar{\theta}_2, \psi_1\right)$ plane; i.e, for each equilibrium, ψ_1 is plotted as a function of the bifurcation parameter $\bar{\theta}_2$. The equilibrium $\boldsymbol{\psi}_{sync2}$ changes stability type at $\bar{\theta}_2 = \frac{\pi}{2}$ from unstable node to stable node. This equilibrium at $\bar{\theta}_2 = \frac{\pi}{2}$ is highly degenerate, having its linearization equal to the zero matrix. Furthermore, we see from the bifurcation diagram (Figure 5.9) that the bifurcation occurs with four equilibria coming together at the point in phase space $(\psi_1, \psi_2) = \left(\frac{3\pi}{2}, \pi\right)$. This bifurcation is one of Thom's seven elementary catastrophes; it is called an *elliptic umbilic* [121].

Catastrophe theory applies to gradient systems, and the elementary catastrophes are classified according to the form of the potential. As we noted earlier, the system (5.20) obeys gradient dynamics, and the associated potential for $K = 2$ is

$$V = \cos\psi_1 + \cos\left(\bar{\theta}_2 - \psi_2\right) + \cos\left(\psi_1 - \psi_2\right). \tag{5.36}$$

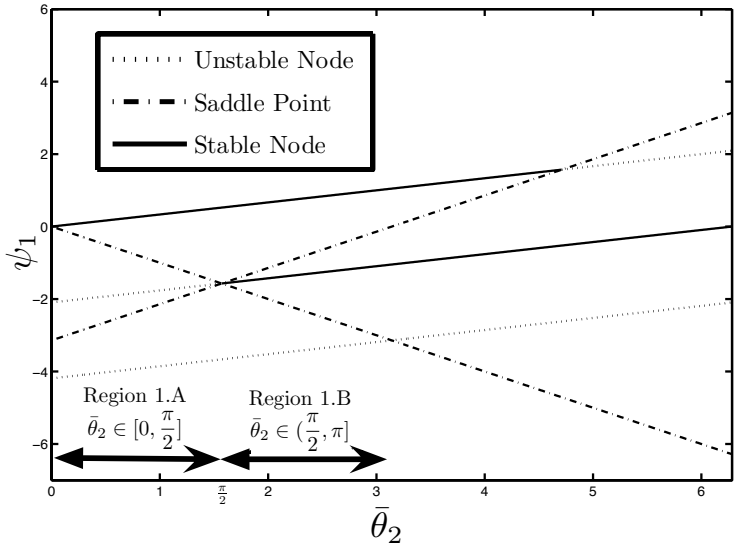

Figure 5.9: Bifurcation diagram in the $\left(\bar{\theta}_2, \psi_1\right)$ plane, i.e. ψ_1 as a function of bifurcation parameter $\bar{\theta}_2$ fixing $K = 2$. Since the equilibria $\boldsymbol{\psi}_{antisync2}$ and $\boldsymbol{\psi}_{S1}$ have the same value for ψ_1 (but different values for ψ_2), we see on this diagram only five equilibria even though there are six. At $\bar{\theta}_2 = \frac{\pi}{2}$ there are only three distinct equilibria; this is the degenerate point of the system. The multiplicity of the equilibrium $\left(\frac{3\pi}{2}, \pi\right)$ is four.

To identify the bifurcation as an elliptic umbilic, we examine the unfolding of this potential near the catastrophe $\left(\psi_1, \psi_2, \bar{\theta}_2\right) = \left(\frac{3\pi}{2}, \pi, \frac{\pi}{2}\right)$. We write the potential given by (5.36) as

$$V = \cos\left(u + \frac{3\pi}{2}\right) + \cos\left(\frac{\pi}{2} + a - (\pi + v)\right) + \cos\left(u + \frac{3\pi}{2} - (\pi + v)\right), \tag{5.37}$$

where u, v and a are, respectively, the deviation of ψ_1 from $\frac{3\pi}{2}$, ψ_2 from π and $\bar{\theta}_2$ from $\frac{\pi}{2}$. A Taylor expansion of (5.37), keeping terms up to third order in u and v, yields

$$V = \frac{(\cos a - 1)}{3!}v^3 + \frac{uv^2}{2} - \frac{vu^2}{2} - \frac{\sin a}{2}v^2 + (1 - \cos a)\, v + \sin a.$$

After the following change of variables:

$$x = \frac{1}{2}\sqrt[3]{\frac{(4\cos a - 1)}{3}}v$$
$$y = \sqrt[3]{\frac{2\sqrt{6}}{\sqrt{4\cos a - 1}}}\left(\frac{1}{\sqrt{6}}u - \frac{1}{2\sqrt{6}}v\right),$$

the potential (5.37) becomes

$$V = x^3 - 3xy^2 - \frac{2 \times 3^{\frac{2}{3}} \sin a}{(4\cos a - 1)^{\frac{2}{3}}}x^2 - \frac{2 \times 3^{\frac{1}{3}} (\cos a - 1)}{(4\cos a - 1)^{\frac{1}{3}}}x + \sin a. \tag{5.38}$$

In (5.38) we recognize the standard unfolding of the potential of an elliptic umbilic as described in [93].

As we previously mentioned, the system is highly degenerate at the bifurcation point $(\psi_1, \psi_2, \psi_3) = (\frac{3\pi}{2}, \pi, \frac{\pi}{2})$. As Figure 5.10 shows there are only three distinct equilibria at this point. The equilibria $\boldsymbol{\psi}_{sync1}$ and $\boldsymbol{\psi}_{antisync1}$ are not affected by the bifurcation and are respectively a stable node K-almost synchronized at $\frac{\bar{\theta}_2}{2} = \frac{\pi}{4}$ and an unstable node K-almost anti-synchronized. The third equilibrium consists of the superposition of four equilibria, three saddles ($\boldsymbol{\psi}_{S1}, \boldsymbol{\psi}_{S2}$ and $\boldsymbol{\psi}_{antisync2}$) and one node ($\boldsymbol{\psi}_{sync2}$) that is unstable before the bifurcation and stable after. This topology in fact is typical for an elliptic umbilic catastrophe, and this equilibrium is called a *monkey-saddle* in the catastrophe theory literature [93]. After the bifurcation the equilibrium $\boldsymbol{\psi}_{sync2}$ is stable; in the context of animal group motion, this result suggests that when the informed subgroups have a disagreement larger than some threshold, inefficient behaviors may arise.

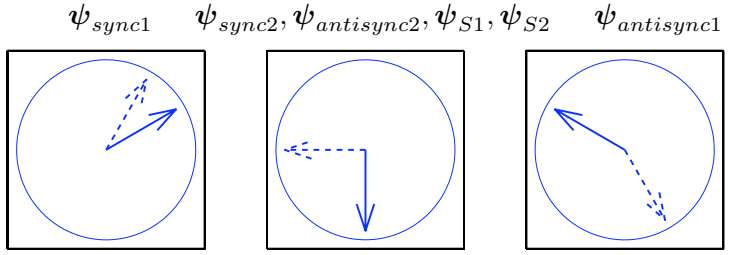

Figure 5.10: These diagrams show the equilibria of the system at the critical point, i.e., when both $K = 2$ and $\bar{\theta}_2 = \frac{\pi}{2}$ there are only three distinct equilibria. The second equilibrium drawn, called a monkey-saddle in the catastrophe theory literature, is the superposition of four equilibria $\boldsymbol{\psi}_{sync2}$, $\boldsymbol{\psi}_{antisync2}$, $\boldsymbol{\psi}_{S1}$ and $\boldsymbol{\psi}_{S2}$; it has multiplicity four.

Bifurcations in the (K, ψ_i) Plane with $\bar{\theta}_2 \in (\frac{\pi}{2}, \pi)$ Fixed

As we proved in Section 5.2.1 with Lemmas 5.2.4 and 5.2.5, the equilibrium $\boldsymbol{\psi}_{sync2}$ exists only if $K > K_1$ and is stable only if $(K, \bar{\theta}) \in [K_1, K_0) \times (\frac{\pi}{2}, \pi)$. We now study the bifurcations in the (K, ψ_i) plane with $\bar{\theta}_2 \in (\frac{\pi}{2}, \pi)$ fixed. Figure 5.11 shows the bifurcation diagram in the (K, ψ_1) plane for $\bar{\theta}_2 = \frac{3\pi}{4}$ as a representative of any case with $\bar{\theta}_2 \in (\frac{\pi}{2}, \pi)$. We observe two

bifurcations: a first one at $K = K_1$ where the two equilibria $\boldsymbol{\psi}_{sync2}$ and $\boldsymbol{\psi}_{antisync2}$ appear and a second one at $K = K_0 > K_1$ where the two equilibria $\boldsymbol{\psi}_{S1}$ and $\boldsymbol{\psi}_{S2}$ disappear. For $K_1 < K < K_0$ there are two stable equilibria, $\boldsymbol{\psi}_{sync1}$ and $\boldsymbol{\psi}_{sync2}$, whereas there is only one stable equilibrium, $\boldsymbol{\psi}_{sync1}$, when K is outside this region. The second stable equilibrium, $\boldsymbol{\psi}_{sync2}$, appears through a saddle-node bifurcation at $K_1 = \left(\cos\left(\frac{\bar{\theta}_2}{2}\right)^{\frac{2}{3}} + \sin\left(\frac{\bar{\theta}_2}{2}\right)^{\frac{2}{3}}\right)^{\frac{3}{2}}$ and becomes unstable through a hypercritical pitchfork at $K_0 = 2/\sin\bar{\theta}_2$.

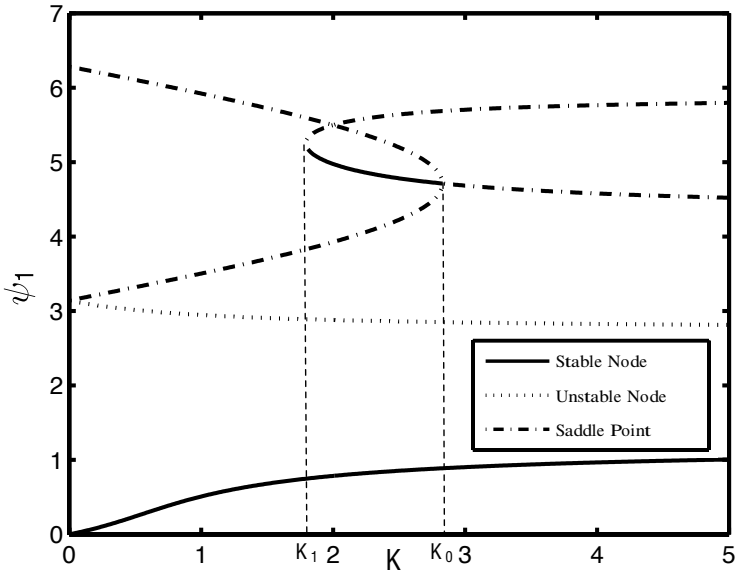

Figure 5.11: Bifurcation diagram in case $\bar{\theta}_2 = \frac{3\pi}{4}$. The bifurcation parameter is K and ψ_1 is plotted as a function of K for all the equilibria of the system. We observe a saddle node bifurcation at $K = K_1$ and a hypercritical pitchfork bifurcation for $K = K_0$.

We prove that the second stable equilibrium $\boldsymbol{\psi}_{sync2}$ appears through a saddle node bifurcation at $K = K_1$. From Lemma 5.2.4, when $K = K_1 = \left(\cos\left(\frac{\bar{\theta}_2}{2}\right)^{\frac{2}{3}} + \sin\left(\frac{\bar{\theta}_2}{2}\right)^{\frac{2}{3}}\right)^{\frac{3}{2}}$ two branches of equilibria $\boldsymbol{\psi}_{sync2}$ and $\boldsymbol{\psi}_{antisync2}$ appear simultaneously. With the change of variable $(\psi_1, \psi_2) \mapsto (\rho, \Psi)$ defined by equation (5.26) where $\rho \in [0, 1]$ and $\Psi \in S^1$, the equilibrium $\boldsymbol{\psi}_{sync2} = \boldsymbol{\psi}_{antisync2} = \boldsymbol{\psi}_*$ for $K = K_1$ becomes $(\rho_*, \Psi_*) = \left(\sqrt{\frac{\cos(\frac{\bar{\theta}_2}{2})^{\frac{2}{3}}}{\cos(\frac{\bar{\theta}_2}{2})^{\frac{2}{3}} + \sin(\frac{\bar{\theta}_2}{2})^{\frac{2}{3}}}}, \frac{\bar{\theta}_2}{2} + \pi\right)$. Using the general theorem for saddle node bifurcations in [40], we prove that the equilibria $\boldsymbol{\psi}_{sync2}$ and $\boldsymbol{\psi}_{antisync2}$ appear through a saddle node bifurcation at $K = K_1$. To apply the

theorem, we check that the system satisfies the following three conditions:

1. *Non-degeneracy of the linearization.*

   The linearization of (5.20) at $\boldsymbol{\psi} = \boldsymbol{\psi}_1$ and $K = K_1$ is

   $$J_1 = \left.\frac{\partial \mathbf{f}}{\partial \boldsymbol{\psi}}\right|_{\boldsymbol{\psi}_*, K_1}$$

   $$= \begin{pmatrix} \cos(\frac{\bar{\theta}_2}{2})\rho_* - \sin(\frac{\bar{\theta}_2}{2})\sqrt{1-\rho_*^2} + \frac{K_1}{2}(1-2\rho_*^2) & \frac{K_1}{2}(2\rho_*^2 - 1) \\ \frac{K_1}{2}(2\rho_*^2 - 1) & \cos(\frac{\bar{\theta}_2}{2})\rho_* - \sin(\frac{\bar{\theta}_2}{2})\sqrt{1-\rho_*^2} + \frac{K_1}{2}(1-2\rho_*^2) \end{pmatrix}$$

   where $\mathbf{f}$ is the vector field given by (5.20) with corresponding state vector $\boldsymbol{\psi} = (\psi_1, \psi_2)$. This linearization is non-degenerate since it has a simple zero eigenvalue. We set $v = \begin{pmatrix} -1 \\ 1 \end{pmatrix}$ and $w = \begin{pmatrix} -1 & 1 \end{pmatrix}$ to be, respectively, the right and left eigenvectors of the linearization for the zero eigenvalue.

2. *Transversality condition to control non-degeneracy with respect to the parameter.*

   For this condition, we check whether the eigenvalues cross the imaginary axis with non-zero speed. We compute

   $$\left.\frac{\partial \mathbf{f}}{\partial K}\right|_{\boldsymbol{\psi}_*, K_1} = \rho_* \sqrt{1-\rho_*^2} \begin{pmatrix} -1 \\ 1 \end{pmatrix},$$

   which implies that $w.\ \frac{\partial \mathbf{f}}{\partial K}\big|_{\boldsymbol{\psi}_*, K_1} = \frac{2\cos(\frac{\bar{\theta}_2}{2})^{\frac{1}{3}}\sin(\frac{\bar{\theta}_2}{2})^{\frac{1}{3}}}{\sqrt{\cos(\frac{\bar{\theta}_2}{2})^{\frac{2}{3}} + \sin(\frac{\bar{\theta}_2}{2})^{\frac{2}{3}}}} \neq 0$. This means that the eigenvalues have non-zero speed at the bifurcation.

3. *Transversality condition to control non-degeneracy with respect to the dominant effect of the quadratic nonlinear term.*

   We check this condition by showing

   $$w.\left(D^2_{\boldsymbol{\psi}} \mathbf{f}(\boldsymbol{\psi}_*, K_1)(v, v)\right) \neq 0,$$

where

$$D^2_{\boldsymbol{\psi}}\mathbf{f}(\boldsymbol{\psi}_*, K_1)(v,v) = \begin{pmatrix} v^T \begin{pmatrix} \frac{\partial^2 f_1}{\partial \psi_1^2} & \frac{\partial^2 f_1}{\partial \psi_1 \partial \psi_2} \\ \frac{\partial^2 f_1}{\partial \psi_1 \partial \psi_2} & \frac{\partial^2 f_1}{\partial \psi_2^2} \end{pmatrix} v \\ v^T \begin{pmatrix} \frac{\partial^2 f_2}{\partial \psi_1^2} & \frac{\partial^2 f_2}{\partial \psi_1 \partial \psi_2} \\ \frac{\partial^2 f_2}{\partial \psi_1 \partial \psi_2} & \frac{\partial^2 f_2}{\partial \psi_2^2} \end{pmatrix} v \end{pmatrix},$$

with f_i being the ith component of the vector field $\mathbf{f}$ given by (5.20). We compute

$$w.\left(D^2_{\boldsymbol{\psi}}\mathbf{f}(\boldsymbol{\psi}_*, K_1)(v,v)\right) = -6K_1\rho_*\sqrt{1-\rho_*^2} \neq 0.$$

With all three condition thus satisfied, the general saddle node theorem in [40] guarantees the existence of a codimension-one saddle node bifurcation at

$$(\rho_*, \Psi_*) = \left(\sqrt{\frac{\cos(\frac{\bar\theta_2}{2})^{\frac{2}{3}}}{\cos(\frac{\bar\theta_2}{2})^{\frac{2}{3}} + \sin(\frac{\bar\theta_2}{2})^{\frac{2}{3}}}}, \frac{\bar\theta_2}{2} + \pi\right)$$

$$K = K_1 = \left(\cos\left(\frac{\bar\theta_2}{2}\right)^{\frac{2}{3}} + \sin\left(\frac{\bar\theta_2}{2}\right)^{\frac{2}{3}}\right)^{\frac{3}{2}}.$$

We now (partially) prove that the second stable equilibrium $\boldsymbol{\psi}_{sync2}$ disappears through a hypercritical pitchfork at $K = K_0$. From Lemma 5.2.1, when $K = K_0 = 2/\sin\bar\theta_2$, the two equilibria $\boldsymbol{\psi}_{S1}$ and $\boldsymbol{\psi}_{S2}$ meet and are equal to $\boldsymbol{\psi}_0 = (\psi_1, \psi_2)_0 = \left(\frac{3\pi}{2}, \bar\theta_2 + \frac{\pi}{2}\right)$. For $K > K_0$, $\boldsymbol{\psi}_{S1}$ and $\boldsymbol{\psi}_{S2}$ no longer exist. With the change of variable $(\psi_1, \psi_2) \mapsto (\rho, \Psi)$ defined by (5.26) where $\rho \in [0,1]$ and $\Psi \in S^1$, the equilibrium $\boldsymbol{\psi}_{S1} = \boldsymbol{\psi}_{S2} = \boldsymbol{\psi}_0$ for $K = K_0$ becomes $(\rho, \Psi)_0 = \left(\sin\frac{\bar\theta_2}{2}, \frac{\bar\theta_2}{2} + \pi\right)$. This equilibrium also solves equation (5.32) and corresponds to $\boldsymbol{\psi}_{sync2}$ at $K = K_0$. Hence a third branch of equilibria from the second set of solutions goes through the bifurcation point $(\boldsymbol{\psi}, K) = (\boldsymbol{\psi}_0, K_0)$. No other branch of equilibria crosses this bifurcation point.

We partially prove that the bifurcation at $K = K_0$ is a *hypercritical pitchfork bifurcation*, using the extension for pitchforks of the general theorem for saddle node bifurcations in [40]. This is only a partial proof because, of the three conditions to check in the theorem, we can verify only the first two.

1. *Non-degeneracy of the linearization.*

The linearization of (5.20) at $\boldsymbol{\psi} = \boldsymbol{\psi}_0$ and $K = K_0$ is

$$J_0 = \left.\frac{\partial \mathbf{f}}{\partial \boldsymbol{\psi}}\right|_{\boldsymbol{\psi}_0, K_0} = \cot\bar{\theta}_2 \begin{pmatrix} 1 & -1 \\ -1 & 1 \end{pmatrix},$$

where $\mathbf{f}$ is the vector field given by (5.20) with corresponding state vector $\boldsymbol{\psi} = (\psi_1, \psi_2)$. This linearization is non-degenerate since it has a simple zero eigenvalue. We set $v = \begin{pmatrix} 1 \\ 1 \end{pmatrix}$ and $w = \begin{pmatrix} 1 & 1 \end{pmatrix}$ to be, respectively, the right and left eigenvectors of the linearization for the zero eigenvalue.

2. *Transversality condition to control non-degeneracy with respect to the parameter.*

   For this condition we first check whether the eigenvalues cross the imaginary axis with non-zero speed. We compute

   $$\left.\frac{\partial^2 \mathbf{f}}{\partial \boldsymbol{\psi} \partial K}\right|_{\boldsymbol{\psi}_0, K_0} = \frac{1}{2}\cos\bar{\theta}_2 \begin{pmatrix} 1 & -1 \\ -1 & 1 \end{pmatrix},$$

   which implies that $w.\left.\frac{\partial^2 \mathbf{f}}{\partial \boldsymbol{\psi} \partial K}\right|_{\boldsymbol{\psi}_0, K_0}.v = 0$. This means that the velocity (with respect to K) of the eigenvalues of the Jacobian (evaluated at $\boldsymbol{\psi}_{sync2} = \boldsymbol{\psi_0}$ and $K = K_0$) is zero when the eigenvalues reach the value zero (at the bifurcation). Because the conditions of this theorem are only sufficient, we can still prove the bifurcation using the more general form of this condition. It remains for us to show that the equilibrium $\boldsymbol{\psi}_{sync2}$ goes from stable to unstable through the bifurcation. From Lemma 5.2.5 we know that $\lambda_1|_{\boldsymbol{\psi}_{sync2}} = \rho_{sync2}\cos\frac{\bar{\theta}_2}{2} - \sqrt{1-\rho_{sync2}^2}\sin\frac{\bar{\theta}_2}{2}$ is negative for $K < K_0$, and positive for $K > K_0$ and that $\lambda_2 = \rho_{sync2}\cos\frac{\bar{\theta}_2}{2} - \sqrt{1-\rho_{sync2}^2}\sin\frac{\bar{\theta}_2}{2} - K(2\rho_{sync2}^2 - 1)$ is always negative. Thus $\boldsymbol{\psi}_{sync2}$ changes from stable node to saddle point through the bifurcation.

3. *Transversality condition to control non-degeneracy with respect to the dominant effect of the cubic nonlinear term.*

   We first check this condition by computing

   $$w_i v_j v_k v_l \left.\frac{\partial^3 f_i}{\partial\psi_j \partial\psi_k \partial\psi_l}\right|_{\boldsymbol{\psi}_0, K_0} = 0$$

for all $i, j, k, l \in \{1, 2\}$, with f_i being the ith component of the vector field $\mathbf{f}$ given by (5.20). Since these terms are all zero, this sufficient condition is not satisfied. Instead, to prove the condition, one could demonstrate that the dynamics on the center manifold have a non-degenerate cubic term. If this can be shown, the sign of the cubic term would be positive, proving that the bifurcation is a hypercritical pitchfork.

Bifurcation in the (K, ψ_i) Plane with $\bar{\theta}_2 = \pi$ Fixed

We set $\bar{\theta}_2 = \pi$, and study the bifurcation in the (K, ψ_i) plane. The system (5.20) dynamics become

$$\begin{aligned} \dot{\psi}_1 &= -\sin\psi_1 + \frac{K}{2}\sin(\psi_2 - \psi_1) \\ \dot{\psi}_2 &= \sin\psi_2 + \frac{K}{2}\sin(\psi_1 - \psi_2)\,. \end{aligned} \tag{5.39}$$

Here the two preferred headings differ by 180 degrees. Since the disagreement is so large, for small values of K each informed subgroup follows its own preferred direction. This kind of splitting is sometimes observed in swarm-bees [66]. We note that this system appears in Chapter 8 of [114]. For this system we can find a closed form expression for all the equilibria. Depending on the value of K, there are four or six equilibria. We consider first the case where $K \in [0, 1)$. In this case there are four equilibria:

1. $\boldsymbol{\psi}_{antisync1} = (\pi, 0)$.

   By Lemma 5.2.3, the equilibrium $\boldsymbol{\psi}_{antisync1}$ is an *unstable node* for $K \in [0, 1]$.

2. $\boldsymbol{\psi}_{antisync2} = (0, \pi)$.

   By a check of the Jacobian, the equilibrium $\boldsymbol{\psi}_{antisync2}$ is a *stable node* $\forall K \in [0, 1)$.

3. $\boldsymbol{\psi}_{S1} = (0, 0)$.

   By Lemma 5.2.1, the equilibrium $\boldsymbol{\psi}_{S1}$ is a *saddle point* for all $K \in [0, 1]$.

4. $\boldsymbol{\psi}_{S2} = (\pi, \pi)$.

   By Lemma 5.2.1, the equilibrium $\boldsymbol{\psi}_{S2}$ is a *saddle point* for all $K \in [0, 1]$.

Next we consider next case where $K > 1$. In this case, there are six equilibria as follows:

1. $\boldsymbol{\psi}_{sync1} = \left(\pi - \arccos\left(-\frac{1}{K}\right), \arccos\left(-\frac{1}{K}\right)\right)$.

   By Lemma 5.2.2, the equilibrium $\boldsymbol{\psi}_{sync1}$ is a *stable node* for $K > 1$.

2. $\boldsymbol{\psi}_{sync2} = \left(\pi + \arccos\left(-\frac{1}{K}\right), -\arccos\left(-\frac{1}{K}\right)\right)$.

   By a check of the Jacobian, the equilibrium $\boldsymbol{\psi}_{sync2}$ is a *stable node* $\forall K > 1$.

3. $\boldsymbol{\psi}_{antisync1} = (\pi, 0)$.

   By Lemma 5.2.3, the equilibrium $\boldsymbol{\psi}_{antisync1}$ is an *unstable node* for $K \geq 1$.

4. $\boldsymbol{\psi}_{antisync2} = (0, \pi)$.

   By a check of the Jacobian, the equilibrium $\boldsymbol{\psi}_{antisync2}$ is a *saddle point* $\forall K > 1$.

5. $\boldsymbol{\psi}_{S1} = (0, 0)$.

   By Lemma 5.2.1, the equilibrium $\boldsymbol{\psi}_{S1}$ is a *saddle point* for all $K \geq 1$.

6. $\boldsymbol{\psi}_{S2} = (\pi, \pi)$.

   By Lemma 5.2.1, the equilibrium $\boldsymbol{\psi}_{S2}$ is a *saddle point* for all $K \geq 1$.

Figure 5.12 shows the bifurcation diagram in the (K, ψ_1) plane; for each equilibrium, ψ_1 is plotted as a function of the bifurcation parameter K. Before the bifurcation, i.e., $K < 1$, the only stable equilibrium is $\boldsymbol{\psi}_{antisync2} = (0, \pi)$. This corresponds to the case where each informed subgroup follows its own preferred direction; there is no compromise between the individuals, and the group splits. When $K < 1$ the strength of the coupling force relative to the strength of the attraction to the preferred direction is too weak to influence the stable steady state of the system. The motion of the group is the same as if there were no coupling between the two informed subgroups. For $K > 1$, there are two stable equilibria, $\boldsymbol{\psi}_{sync1}$ and $\boldsymbol{\psi}_{sync2}$. These correspond, respectively, to the motion in the directions $\Psi = \frac{\bar{\theta}_2}{2} = \frac{\pi}{2}$ and $\Psi = \frac{\bar{\theta}_2}{2} + \pi = \frac{3\pi}{2}$. As we increase the bifurcation parameter K, the two directions ψ_1 and ψ_2 become synchronized. $\bar{\theta}_2 = \pi$ is the only case where we have two stable equilibria for large value of K. At $K = 1$, the equilibrium $\boldsymbol{\psi}_{antisync2}$ changes stability type from being a stable node to being a saddle through a *supercritical pitchfork bifurcation*. We prove this, by using the extension for pitchforks of the general theorem for saddle node bifurcations in

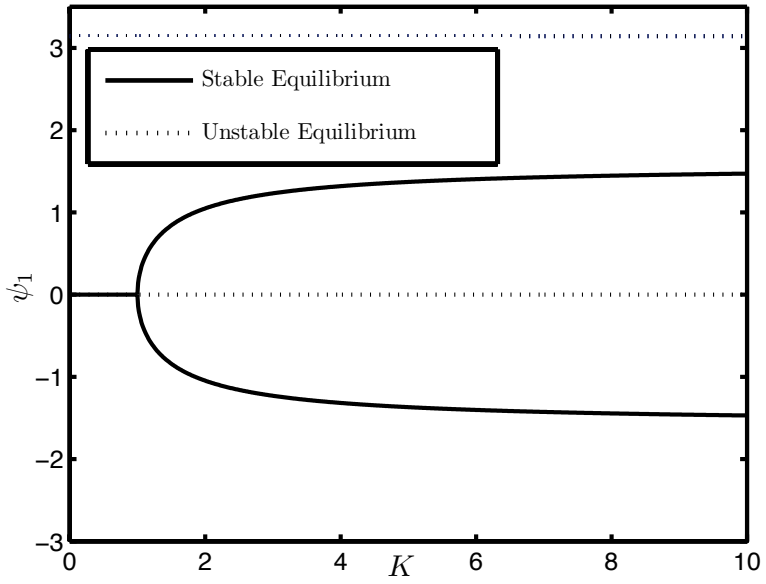

Figure 5.12: Bifurcation diagram in the (K, ψ_1) plane, i.e, ψ_1 as a function of bifurcation parameter K fixing $\bar{\theta}_2 = \pi$. At $K = 1$ we have a supercritical pitchfork bifurcation. We have one stable equilibrium for $K < 1$ and two stable equilibria for $K > 1$.

[40]. There are three conditions to check in the theorem. We define $\boldsymbol{\psi}_0 = (\psi_1, \psi_2)_0 = (0, \pi)$, $K_0 = 1$.

1. *Non-degeneracy of the linearization.*

   The linearization of (5.39) at $\boldsymbol{\psi} = \boldsymbol{\psi}_0$ and $K = K_0$ is

   $$J_0 = \left.\frac{\partial \mathbf{f}}{\partial \boldsymbol{\psi}}\right|_{\boldsymbol{\psi}_0, K_0} = \begin{pmatrix} -\frac{1}{2} & -\frac{1}{2} \\ -\frac{1}{2} & -\frac{1}{2} \end{pmatrix},$$

   where $\mathbf{f}$ is the vector field given by (5.39) with corresponding state vector $\boldsymbol{\psi} = (\psi_1, \psi_2)$. This linearization is non-degenerate since it has a simple zero eigenvalue. We set $v = \begin{pmatrix} 1 \\ -1 \end{pmatrix}$ and $w = \begin{pmatrix} 1 & -1 \end{pmatrix}$ to be, respectively, the right and left eigenvectors of the linearization for the zero eigenvalue.

2. *Transversality condition to control non-degeneracy with respect to the parameter.*

For this condition we check whether the eigenvalues cross the imaginary axis with non-zero speed. We compute

$$\left.\frac{\partial^2 \mathbf{f}}{\partial \boldsymbol{\psi} \partial K}\right|_{\boldsymbol{\psi}_0, K_0} = \frac{1}{2}\begin{pmatrix} 1 & -1 \\ -1 & 1 \end{pmatrix},$$

which implies that $w. \left.\frac{\partial^2 \mathbf{f}}{\partial \boldsymbol{\psi} \partial K}\right|_{\boldsymbol{\psi}_0, K_0} .v = 2 \neq 0$. Hence, the eigenvalues cross the imaginary axis with non-zero speed.

3. *Transversality condition to control non-degeneracy with respect to the dominant effect of the cubic nonlinear term.*

   For this condition we compute

$$w_i v_j v_k v_l \left.\frac{\partial^3 f_i}{\partial \psi_j \partial \psi_k \partial \psi_l}\right|_{\boldsymbol{\psi}_0, K_0} = -6 < 0$$

   for all $i, j, k, l \in \{1, 2\}$, with f_i being the ith component of $\mathbf{f}$. Since we get a strictly negative number, the pitchfork is supercritical.

This last condition completes the proof of the existence of a codimension-one supercritical pitchfork bifurcation at $\boldsymbol{\psi} = (0, \pi)$, $K = 1$.

We have modelled the dynamics of motion for a group of $N = N_1 + N_2 + N_3$ coupled individuals moving in the plane. We studied the full phase space dynamics of the reduced model in the case of a group having N_1 informed individuals with a preferred direction $\bar{\theta}_1 = 0$, $N_2 = N_1$ informed individuals with a preferred direction $\bar{\theta}_2$, and no naive (uninformed) individuals. We proved that the system has either one or two stable equilibria. The equilibrium $\boldsymbol{\psi}_{sync1}$ is stable for all values of $(K, \bar{\theta}_2)$. It correspond to a K-almost synchronized motion of the group in the direction $\Psi = \frac{\bar{\theta}_2}{2}$. For large values of K, this equilibrium corresponds to the whole group moving together in the average of the preferred directions. This result is consistent with simulations from the discrete-time model used in Chapter 4, although only for values of $\bar{\theta}_2$ below a threshold. In the discrete-time model, for $\bar{\theta}_2$ greater than a threshold, the group is observed to move together in one of the preferred directions. Our continuous-time model does not exhibit this transition and never yield the behavior

where the group collectively selects one of the two preferred directions. Furthermore, for $(K, \bar{\theta}_2) \in (K_1, K_0) \times [\frac{\pi}{2}, \pi)$ the equilibrium $\boldsymbol{\psi}_{sync2}$ is stable. It corresponds to a K-almost synchronized motion of the group in the direction $\Psi = \frac{\bar{\theta}_2}{2} + \pi$. For large values of K, this equilibrium corresponds to the whole group moving together in a direction opposite to the average of the preferred directions. The region of attraction of this equilibrium is relatively small, which can explain why this behavior was not observed in the simulation of the discrete-time model.

Figure 5.13 shows the phase portrait for the subgroup heading directions ψ_1 and ψ_2 for two values of $\bar{\theta}_2$ and three values of K. The vertical (and likewise horizontal) edges are identified since the phase space is the torus. Some of the stable and unstable manifolds are plotted as solid lines and the vector field is plotted as arrows so that the flow can be readily observed. For example, as described above, in the right, middle plot, these manifolds illustrate the region of attraction for the second stable equilibrium $\boldsymbol{\psi}_{sync2}$. The middle plots together show before (left) and after (right) the elliptic umbilic catastrophe. The three panels in the left column, corresponding to $\bar{\theta}_2 = \frac{\pi}{4}$, show equilibria with $K = 1$ for the top plot, $K = 2.5$ for the middle plot, and $K = 4$ for the bottom plot. For example, the single stable equilibrium can be observed to be near the point $\psi_1 = \psi_2 = \frac{\pi}{8}$, i.e., the K-almost synchronized equilibrium $\boldsymbol{\psi}_{sync1}$ at $\frac{\bar{\theta}_2}{2} = \frac{\pi}{8}$. Likewise, the three panels in the right column, corresponding to $\bar{\theta}_2 = \frac{3\pi}{4}$, show equilibria that can also be observed in the bifurcation plot of Figure 5.11 at $K = 1$ for the top plot, $K = 2.5$ for the middle plot, and $K = 4$ for the bottom plot.

We illustrate in Figure 5.14 the dynamics near one of the instabilities with a simulation in the case $N_1 = N_2 = 5$. Snapshots of the positions and heading directions of all 10 individuals are shown at three different times in the three left column plots. The corresponding heading directions of all 10 individuals are plotted on the unit circle together with the preferred heading directions in the right column plots. The initial condition, shown in Figures 5.14(a) and (b) is close to the saddle point $\boldsymbol{\psi}_{sync2}$ shown in the bottom right plot of Figure 5.13, i.e., the individuals are heading in the opposite direction of the compromise of the preferred

directions. First, as expected (but not shown in Figure 5.14), the individuals with the same preferred direction synchronize. Then more slowly, the two lumped subgroups both move away from the unstable solution (in the counter-clockwise direction around the unit circle). Figures 5.14(c) and (d) show that they are close together as they move and practically all synchronized as they pass through the preferred direction of subgroup 1. Figures 5.14(e) and (f) show the convergence to the stable solution $\boldsymbol{\psi}_{sync1}$.

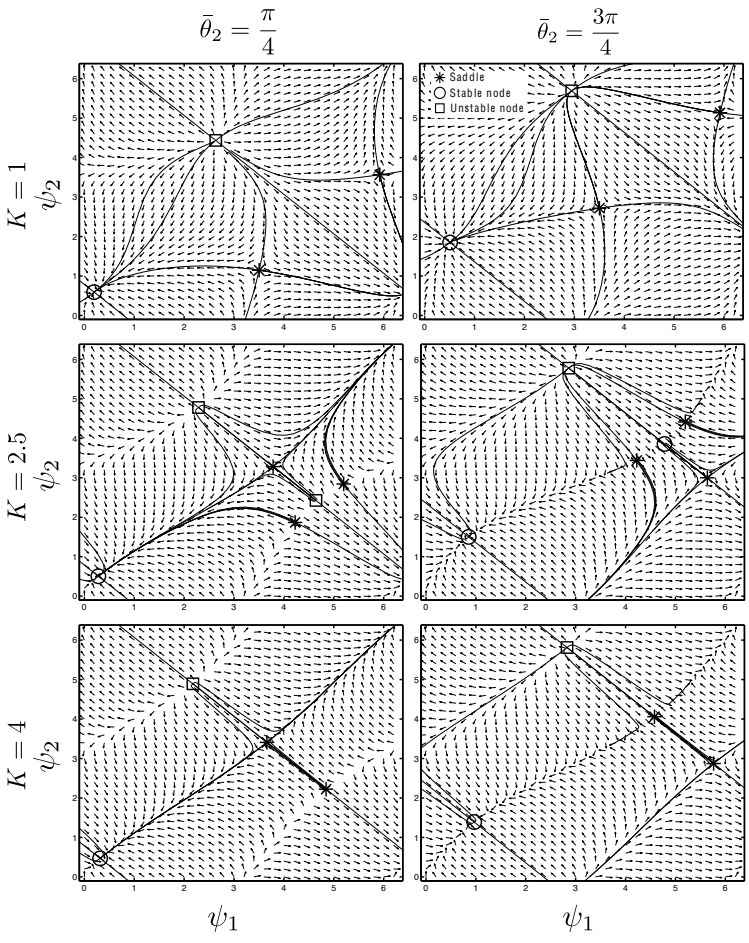

Figure 5.13: Phase portrait for heading directions ψ_1 and ψ_2 at three different values of K and two different values of $\bar{\theta}_2$.

In the next section, we explore, through simulations, several extensions of the continuous-time model with the motivation of testing the robustness of the continuous-time model.

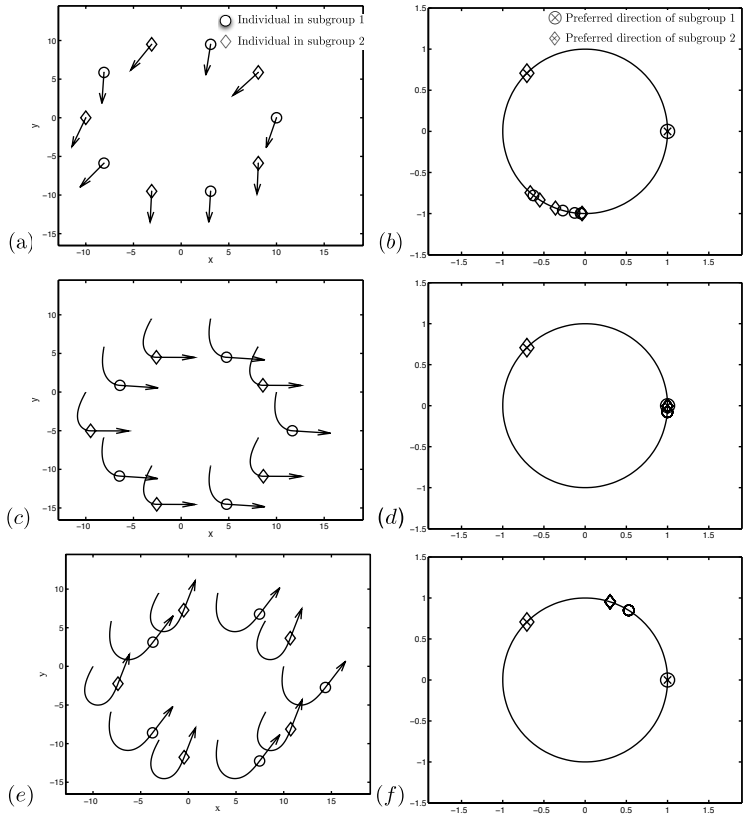

Figure 5.14: Simulation for two informed subgroups with each a population of 5 individuals in the physical plane. The phases of the individuals are initially started near the equilibrium $\boldsymbol{\psi}_{sync2}$ with $K = 70, \bar{\theta}_2 = \frac{3\pi}{4}$.

5.3 Extensions and Robustness of the Model

In this section we consider several extensions of the model (5.1). We first look at the case where $N_1 \neq N_2$ and $N_3 = 0$; we show that the qualitative behavior of the system remains identical and interpret the quantitative changes. We then look at the case where the subgroups are not homogeneous, introducing heterogeneity both at the informed and uninformed individual level. Here again, the qualitative behavior remains identical and we interpret the quantitative changes. Finally, we consider a forgetting factor feedback in the form of a dynamic gain on the relative strength of the attraction to the preferred direction. This feedback factor is analogous to the feedback on the weight ω used in some

simulations in [19] which reinforces or diminishes the gain ω if informed individuals find themselves moving towards or away from their preferred direction. In this case, we show that consensus is always achieved, the group traveling either in the average of the preferred directions or in one of the two preferred directions. In this case the continuous-time model reproduces the discrete-time model results.

5.3.1 Uneven Informed Subgroups

The first extension we consider is the case where the two informed subgroups do not have identical populations ($N_1 \neq N_2$). In this case, the time-scale separation of the model (5.1) still holds and the reduced dynamics (5.14) become

$$\begin{aligned} \dot{\psi}_1 &= -\sin(\psi_1) + \frac{KN_2}{N}\sin(\psi_2 - \psi_1) \\ \dot{\psi}_2 &= \sin\left(\bar{\theta}_2 - \psi_2\right) + \frac{KN_1}{N}\sin(\psi_1 - \psi_2). \end{aligned} \tag{5.40}$$

For this system, the nature of the persistent stable motion remains unchanged. That is, there is still one persistent stable equilibrium (corresponding to $\boldsymbol{\psi}_{sync1}$ in the case $N_1 = N_2$) where for large values of K the two informed subgroups are synchronized. However, synchronization no longer occurs at $\Psi = \frac{\bar{\theta}_2}{2}$, the average of the preferred directions. Instead, synchronization occurs at a weighted average of the two preferred directions, 0 and $\bar{\theta}_2$. If $N_1 > N_2$, the value of Ψ for the persistent stable equilibrium is "closer" to 0 than to $\bar{\theta}_2$; if $N_2 > N_1$, the value of Ψ for the persistent stable equilibrium is "closer" to $\bar{\theta}_2$ than to 0. Figure 5.15 shows the evolution of Ψ for the persistent stable equilibrium $\boldsymbol{\psi}_{sync1}$ with $N_2 = 10$ fixed and N_1 increasing such that the ratio $\frac{N_1}{N_2}$ increases from $\frac{1}{10}$ to 10. The value of Ψ for the persistent stable equilibrium (corresponding to $\boldsymbol{\psi}_{sync1}$ in the $N_1 = N_2$ case), goes from being asymptotically close to $\bar{\theta}_2 = 2$ rad to asymptotically approaching 0.

5.3.2 Heterogeneous Subgroups

The continuous-time model (5.1) that we studied in this chapter assumes some homogeneity in the group; specifically individuals in the same subgroup are assumed to be strictly identical although have heterogeneous initial conditions. Here we consider extensions of

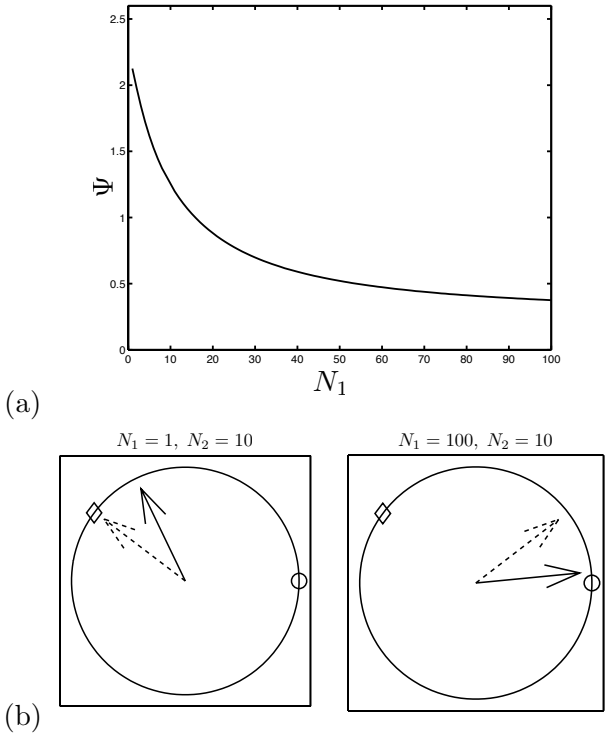

Figure 5.15: (a) The value of Ψ corresponding to the stable motion $\boldsymbol{\psi}_{sync1}$ as a function of subgroup population size N_1 for fixed subgroup population size $N_2 = 10$. As the ratio $\frac{N_1}{N_2}$ increases from $\frac{1}{10}$ to 10 (i.e., N_1 goes from 1 to 100), the value of Ψ goes from being asymptotically close to $\bar{\theta}_2 = 2$ to being asymptotically close to $\bar{\theta}_1 = 0$. (b) The persistent stable equilibrium $\boldsymbol{\psi}_{sync1}$ for the two extreme values of N_1. The motion of the group is closer to $\bar{\theta}_2 = 2$ rad when $1 = N_1 < N_2 = 10$. The motion of the group is closer to $\bar{\theta}_1 = 0$ rad when $100 = N_1 > N_2 = 10$. The circle and the diamond represent respectively the preferred direction of the first and second informed subgroups.

this homogeneity assumption by introducing heterogeneity both at the level of informed and uniformed individuals. For each extension, we give the modified equations of the model (5.1) and present and interpret simulation results. With either type of heterogeneity the time-scale separation and the nature of the stable motions remain unchanged.

Although we only discuss here the heterogeneous case with simulations, the two types of heterogeneity have been formally studied in [72]. In this work we studied the coarse-grained (i.e., group-level) alignment dynamics of the model (5.1) adding the two type of heterogeneity mentioned above. Choosing convenient coarse-grained variables (suggested by the time

scale separation proven in this chapter) that account for rapidly developing correlations during initial transients, we performed efficient computations of coarse-grained steady states and their bifurcation analysis. The saddle-node bifurcation and the hypercritical pitchfork bifurcation proven in Section 5.2.2 were observed with either type of heterogeneity.

We introduce a first type of heterogeneity, at the uninformed level, by considering a group composed of N_1 individuals, all with preferred direction $\bar{\theta}_1 = 0$; N_2 individuals all with preferred direction $\bar{\theta}_2$; and N_3 heterogeneous naive (uninformed) individuals where the heterogeneity is expressed with a tendency to deviate from the average direction, following a random distribution. The system (5.1) becomes

$$\begin{aligned}
\dot{\theta}_j &= \sin\left(\bar{\theta}_1 - \theta_j\right) + \frac{K}{N}\sum_{l=1}^{N}\sin\left(\theta_l - \theta_j\right), \quad j \in \mathcal{N}_1 \\
\dot{\theta}_j &= \sin\left(\bar{\theta}_2 - \theta_j\right) + \frac{K}{N}\sum_{l=1}^{N}\sin\left(\theta_l - \theta_j\right), \quad j \in \mathcal{N}_2 \\
\dot{\theta}_j &= \omega_j + \frac{K}{N}\sum_{l=1}^{N}\sin\left(\theta_l - \theta_j\right), \quad j \in \mathcal{N}_3\,,
\end{aligned} \tag{5.41}$$

where the parameters ω_j are independent draws from a gaussian distribution function $f(\omega)$ with a mean of 0 and a given variance. Figures 5.16 and 5.17 present simulation results of the system (5.41). For these simulations, we considered two informed subgroups of 10 individuals each and a naive (uninformed) subgroup of 80 individuals. The parameters were set as $K = 1$ and $\bar{\theta}_2 = 2.5$ rad. The parameters ω_j were taken from a normal distribution with zero mean and a variance of 0.05. In Figure 5.16 the observed stable motion corresponds to the equilibrium $\boldsymbol{\psi}_{sync1}$, with the group traveling towards the average of the preferred direction. In Figure 5.17 the observed stable motion corresponds to the equilibrium $\boldsymbol{\psi}_{sync2}$, with the group traveling in a direction opposite to the average of the preferred directions. The initial conditions of the phases to get this equilibrium had to be chosen in a fairly tight region around $\frac{\bar{\theta}_2}{2} + \pi$, highlighting that the region of attraction of the equilibrium $\boldsymbol{\psi}_{sync2}$ is smaller than the region of attraction of $\boldsymbol{\psi}_1$. In this model, as in the model (5.1), the naive individuals do not completely synchronize in the direction $\frac{\bar{\theta}_2}{2}$ for $\boldsymbol{\psi}_{sync1}$ ($\frac{\bar{\theta}_2}{2} + \pi$ for $\boldsymbol{\psi}_{sync2}$). Rather, they form a clump centered at $\frac{\bar{\theta}_2}{2}$ for $\boldsymbol{\psi}_{sync1}$ ($\frac{\bar{\theta}_2}{2} + \pi$ for

$\boldsymbol{\psi}_{sync2}$), as shown in Figure 5.16 for $\boldsymbol{\psi}_{sync1}$ (Figure 5.17 for $\boldsymbol{\psi}_{sync2}$). Simulations show that larger values of the coupling gain K yield tighter clumps. In [72], we showed that some of the same bifurcations proven in Section 5.2.2 can be recovered numerically for the system (5.41), suggesting a measure of robustness for the model (5.1) .

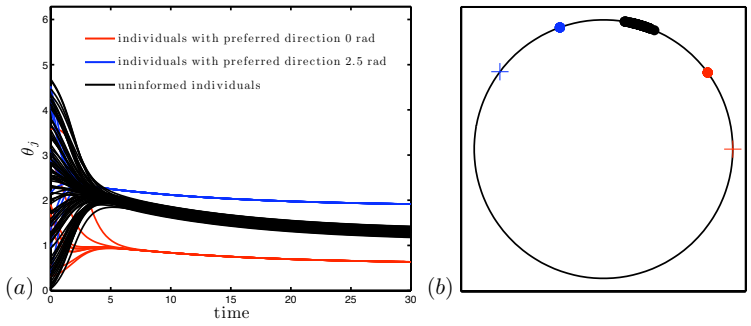

Figure 5.16: (a) Phase angle for each individual in the group versus time for $K = 1$. For this simulation there are 10 individuals with preferred direction 0 rad, 10 individuals with preferred direction 2.5 rad, and 80 heterogeneous individuals with no preferred direction. Heterogeneity is introduced at the uninformed level with a tendency of the uninformed individuals to deviate from the average direction, following a random distribution as expressed in equations (5.41). During a short initial transient time, the heading angles of the individuals in the informed subgroups synchronize and the ones in the uninformed subgroup clump. Subsequently, the directions slowly drift to the steady state value towards the average of the preferred directions. (b) Phase angle for each individual after reaching the steady state. The uninformed individuals are clumped around $\frac{\bar{\theta}_2}{2} = 1.25$ rad and the informed individuals are synchronized by subgroups, each subgroup flanking the uninformed individuals.

We next introduce a second type of heterogeneity by considering a group composed of two subgroups of heterogeneous informed agents, where heterogeneity is expressed with randomness in the preferred direction. More precisely, each of the N_1 individuals in the first informed subgroup have a preferred direction $\bar{\theta}_1^j$, $j \in \mathcal{N}_1$, drawn from a normal random distribution with a mean of $\bar{\theta}_1$, and a given variance; each of the $N_2 = N_1$ individuals in the second informed subgroup have a preferred direction $\bar{\theta}_2^j$, $j \in \mathcal{N}_2$, drawn from another independent normal random distribution with a mean of $\bar{\theta}_2$, and a given variance. The

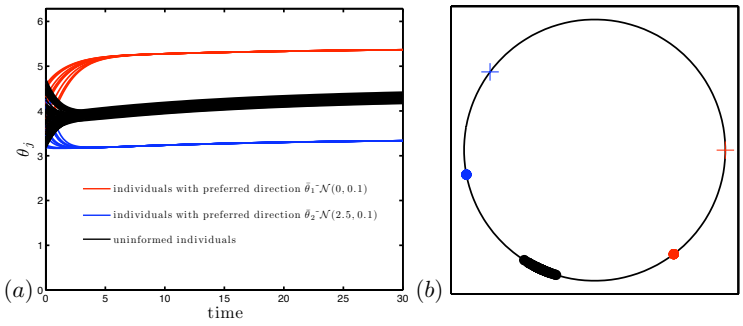

Figure 5.17: (a) Phase angle for each individual in the group versus time for $K = 1$. For this simulation there are 10 individuals with preferred direction 0 rad, 10 individuals with preferred direction 2.5 rad, and 80 heterogeneous individuals with no preferred direction. Heterogeneity is introduced at the uninformed level with a tendency of the uninformed individuals to deviate from the average direction, following a random distribution as expressed in equations (5.41). During a short initial transient time, the heading angles of the individuals in the informed subgroups synchronize and the ones in the uninformed subgroup clump. Subsequently, the directions slowly drift to the steady state value in a direction opposite to the average of the preferred directions. (b) Phase angle for each individual after reaching the steady state. The uninformed individuals are clumped around $\frac{\bar{\theta}_2}{2} + \pi = 4.39$ rad, and the informed individuals are synchronized by subgroups, each subgroup flanking the uninformed individuals.

group also has N_3 identical naive (uninformed) individuals. The system (5.1) becomes

$$\begin{aligned}
\dot{\theta}_j &= \sin\left(\bar{\theta}_1^j - \theta_j\right) + \frac{K}{N}\sum_{l=1}^{N}\sin\left(\theta_l - \theta_j\right), \quad j \in \mathcal{N}_1 \\
\dot{\theta}_j &= \sin\left(\bar{\theta}_2^j - \theta_j\right) + \frac{K}{N}\sum_{l=1}^{N}\sin\left(\theta_l - \theta_j\right), \quad j \in \mathcal{N}_2 \\
\dot{\theta}_j &= \frac{K}{N}\sum_{l=1}^{N}\sin\left(\theta_l - \theta_j\right), \quad j \in \mathcal{N}_3\,,
\end{aligned} \tag{5.42}$$

Figures 5.18 and 5.19 present simulation results of the system (5.42). For the simulations, we considered two equal informed population of 10 individuals and a naive (uninformed) population of 80 individuals. The parameters $\bar{\theta}_1^j$ are taken from a normal distribution with a mean of 0 and a variance of 0.1, the parameters $\bar{\theta}_2^j$ are taken from a normal distribution with a mean of 2.5 and a variance of 0.1, and the parameter K is set to 1. In Figure 5.18, the observed stable motion corresponds to the equilibrium $\boldsymbol{\psi}_{sync1}$, with the group traveling toward the average of the preferred direction. In Figure 5.19 the observed stable motion corresponds to the equilibrium $\boldsymbol{\psi}_{sync2}$, with the group traveling in a direction opposite to the average of the preferred directions. The initial conditions of the phases to get this equilibrium also had to be chosen in a fairly tight region around $\frac{\bar{\theta}_2}{2}+\pi$, highlighting that the region of attraction of the equilibrium $\boldsymbol{\psi}_{sync2}$ is smaller than the region of attraction of $\boldsymbol{\psi}_1$. For this model, as in model (5.1), the informed subgroups do not completely synchronize. Rather, they form clumps distributed around a given equilibrium value. Simulations show that larger values of the coupling gain K yield tighter clumps. In [72], we showed that some of the same bifurcations proven in Section 5.2.2 can be recovered numerically for the system (5.41), suggesting a measure of robustness for the model (5.1) .

For each of the three extensions we considered, simulation results suggest that the time-scale separation, the nature of the stable motion, and some of the bifurcations proven in Section 5.2.2 are preserved, implying some level of robustness of the model (5.1). However, unlike the discrete-time model studied in Chapter 4 and in [19], neither the continuous-time model (5.1) nor its extensions exhibit full synchronization of the group unless the coupling gain K is very large (which is equivalent to the weight ω of the preferred direction in (4.2)

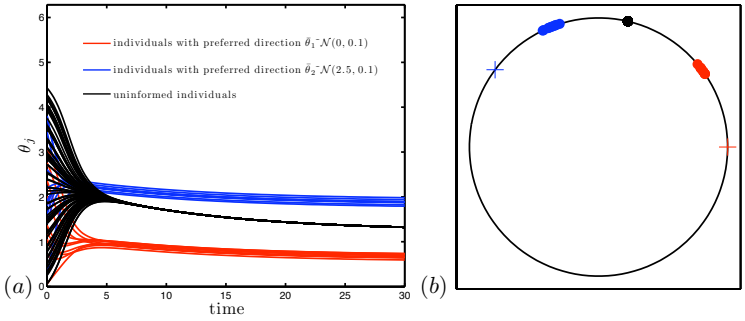

Figure 5.18: (a) Phase angle for each individual in the group versus time for $K = 1$. For this simulation there are 10 individuals with a preferred direction taken from a normal distribution with a mean of 0 rad and a variance of .1, 10 individuals with a preferred direction taken from a normal distribution with a mean of 2.5 rad and a variance of .1, and 80 individuals with no preferred direction. Heterogeneity is introduced at the informed level with randomness assumed in the choice of preferred direction as described in equations (5.42). During a short initial transient time, the heading angles of the individuals in the informed subgroups get clumped and the heading angles of the uninformed individuals synchronize. Subsequently, the directions slowly drift to the steady state value in the direction of the average of the preferred directions. (b) Phase angle for each individual after reaching the steady state. The uninformed individuals are synchronized at $\frac{\bar{\theta}_2}{2} = 1.25$ rad, and the informed individuals are clumped by subgroups with each clump flanking the uninformed individuals.

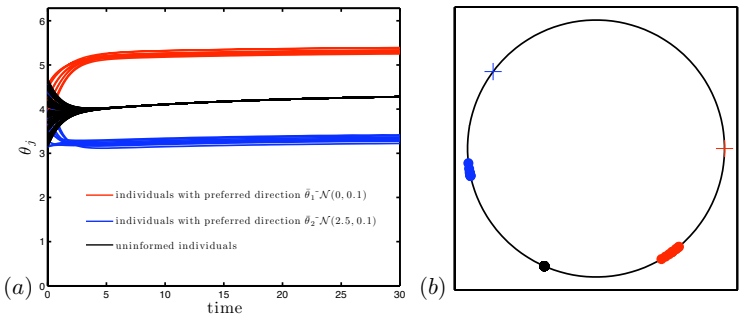

Figure 5.19: (a) Phase angle for each individual in the group versus time for $K = 1$. For this simulation there are 10 individuals with preferred direction taken from a normal distribution with a mean of 0 rad and a variance of .1, 10 individuals with preferred direction taken from a normal distribution with a mean of 2.5 rad and a variance of .1, and 80 individuals with no preferred direction. Heterogeneity is introduced at the informed level with randomness assumed in the choice of preferred direction as described in equations (5.42). During a short initial transient time, the heading angles of the individuals in the informed subgroups get clumped and the heading angles of the uninformed individuals synchronize. Subsequently, the directions slowly drift to the steady state value in a direction opposite to the average of the preferred directions. (b) Phase angle for each individual after reaching the steady state. The uninformed individuals are synchronized at $\frac{\bar{\theta}_2}{2} + \pi = 3.39$ rad, and the informed individuals are clumped by subgroups, with each clump flanking the uninformed individuals.

being very small). This means that for small values of K, a population modelled by (5.1) does not fully aggregate and the group splits. With this model, it is impossible moreover for the group to select one of the preferred direction as was the case in [19] and in Chapter 4. We now consider one last extension of the model (5.1) in which we introduce a "forgetting factor" feedback in the form of a dynamic gain on the relative strength of the attraction to the preferred directions. Simulations results then resemble more closely the results from Chapter 4 and from [19].

5.3.3 Forgetting Factor Feedback

We present an extension of the model (5.1) which, when investigated numerically, yields the same type of bifurcation observed in [19] and in Chapter 4. In this extension, individuals are increasingly or decreasingly influenced by their preferred direction, depending on how close they are to it. When individuals are heading in their preferred direction, their attraction to it is maximum; this influence fades as the heading of an individual moves away from its preferred direction. To model this effect, we multiply the "preferred direction" term of equation (5.1) by a gaussian shaped gain, as follow:

$$\begin{aligned}
\dot{\theta}_j &= e^{-\frac{\sin^2\left(\bar{\theta}_1-\theta_j\right)}{\alpha}} \sin(\bar{\theta}_1-\theta_j) + \frac{K}{N}\sum_{l=1}^{N}\sin\left(\theta_l-\theta_j\right), \quad j\in\mathcal{N}_1 \\
\dot{\theta}_j &= e^{-\frac{\sin^2\left(\bar{\theta}_2-\theta_j\right)}{\alpha}} \sin(\bar{\theta}_2-\theta_j) + \frac{K}{N}\sum_{l=1}^{N}\sin\left(\theta_l-\theta_j\right), \quad j\in\mathcal{N}_2 \\
\dot{\theta}_j &= \frac{K}{N}\sum_{l=1}^{N}\sin\left(\theta_l-\theta_j\right), \quad j\in\mathcal{N}_3,
\end{aligned} \tag{5.43}$$

where α is a positive constant chosen to control the width of the gaussian. The smaller α is the "quicker" an individual gives up his preferred direction. Simulations of the model (5.43) shown in Figure 5.20, suggest that, as in the model (5.1), there are two time-scales in the dynamics. At first the heading angles of the individuals in each subgroup synchronize, then the three average subgroup directions slowly drift to reach a steady state. We note that at the steady state the three subgroups are synchronized. With the initial conditions used in this simulation, synchronization occurs at the preferred direction of the second informed

subgroup. Assuming further that $N_1 = N_2$ and $N_3 = 0$, we conjecture that the reduced dynamics are given by

$$\begin{aligned}\dot{\psi}_1 &= -e^{-\frac{\sin^2(\psi_1)}{\alpha}} \sin\psi_1 + \frac{K}{2}\sin(\psi_2 - \psi_1) \\ \dot{\psi}_2 &= e^{-\frac{\sin^2(\bar{\theta}_2 - \psi_2)}{\alpha}} \sin\left(\bar{\theta}_2 - \psi_2\right) + \frac{K}{2}\sin(\psi_2 - \psi_1)\,.\end{aligned} \tag{5.44}$$

Figure 5.21 shows for the system (5.44) the bifurcation diagram with $(K, \alpha) = (2.5, 0.2)$.

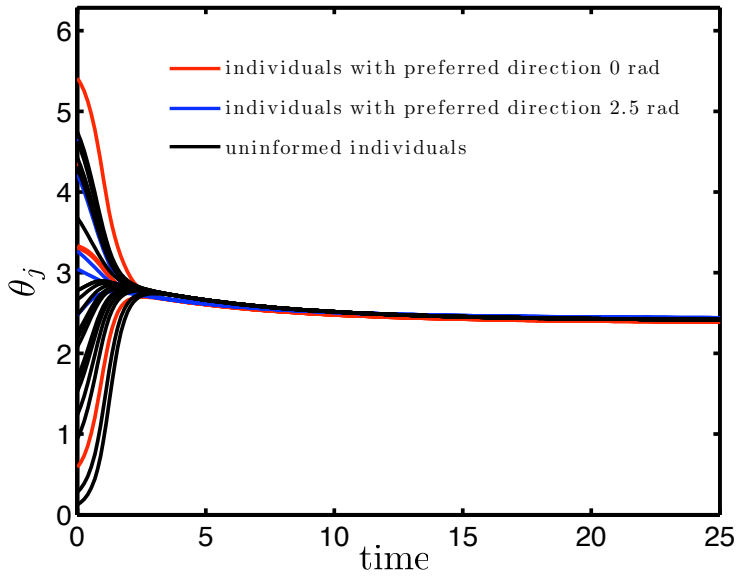

Figure 5.20: Phase angle of each individual in the group versus time for $(K, \alpha) = (2.5, 0.2)$. For this simulation there are 5 individuals with preferred direction 0 rad, 5 individuals with preferred direction 2.5 rad, and 20 individuals with no preferred direction. As in model (5.1), two time-scales in the dynamics are observed. During a short transient time, the heading angles of the individuals in each subgroup synchronize. Subsequently the three average subgroup directions drift slowly to their steady state values. For the initial conditions used in this simulation the steady state solution corresponds to all three subgroup synchronized in the preferred direction of the second informed subgroup.

The bifurcation parameter is $\bar{\theta}_2$, and ψ_1 is plotted as a function of $\bar{\theta}_2$ for all equilibria of the system. Figure 5.21 shows a bifurcation for $K = 2.5, \alpha = 0.2$. For $\bar{\theta}_2 < \bar{\theta}_2^*$ there is only one stable equilibrium corresponding to the synchronized motion of both informed subgroups in the average of the preferred directions. For $\bar{\theta}_2 > \bar{\theta}_2^*$ there are two stable equilibria, each corresponding to the synchronized motion of both informed subgroups in

each of the two preferred directions. The system stabilizes to one preferred direction or the other, depending on the initial conditions only. This behavior matches closely the results in [19] where depending on the level of disagreement the group either follows the average of the preferred directions or collectively select one of the preferred directions. In the region of parameter space where the group selects one of the preferred directions, the choice of one preferred direction over the other is solely driven by the initial conditions of the system.

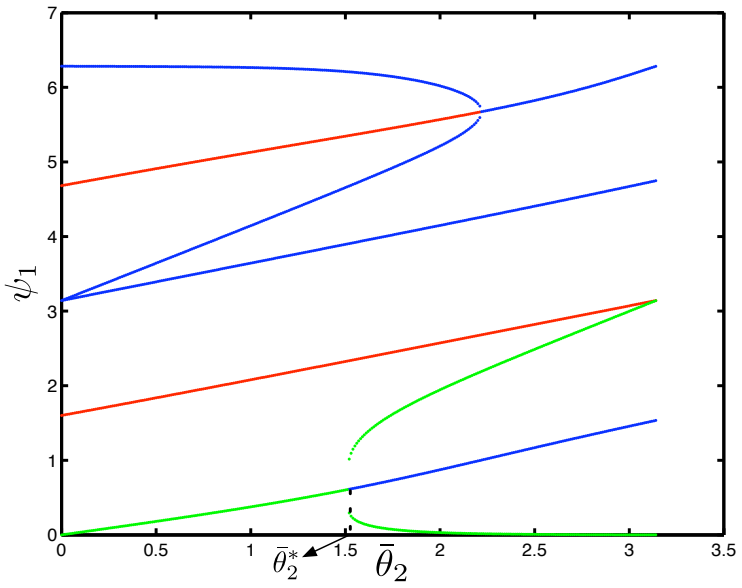

Figure 5.21: Bifurcation diagram for the system (5.44) with fixed $K = 2.5, \alpha = 0.2$. The bifurcation parameter is $\bar{\theta}_2$ and ψ_1 is plotted as a function of $\bar{\theta}_2$ for all equilibria of the system. We observe the supercritical pitchfork bifurcation at $\bar{\theta}_2 = \bar{\theta}_2^*$.

Motivated by the observed deviations between the qualitative behavior of the discrete-time model studied in Chapter 4 and that of the continuous-time model (5.1), we derive and study in the next chapter a more complicated continuous-time model relaxing two of the model (5.1)'s simplifying assumptions. First, an all-to-all communication topology is no longer assumed; instead we assume a time-varying, possibly incomplete, connecting topology where the rate of change of the level of interaction between pairs of individuals depends on their current states. Second, we consider the presence of uninformed/naive (i.e., individuals without a preferred direction of travel). By relaxing these two assumptions, the yielded

model produces qualitative behaviors closer, though not identical, to the ones observed in [19] and in Chapter 4. The observed resulting deviations draw our attention to the importance of a remaining simplifying assumption, namely, that our model describes the dynamics of the heading angles for all individuals in the population independent of their positions.

Chapter 6

Collective Decision Making: Analytical Model with Time-Varying Connecting Topology

In this chapter, we derive and study the dynamics of a low-dimensional, deterministic, coordinated control system. This model, a more complex version of the model presented and studied in Chapter 5, relaxes two of that model's simplifying assumptions. In Section 6.1 we present the model and identify invariant manifolds. In Section 6.2 we summarize the conditions for each manifold to be attractive and describe the stable motions on these invariant manifolds in the context of animal group motion. In Section 6.3 we study the attractiveness of the identified invariant manifolds and the full phase-space reduced dynamics on the attractive invariant manifolds. In Section 6.4 we consider an extension of the model to test its robustness.

6.1 Model and Invariant Manifolds

The continuous-time model we present here is motivated by the observed deviations between the realistic qualitative behavior of the discrete-time model studied in Chapter 4 and that of the continuous-time model presented in Chapter 5. In order to formulate this new continuous-time model, we relax two simplifying assumptions made in the model presented in Chapter 5. First, an all-to-all communication topology is no longer assumed; instead we assume a time-varying, possibly incomplete, connecting topology where the rate of change of the level of interaction between pairs of individuals depends on their current states. Second, whereas in the analyses of the previous model we ignored the presence of uninformed/naive individuals (i.e., individuals without a preferred direction of travel), here we consider their presence. With these two assumptions relaxed, the yielded model produces qualitative behaviors that are closer, though not identical, to the ones observed in [19] and in Chapter 4. The observed resulting deviations draw our attention to the importance of a remaining simplifying assumption, namely, that we are considering only the dynamics of the phases and not the complete spatial dynamics of the individuals in the group.

6.1.1 Particle Model

Following the notation used in Chapter 5, we consider a population of N interacting individuals, each described as a unit mass Newtonian particle moving in the plane at constant speed and controlled by its steering rate. The steering rate evolves through time under the influence of inter-particle measurements and, where applicable, information represented by a preferred direction of travel. Unlike in the model presented in the previous chapter, in this model we do not assume a fixed all-to-all communication topology in the group. Rather, we consider a time-varying, possibly incomplete, undirected communication topology in which the rate of change of the level of interaction between individuals depends on their current states. We denote as $a_{lj}(t)$, $l \in \{1, \ldots, N\},\ j \in \{1, \ldots, N\}$, the coupling gain quantifying the level of interaction between agent l and agent j, where $a_{lj}(t) = a_{jl}(t)$ is allowed to take any value between 0 and 1. In the case where $a_{lj} = 0$, agents l and j are not interacting.

In the case where $a_{lj} = 1$, the interaction between agents l and j is maximum.

The model we define consists of a set of differential equations describing the dynamics of the instantaneous heading directions θ_j and interaction gains a_{lj}. The dynamics for the heading angles are modeled with steering terms that depend on relative heading angles, as in the previous chapter; the dynamics of the interaction gains are modelled with a saturated integrator dynamics written as

$$\begin{aligned}
\dot{\theta}_j &= \sin\left(\bar{\theta}_1 - \theta_j\right) + \frac{K_1}{N}\sum_{l=1}^{N} a_{jl}\sin\left(\theta_l - \theta_j\right), && j \in \mathcal{N}_1 \\
\dot{\theta}_j &= \sin\left(\bar{\theta}_2 - \theta_j\right) + \frac{K_1}{N}\sum_{l=1}^{N} a_{jl}\sin\left(\theta_l - \theta_j\right), && j \in \mathcal{N}_2 \\
\dot{\theta}_j &= \frac{K_1}{N}\sum_{l=1}^{N} a_{jl}\sin\left(\theta_l - \theta_j\right), && j \in \mathcal{N}_3 \\
\dot{\eta}_{lj} &= K_2(\rho_{lj} - r), && l \in \{1,\ldots,N\},\, j \in \{l+1,\ldots,N\} \\
a_{lj} &= \frac{1}{1+e^{-\eta_{lj}}}, && l \in \{1,\ldots,N\},\, j \in \{l+1,\ldots,N\},
\end{aligned} \tag{6.1}$$

where $\eta_{lj} = \eta_{jl} \in \mathbb{R}$ is an integrated variable, $\rho_{lj} = |\frac{e^{i\theta_l}+e^{i\theta_j}}{2}|$ gives a measure of the level of synchrony between agents l and j, the parameter $K_1 > 0$ weights the attention paid to other individuals versus the preferred direction, the parameter $K_2 > 0$ quantifies the speed at which the interaction gains evolve, and $r \in [0, 1]$ is a fixed threshold. If $\rho_{lj} > r$, i.e., synchrony is above the threshold, then η_{lj} increases and a_{lj} eventually converges to 1, the maximum interaction strength. If $\rho_{lj} < r$, i.e., synchrony is below the threshold, then η_{lj} decreases and a_{lj} eventually converges to 0, no interconnection. The use of such dynamics for the interaction gains allows us to include the effect of memory on the interactions between individuals. This formulation is similar to the drift diffusion dynamics used to model "two-alternative forced choice tasks" in psychological studies such as [7]. The dynamics of a_{lj} can be written in a simpler form, substituting the dynamics of η_{lj}, as

$$\dot{a}_{lj} = K_2(1 - a_{lj})a_{lj}(\rho_{lj} - r), \;\; l \in \{1,\ldots,N\},\; j \in \{l+1,\ldots,N\}. \tag{6.2}$$

We will use this formulation in the remainder of the analysis.

6.1.2 Invariant Manifolds in the Model

Like the model (5.1) discussed in the previous chapter, the $(N+\frac{N(N-1)}{2})$-dimensional model (6.1) is challenging to study. Simulations of the model (6.1) shown in Figures 6.1 suggest, however, that we can reduce the complexity of the system using time scale arguments, as we did in the previous chapter. During an initial transient time, the heading angles of the individuals in each subgroup synchronize and the interaction gains between subgroups converge to a fixed value (zero or one). Then, the three average subgroup directions slowly drift to reach a steady state. This means that, as was true for the model presented in the previous chapter, the long-term dynamics of the model (6.1) can be described by ψ_1, ψ_2 and ψ_3, which are the average heading directions of the three subgroups. However, unlike the model (5.1) which has only one invariant manifold the system (6.1) has several, each characterized by a set of interaction gains between the different subgroups. Figures 6.2 - 6.5 present simulations illustrating six different invariant manifolds (each corresponding to a different interconnection topology between the subgroups) to which the system can converge during the fast time scale. We note that for these simulations, the gain K_2 used is smaller than the one used in Figure 6.1. Even without a sharp distinction of the two time scales, the nature of the long term behavior is preserved.

In Figure 6.2 all three simulations presented have the same parameter values $K_1 = 2,\ K_2 = 5,\ N_1 = N_2 = 10,\ N_3 = 30,\ r = .8,\ \bar{\theta}_1 = 0$ rad, $\bar{\theta}_2 = 3$ rad but each has a different initial conditions. The first simulation is shown in panels (a), (b), (c), the second in panels (d), (e), (f) and the third in panels (g), (h), (i). In the first simulation, all interaction gains converge to 1. At the steady state, each informed subgroup compromises between its preferred direction and the average of the two preferred directions, while the uninformed subgroup travels in a direction corresponding to the average of the preferred directions. In the second simulation, the interaction gains between individuals in the first informed subgroup and individuals in the uninformed subgroup converge to 1, the interaction gains between individuals in the second informed subgroup and individuals in the other two subgroups (the uninformed subgroup and the first informed subgroup) converge to zero.

At the steady state, the first informed subgroup travels in its preferred direction along with the uninformed subgroup, while the second informed subgroup, disconnected from the two other subgroups, travels in its preferred direction. In the third simulation, the scenario is symmetrical to the previous one: the second informed subgroup travels in its preferred direction along with the uninformed subgroup, while the first informed subgroup, disconnected from the two other subgroups, travels in its preferred direction.

In Figure 6.3 the values of the parameters $K_1,\ K_2,\ r$ and $\bar{\theta}_1$ are identical to the ones used in Figure 6.2, but the preferred direction of the second subgroup is set to $\bar{\theta}_2 = .5$ rad. In this simulation, the interaction gains between individuals in the first informed subgroup and individuals in the second informed subgroup converge to 1 and the interaction gains between individuals in the uninformed subgroup and individuals in the other two subgroups (the first and second informed subgroups) converge to zero. At the steady state, the two informed subgroups compromise between their preferred directions and the average of the preferred directions, while the uninformed subgroup, disconnected from the two other subgroups, travels in its initial heading.

In Figure 6.4 the values of the parameter $K_1,\ K_2$ are identical to the ones in Figures 6.2 and 6.3. The threshold r is set to .95 and the preferred directions of the first and second informed subgroups are set to $\bar{\theta}_1 = 1$ rad and $\bar{\theta}_2 = 3.1$ rad, respectively. In this simulation, all interaction gains between individuals in different subgroups converge to zero. At the steady state, there are no interactions between subgroups, each informed subgroup travels in its preferred direction and the uninformed subgroup travels in its initial direction.

In Figure 6.5 the values of the parameters are chosen as $K_1 = 2,\ K_2 = 7,\ N_1 = N_2 = 10,\ N_3 = 30,\ r = .85,\ \bar{\theta}_1 = \frac{\pi}{4}$ rad and $\bar{\theta}_2 = \frac{5\pi}{4}$ rad. In this simulation, the interaction gains between individuals in the first informed subgroup and individuals in the second subgroup converge to zero and the interaction gains between individuals in the uninformed subgroup and individuals in both of the informed subgroups converge to 1. At the steady state, each of the two informed subgroups, although not directly connected to the other, compromises between its preferred direction and the average of the two preferred directions;

the uninformed subgroup, "linking" the two informed subgroups, travels in the average of the preferred directions.

In order to formalize the time scale separation, we define a new set of independent variables that distinguishes between slow and fast variables. As in the previous chapter, we choose ψ_1, ψ_2 and ψ_3 as the slow variables since they characterize the direction of travel of the three subgroups. We choose as the fast variables of the system the variables $\alpha_{p_{(k,q)}}$, $k = 1, 2, 3$, $q \in \{1, \dots N_k - 1\}$ defined in equation (5.3) and the variables a_{lj}, $l \in \{1, \dots, N\}$, $j \in \{l+1, \dots, N\}$. Following the calculations used in the previous chapter, we rewrite the coupled multi-agent system dynamics (6.1) as

$$
\begin{aligned}
\dot{\psi}_1 &= \frac{1}{N_1\rho_1} \sum_{l\in\mathcal{N}_1} \left(\sin\left(\bar{\theta}_1 - \theta_l\right) + \frac{K_1}{N} \left(\sum_{n=1}^{N} a_{ln} \sin\left(\theta_n - \theta_l\right) \right) \right) \cos\left(\psi_1 - \theta_l\right) \\
\dot{\psi}_2 &= \frac{1}{N_2\rho_2} \sum_{l\in\mathcal{N}_2} \left(\sin\left(\bar{\theta}_2 - \theta_l\right) + \frac{K_1}{N} \left(\sum_{n=1}^{N} a_{ln} \sin\left(\theta_n - \theta_l\right) \right) \right) \cos\left(\psi_2 - \theta_l\right) \\
\dot{\psi}_3 &= \frac{1}{N_3\rho_3} \sum_{l\in\mathcal{N}_3} \left(\frac{K_1}{N} \left(\sum_{n=1}^{N} a_{ln} \sin\left(\theta_n - \theta_l\right) \right) \right) \cos\left(\psi_3 - \theta_l\right) \\
\dot{\alpha}_p &= iN_1\alpha_p \Big(\left(\sin\left(\bar{\theta}_1 - \theta_p\right) - \rho_1 \sin\left(\bar{\theta}_1 - \psi_1\right) \right) \\
&\quad + \frac{K_1}{N} \left(\sum_{n=1}^{N} a_{pn} \sin(\theta_n - \theta_p) - \frac{1}{N_1} \sum_{l\in\mathcal{N}_1} \sum_{n=1}^{N} a_{ln} \sin(\theta_n - \theta_l) \right) \Big), \qquad p \in \mathcal{N}_1,\ p \neq p_{(1,N_1)} \\
\dot{\alpha}_p &= iN_2\alpha_p \Big(\left(\sin\left(\bar{\theta}_2 - \theta_p\right) - \rho_1 \sin\left(\bar{\theta}_2 - \psi_2\right) \right) \\
&\quad + \frac{K_1}{N} \left(\sum_{n=1}^{N} a_{pn} \sin(\theta_n - \theta_p) - \frac{1}{N_2} \sum_{l\in\mathcal{N}_2} \sum_{n=1}^{N} a_{ln} \sin(\theta_n - \theta_l) \right) \Big), \qquad p \in \mathcal{N}_2,\ p \neq p_{(2,N_2)} \\
\dot{\alpha}_p &= iN_3\alpha_p \frac{K_1}{N} \left(\sum_{n=1}^{N} a_{pn} \sin(\theta_n - \theta_p) - \frac{1}{N_3} \sum_{l\in\mathcal{N}_3} \sum_{n=1}^{N} a_{ln} \sin(\theta_n - \theta_l) \right), \ p \in \mathcal{N}_3,\ p \neq p_{(3,N_3)} \\
\dot{a}_{lj} &= K_2(1 - a_{lj}) a_{lj} (\rho_{lj} - r), \qquad l \in \{1, \dots, N\},\ j \in \{l+1, \dots, N\},
\end{aligned}
\tag{6.3}
$$

for $\rho_k \neq 0$, $k = 1, 2, 3$.

This system has several invariant manifolds. The ones we consider are those having all individuals synchronized within their respective subgroups (i.e., $\theta_p = \psi_k$, $p \in \mathcal{N}_k$, $k = 1, 2, 3$),

each with one of eight possible interconnection topologies between the three subgroups. We call these invariant manifolds $\mathcal{M}_1, \ldots, \mathcal{M}_8$. These manifolds are given by $\alpha_p = 1$ for $p \in \mathcal{N}_k$, $k = 1, 2, 3$; $a_{lj} = 1$ for $l, j \in \mathcal{N}_k$, $k = 1, 2, 3$ and

- $\mathcal{M}_1$: $a_{lj} = 1$ for $l \in \mathcal{N}_1,\ j \in \mathcal{N}_2$; $a_{lj} = 0$ for $l \in \mathcal{N}_1,\ j \in \mathcal{N}_3$; $a_{lj} = 1$ for $l \in \mathcal{N}_2,\ j \in \mathcal{N}_3$.
- $\mathcal{M}_2$: $a_{lj} = 1$ for $l \in \mathcal{N}_1,\ j \in \mathcal{N}_2$; $a_{lj} = 1$ for $l \in \mathcal{N}_1,\ j \in \mathcal{N}_3$;$a_{lj} = 0$ for $l \in \mathcal{N}_2,\ j \in \mathcal{N}_3$.
- $\mathcal{M}_3$: $a_{lj} = 0$ for $l \in \mathcal{N}_1,\ j \in \mathcal{N}_2$; $a_{lj} = 0$ for $l \in \mathcal{N}_1,\ j \in \mathcal{N}_3$; $a_{lj} = 0$ for $l \in \mathcal{N}_2,\ j \in \mathcal{N}_3$.
- $\mathcal{M}_4$: $a_{lj} = 0$ for $l \in \mathcal{N}_1,\ j \in \mathcal{N}_2$; $a_{lj} = 1$ for $l \in \mathcal{N}_1,\ j \in \mathcal{N}_3$; $a_{lj} = 0$ for $l \in \mathcal{N}_2,\ j \in \mathcal{N}_3$.
- $\mathcal{M}_5$: $a_{lj} = 0$ for $l \in \mathcal{N}_1,\ j \in \mathcal{N}_2$; $a_{lj} = 0$ for $l \in \mathcal{N}_1,\ j \in \mathcal{N}_3$; $a_{lj} = 1$ for $l \in \mathcal{N}_2,\ j \in \mathcal{N}_3$.
- $\mathcal{M}_6$: $a_{lj} = 1$ for $l \in \mathcal{N}_1,\ j \in \mathcal{N}_2$; $a_{lj} = 0$ for $l \in \mathcal{N}_1,\ j \in \mathcal{N}_3$; $a_{lj} = 0$ for $l \in \mathcal{N}_2,\ j \in \mathcal{N}_3$.
- $\mathcal{M}_7$: $a_{lj} = 0$ for $l \in \mathcal{N}_1,\ j \in \mathcal{N}_2$; $a_{lj} = 1$ for $l \in \mathcal{N}_1,\ j \in \mathcal{N}_3$; $a_{lj} = 1$ for $l \in \mathcal{N}_2,\ j \in \mathcal{N}_3$.
- $\mathcal{M}_8$: $a_{lj} = 1$ for $l \in \mathcal{N}_1,\ j \in \mathcal{N}_2$; $a_{lj} = 1$ for $l \in \mathcal{N}_1,\ j \in \mathcal{N}_3$; $a_{lj} = 1$ for $l \in \mathcal{N}_2,\ j \in \mathcal{N}_3$.

In physical terms this means that if we start with all individuals synchronized within their respective subgroups and any of the above sets of interaction gains between individuals, the individuals will remain synchronized and the interaction gains will keep the same values for all time.

We prove the time-scale reduction by rewriting the model (6.3) in the form of a singular perturbation model, decomposing it into a boundary layer (fast) model and a reduced (slow) model. We suppose that $K_1 >> 1$ and $K_2 >> 1$ and let $\epsilon = \max(\frac{1}{K_1}, \frac{1}{K_2})$ so that ϵK_1 and ϵK_2 are $O(1)$. Given these assumptions the coupled multi-agent system dynamics (6.3)

become

$$\dot{\psi}_1 = \frac{1}{N_1\rho_1}\sum_{l\in\mathcal{N}_1}\left(\sin\left(\bar{\theta}_1-\theta_l\right)+\frac{K_1}{N}\left(\sum_{n=1}^{N}a_{ln}\sin\left(\theta_n-\theta_l\right)\right)\right)\cos\left(\psi_1-\theta_l\right) \tag{6.4}$$

$$\dot{\psi}_2 = \frac{1}{N_2\rho_2}\sum_{l\in\mathcal{N}_2}\left(\sin\left(\bar{\theta}_2-\theta_l\right)+\frac{K_1}{N}\left(\sum_{n=1}^{N}a_{ln}\sin\left(\theta_n-\theta_l\right)\right)\right)\cos\left(\psi_2-\theta_l\right) \tag{6.5}$$

$$\dot{\psi}_3 = \frac{1}{N_3\rho_3}\sum_{l\in\mathcal{N}_3}\left(\frac{K_1}{N}\left(\sum_{n=1}^{N}a_{ln}\sin\left(\theta_n-\theta_l\right)\right)\right)\cos\left(\psi_3-\theta_l\right) \tag{6.6}$$

$$\begin{aligned}\epsilon\dot{\alpha}_p = {} & iN_1\alpha_p\Big(\epsilon\left(\sin\left(\bar{\theta}_1-\theta_p\right)-\rho_1\sin\left(\bar{\theta}_1-\psi_1\right)\right)\\ & +\frac{\epsilon K_1}{N}\left(\sum_{n=1}^{N}a_{pn}\sin(\theta_n-\theta_p)-\frac{1}{N_1}\sum_{l\in\mathcal{N}_1}\sum_{n=1}^{N}a_{ln}\sin(\theta_n-\theta_l)\right)\Big),\qquad p\in\mathcal{N}_1,\ p\neq p_{(1,N_1)}\end{aligned} \tag{6.7}$$

$$\begin{aligned}\epsilon\dot{\alpha}_p = {} & iN_2\alpha_p\Big(\epsilon\left(\sin\left(\bar{\theta}_2-\theta_p\right)-\rho_2\sin\left(\bar{\theta}_2-\psi_2\right)\right)\\ & +\frac{\epsilon K_1}{N}\left(\sum_{n=1}^{N}a_{pn}\sin(\theta_n-\theta_p)-\frac{1}{N_2}\sum_{l\in\mathcal{N}_2}\sum_{n=1}^{N}a_{ln}\sin(\theta_n-\theta_l)\right)\Big),\qquad p\in\mathcal{N}_2,\ p\neq p_{(2,N_2)}\end{aligned} \tag{6.8}$$

$$\epsilon\dot{\alpha}_p = iN_3\alpha_p\frac{\epsilon K_1}{N}\left(\sum_{n=1}^{N}a_{pn}\sin(\theta_n-\theta_p)-\frac{1}{N_3}\sum_{l\in\mathcal{N}_3}\sum_{n=1}^{N}a_{ln}\sin(\theta_n-\theta_l)\right),\ p\in\mathcal{N}_3,\ p\neq p_{(3,N_3)} \tag{6.9}$$

$$\epsilon\dot{a}_{lj} = \epsilon K_2(1-a_{lj})a_{lj}(\rho_{lj}-r),\qquad l\in\{1,\ldots,N\},\ j\in\{l+1,\ldots,N\}, \tag{6.10}$$

for $\rho_k\neq 0$, $k=1,2,3$.

With $\epsilon << 1$, the model (6.4)-(6.10) has the form of a singular perturbation model (as described in [54]). The $(N-3+\frac{N(N-1)}{2})$-dimensional boundary layer (fast) model is represented by (6.7) - (6.10) and the 3-dimensional reduced (slow) model is represented by (6.4) - (6.6). The reduced dynamics on the invariant manifolds $\mathcal{M}_q$, $q=1,\ldots,8$ are given by

$$\begin{aligned}\dot{\psi}_1 &= \sin\left(\bar{\theta}_1-\psi_1\right)+K_1\frac{A_{12}N_2}{N}\sin\left(\psi_2-\psi_1\right)+K_1\frac{A_{13}N_3}{N}\sin\left(\psi_3-\psi_1\right)\\ \dot{\psi}_2 &= \sin\left(\bar{\theta}_2-\psi_2\right)+K_1\frac{A_{12}N_1}{N}\sin\left(\psi_1-\psi_2\right)+K_1\frac{A_{23}N_3}{N}\sin\left(\psi_3-\psi_2\right)\\ \dot{\psi}_3 &= K_1\frac{A_{13}N_1}{N}\sin\left(\psi_1-\psi_3\right)+K_1\frac{A_{23}N_2}{N}\sin\left(\psi_2-\psi_3\right),\end{aligned} \tag{6.11}$$

where A_{12}, A_{13}, A_{23} (each equal to 0 or 1) are the values to which the interaction gains between each pair of subgroups converge after the fast time-scale. It is interesting to note that the net interconnection strengths are weighted by $\frac{N_1}{N}$, $\frac{N_2}{N}$ and $\frac{N_3}{N}$ as in Chapter 5.

To investigate the attractiveness of the manifolds $\mathcal{M}_q$, $q = 1, \ldots, 8$, we determine whether or not each $\mathcal{M}_q$ is an exponentially stable manifold of the boundary layer dynamics. We do so by evaluating the Jacobian of the boundary layer dynamics at $\boldsymbol{\psi}_0$, the stable motion of the reduced dynamics on the invariant manifold. If the yielded matrix is Hurwitz (i.e., all its eigenvalues are strictly negative), then the corresponding invariant manifold is locally stable, i.e., trajectories of the unreduced dynamics starting "near" this invariant manifold and having reduced variables "near" $\boldsymbol{\psi}_0$ remain close to the solution of the corresponding reduced dynamics. Following the calculations in Section 5.1.2, the Jacobian of the boundary layer dynamics can be proven to be an $(N - 3 + \frac{N(N-1)}{2})$ upper triangular matrix J with its diagonal terms given by

$$J_{jj} = -\frac{1}{N}\left(1 - \frac{1}{N_k}\right)\left(N_k + \sum_{l \neq k} N_l A_{kl} \cos(\psi_l - \psi_k)\right) \quad l \in \mathcal{N}_k, l \neq j_{(k,N_k)}, k = 1, 2, 3 \tag{6.12}$$

for $j \in \{1, \ldots, N-3\}$ and

$$J_{jj} = \left.\frac{\partial \dot{a}_{lp}}{\partial a_{lp}}\right|_{\mathcal{M}_q} \quad l \in \{1, \ldots, N\},\ p \in \{l+1, \ldots, N\} \tag{6.13}$$

for $j \in \{N-2, \ldots, N-3+\frac{N(N-1)}{2}\}$, where

$$\left.\frac{\partial \dot{a}_{lp}}{\partial a_{lp}}\right|_{\mathcal{M}_q} = \begin{cases} r - 1 & \text{if } l, p \in \mathcal{N}_k, k = 1, 2, 3 \\ (1 - 2A_{12})(\rho_{12} - r)|_{\mathcal{M}_q} & \text{if } l \in \mathcal{N}_1, p \in \mathcal{N}_2 \\ (1 - 2A_{13})(\rho_{13} - r)|_{\mathcal{M}_q} & \text{if } l \in \mathcal{N}_1, p \in \mathcal{N}_3 \\ (1 - 2A_{23})(\rho_{23} - r)|_{\mathcal{M}_q} & \text{if } l \in \mathcal{N}_2, p \in \mathcal{N}_3. \end{cases}$$

We note that that j is a simple index to keep count of the diagonal elements (but it's relationship to k and l is not important).

In the next two sections, we consider each of the invariant manifolds $\mathcal{M}_q$, $q = 1, \ldots, 8$ individually and determine using the linearization computed above whether they are attractive or not. For the manifolds that are attractive, we also describe the stable and unstable

equilibria of the corresponding reduced model. In Section 6.2 we summarize the conditions for each manifold to be attractive and describe the stable motions on these invariant manifolds; we then interpret the stable motions in the context of animal group motion. In Section 6.3 we present the corresponding technical analysis.

6.2 Attractiveness of the Invariant Manifolds: Results and Interpretation

As we demonstrated in the previous section, the system (6.1) has several invariant manifolds. In this section we state the conditions for each manifold to be attractive and give the stable motions on each attractive invariant manifold. We then interpret the stable equilibria in the context of group motion. The technical analysis of the stability results is presented in Section 6.3.

Without loss of generality we assume that $\bar{\theta}_1 = 0$. We also assume that the two informed subgroups are equal in numbers (i.e., $N_1 = N_2$). We first note that the reduced model (6.11) is a gradient system. The dynamics are gradient such that

$$\dot{\psi}_k = -\frac{\partial V}{\partial \psi_k}, \quad k = 1, 2, 3.$$

The potential V is given by

$$V(\psi_1, \psi_2, \psi_3) = -\cos(\psi_1) - \cos(\bar{\theta}_2 - \psi_2) + \frac{1}{2} K_1 \langle e^{i\Psi}, L e^{i\Psi} \rangle, \tag{6.14}$$

where $\Psi = (\psi_1, \psi_2, \psi_3)^T$, $e^{\Psi} = (e^{\psi_1}, e^{\psi_2}, e^{\psi_3})^T$, L is the Laplacian of the interconnecting graph between the subgroups given by

$$L = \frac{1}{N} \begin{pmatrix} A_{12}N_1 + A_{13}N_3 & -A_{12}N_1 & -A_{13}N_3 \\ -A_{12}N_1 & A_{12}N_1 + A_{23}N_3 & -A_{23}N_3 \\ -A_{13}N_1 & -A_{23}N_1 & A_{13}N_1 + A_{23}N_1 \end{pmatrix},$$

and the inner product $\langle ., . \rangle$ is defined by $\langle z_1, z_2 \rangle = \mathrm{Re}\{z_1^* z_2\}$ for $z_1, z_2 \in \mathbb{C}$, with $*$ denoting the complex conjugate. Given the gradient dynamics, all solutions converge to the set of

critical points of $V(\psi_1, \psi_2, \psi_3)$ and there are no periodic solutions. The form of the potential V given by (6.14) has been previously used in [103, 107].

Out of the eight manifolds $\mathcal{M}_1, \ldots, \mathcal{M}_8$, two are never attractive and the six others may be attractive given some assumptions on the parameters of the model. The first two invariant manifolds $\mathcal{M}_1$ and $\mathcal{M}_2$ are always unstable. The dynamics on these two manifolds, where $(A_{12}, A_{13}, A_{23}) = (1, 0, 1)$ and $(A_{12}, A_{13}, A_{23}) = (1, 1, 0)$ respectively, are symmetric; in each case the uninformed subgroup is connected to only one informed subgroup and the two informed subgroups are connected to each other.

The invariant manifold $\mathcal{M}_3$ is attractive if and only if $r, \bar{\theta}_2$ and $\psi_3(0)$ are chosen such that

$$\begin{aligned} \left|1 + e^{i\bar{\theta}_2}\right| - 2r < 0 \\ \left|1 + e^{i\psi_3(0)}\right| - 2r < 0 \\ \left|e^{i\psi_3(0)} + e^{i\bar{\theta}_2}\right| - 2r < 0. \end{aligned} \tag{6.15}$$

On this invariant manifold, the stable equilibrium is $\psi_{\mathcal{M}_3,1} = (0, \bar{\theta}_2, \psi_3(0))$. In this case, the directions in which the subgroups are heading are "different enough" that they do not "see" each other (i.e., $\rho_{ij} - r < 0$ for all $i \neq j \in 1, 2, 3$). At the steady state, each informed subgroup follows its preferred direction while the uninformed subgroup follows its initial heading. At this equilibrium, there is no information transfer between the different subgroups.

The invariant manifolds $\mathcal{M}_4$ and $\mathcal{M}_5$ are attractive if and only if the parameters r and $\bar{\theta}_2$ are chosen such that

$$\left|1 + e^{i\bar{\theta}_2}\right| - 2r < 0. \tag{6.16}$$

The dynamics on these manifolds, where $(A_{12}, A_{13}, A_{23}) = (0, 1, 0)$ and $(A_{12}, A_{13}, A_{23}) = (0, 0, 1)$, respectively, are symmetric; in each case the uninformed subgroup is connected to only one informed subgroup and the two informed subgroups are disconnected from each other. The stable equilibrium on each invariant manifold is $\psi_{\mathcal{M}_4,1} = (0, \bar{\theta}_2, 0)$ and $\psi_{\mathcal{M}_5,1} = (0, \bar{\theta}_2, \bar{\theta}_2)$, respectively. The directions in which the two informed subgroups are heading are "different enough" that they do not "see" each other (i.e., $\rho_{12} - r < 0$). Each

informed subgroup travels in its preferred direction; the uninformed subgroup follows either the first informed subgroup on $\mathcal{M}_4$ and the second informed subgroup, on $\mathcal{M}_5$.

On the invariant manifold $\mathcal{M}_6$ the dynamics of the two informed subgroups are interconnected but decoupled from the dynamics of the uninformed subgroup. The two informed subgroups behave according to the model (5.20) studied in Section 5.2, and the uninformed subgroup travels in its original heading (i.e., $\psi_3(t) = \psi_3(0)$ for $t > 0$). We can hence write an equilibrium of the system (6.22) as $(\boldsymbol{\psi}, \psi_3(0))$, where $\boldsymbol{\psi}$ is an equilibrium of the system (5.20) with the gain K in (5.20) defined as $K_1 = \frac{KN}{2N_1}$. From the analysis in Section 5.2 we know that, depending on the values of the parameters $\bar{\theta}_2$ and K_1, the reduced model (6.11) can have up to two stable motions $\boldsymbol{\psi}_{\mathcal{M}_6,1} = (\boldsymbol{\psi}_{sync1}, \psi_3(0))$ and $\boldsymbol{\psi}_{\mathcal{M}_6,2} = (\boldsymbol{\psi}_{sync2}, \psi_3(0))$.

The manifold $\mathcal{M}_6$ is attractive near the equilibrium $\boldsymbol{\psi}_{\mathcal{M}_6,1}$ if r, $\bar{\theta}_2$ and $\psi_3(0)$ are chosen such that

$$\begin{aligned} 2r - \left|1 + e^{i\bar{\theta}_2}\right| &< 0 \\ \left|1 + e^{i\psi_3(0)}\right| - 2r &< 0 \\ \left|e^{i\bar{\theta}_2} + e^{i\psi_3(0)}\right| - 2r &< 0. \end{aligned}$$

If, on the other hand, r, $\bar{\theta}_2$ and $\psi_3(0)$ are chosen such that

$$\begin{aligned} r - \sqrt{1-\alpha^2} &< 0 \\ \left|e^{i\psi_3(0)} - e^{i\left(\frac{\bar{\theta}_2}{2} + \arcsin\alpha\right)}\right| - 2r &< 0 \\ \left|ie^{i\left(\frac{\bar{\theta}_2}{2} + \arccos\alpha\right)} + e^{i\psi_3(0)}\right| - 2r &< 0, \end{aligned}$$

where $\alpha = \left(\frac{N \sin\frac{\bar{\theta}_2}{2}}{2N_1K_1}\right)^{\frac{1}{3}}$, then $\mathcal{M}_6$ is attractive near the equilibrium $\boldsymbol{\psi}_{\mathcal{M}_6,2}$. In physical terms, the conditions mean that the preferred directions of the informed subgroups are "close enough" to allow these two subgroups to "see" each other and that the heading in which the uninformed subgroup initially travels is "different enough" from both preferred directions that this subgroup does not "see" the other two. "Different" and "close enough" are quantified with the threshold r. The two sets of conditions are similar except for the

fact that the uninformed subgroup has to initially head in a direction almost opposite to the average of the two preferred directions for the first set of conditions and in a direction close to the average of the two preferred directions for the second set of conditions.

For the stable motion $\boldsymbol{\psi}_{\mathcal{M}_6,1}$, each informed subgroup compromises between its preferred direction and the average of the two preferred directions, while the uninformed subgroup travels in a direction "different enough" from that of either informed subgroup. For the stable motion $\boldsymbol{\psi}_{\mathcal{M}_6,2}$, the headings of two informed subgroups flank the heading opposite the average of the preferred directions, while the uninformed subgroup travels in a direction "different enough" from that of either informed subgroup.

The invariant manifold $\mathcal{M}_7$ is attractive if and only if the parameters r and $\bar{\theta}_2$ are chosen such that

$$\frac{1}{\sqrt{1+\nu^2}} < r < \sqrt{\frac{1}{2} + \frac{1}{2\sqrt{1+\nu^2}}},$$

where $\nu = \frac{N \sin \frac{\bar{\theta}_2}{2}}{N_3 K_1 + N \cos \frac{\bar{\theta}_2}{2}}$. On this manifold, the uninformed subgroup is connected to both informed subgroups but the two informed subgroups are not connected to each other. The equilibrium $\psi_{\mathcal{M}_7,6} = \left(\frac{\bar{\theta}_2}{2} + \arctan \nu, \frac{\bar{\theta}_2}{2} - \arctan \nu, \frac{\bar{\theta}_2}{2}\right)$ is the only stable one on this manifold. In the motion corresponding to this equilibrium, the direction of the uninformed subgroup is the average of the preferred directions of the two informed subgroups; the direction of two informed subgroups flank it. The headings of the two informed subgroups are "different enough" so that they do not "see" each other (i.e., $\rho_{12} - r < 0$). However, they are not "too different" i.e., each informed subgroup is connected to the uninformed subgroup which travels in a direction corresponding to the average of their preferred directions.

On the invariant manifold $\mathcal{M}_8$, the group is connected with an all-to-all connecting topology and the analysis from Section 5.2 can be adapted to compute the equilibria of the reduced dynamics on $\mathcal{M}_8$ and evaluate their stability. Depending on the values of the parameters $\bar{\theta}_2$ and K_1, the reduced model (6.11) can have up to two stable motions, $\boldsymbol{\psi}_{\mathcal{M}_8,8}$ and $\boldsymbol{\psi}_{\mathcal{M}_8,11}$. In the first, the informed subgroups compromise between their preferred direction and the average of the two preferred directions while the uninformed subgroup travels in the average of the preferred directions. The second is symmetrical to the first:

the informed subgroups compromise between their preferred direction and the opposite of the average of the two preferred directions while the uninformed subgroup travels in a direction opposite to the average of the preferred directions. These results are similar to the ones proven in Section 5.2. There is however a critical difference due to the presence of uninformed individuals in the group. In the case where the number of uninformed individuals exceeds a threshold given by $N_3 > 2N_1\left(1-\left(\frac{2N_1K_1}{N\sin\frac{\bar{\theta}_2}{2}}\right)^{\frac{2}{3}}\right)^{\frac{3}{2}}$, the symmetric equilibrium with the group traveling towards the opposite of the average of the preferred directions no longer exists. This observation is consistent with the analysis from Chapter 4. The manifold $\mathcal{M}_8$ is attractive near the equilibrium $\boldsymbol{\psi}_{\mathcal{M}_8,8}$ if the parameters $r, \bar{\theta}_2$ are chosen such that

$$2r - |1 + e^{i\bar{\theta}_2}| < 0.$$

In physical terms the condition means that the preferred directions of the informed subgroups are close enough to allow individuals traveling in such directions to "see" each other.

The stability of the equilibrium $\boldsymbol{\psi}_{\mathcal{M}_8,11}$ is not proven in Section 6.3 so we are unable to give conditions for the attractiveness of the manifold $\mathcal{M}_8$ near that equilibrium.

6.3 Attractiveness and Phase Space Dynamics of the Reduced Models

As we discussed in Section 6.1, the system (6.1) has several invariant manifolds, some of which are attractive under certain conditions on the parameters of the system. In this section we present the technical proof for the attractiveness of each invariant manifold. In the case where a manifold is shown to be attractive, we describe the stable and unstable equilibria of the reduced model.

6.3.1 Invariant manifolds $\mathcal{M}_1$ and $\mathcal{M}_2$, $(A_{12}, A_{13}, A_{23}) = (1, 0, 1)$ or $(1, 1, 0)$

The cases where $(A_{12}, A_{13}, A_{23}) = (1, 0, 1)$ and $(A_{12}, A_{13}, A_{23}) = (1, 1, 0)$ are symmetric, each corresponding to the uninformed subgroup being connected to only one informed sub-

group and the two informed subgroups being connected to each other. Given this symmetry we investigate the stability of the manifold for $(A_{12}, A_{13}, A_{23}) = (1, 0, 1)$ as a representative of both cases. In the case where $(A_{12}, A_{13}, A_{23}) = (1, 0, 1)$, the system (6.11) becomes

$$\begin{aligned}
\dot{\psi}_1 &= -\sin(\psi_1) + \frac{N_1}{N} K_1 \sin(\psi_2 - \psi_1) \\
\dot{\psi}_2 &= \sin\left(\bar{\theta}_2 - \psi_2\right) + \frac{N_1}{N} K_1 \sin(\psi_1 - \psi_2) + \frac{N_3}{N} K_1 \sin(\psi_3 - \psi_2) \,. \\
\dot{\psi}_3 &= \frac{N_3}{N} K_1 \sin(\psi_2 - \psi_3)
\end{aligned} \tag{6.17}$$

The equilibria of this system have to lie on one of the ψ_3-null-clines. The ψ_3-null-clines are given by $\psi_3 = \psi_2$ and $\psi_3 = \psi_2 + \pi$. We show that on either null-cline the invariant manifold $\mathcal{M}_1$ cannot be attractive. The diagonal terms of the Jacobian of the boundary layer dynamics J (6.12), (6.13) evaluated on the invariant manifold $\mathcal{M}_1$ are given by

$$J_{jj} = \begin{cases} -\frac{1}{N}\left(1 - \frac{1}{N_1}\right)(N_1 + N_1 \cos(\psi_2 - \psi_1)) & j \in \mathcal{N}_1, j \neq j_{(1,N_1)} \\ -\frac{1}{N}\left(1 - \frac{1}{N_1}\right)(N_1 + N_1 \cos(\psi_1 - \psi_2) + N_3) & j \in \mathcal{N}_2, j \neq j_{(2,N_2)} \\ -\frac{1}{N}\left(1 - \frac{1}{N_3}\right)(N_1 + N_3) & j \in \mathcal{N}_3, j \neq j_{(3,N_3)} \end{cases}$$

for $j \in \{1, \ldots, N-3\}$ and

$$J_{jj} = \left.\frac{\partial \dot{a}_{lp}}{\partial a_{lp}}\right|_{\mathcal{M}_1} \qquad l \in \{1, \ldots, N\}, p \in \{l+1, N\},$$

for $j \in \{N-2, \ldots, N-3+\frac{N(N-1)}{2}\}$ where

$$\left.\frac{\partial \dot{a}_{lj}}{\partial a_{lj}}\right|_{\mathcal{M}_1} = \begin{cases} r - 1 & \text{if } \; l, j \in \mathcal{N}_k, k = 1, 2, 3 \\ -(\rho_{12} - r) & \text{if } \; l \in \mathcal{N}_1, j \in \mathcal{N}_2 \\ (\rho_{13} - r) & \text{if } \; l \in \mathcal{N}_1, j \in \mathcal{N}_3 \\ -(\rho_{23} - r) & \text{if } \; l \in \mathcal{N}_2, j \in \mathcal{N}_3. \end{cases}$$

On the ψ_3-null-cline given by $\psi_3 = \psi_2$, $\rho_{12} = \rho_{13}$; hence it is not possible to have both $-(\rho_{12} - r) < 0$ and $(\rho_{13} - r) < 0$. On the ψ_3-null-cline given by $\psi_3 = \psi_2 + \pi$, $\rho_{23} = 0$, implying that $-(\rho_{23} - r) = r > 0$. These invariant manifolds are thus unstable for all $r \in [0, 1]$, $\bar{\theta}_2 \in [0, \pi]$.

6.3.2 Invariant Manifold $\mathcal{M}_3$, $(A_{12}, A_{13}, A_{23}) = (0, 0, 0)$

In the case where $(A_{12}, A_{13}, A_{23}) = (0, 0, 0)$, the system (6.11) becomes

$$\begin{aligned} \dot{\psi}_1 &= -\sin(\psi_1) \\ \dot{\psi}_2 &= \sin\left(\bar{\theta}_2 - \psi_2\right). \\ \dot{\psi}_3 &= 0 \end{aligned} \tag{6.18}$$

We compute the equilibria of the system (6.18) and determine the stability of each. We note that there are no dynamics for ψ_3; therefore, $\psi_3(t) = \psi_3(0)$ for all $t > 0$. The dynamics of ψ_1 and ψ_2 are decoupled and it is possible to find closed form expressions for all equilibria. Stability of each equilibrium is determined from the eigenvalues of the Jacobian. There are a total of four equilibria, given by

1. $\psi_{\mathcal{M}_3,1} = (0, \bar{\theta}_2, \psi_3(0))$, stable for $\bar{\theta}_2 \in [0, \pi]$.
2. $\psi_{\mathcal{M}_3,2} = (0, \bar{\theta}_2 + \pi, \psi_3(0))$, unstable for $\bar{\theta}_2 \in [0, \pi]$.
3. $\psi_{\mathcal{M}_3,3} = (\pi, \bar{\theta}_2, \psi_3(0))$, unstable for $\bar{\theta}_2 \in [0, \pi]$.
4. $\psi_{\mathcal{M}_3,4} = (\pi, \bar{\theta}_2 + \pi, \psi_3(0))$, unstable for $\bar{\theta}_2 \in [0, \pi]$.

The only stable equilibrium being $\psi_{\mathcal{M}_3,1} = (0, \bar{\theta}_2, \psi_3(0))$, we now determine the range of parameter values for $\bar{\theta}_2$ and r for which the invariant manifold $\mathcal{M}_3$ is attractive. The Jacobian of the boundary layer dynamics J given by equation (6.12), (6.13) evaluated on the invariant manifold $\mathcal{M}_3$ at the stable equilibrium $\psi_{\mathcal{M}_3,1} = (0, \bar{\theta}_2, \psi_3(0))$ is given by

$$J_{jj} = -\frac{N_k}{N}\left(1 - \frac{1}{N_k}\right) \qquad j \in \mathcal{N}_k, j \neq j_{(k,N_k)}, k = 1, 2, 3$$

for $j \in \{1, \ldots, N-3\}$ and

$$J_{jj} = \left.\frac{\partial \dot{a}_{lp}}{\partial a_{lp}}\right|_{\mathcal{M}_3, \psi_{\mathcal{M}_3,1}} \qquad l \in \{1, \ldots, N\}, p \in \{l+1, N\},$$

for $j \in \{N-2, \ldots, N-3+\frac{N(N-1)}{2}\}$ where

$$\left.\frac{\partial \dot{a}_{lj}}{\partial a_{lj}}\right|_{\mathcal{M}_3,\psi_{\mathcal{M}_3,1}} = \begin{cases} r-1 & \text{if } l,j \in \mathcal{N}_k, k=1,2,3 \\ (\rho_{12}-r)|_{\psi_{\mathcal{M}_3,1}} & \text{if } l \in \mathcal{N}_1, j \in \mathcal{N}_2 \\ (\rho_{13}-r)|_{\psi_{\mathcal{M}_3,1}} & \text{if } l \in \mathcal{N}_1, j \in \mathcal{N}_3 \\ (\rho_{23}-r)|_{\psi_{\mathcal{M}_3,1}} & \text{if } l \in \mathcal{N}_2, j \in \mathcal{N}_3. \end{cases}$$

Substituting in for ρ_{12}, ρ_{13}, and ρ_{23}, the invariant manifold $\mathcal{M}_3$ is attractive if and only if r, $\bar{\theta}_2$ and $\psi_3(0)$ are chosen such that

$$\begin{aligned} \left|1+e^{i\bar{\theta}_2}\right| - 2r < 0 \\ \left|1+e^{i\psi_3(0)}\right| - 2r < 0 \\ \left|e^{i\psi_3(0)}+e^{i\bar{\theta}_2}\right| - 2r < 0. \end{aligned} \tag{6.19}$$

Physically the conditions mean that the preferred directions of the informed subgroups are "different enough" from each other and that the uninformed subgroup initially travels at a heading "different enough" from both preferred directions. "Different enough" is quantified with the threshold r.

6.3.3 Invariant Manifolds $\mathcal{M}_4$ and $\mathcal{M}_5$, $(A_{12}, A_{13}, A_{23}) = (0,1,0)$ or $(0,0,1)$

The cases where $(A_{12}, A_{13}, A_{23}) = (0,1,0)$ and $(A_{12}, A_{13}, A_{23}) = (0,0,1)$ are symmetrical, each corresponding to the uninformed subgroup being connected to only one informed subgroup and the two informed subgroups being disconnected. Given this symmetry, we compute the equilibria and investigate stability only for $(A_{12}, A_{13}, A_{23}) = (0,1,0)$ as representative of both cases. In the case where $(A_{12}, A_{13}, A_{23}) = (0,1,0)$, the system (6.11) becomes

$$\begin{aligned} \dot{\psi}_1 &= -\sin(\psi_1) + K_1 \frac{N_3}{N} \sin(\psi_3 - \psi_1) \\ \dot{\psi}_2 &= \sin\left(\bar{\theta}_2 - \psi_2\right) \\ \dot{\psi}_3 &= K_1 \frac{N_1}{N} \sin(\psi_1 - \psi_3). \end{aligned} \tag{6.20}$$

We compute the equilibria of the system (6.20) and determine the stability of each. It is possible to find closed form expressions for all equilibria. The stability of each equilibrium

is determined from the eigenvalues of the Jacobian. There are a total of eight equilibria given by

1. $\psi_{\mathcal{M}_4,1} = (0, \bar{\theta}_2, 0)$, stable for $\bar{\theta}_2 \in [0, \pi], K_1 > 0$.
2. $\psi_{\mathcal{M}_4,2} = (0, \bar{\theta}_2, \pi)$, unstable for $\bar{\theta}_2 \in [0, \pi], K_1 > 0$.
3. $\psi_{\mathcal{M}_4,3} = (0, \bar{\theta}_2 + \pi, 0)$, unstable for $\bar{\theta}_2 \in [0, \pi], K_1 > 0$.
4. $\psi_{\mathcal{M}_4,4} = (0, \bar{\theta}_2 + \pi, \pi)$, unstable for $\bar{\theta}_2 \in [0, \pi], K_1 > 0$.
5. $\psi_{\mathcal{M}_4,5} = (\pi, \bar{\theta}_2, \pi)$, unstable for $\bar{\theta}_2 \in [0, \pi], K_1 > 0$.
6. $\psi_{\mathcal{M}_4,6} = (\pi, \bar{\theta}_2, 0)$, unstable for $\bar{\theta}_2 \in [0, \pi], K_1 > 0$.
7. $\psi_{\mathcal{M}_4,7} = (\pi, \bar{\theta}_2 + \pi, \pi)$, unstable for $\bar{\theta}_2 \in [0, \pi], K_1 > 0$.
8. $\psi_{\mathcal{M}_4,8} = (\pi, \bar{\theta}_2 + \pi, 0)$, unstable for $\bar{\theta}_2 \in [0, \pi], K_1 > 0$.

The only stable equilibrium being $\psi_{\mathcal{M}_4,1} = (0, \bar{\theta}_2, 0)$, we now determine the range of parameter values for $\bar{\theta}_2$ and r for which the invariant manifold $\mathcal{M}_4$ is attractive. The diagonal terms of the Jacobian of the boundary layer dynamics J (6.12) evaluated on the invariant manifold $\mathcal{M}_4$ at the stable equilibrium $\psi_{\mathcal{M}_4,1}$ is given by

$$J_{jj} = \begin{cases} -\frac{1}{N}\left(1 - \frac{1}{N_1}\right)(N_1 + N_3) & j \in \mathcal{N}_1, j \neq j_{(1,N_1)} \\ -\frac{N_1}{N}\left(1 - \frac{1}{N_1}\right) & j \in \mathcal{N}_2, j \neq j_{(2,N_2)} \\ -\frac{1}{N}\left(1 - \frac{1}{N_3}\right)(N_1 + N_3) & j \in \mathcal{N}_3, j \neq j_{(3,N_3)} \end{cases}$$

for $j \in \{1, \ldots, N-3\}$ and

$$J_{jj} = \left.\frac{\partial \dot{a}_{lj}}{\partial a_{lj}}\right|_{\mathcal{M}_4, \psi_{\mathcal{M}_4,1}} \qquad l \in \{1, \ldots, N\}, p \in \{l+1, N\},$$

for $j \in \{N-2, \ldots, N-3+\frac{N(N-1)}{2}\}$ where

$$\left.\frac{\partial \dot{a}_{lj}}{\partial a_{lj}}\right|_{\mathcal{M}_4, \psi_{\mathcal{M}_4,1}} = \begin{cases} r - 1 & \text{if } l, j \in \mathcal{N}_k, k = 1, 2, 3 \\ (\rho_{12} - r)|_{\psi_{\mathcal{M}_4,1}} & \text{if } l \in \mathcal{N}_1, j \in \mathcal{N}_2 \\ -(\rho_{13} - r)|_{\psi_{\mathcal{M}_4,1}} & \text{if } l \in \mathcal{N}_1, j \in \mathcal{N}_3 \\ (\rho_{23} - r)|_{\psi_{\mathcal{M}_4,1}} & \text{if } l \in \mathcal{N}_2, j \in \mathcal{N}_3. \end{cases}$$

The invariant manifold $\mathcal{M}_4$ is attractive if and only if r and $\bar{\theta}_2$ are chosen such that

$$\left|1 + e^{i\bar{\theta}_2}\right| - 2r < 0. \tag{6.21}$$

This means physically that the preferred directions of the informed subgroups are "different enough", given the threshold r.

6.3.4 Invariant Manifold $\mathcal{M}_6$, $(A_{12}, A_{13}, A_{23}) = (1, 0, 0)$

In the case where $(A_{12}, A_{13}, A_{23}) = (1, 0, 0)$, the system (6.11) becomes

$$\begin{aligned}
\dot{\psi}_1 &= -\sin(\psi_1) + \frac{K_1 N_1}{N}\sin(\psi_2 - \psi_1) \\
\dot{\psi}_2 &= \sin\left(\bar{\theta}_2 - \psi_2\right) + \frac{K_1 N_1}{N}\sin(\psi_1 - \psi_2) \\
\dot{\psi}_3 &= 0.
\end{aligned} \tag{6.22}$$

In this case the two informed subgroups behave according to the model (5.20) studied in Section 5.2, and the naive group travels in its original heading (i.e., $\psi_3(t) = \psi_3(0)$ for $t > 0$). The dynamics of the two informed subgroups are decoupled from the dynamics of the uninformed subgroup. We can hence write an equilibrium of the system (6.22) as $(\boldsymbol{\psi}, \psi_3(0))$, where $\boldsymbol{\psi}$ is an equilibrium of the system (5.20) with the K in (5.20) defined by $K_1 = \frac{KN}{2N_1}$. From the analysis in Section 5.2 we know that, depending on the values of the parameters $\bar{\theta}_2$ and K_1, the reduced model (6.11) can have up to two stable motions: $\boldsymbol{\psi}_{\mathcal{M}_6,1} = (\boldsymbol{\psi}_{sync1}, \psi_3(0))$ and $\boldsymbol{\psi}_{\mathcal{M}_6,2} = (\boldsymbol{\psi}_{sync2}, \psi_3(0))$. From Lemmas 5.2.2 and 5.2.5, using the re-parameterization defined above, the equilibrium $\boldsymbol{\psi}_{\mathcal{M}_6,1}$ is stable for all $\bar{\theta}_2 \in [0, \pi]$, $K_1 > 0$ whereas the equilibrium $\boldsymbol{\psi}_{\mathcal{M}_6,2}$ is stable if and only if $\bar{\theta}_2 \in [\frac{\pi}{2}, \pi]$ and $K_1 \in \left[\frac{2N}{N_1}\left(\cos\left(\frac{\bar{\theta}_2}{2}\right)^{\frac{2}{3}} + \sin\left(\frac{\bar{\theta}_2}{2}\right)^{\frac{2}{3}}\right)^{\frac{3}{2}}, \frac{4N}{N_1 \sin\theta_2}\right]$.

We now determine the ranges of parameter values for $\bar{\theta}_2$ and r for which the invariant manifold $\mathcal{M}_6$ is stable near $\boldsymbol{\psi}_{\mathcal{M}_6,1}$ and $\boldsymbol{\psi}_{\mathcal{M}_6,2}$. The diagonal terms of the Jacobian of the boundary layer dynamics J evaluated on $\mathcal{M}_6$ at $\boldsymbol{\psi}_{\mathcal{M}_6,1}$ are given by

$$J_{jj} = \begin{cases}
-\frac{1}{N}\left(1 - \frac{1}{N_1}\right)\left(N_1 + N_1\cos(\psi_2 - \psi_1)\right)\big|_{\boldsymbol{\psi}_{\mathcal{M}_6,1}} & j \in \mathcal{N}_1, j \neq j_{(1,N_1)} \\
-\frac{1}{N}\left(1 - \frac{1}{N_1}\right)\left(N_1 + N_1\cos(\psi_1 - \psi_2)\right)\big|_{\boldsymbol{\psi}_{\mathcal{M}_6,1}} & j \in \mathcal{N}_2, j \neq j_{(2,N_2)} \\
-\frac{N_3}{N}\left(1 - \frac{1}{N_3}\right) & j \in \mathcal{N}_3, j \neq j_{(3,N_3)}
\end{cases} \tag{6.23}$$

for $j \in \{1, \ldots, N-3\}$ and

$$J_{jj} = \left.\frac{\partial \dot{a}_{lj}}{\partial a_{lj}}\right|_{\mathcal{M}_6, \psi_{\mathcal{M}_6,1}} \qquad l \in \{1, \ldots, N\}, p \in \{l+1, N\}, \tag{6.24}$$

for $j \in \{N-2, \ldots, N-3+\frac{N(N-1)}{2}\}$ where

$$\left.\frac{\partial \dot{a}_{lj}}{\partial a_{lj}}\right|_{\mathcal{M}_6, \boldsymbol{\psi}_{\mathcal{M}_6,1}} = \begin{cases} r-1 & \text{if } l, j \in \mathcal{N}_k, k = 1,2,3 \\ -(\rho_{12} - r)|_{\boldsymbol{\psi}_{\mathcal{M}_6,1}} & \text{if } l \in \mathcal{N}_1, j \in \mathcal{N}_2 \\ (\rho_{13} - r)|_{\boldsymbol{\psi}_{\mathcal{M}_6,1}} & \text{if } l \in \mathcal{N}_1, j \in \mathcal{N}_3 \\ (\rho_{23} - r)|_{\boldsymbol{\psi}_{\mathcal{M}_6,1}} & \text{if } l \in \mathcal{N}_2, j \in \mathcal{N}_3. \end{cases}$$

The Jacobian of the boundary layer dynamics on the manifold $\mathcal{M}_6$, at the equilibrium $\boldsymbol{\psi}_{\mathcal{M}_6,1}$ is Hurwitz if and only if all the terms given by equation (6.23), (6.24) are strictly negative. From the analysis in Section 5.2.1 we know that for the equilibrium $\boldsymbol{\psi}_{\mathcal{M}_6,1}$, the principle value of the heading of the first and second informed subgroups are between 0 and $\frac{\bar{\theta}_2}{2}$ and between $\frac{\bar{\theta}_2}{2}$ and $\bar{\theta}_2$ respectively. Using these bounds for the heading of the informed subgroups we obtain the following set of sufficient conditions to guarantee the attractiveness of $\mathcal{M}_6$ near $\boldsymbol{\psi}_{\mathcal{M}_6,1}$:

$$\begin{aligned} 2r - \left|1 + e^{i\bar{\theta}_2}\right| &< 0 \\ \left|1 + e^{i\psi_3(0)}\right| - 2r &< 0 \\ \left|e^{i\bar{\theta}_2} + e^{i\psi_3(0)}\right| - 2r &< 0. \end{aligned}$$

In physical terms the conditions mean that the preferred directions of the informed subgroups are "close enough" and that the uninformed subgroup initially travels at a heading "different enough" from both preferred directions. "Different" and "close enough" are quantified with the threshold r.

For the attractiveness of $\mathcal{M}_6$ near $\boldsymbol{\psi}_{\mathcal{M}_6,2}$ it is also possible to give sufficient conditions that guarantee it. From Lemma 5.2.4, we have

$$\sqrt{1-\alpha^2} < \rho_{sync2} < 1,$$

where $\alpha^2 = \left(\frac{N \sin\frac{\bar{\theta}_2}{2}}{2N_1 K_1}\right)^{\frac{2}{3}}$. This means that the headings of the first and second informed subgroups are between $\frac{\bar{\theta}_2}{2} + \pi$ and $\frac{\bar{\theta}_2}{2} + \pi + \arcsin\alpha$ and between $\frac{\bar{\theta}_2 + \pi}{2} + \arccos\alpha$ and $\frac{\bar{\theta}_2}{2} + \pi$,

respectively. Using these bounds for the headings of the informed subgroups we obtain the following set of sufficient conditions to guarantee the attractiveness of $\mathcal{M}_6$ near $\boldsymbol{\psi}_{\mathcal{M}_6,2}$:

$$\begin{aligned} r - \sqrt{1-\alpha^2} &< 0 \\ \left| e^{i\psi_3(0)} - e^{i\left(\frac{\bar{\theta}_2}{2} + \arcsin\alpha\right)} \right| - 2r &< 0 \\ \left| ie^{i\left(\frac{\bar{\theta}_2+\pi}{2} + \arccos\alpha\right)} + e^{i\psi_3(0)} \right| - 2r &< 0. \end{aligned}$$

The uninformed subgroup is heading in a different enough direction from both informed subgroups that informed individuals and uninformed individuals do not "see" each other (i.e., $\rho_{13} - r < 0$ and $\rho_{23} - r < 0$).

6.3.5 Invariant Manifold $\mathcal{M}_7$, $(A_{12}, A_{13}, A_{23}) = (0, 1, 1)$

In the case where $(A_{12}, A_{13}, A_{23}) = (0, 1, 1)$, the system (6.11) becomes

$$\begin{aligned} \dot{\psi}_1 &= -\sin(\psi_1) + \frac{K_1 N_3}{N}\sin(\psi_3 - \psi_1) \\ \dot{\psi}_2 &= \sin\left(\bar{\theta}_2 - \psi_2\right) + \frac{K_1 N_3}{N}\sin(\psi_3 - \psi_2) \\ \dot{\psi}_3 &= \frac{K_1 N_1}{N}\sin(\psi_1 - \psi_3) + \frac{K_1 N_1}{N}\sin(\psi_2 - \psi_3) \end{aligned} \quad . \tag{6.25}$$

We compute the equilibria of the system (6.11) and determine the stability of each equilibria. It is possible for this system to find closed form expressions for all equilibria. The stability of each equilibrium is determined using the Routh stability criterion. There are a total of six equilibria given by

1. $\psi_{\mathcal{M}_7,1} = \left(\pi + \arcsin\gamma, \bar{\theta}_2 + \arcsin\gamma, \frac{\pi+\bar{\theta}_2}{2} + \arcsin\gamma\right)$, where $\gamma = \frac{N_3 K_1}{N}\cos\frac{\bar{\theta}_2}{2}$. This equilibrium is unstable for $\bar{\theta}_2 \in [0, \pi],\ K_1 > \frac{N}{N_3}$.

2. $\psi_{\mathcal{M}_7,2} = \left(-\arcsin\gamma, \pi + \bar{\theta}_2 - \arcsin\gamma, \frac{\pi+\bar{\theta}_2}{2} - \arcsin\gamma\right)$, unstable for $\bar{\theta}_2 \in [0, \pi],\ K_1 > 0$.

3. $\psi_{\mathcal{M}_7,3} = \left(\frac{\pi+\bar{\theta}_2}{2}, \frac{\bar{\theta}_2-\pi}{2}, \frac{\bar{\theta}_2}{2} + \arccos\left(-\frac{N}{K_1 N_3}\cos\frac{\bar{\theta}_2}{2}\right)\right)$, unstable for $\bar{\theta}_2 \in [0, \pi],\ K_1 > 0$.

4. $\psi_{\mathcal{M}_7,4} = \left(\frac{\pi+\bar{\theta}_2}{2}, \frac{\bar{\theta}_2-\pi}{2}, \frac{\bar{\theta}_2}{2} - \arccos\left(-\frac{N}{K_1 N_3}\cos\frac{\bar{\theta}_2}{2}\right)\right)$, unstable for $\bar{\theta}_2 \in [0, \pi],\ K_1 > 0$.

5. $\psi_{\mathcal{M}_7,5} = \left(\frac{\bar{\theta}_2}{2} + \pi + \arctan\nu, \frac{\bar{\theta}_2}{2} + \pi - \arctan\nu, \frac{\bar{\theta}_2}{2}\right)$, where $\nu = \frac{N\sin\frac{\bar{\theta}_2}{2}}{N_3K_1 + N\cos\frac{\bar{\theta}_2}{2}}$. This equilibrium is unstable for $\bar{\theta}_2 \in [0,\pi],\ K_1 > \frac{N}{N_3}$.

6. $\psi_{\mathcal{M}_7,6} = \left(\frac{\bar{\theta}_2}{2} + \arctan\nu, \frac{\bar{\theta}_2}{2} - \arctan\nu, \frac{\bar{\theta}_2}{2}\right)$, stable for $\bar{\theta}_2 \in [0,\pi],\ K_1 > \frac{N}{N_3}$.

We now determine the ranges of parameter values for $\bar{\theta}_2$ and r for which the invariant manifold $\mathcal{M}_7$ is stable near $\boldsymbol{\psi}_{\mathcal{M}_7,6}$. The diagonal terms of the Jacobian of the boundary layer dynamics J evaluated on $\mathcal{M}_7$ at $\boldsymbol{\psi}_{\mathcal{M}_7,6}$ are given by

$$J_{jj} = \begin{cases} -\frac{1}{N}\left(1 - \frac{1}{N_1}\right)\left(N_1 + N_3\cos(\psi_3 - \psi_1)\right)|_{\boldsymbol{\psi}_{\mathcal{M}_7,6}} & j \in \mathcal{N}_1, j \neq j_{(1,N_1)} \\ -\frac{1}{N}\left(1 - \frac{1}{N_1}\right)\left(N_1 + N_3\cos(\psi_3 - \psi_2)\right)|_{\boldsymbol{\psi}_{\mathcal{M}_7,6}} & j \in \mathcal{N}_2, j \neq j_{(2,N_2)} \\ -\frac{1}{N}\left(1 - \frac{1}{N_3}\right)\left(N_3 + N_1\cos(\psi_1 - \psi_3) + N_1\cos(\psi_2 - \psi_3)\right)|_{\boldsymbol{\psi}_{\mathcal{M}_7,6}} & j \in \mathcal{N}_3, j \neq j_{(3,N_3)} \end{cases}$$

for $j \in \{1,\ldots,N-3\}$ and

$$J_{jj} = \left.\frac{\partial \dot{a}_{lj}}{\partial a_{lj}}\right|_{\mathcal{M}_7,\boldsymbol{\psi}_{\mathcal{M}_7,6}} \qquad l \in \{1,\ldots,N\}, p \in \{l+1, N\},$$

for $j \in \{N-2,\ldots,N-3+\frac{N(N-1)}{2}\}$ where

$$\left.\frac{\partial \dot{a}_{lj}}{\partial a_{lj}}\right|_{\mathcal{M}_7,\boldsymbol{\psi}_{\mathcal{M}_7,6}} = \begin{cases} r-1 & \text{if } l,j \in \mathcal{N}_k, k = 1,2,3 \\ (\rho_{12} - r)|_{\boldsymbol{\psi}_{\mathcal{M}_7,6}} & \text{if } l \in \mathcal{N}_1, j \in \mathcal{N}_2 \\ -(\rho_{13} - r)|_{\boldsymbol{\psi}_{\mathcal{M}_7,6}} & \text{if } l \in \mathcal{N}_1, j \in \mathcal{N}_3 \\ -(\rho_{23} - r)|_{\boldsymbol{\psi}_{\mathcal{M}_7,6}} & \text{if } l \in \mathcal{N}_2, j \in \mathcal{N}_3. \end{cases}$$

Using the expressions of the phases ψ_1, ψ_2 and ψ_3 at the equilibrium $\boldsymbol{\psi}_{\mathcal{M}_7,6}$ we obtain the following necessary and sufficient condition for the invariant manifold $\mathcal{M}_7$ to be attractive near $\boldsymbol{\psi}_{\mathcal{M}_7,6}$:

$$\frac{1}{\sqrt{1+\nu^2}} < r < \sqrt{\frac{1}{2} + \frac{1}{2\sqrt{1+\nu^2}}}. \tag{6.26}$$

In this case, the uninformed subgroup is heading in a "close enough" direction from both informed subgroup that informed individuals and uninformed individuals "see" each other. The two informed subgroups, however, are heading in "different enough" directions that they do not "see" each other, although they are indirectly interacting with each other through the uninformed subgroup.

6.3.6 Invariant Manifold $\mathcal{M}_8$, $(A_{12}, A_{13}, A_{23}) = (1, 1, 1)$

In the case where $(A_{12}, A_{13}, A_{23}) = (1, 1, 1)$, the system (6.11) becomes

$$\begin{aligned}
\dot{\psi}_1 &= -\sin(\psi_1) + \frac{K_1 N_1}{N}\sin(\psi_2 - \psi_1) + \frac{K_1 N_3}{N}\sin(\psi_3 - \psi_1) \\
\dot{\psi}_2 &= \sin\left(\bar{\theta}_2 - \psi_2\right) + \frac{K_1 N_1}{N}\sin(\psi_1 - \psi_2) + \frac{K_1 N_3}{N}\sin(\psi_3 - \psi_2)\,. \\
\dot{\psi}_3 &= \frac{K_1 N_1}{N}\sin(\psi_1 - \psi_3) + \frac{K_1 N_1}{N}\sin(\psi_2 - \psi_3)
\end{aligned} \tag{6.27}$$

We compute the equilibria of the system (6.27) but note that, except for specific values of the parameters $K_1, \bar{\theta}_2$, we cannot find closed form expressions for all of them. For each equilibrium we nevertheless describe how its value and stability changes as the bifurcation parameters $K, \bar{\theta}_2$ vary. The equilibria are given by

$$\begin{aligned}
-\sin(\psi_1) + \frac{K_1 N_1}{N}\sin(\psi_2 - \psi_1) + \frac{K_1 N_3}{N}\sin(\psi_3 - \psi_1) &= 0 \\
\sin\left(\bar{\theta}_2 - \psi_2\right) + \frac{K_1 N_1}{N}\sin(\psi_1 - \psi_2) + \frac{K_1 N_3}{N}\sin(\psi_3 - \psi_2) &= 0 \\
\frac{K_1 N_1}{N}\sin(\psi_1 - \psi_3) + \frac{K_1 N_1}{N}\sin(\psi_2 - \psi_3) &= 0.
\end{aligned}$$

There are three sets of solutions, the first set given by

$$\begin{aligned}
\psi_1 &= \frac{\bar{\theta}_2 - \pi}{2} \\
\psi_2 &= \frac{\bar{\theta}_2 + \pi}{2} \\
\cos\left(\psi_3 - \frac{\bar{\theta}_2}{2}\right) &= -\frac{N}{K_1 N_3}\cos\frac{\bar{\theta}_2}{2},
\end{aligned} \tag{6.28}$$

the second set given by

$$\psi_1 = \pi - \bar{\theta}_2 + \psi_2 \tag{6.29}$$

$$\sin\left(\psi_2 - \bar{\theta}_2\right) = \frac{K_1 N_1}{N}\sin\bar{\theta}_2 + \frac{K_1 N_3}{N}\cos\frac{\bar{\theta}_2}{2} \tag{6.30}$$

$$\psi_3 = \frac{\psi_1 + \psi_2}{2}, \tag{6.31}$$

and the third set given by

$$\psi_1 = \bar{\theta}_2 - \psi_2 \tag{6.32}$$

$$\sin\left(\bar{\theta}_2 - \psi_2\right) + \frac{K_1 N_1}{N}\sin\left(\bar{\theta}_2 - 2\psi_2\right) = \frac{K_1 N_3}{N}\sin\left(\frac{\bar{\theta}_2}{2} - \psi_2\right) \tag{6.33}$$

$$\psi_3 = \frac{\psi_1 + \psi_2}{2}. \tag{6.34}$$

In the first set of solutions, we can find a closed form expression of each equilibrium. Equation (6.28) has two solutions $\psi_3 = \frac{\bar{\theta}_2}{2} + \pi \pm \arccos\left(\frac{N}{K_1 N_3}\cos\frac{\bar{\theta}_2}{2}\right)$. These two solutions exist if and only if $\left|\frac{N}{K_1 N_3}\cos\frac{\bar{\theta}_2}{2}\right| \leq 1$.

Lemma 6.3.1 *If* $\left|\frac{N}{K_1 N_3}\cos\frac{\bar{\theta}_2}{2}\right| \leq 1$*, then the two equilibria* $\boldsymbol{\psi}_{\mathcal{M}_8,1}$ *and* $\boldsymbol{\psi}_{\mathcal{M}_8,2}$ *satisfying (6.28) and given by*

$$\boldsymbol{\psi}_{\mathcal{M}_8,1} = \left(\frac{\bar{\theta}_2 - \pi}{2}, \frac{\bar{\theta}_2 + \pi}{2}, \frac{\bar{\theta}_2}{2} + \pi + \arccos\left(\frac{N}{K_1 N_3}\cos\frac{\bar{\theta}_2}{2}\right)\right) \tag{6.35}$$

$$\boldsymbol{\psi}_{\mathcal{M}_8,2} = \left(\frac{\bar{\theta}_2 - \pi}{2}, \frac{\bar{\theta}_2 + \pi}{2}, \frac{\bar{\theta}_2}{2} + \pi - \arccos\left(\frac{N}{K_1 N_3}\cos\frac{\bar{\theta}_2}{2}\right)\right), \tag{6.36}$$

are unstable $\forall K_1 > min(\frac{N\sin\frac{\bar{\theta}_2}{2}}{N_1}, \frac{N}{N_3}\sqrt{\frac{1+\cos\bar{\theta}_2}{2}})$.

Proof: The proof of Lemma 6.3.1 can be found in Appendix B.

In the second set of solutions, it is also possible to find a closed form expression for each equilibrium. Equation (6.30) has two solutions $\psi_2 = \bar{\theta}_2 + \arcsin\left(\frac{K_1 N_1}{N}\sin\bar{\theta}_2 + \frac{K_1 N_3}{N}\cos\frac{\bar{\theta}_2}{2}\right)$ or $\psi_2 = \bar{\theta}_2 + \pi - \arcsin\left(\frac{K_1 N_1}{N}\sin\bar{\theta}_2 + \frac{K_1 N_3}{N}\cos\frac{\bar{\theta}_2}{2}\right)$ yielding a total of four equilibria. These four equilibria exist if and only if $\left|\frac{K_1 N_1}{N}\sin\bar{\theta}_2 + \frac{K_1 N_3}{N}\cos\frac{\bar{\theta}_2}{2}\right| \leq 1$. For each value of $\bar{\theta}_2$, there is a range of values for K_1 for which these equilibria exist. As $\bar{\theta}_2$ approaches π the range of values of K_1 for which these equilibria exist becomes larger. We consider here the case where these equilibria do not exist i.e., $K_1 > \frac{N}{N_1\sin\bar{\theta}_2 + N_3\cos\frac{\bar{\theta}_2}{2}}$. We note that for the simulation presented in Figure 6.2, the choice of parameters we made satisfy the conditions for these equilibria to exist, but with the chosen initial conditions, the system does not converge to any of these four equilibria.

For the equilibria in the third set of solutions given by (6.32) - (6.34) we make the same change of variables as in Chapter 5, equation (5.26), $(\psi_1, \psi_2) \mapsto \left(\hat{\rho}, \hat{\Psi}\right)$ where $\hat{\rho} \in [0,1]$ and $\hat{\Psi} \in S^1$ are defined by

$$\hat{\rho}e^{i\hat{\Psi}} = \frac{1}{2}\left(e^{i\psi_1} + e^{i\psi_2}\right) = \cos\left(\frac{\psi_1 - \psi_2}{2}\right)e^{i(\psi_1+\psi_2)/2} \tag{6.37}$$

$$= \cos\left(\frac{\bar{\theta}_2}{2} - \psi_2\right)\left(\cos\frac{\bar{\theta}_2}{2} + i\sin\frac{\bar{\theta}_2}{2}\right). \tag{6.38}$$

Equation (6.38) is obtained by using equation (6.32) in (6.37). For $\bar{\theta}_2 \in (0,\pi]$, $\psi_1 = \bar{\theta}_2 - \psi_2$ implies that $\hat{\Psi} = \frac{\bar{\theta}_2}{2}$ or $\hat{\Psi} = \frac{\bar{\theta}_2}{2} + \pi$. An equilibrium of the system (6.27) can hence be written as $(\hat{\rho}, \hat{\boldsymbol{\psi}}, \psi_3^*)$, where ψ_3^* is the solution obtained from equation (6.34). We further rewrite (6.33) as

$$\left(\sin\frac{\bar{\theta}_2}{2} + \frac{2K_1N_1}{N}\sin\left(\frac{\bar{\theta}_2}{2} - \psi_2\right)\right)\cos\left(\frac{\bar{\theta}_2}{2} - \psi_2\right) + \left(\cos\frac{\bar{\theta}_2}{2} + \frac{K_1N_3}{N}\right)\sin\left(\frac{\bar{\theta}_2}{2} - \psi_2\right) = 0. \tag{6.39}$$

For $\hat{\Psi} = \frac{\bar{\theta}_2}{2}$, (6.38) implies that $\cos\left(\frac{\bar{\theta}_2}{2} - \psi_2\right) = \hat{\rho}$ and $\sin\left(\frac{\bar{\theta}_2}{2} - \psi_2\right) = \pm\sqrt{1-\hat{\rho}^2}$. Accordingly, (6.39) implies that $\hat{\rho}$ satisfies

$$\hat{\rho}\sin\frac{\bar{\theta}_2}{2} + \sqrt{1-\hat{\rho}^2}\left(\cos\frac{\bar{\theta}_2}{2} + \frac{K_1N_3}{N}\right) + \frac{2K_1N_1}{N}\hat{\rho}\sqrt{1-\hat{\rho}^2} = 0 \tag{6.40}$$

or

$$\hat{\rho}\sin\frac{\bar{\theta}_2}{2} - \sqrt{1-\hat{\rho}^2}\left(\cos\frac{\bar{\theta}_2}{2} + \frac{K_1N_3}{N}\right) - \frac{2K_1N_1}{N}\hat{\rho}\sqrt{1-\hat{\rho}^2} = 0. \tag{6.41}$$

For $\hat{\Psi} = \frac{\bar{\theta}_2}{2} + \pi$, (6.38) implies that $\cos\left(\frac{\bar{\theta}_2}{2} - \psi_2\right) = -\hat{\rho}$ and $\sin\left(\frac{\bar{\theta}_2}{2} - \psi_2\right) = \pm\sqrt{1-\hat{\rho}^2}$. Accordingly, (6.39) implies that $\hat{\rho}$ satisfies

$$-\hat{\rho}\sin\frac{\bar{\theta}_2}{2} + \sqrt{1-\hat{\rho}^2}\left(\cos\frac{\bar{\theta}_2}{2} + \frac{K_1N_3}{N}\right) - \frac{2K_1N_1}{N}\hat{\rho}\sqrt{1-\hat{\rho}^2} = 0 \tag{6.42}$$

or

$$-\hat{\rho}\sin\frac{\bar{\theta}_2}{2} - \sqrt{1-\hat{\rho}^2}\left(\cos\frac{\bar{\theta}_2}{2} + \frac{K_1N_3}{N}\right) + \frac{2K_1N_1}{N}\hat{\rho}\sqrt{1-\hat{\rho}^2} = 0. \tag{6.43}$$

We now consider equations (6.40)-(6.43) individually and determine the existence and nature of the equilibria that they yield.

Equation (6.40) does not have any solution for $(\hat{\rho}, \bar{\theta}_2) \in [0,1] \times (0,\pi)$ since all of the terms on the left hand side of the equation are strictly positive.

Equation (6.41) has one solution for $(\hat{\rho}, \bar{\theta}_2) \in [0,1] \times (0,\pi)$; we call this solution $\hat{\rho}_{sync1}$. It yields two equilibria $\boldsymbol{\psi}_{\mathcal{M}_8,7} = (\hat{\rho}_{sync1}, \frac{\bar{\theta}_2}{2}, \frac{\bar{\theta}_2}{2})$ and $\boldsymbol{\psi}_{\mathcal{M}_8,8} = (\hat{\rho}_{sync1}, \frac{\bar{\theta}_2}{2}, \frac{\bar{\theta}_2}{2} + \pi)$. For large values of K_1 in both equilibria, the two informed subgroups become synchronized, with synchronization occurring at $\hat{\Psi} = \frac{\bar{\theta}_2}{2}$. The uninformed subgroup is heading in the average of the preferred directions $\frac{\bar{\theta}_2}{2}$ for the equilibrium $\boldsymbol{\psi}_{\mathcal{M}_8,7}$ and in an opposite direction for $\boldsymbol{\psi}_{\mathcal{M}_8,8}$.

Lemma 6.3.2 *The equilibrium $\boldsymbol{\psi}_{\mathcal{M}_8,7}$ is stable for all $\left(K, \bar{\theta}_2\right) \in [0,\infty) \times (0,\pi)$.*

Proof: The proof of Lemma 6.3.2 can be found in Appendix B.

Lemma 6.3.3 *The equilibrium $\boldsymbol{\psi}_{\mathcal{M}_8,8}$ is unstable for all $\left(K, \bar{\theta}_2\right) \in [0,\infty) \times (0,\pi)$.*

Proof: The proof of Lemma 6.3.3 can be found in Appendix B.

Equation (6.42) has one solution for $(\hat{\rho}, \bar{\theta}_2) \in [0,1] \times (0,\pi)$; we call this solution $\hat{\rho}_{antisync1}$. It yields two equilibria $\boldsymbol{\psi}_{\mathcal{M}_8,9} = (\hat{\rho}_{antisync1}, \frac{\bar{\theta}_2}{2}, \frac{\bar{\theta}_2}{2})$ and $\boldsymbol{\psi}_{\mathcal{M}_8,10} = (\hat{\rho}_{antisync1}, \frac{\bar{\theta}_2}{2}, \frac{\bar{\theta}_2}{2} + \pi)$. For large values of K_1 in both equilibria, the two informed subgroups become anti-synchronized. The uninformed subgroup is heading in the average of the preferred directions $\frac{\bar{\theta}_2}{2}$ for the equilibrium $\boldsymbol{\psi}_{\mathcal{M}_8,9}$ and in an opposite direction for $\boldsymbol{\psi}_{\mathcal{M}_8,10}$.

Lemma 6.3.4 *The equilibria $\boldsymbol{\psi}_{\mathcal{M}_8,9}$ and $\boldsymbol{\psi}_{\mathcal{M}_8,10}$ are unstable for all $\left(K, \bar{\theta}_2\right) \in [0,\infty) \times (0,\pi)$.*

Proof: The proof of Lemma 6.3.4 can be found in Appendix B.

Equation (6.43) has between zero and two solutions for $(\hat{\rho}, \bar{\theta}_2) \in [0,1] \times (0,\pi)$. The two solutions, when they exist, are called $\hat{\rho}_{sync2}$ and $\hat{\rho}_{antisync2}$. They yield four equilibria $\boldsymbol{\psi}_{\mathcal{M}_8,11} = (\hat{\rho}_{sync2}, \frac{\bar{\theta}_2}{2}, \frac{\bar{\theta}_2}{2})$, $\boldsymbol{\psi}_{\mathcal{M}_8,12} = (\hat{\rho}_{sync2}, \frac{\bar{\theta}_2}{2}, \frac{\bar{\theta}_2}{2} + \pi)$, $\boldsymbol{\psi}_{\mathcal{M}_8,13} = (\hat{\rho}_{antisync2}, \frac{\bar{\theta}_2}{2} + \pi, \frac{\bar{\theta}_2}{2})$ and $\boldsymbol{\psi}_{\mathcal{M}_8,14} = (\hat{\rho}_{antisync2}, \frac{\bar{\theta}_2}{2} + \pi, \frac{\bar{\theta}_2}{2} + \pi)$. For large values of K_1 in the two equilibria $\boldsymbol{\psi}_{\mathcal{M}_8,11}$ and $\boldsymbol{\psi}_{\mathcal{M}_8,12}$, the two informed subgroups become synchronized, with synchronization occurring at $\hat{\Psi} = \frac{\bar{\theta}_2}{2} + \pi$. The uninformed subgroup is heading in the average of the preferred

directions $\frac{\bar{\theta}_2}{2}$ for the equilibrium $\boldsymbol{\psi}_{\mathcal{M}_8,11}$ and in an opposite direction for $\boldsymbol{\psi}_{\mathcal{M}_8,12}$. For the two equilibria $\boldsymbol{\psi}_{\mathcal{M}_8,13}$ and $\boldsymbol{\psi}_{\mathcal{M}_8,14}$, the two informed subgroups become anti-synchronized. The uninformed subgroup is heading in the average of the preferred directions $\frac{\bar{\theta}_2}{2}$ for the equilibrium $\boldsymbol{\psi}_{\mathcal{M}_8,13}$ and in an opposite direction for $\boldsymbol{\psi}_{\mathcal{M}_8,14}$.

Lemma 6.3.5 *Equation (6.43) has two solutions when* $(2N_1K_1)^{\frac{2}{3}} - (N\sin\frac{\bar{\theta}_2}{2})^{\frac{2}{3}} > (N_3K_1 - N\cos\frac{\bar{\theta}_2}{2})^{\frac{2}{3}}$. *If* $N_3 > 2N_1\left(1-\left(\frac{2N_1K_1}{N\sin\frac{\bar{\theta}_2}{2}}\right)^{\frac{2}{3}}\right)^{\frac{3}{2}}$, *then equation (6.43) has no solutions* $\forall$ $K_1, N_1, \bar{\theta}_2 \in [0,\infty)^2 \times (0,\pi]$.

Proof: Let $K' = \frac{2N_1K_1}{N\sin\frac{\bar{\theta}_2}{2}}$ which is well defined for $\bar{\theta}_2 \in (0,\pi]$. Equation (6.43) can be rewritten as

$$\hat{\rho}\left(\frac{1}{\sqrt{1-\hat{\rho}^2}} - K'\right) + \frac{N_3}{2N_1}K' = -\cot\frac{\bar{\theta}_2}{2}. \tag{6.44}$$

The solutions of (6.43) exist when the function $h(\hat{\rho}) = \hat{\rho}(\frac{1}{\sqrt{1-\hat{\rho}^2}} - K') + \frac{N_3}{2N_1}K'$ intersects the constant $y = -\cot\frac{\bar{\theta}_2}{2} < 0$. The function $h(\hat{\rho})$ goes to $\frac{N_3K'}{2N_1}$ when $\hat{\rho} \mapsto 0$, approaches $+\infty$ when $\hat{\rho} \mapsto 1$, and reaches its minimum of $-K'(\hat{\rho}^*)^3 + \frac{N_3K'}{2N_1}$ at $\hat{\rho}^* = \sqrt{1-\frac{1}{K'^{2/3}}}$. Equation (6.43) has two solutions $(\hat{\rho}_1, \hat{\rho}_2)$ flanking $\hat{\rho}^*$ if and only if $h(\hat{\rho}^*) < -\cot\frac{\bar{\theta}_2}{2}$; this last inequality is satisfied if and only if

$$(2N_1K_1)^{\frac{2}{3}} - (N\sin\frac{\bar{\theta}_2}{2})^{\frac{2}{3}} > (N_3K_1 - N\cos\frac{\bar{\theta}_2}{2})^{\frac{2}{3}}. \tag{6.45}$$

If $N_3 > 2N_1\left(1-\left(\frac{2N_1K_1}{N\sin\frac{\bar{\theta}_2}{2}}\right)^{\frac{2}{3}}\right)^{\frac{3}{2}}$, then $h(\hat{\rho}) > 0$ $\forall \hat{\rho} \in [0,1]$ and equation (6.43) has no solution $\forall$ $K_1, N_1, \bar{\theta}_2 \in [0,\infty)^2 \times (0,\pi]$. $\square$

We do not prove here the stability of these equilibria but given the analyses from Chapter 5, it is natural to conjecture that the equilibria $\boldsymbol{\psi}_{\mathcal{M}_8,12}$, $\boldsymbol{\psi}_{\mathcal{M}_8,13}$ and $\boldsymbol{\psi}_{\mathcal{M}_8,14}$ are always unstable and that for large enough values of $\bar{\theta}_2$ there exists a range of values for K_1 such that the equilibrium $\boldsymbol{\psi}_{\mathcal{M}_8,11}$ is stable.

We now determine the ranges of parameter values for $\bar{\theta}_2$ and r for which the invariant manifold $\mathcal{M}_8$ is attractive near $\boldsymbol{\psi}_{\mathcal{M}_8,7}$. The diagonal terms of the Jacobian of the boundary

layer dynamics J evaluated on $\mathcal{M}_8$ at $\boldsymbol{\psi}_{\mathcal{M}_8,7}$ are given by

$$J_{jj} = \begin{cases} -\frac{1}{N}\left(1-\frac{1}{N_1}\right)\left(N_1 + N_1\cos(\psi_2-\psi_1) + N_3\cos(\psi_3-\psi_1)\right)|_{\boldsymbol{\psi}_{\mathcal{M}_8,7}} & j \in \mathcal{N}_1, j \neq j_{(1,N_1)} \\ -\frac{1}{N}\left(1-\frac{1}{N_1}\right)\left(N_1 + N_1\cos(\psi_1-\psi_2) + N_3\cos(\psi_3-\psi_2)\right)|_{\boldsymbol{\psi}_{\mathcal{M}_8,7}} & j \in \mathcal{N}_2, j \neq j_{(2,N_2)} \\ -\frac{1}{N}\left(1-\frac{1}{N_3}\right)\left(N_3 + N_1\cos(\psi_1-\psi_3) + N_1\cos(\psi_2-\psi_3)\right)|_{\boldsymbol{\psi}_{\mathcal{M}_8,7}} & j \in \mathcal{N}_3, j \neq j_{(3,N_3)} \end{cases}$$

for $j \in \{1, \ldots, N-3\}$ and

$$J_{jj} = \left.\frac{\partial \dot{a}_{lj}}{\partial a_{lj}}\right|_{\mathcal{M}_8, \boldsymbol{\psi}_{\mathcal{M}_8,7}} \qquad l \in \{1,\ldots,N\}, p \in \{l+1, N\},$$

for $j \in \{N-2, \ldots, N-3+\frac{N(N-1)}{2}\}$ where

$$\left.\frac{\partial \dot{a}_{lj}}{\partial a_{lj}}\right|_{\mathcal{M}_8, \boldsymbol{\psi}_{\mathcal{M}_8,7}} = \begin{cases} r-1 & \text{if } l,j \in \mathcal{N}_k, k = 1,2,3 \\ -\left(\rho_{12} - r\right)|_{\boldsymbol{\psi}_{\mathcal{M}_8,7}} & \text{if } l \in \mathcal{N}_1, j \in \mathcal{N}_2 \\ -\left(\rho_{13} - r\right)|_{\boldsymbol{\psi}_{\mathcal{M}_8,7}} & \text{if } l \in \mathcal{N}_1, j \in \mathcal{N}_3 \\ -\left(\rho_{23} - r\right)|_{\boldsymbol{\psi}_{\mathcal{M}_8,7}} & \text{if } l \in \mathcal{N}_2, j \in \mathcal{N}_3. \end{cases}$$

From the analysis in Section 5.2, we know that for the equilibrium $\boldsymbol{\psi}_{\mathcal{M}_7,6}$, the principal values of the headings of the first and second informed subgroups are respectively, between 0 and $\frac{\bar{\theta}_2}{2}$ and between $\frac{\bar{\theta}_2}{2}$ and $\bar{\theta}_2$. Given these bounds, the worst case scenario to satisfy the stability criterium is when $\psi_1 = 0$ and $\psi_2 = \bar{\theta}_2$, yielding the following sufficient condition to guarantee the attractiveness of $\mathcal{M}_8$ near $\boldsymbol{\psi}_{\mathcal{M}_8,7}$:

$$2r - \left|1 + e^{i\bar{\theta}_2}\right| < 0.$$

In physical terms, the condition means that the preferred directions of the two informed subgroups are "close enough" given the threshold r that the interaction gain between two individuals, one heading in the preferred direction of the first informed subgroup and the other heading in the preferred direction of the second informed subgroup, would increase given the dynamics (6.2).

6.4 Summary and Forgetting Factor Feedback Extension

6.4.1 Summary

In this chapter we have extended the model (5.1) of the dynamics of motion for a group of $N = N_1 + N_2 + N_3$ coupled individuals moving in the plane by relaxing the all-to-all coupling assumption made in Chapter 5 and including uninformed individuals in the analysis. We described eight invariant manifolds of the system and determined which ones could be attractive and which ones could not. For each attractive manifold, we described the stable and unstable equilibria of the corresponding reduced model and interpreted the stable equilibria in the context of animal group motion. We proved that relaxing the all-to-all connecting topology assumption yields a much richer behavior. Depending on the values of the parameters $\bar{\theta}_2$, r and K_1, eight different group motions can occur.

We first observed an equilibrium similar to the persistent stable motion $\boldsymbol{\psi}_{sync1}$ observed in Chapter 5 where the two informed subgroups compromise between their preferred direction and the average of the preferred direction. We proved in this present chapter that the equilibrium $\boldsymbol{\psi}_{\mathcal{M}_{8,7}}$ is stable for all values of the parameters $K_1, \bar{\theta}_2$. This equilibrium is a K_1-almost synchronized motion of the group in the direction $\frac{\bar{\theta}_2}{2}$. For moderate values of K_1, the two informed subgroups compromise between their preferred direction and the average of the preferred directions while the uninformed subgroup travels in a direction corresponding to the average of the preferred directions. For large values of K_1, this equilibrium corresponds to the whole group moving together in the average of the preferred directions. We also showed that similar motion could be obtained in the invariant manifolds $\mathcal{M}_6$ and $\mathcal{M}_7$. On the invariant manifold $\mathcal{M}_6$, the two informed subgroups behave exactly according to the model (5.1) studied in Section 5.2. In this case, the two informed subgroups compromise between their preferred direction and the average of the preferred directions while the uninformed subgroup travels in its original heading. On the invariant manifold $\mathcal{M}_7$, the two informed subgroups also compromise between their preferred direction and the average of the preferred directions and the uninformed subgroup travels in the average of

the preferred directions. In this case, however, the two informed subgroups are not directly connected to each other (i.e., $A_{12} = 0$); rather they are connected indirectly through their mutual connection to the uninformed subgroup.

In contrast to the model (5.1), where informed individuals always compromise on their preferred directions, we showed that with the model (6.1) it is possible to have informed individuals travel exactly in their preferred direction. We observed this for three invariant manifolds, $\mathcal{M}_3, \mathcal{M}_4$ and $\mathcal{M}_5$. In each case, the two informed subgroups become disconnected from each other and follow their respective preferred directions. On the manifold $\mathcal{M}_3$ the stable motion corresponds to each informed subgroup traveling in its preferred direction and the uninformed subgroup traveling in its initial heading. For the manifolds $\mathcal{M}_4$ and $\mathcal{M}_5$, each informed subgroup travels in its preferred direction with the uninformed subgroup following the first informed subgroup for $\mathcal{M}_4$ and the second informed subgroup for $\mathcal{M}_5$.

We also noted that when the number of uninformed individuals in the group exceeds a certain threshold, the inefficient motion $\psi_{\mathcal{M}_8,11}$, where the group heads in a direction as divergent as possible from both preferred directions, disappears. This observation is consistent with the analysis from Chapter 4, where using the discrete-time model from [19], we argued that under certain circumstances, informed individuals derive a benefit in associating with uninformed individuals.

However, as with the continuous-time model presented in the previous chapter, the continuous-time model presented here does not reproduce the behavior we observed both in [19] and in Chapter 4, where the group collectively selects one of the preferred directions. As we explained above, informed individuals can follow their preferred direction only if they are not connected to individuals of the other informed subgroup (i.e., $A_{12} = 0$). Moreover, full synchronization of the group cannot occur unless the coupling gain K_1 is very large. This means that, for relatively small weight on the coupling in the model, the individuals in the population do not fully aggregate and the group splits - although in some cases we showed that the uninformed individuals do become synchronized with one or the other of the informed subgroups. This deviation indirectly reveals the importance of a remaining

simplifying assumption, namely, that we consider only the dynamics of the phases and not the complete spatial dynamics of the individuals in the group. For the simulations used in [19] and in Chapter 4, we observed that in the case where the group collectively selects one of the preferred directions, the leading informed subgroup travels in front, followed by the uninformed subgroups, followed in turn by the other informed subgroup. With the uninformed subgroup in between the two informed subgroups, the distance between the informed individuals of the two subgroups could in some circumstances be large enough that they would not interact with each other although travel in the same direction. As we have mentioned earlier, our phase model requires that individuals traveling in the same direction be connected.

With a model that only considers the phase dynamics, however, it is still possible to reproduce the same behavior by introducing a forgetting factor feedback in the form of a dynamic gain on the relative strength of the attraction to the preferred direction. This feedback is analogous to the feedback on the weight ω in [19], which reinforces (diminishes) the gain if individuals find themselves moving towards (away from) their preferred direction. In the next section we present an extension of the model (6.1) where we implement such a forgetting factor feedback.

6.4.2 Forgetting Factor Feedback

We now study an extension of the model (6.1), by considering a forgetting factor feedback in the form of a dynamic gain on the relative strength of the attraction to the preferred direction. Informed individuals are more or less influenced by their preferred directions depending on how close they are to it. When informed individuals are heading in a direction close to their preferred direction, their attraction to it increases; this influence fades as the heading of an individual strays from its preferred direction. To add this effect, we multiply the "preferred direction" term of equation (6.1) by a coupling gain $a_{j\bar{\theta}_k}$, quantifying the level of interaction between an informed agent j and its preferred direction $\bar{\theta}_k$, $j \in \mathcal{N}_k$. The coupling gain $a_{j\bar{\theta}_k}$ is allowed to take any value between 0 and 1. In the case where

$a_{j\bar{\theta}_k} = 0$, the informed agent j is not influenced by its preferred direction. In the case where $a_{j\bar{\theta}_k} = 1$, the attention paid by agent j to its preferred direction is maximum. We show through simulations that, with this feedback, the group can achieve consensus with the group heading either in one of the preferred directions or else in a direction close to the average of the preferred directions. We will later explain what we mean by "close to the average of the preferred directions".

This forgetting factor feedback is different from the static feedback considered in Section 5.3 in that it includes a memory effect. If an informed individual is traveling close to its preferred direction for a significant amount of time but subsequently finds itself traveling in a different direction, its attraction to the preferred direction will start decreasing but will not vanish immediately. The attraction of informed individuals to their preferred directions depends not only on their current direction of travel but also on their direction of travel in the "recent" past, recent being quantified by the speed of the dynamics for the gain $a_{j\bar{\theta}_k}$ relative to the speed of the dynamic of the phase angle θ_j.

The dynamics of the interaction gains between the informed individuals and their preferred directions are modelled here with a saturated integrator dynamics identical to those used previously in this chapter to model the interactions between individuals. The dynamics of these interaction gains can be written as

$$\begin{aligned} \dot{\eta}_{j\bar{\theta}_k} &= K_2(\rho_{j\bar{\theta}_k} - r), \quad j \in \mathcal{N}_k,\ k = 1, 2 \\ a_{j\bar{\theta}_k} &= \frac{1}{1 + e^{-\eta_{j\bar{\theta}_k}}}, \qquad j \in \mathcal{N}_k,\ k = 1, 2, \end{aligned} \tag{6.46}$$

where $\eta_{j\bar{\theta}_k} \in \mathbb{R}$ is an integrated variable, $\rho_{j\bar{\theta}_k} = |\frac{e^{i\theta_j} + e^{i\bar{\theta}_k}}{2}|$ gives a measure of the level of synchrony between agent j and its preferred direction $\bar{\theta}_k$, the parameter $K_2 > 0$ quantifies the speed at which the interaction gains evolve, and $r \in [0, 1]$ is a threshold. If $\rho_{j\bar{\theta}_k} > r$, then $\eta_{j\bar{\theta}_k}$ increases and $a_{j\bar{\theta}_k}$ eventually converges to 1; if $\rho_{j\bar{\theta}_k} < r$, then $\eta_{j\bar{\theta}_k}$ decreases and $a_{j\bar{\theta}_k}$ eventually converges to 0. As we explained above, the use of such dynamics for the interaction gains allows us to include the effect of memory on the interactions between informed individuals and their preferred directions. As for the interaction between individuals, the dynamics of $a_{j\bar{\theta}_k}$ can be written in a simpler form, using the dynamics of

$\eta_{j\bar{\theta}_k}$, as

$$\dot{a}_{j\bar{\theta}_k} = K_2(1 - a_{j\bar{\theta}_k})a_{j\bar{\theta}_k}(\rho_{j\bar{\theta}_k} - r), \qquad j \in \mathcal{N}_k.$$

We use this formulation in the remainder of the analysis. The modified model for the dynamics of the group can now be written as

$$\begin{aligned}
\dot{\theta}_j &= a_{j\bar{\theta}_1} \sin\left(\bar{\theta}_1 - \theta_j\right) + \frac{K_1}{N}\sum_{l=1}^{N} a_{jl}\sin\left(\theta_l - \theta_j\right), && j \in \mathcal{N}_1 \\
\dot{\theta}_j &= a_{j\bar{\theta}_2} \sin\left(\bar{\theta}_2 - \theta_j\right) + \frac{K_1}{N}\sum_{l=1}^{N} a_{jl}\sin\left(\theta_l - \theta_j\right), && j \in \mathcal{N}_2 \\
\dot{\theta}_j &= \frac{K_1}{N}\sum_{l=1}^{N} a_{jl}\sin\left(\theta_l - \theta_j\right), && j \in \mathcal{N}_3 \\
\dot{a}_{lj} &= K_2(1 - a_{lj})a_{lj}(\rho_{lj} - r), \;\; l \in \{1,\ldots,N\},\; j \in \{l+1,\ldots,N\} \\
\dot{a}_{j\bar{\theta}_k} &= K_2(1 - a_{j\bar{\theta}_k})a_{j\bar{\theta}_k}(\rho_{j\bar{\theta}_k} - r), && j \in \mathcal{N}_k.
\end{aligned} \tag{6.47}$$

Simulations of the model (6.47) shown in Figures 6.6 suggest that the time-scale separation observed in model (6.1) still occurs. At first the heading angles of the individuals in each subgroup synchronize, then the three average subgroup directions slowly drift to reach their steady state. We note that, for the case plotted, all three subgroups are synchronized at the steady state. This model is similar to the model (6.1). The similarity makes it easy, given the knowledge on the invariant manifolds of (6.1), to identify the invariant manifolds of (6.47). The invariant manifolds of the model (6.47) are each characterized by a set of interaction gains between the different subgroups, as was the case with the model (6.1); here the invariant manifolds are also characterized by the set of interaction gains between the informed subgroups and their respective preferred directions. Consequently, each invariant manifold of the model (6.1) yields four invariant manifolds of the model (6.47): one in which each informed subgroup is connected to its preferred direction, one in which no informed subgroup is connected to its preferred directions and two in which one informed subgroup is connected to its preferred direction and the other is not. Although a rigorous analysis of the attractiveness of each of these thirty-two invariant manifolds and the stability analysis of the equilibria on each of these invariant manifolds could be carried out, as was done in

Section 6.3 for the model (6.1), we limit ourselves here to presenting qualitative observations on some interesting behaviors obtained with this model.

Figures 6.7 - 6.9 present simulations illustrating three different invariant manifolds each exhibiting a biologically-relevant behavior. The simulations presented in Figures 6.7 and 6.8 were carried out with the following parameter values : $K_1 = 2,\ K_2 = 7,\ N_1 = N_2 = 10,\ N_3 = 30,\ r = .8,\ \bar{\theta}_1 = 1$ rad and $\bar{\theta}_2 = 3$ rad. In these cases, the preferred directions are different enough that two individuals each traveling in a different one of the two preferred directions would not "see" each other and their coupling gain would decrease until reaching zero. With the initial conditions used in the simulation presented in Figure 6.7, the interaction gains between every pair of individuals converge to 1; the interaction gains between individuals in the first informed subgroup and their common preferred direction converge to 1 while the interaction gains between individuals in the second informed subgroup and their common preferred direction converge to 0. At the steady state, the group achieves consensus with all three subgroups synchronized, traveling in the preferred direction of the first informed subgroup. With the initial conditions used in Figure 6.8, we obtain a symmetrical scenario in which the group achieves consensus with all three subgroups synchronized, traveling in the preferred direction of the second informed subgroup.

The simulation presented in Figure 6.9 was carried out with the following parameter values: $K_1 = 5,\ K_2 = 7,\ N_1 = N_2 = 10,\ N_3 = 30,\ r = .9,\ \bar{\theta}_1 = 0$ rad and $\bar{\theta}_2 = \pi$ rad. Compared to the simulations from Figures 6.7 and 6.8, the difference between the preferred directions is greater and r is greater as well, meaning that individuals need to be closer to each other to have increasing interaction gains and informed individuals need to travel in a direction closer to their preferred direction to remain under its influence. In this case, the initial conditions are such that the interaction gains between every pair of individuals also converge to 1; however unlike in the other simulations, here the interaction gain between each informed individual and its preferred directions converges to 0. On the

reduced manifold, the system becomes

$$\begin{aligned}
\dot{\psi}_1 &= \frac{K_1 N_1}{N} \sin(\psi_2 - \psi_1) + \frac{K_1 N_3}{N} \sin(\psi_3 - \psi_1) \\
\dot{\psi}_2 &= \frac{K_1 N_1}{N} \sin(\psi_1 - \psi_2) + \frac{K_1 N_3}{N} \sin(\psi_3 - \psi_2) \\
\dot{\psi}_3 &= \frac{K_1 N_1}{N} \sin(\psi_1 - \psi_3) + \frac{K_1 N_1}{N} \sin(\psi_2 - \psi_3)
\end{aligned} . \tag{6.48}$$

We recognize here a variation of the Kuramoto model for coupled oscillator dynamics [60] with zero natural frequency and non-identical coupling gains; the steady state solution is thus one in which the three subgroups synchronize, traveling in the average of the initial headings. In the simulation presented in Figure 6.9, it appears that the steady state value is very close to the average of the preferred directions. This observation is not specific to the initial conditions used here. Rather in the range of initial conditions in which this manifold is attractive, the steady state value is near the average of the preferred directions. This owes to the fact that the steady state value has to be "away" from both preferred direction (otherwise the interaction gain between one informed subgroup and its preferred direction would start increasing again and we would get one of the two solutions illustrated in Figures 6.7 and 6.8). We note however that, with the appropriate initial conditions, it is possible to obtain a symmetric steady state solution with the group heading near the opposite of the average of the preferred directions. This solution is interesting because the group acts as if it is averaging the preferred directions, but when it is doing so, no individual is influenced by its preferred direction.

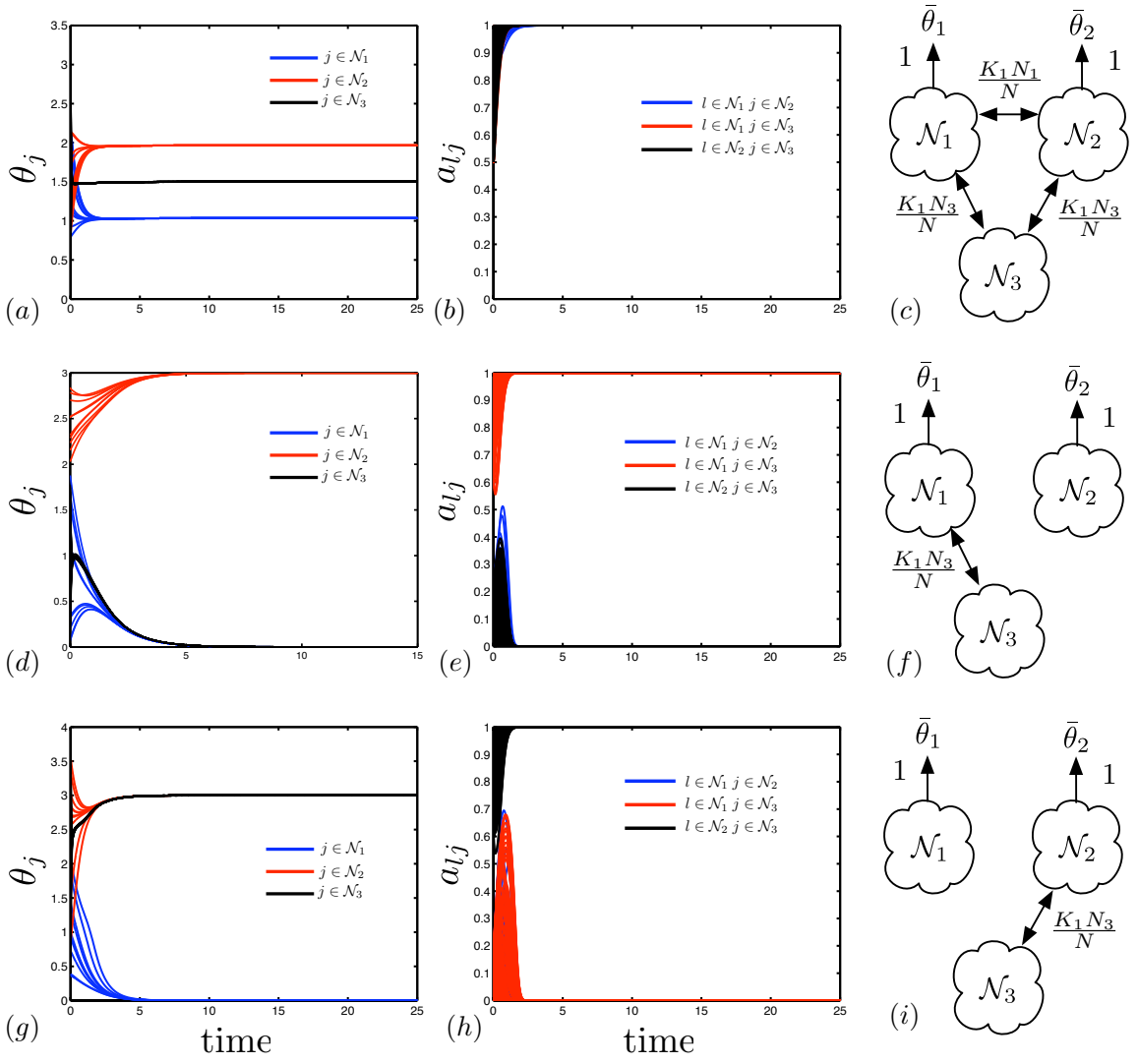

Figure 6.1: Simulations of the model (6.1) with $K_1 = 2$, $K_2 = 20$ and $r = .8$, $N_1 = 10$ individuals with preferred direction 0 rad, $N_2 = 10$ individuals with preferred direction 3 rad and $N_3 = 30$ individuals with no preferred direction. (a), (d), (g) Phase angle of each individual in the group versus time for each of the three sets of initial conditions. For these simulations two time-scales can be observed in the dynamics can be observed. During a short initial transient time, the heading angles of the individuals in each subgroup synchronize. Then the three average subgroup directions change slowly to their steady states values. (b), (e), (h) Interaction gains for each pair of individuals in different subgroup. The interaction gains between individuals in different subgroups converge "quickly" to either 1 for the set of parameter values and the set of initial conditions of the gains and phase angles used. (c), (f), (i) Diagrams for the interconnection topology between the different subgroups after the transient.

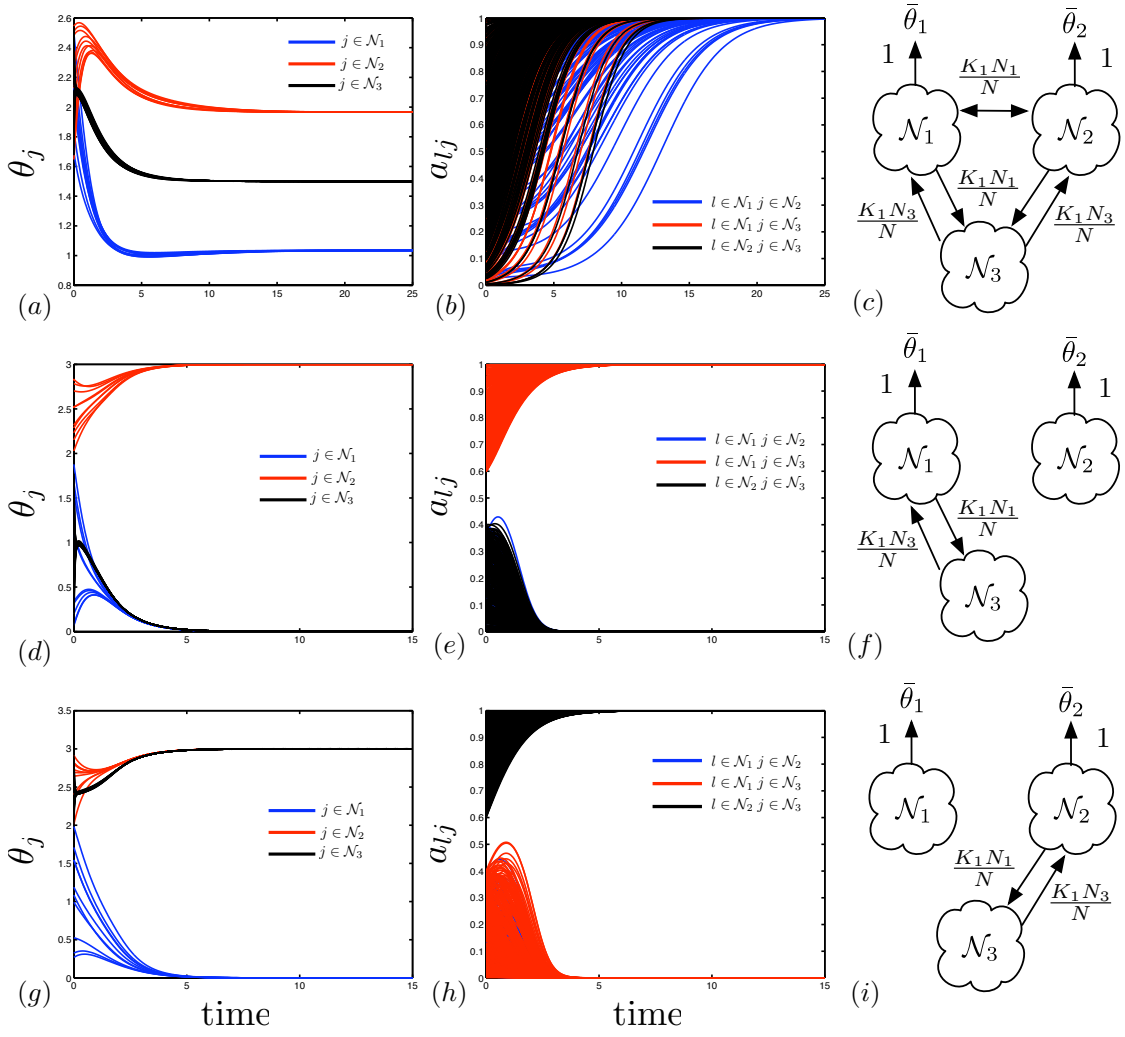

Figure 6.2: Simulations of the model (6.1) for three distinct set of initial conditions with $K_1 = 2$, $K_2 = 5$ and $r = .8$, $N_1 = 10$ individuals with preferred direction 0 rad, $N_2 = 10$ individuals with preferred direction 3 rad and $N_3 = 30$ individuals with no preferred direction. (a),(d),(g) Phase angle of each individual in the group versus time for each of the three sets of initial conditions. For these simulations two time-scales can be observed in the dynamics can be observed. During a short initial transient time, the heading angles of the individuals in each subgroup synchronize. Then the three average subgroup directions change slowly to their steady states values. (b), (e), (h) Interaction gains for each pair of individuals in different subgroup. The interaction gains between individuals in different subgroups converge to either 0 or 1 depending on the initial conditions of the gains and phase angles. (c), (f), (i) Diagrams for the interconnection topology between the different subgroups after the transient.

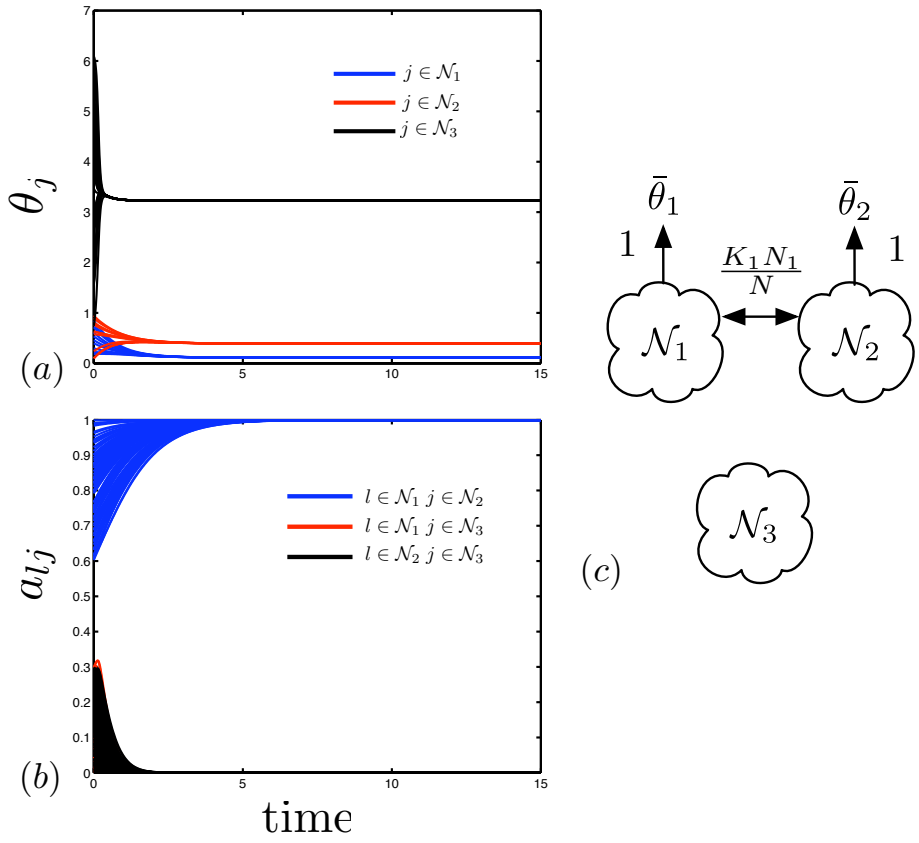

Figure 6.3: Simulation of the model (6.1) with $K_1 = 2,\ K_2 = 5,\ N_1 = N_2 = 10,\ N_3 = 30,\ r = .8,\ \bar{\theta}_1 = 0$ rad and $\bar{\theta}_2 = .5$ rad. (a) Phase angle of each individual in the group versus time. Two time-scales in the dynamics can be observed. During a short initial transient time, the heading angles of the individuals in each subgroup synchronize. Then the three average subgroup directions change slowly to their steady states values. (b) Interaction gains for each pair of individuals in different subgroup. The interaction gains between individuals in different subgroups converge to 1 for every pair of individuals between subgroups one and two and to zero otherwise. (c) Diagrams for the interconnection topology between the different subgroups after the fast time scale.

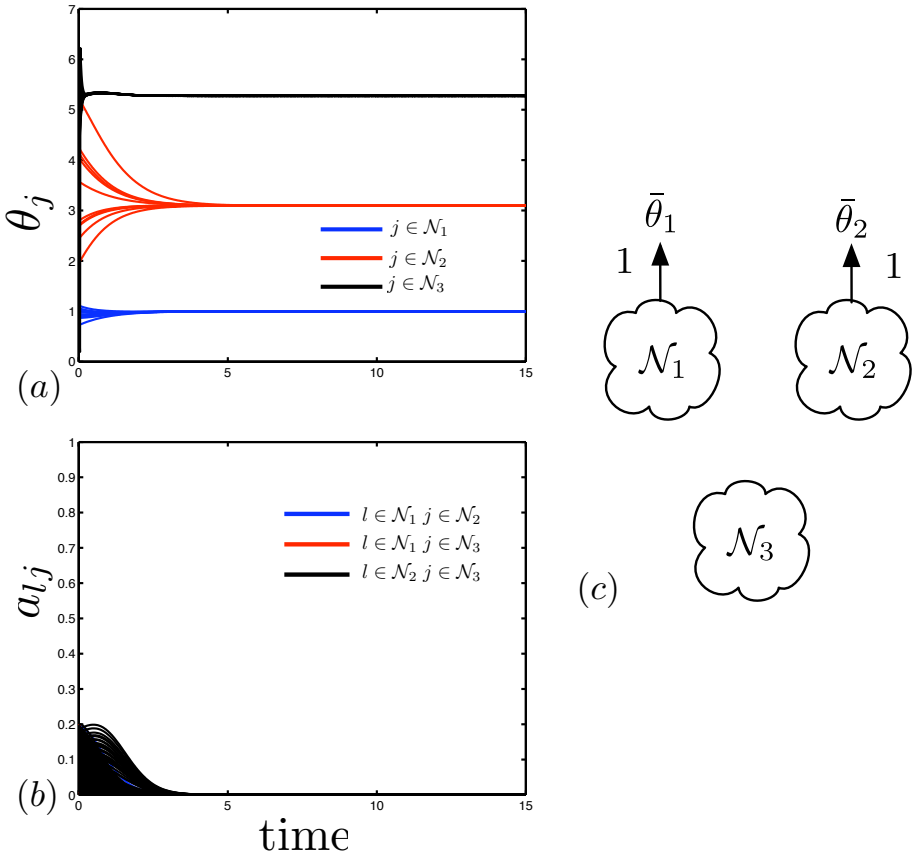

Figure 6.4: Simulation of the model (6.1) with $K_1 = 2$, $K_2 = 5$, $N_1 = N_2 = 10$, $N_3 = 30$, $r = .95$, $\bar{\theta}_1 = 1$ rad and $\bar{\theta}_2 = 3.1$ rad. (a) Phase angle of each individual in the group versus time. Two time-scales in the dynamics can be observed. During a short initial transient time, the heading angles of the individuals in each subgroup synchronize. Then the three average subgroup directions change slowly to their steady states values. (b) Interaction gains for each pair of individuals in different subgroup. The interaction gains between individuals in different subgroups converge to 0 for every pair of individuals between subgroups. (c) Diagrams for the interconnection topology between the different subgroups after the fast time scale.

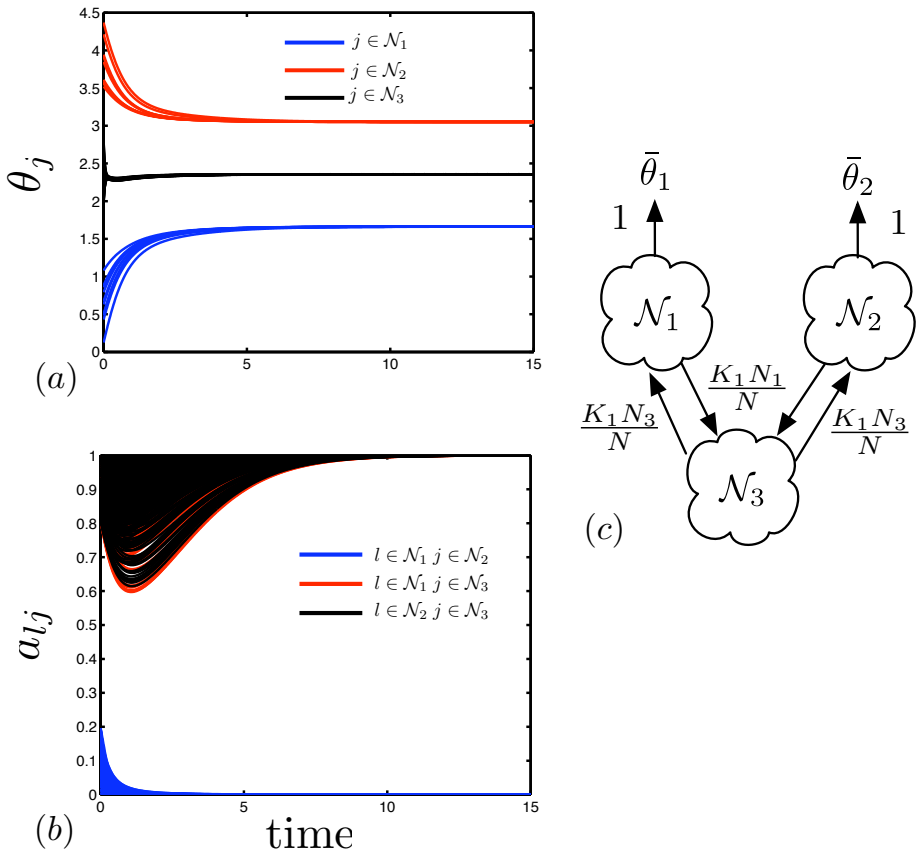

Figure 6.5: Simulation of the model (6.1) with $K_1 = 2$, $K_2 = 7$, $N_1 = N_2 = 10$, $N_3 = 30$, $r = .85$, $\bar{\theta}_1 = \frac{\pi}{4}$ rad and $\bar{\theta}_2 = \frac{5\pi}{4}$ rad. (a) Phase angle of each individual in the group versus time with. Two time-scales in the dynamics can be observed. During a short initial transient time, the heading angles of the individuals in each subgroup synchronize. Then the three average subgroup directions change slowly to their steady states values. (b) Interaction gains for each pair of individuals in different subgroup. The interaction gains between individuals in different subgroups converge to 0 for every pair of individuals between the two informed subgroups and to one otherwise. (c) Diagrams for the interconnection topology between the different subgroups after the fast time scale.

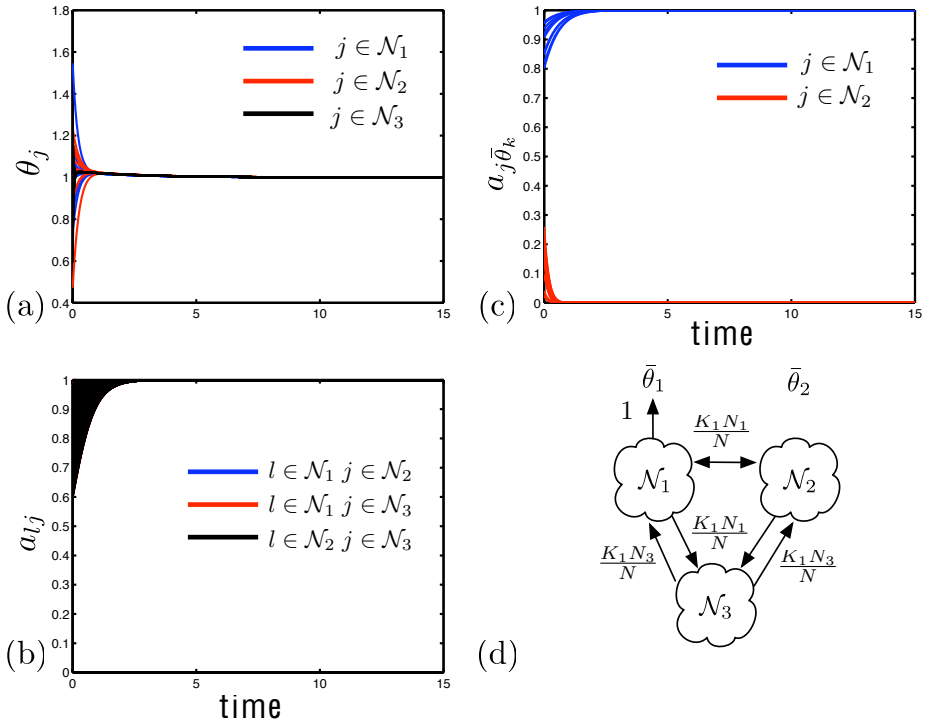

Figure 6.6: Simulation of the model (6.47) with $K_1 = 2,\ K_2 = 20,\ N_1 = N_2 = 10,\ N_3 = 30,\ r = .8,\ \bar{\theta}_1 = 1$ rad and $\bar{\theta}_2 = 3$ rad. (a) Phase angle of each individual in the group versus time with. Two time-scales in the dynamics can be observed. During a short initial transient time, the heading angles of the individuals in each subgroup synchronize. Then the three average subgroup directions change slowly to their steady states values. We note that at the steady state, the three subgroups are synchronized heading in the preferred direction of the first informed subgroup. (b) Interaction gains for each pair of individuals in different subgroup. The interaction gains between individuals in different subgroups converge "quickly" (as fast as the individuals in the same subgroup synchronize) to 1 for every pair of individuals between subgroups. (c) Interaction for each informed individuals with its preferred direction. The interaction gains between informed individuals in the first informed subgroup and their preferred direction all converge to 1 while the interaction gains between individuals in the second informed subgroup and their preferred direction converge to 0. (d) Diagrams for the interconnection topology between the different subgroups after the fast time scale.

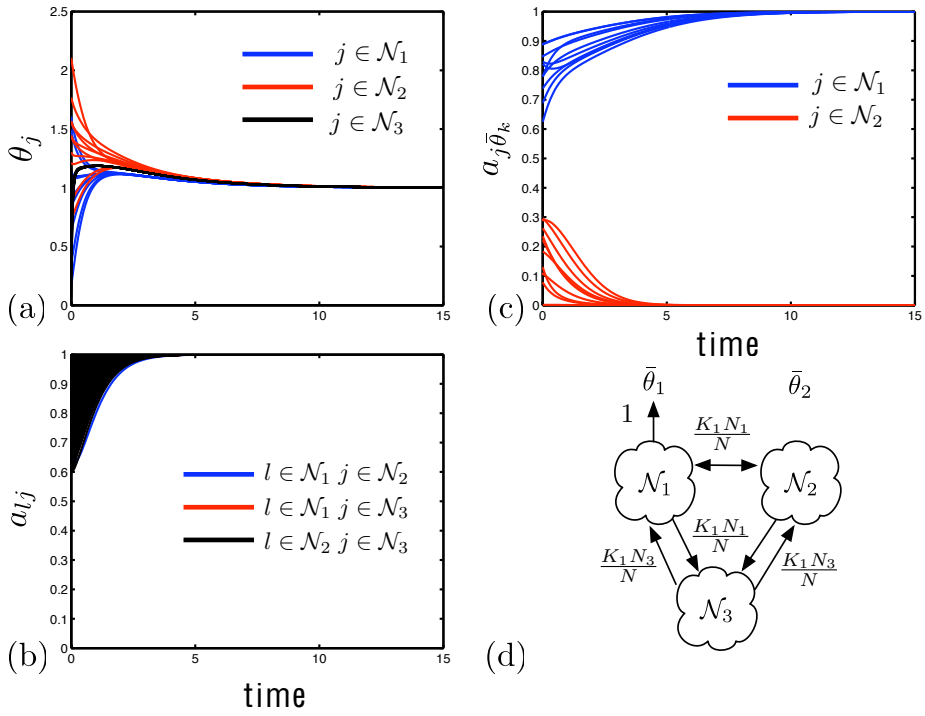

Figure 6.7: Simulation of the model (6.47) with $K_1 = 2$, $K_2 = 7$, $N_1 = N_2 = 10$, $N_3 = 30$, $r = .8$, $\bar{\theta}_1 = 1$ rad and $\bar{\theta}_2 = 3$ rad. (a) Phase angle of each individual in the group versus time with. Two time-scales in the dynamics can be observed. During a short initial transient time, the heading angles of the individuals in each subgroup synchronize. Then the three average subgroup directions change slowly to their steady states values. We note that at the steady state, the three subgroups are synchronized heading in the preferred direction of the first informed subgroup. (b) Interaction gains for each pair of individuals in different subgroup. The interaction gains between individuals in different subgroups converge to 1 for every pair of individuals between subgroups. (c) Interaction for each informed individuals with its preferred direction. The interaction gains between informed individuals in the first informed subgroup and their preferred direction all converge to 1 while the interaction gains between individuals in the second informed subgroup and their preferred direction converge to 0. (d) Diagrams for the interconnection topology between the different subgroups after the fast time scale.

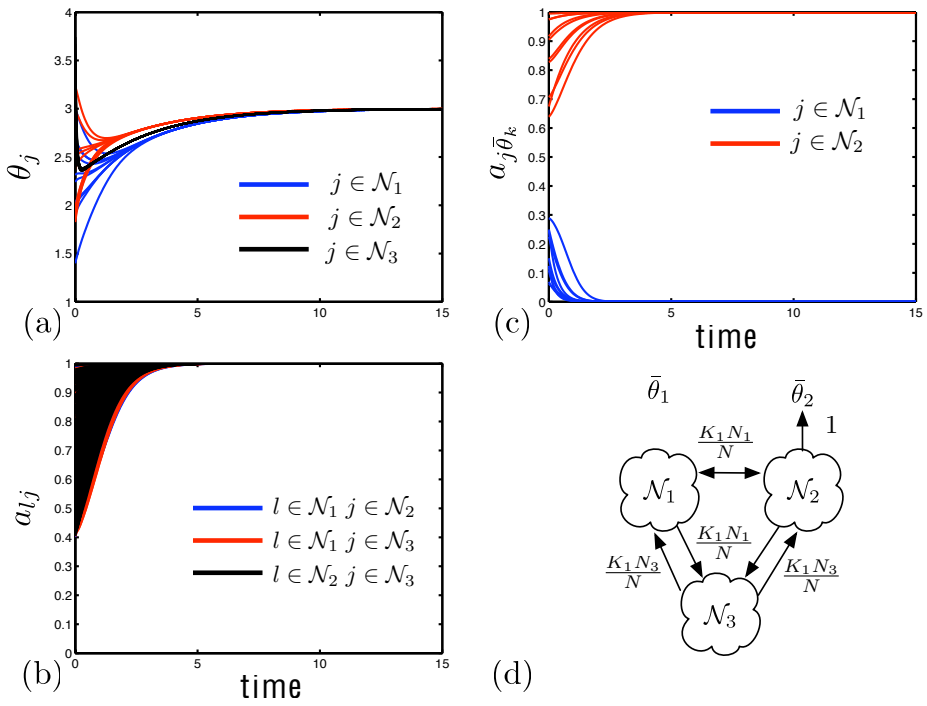

Figure 6.8: Simulation of the model (6.47) with $K_1 = 2,\ K_2 = 7,\ N_1 = N_2 = 10,\ N_3 = 30,\ r = .8, \bar{\theta}_1 = 1$ rad and $\bar{\theta}_2 = 3$ rad. (a) Phase angle of each individual in the group versus time. Two time-scales in the dynamics can be observed. During a short initial transient time, the heading angles of the individuals in each subgroup synchronize. Then the three average subgroup directions change slowly to their steady states values. We note that at the steady state, the three subgroups are synchronized heading in the preferred direction of the second informed subgroup. (b) Interaction gains for each pair of individuals in different subgroup. The interaction gains between individuals in different subgroups converge to 1 for every pair of individuals between subgroups. (c) Interaction for each informed individuals with its preferred direction. The interaction gains between informed individuals in the first informed subgroup and their preferred direction all converge to 0 while the interaction gains between individuals in the second informed subgroup and their preferred direction converge to 1. (d) Diagrams for the interconnection topology between the different subgroups after the fast time scale.

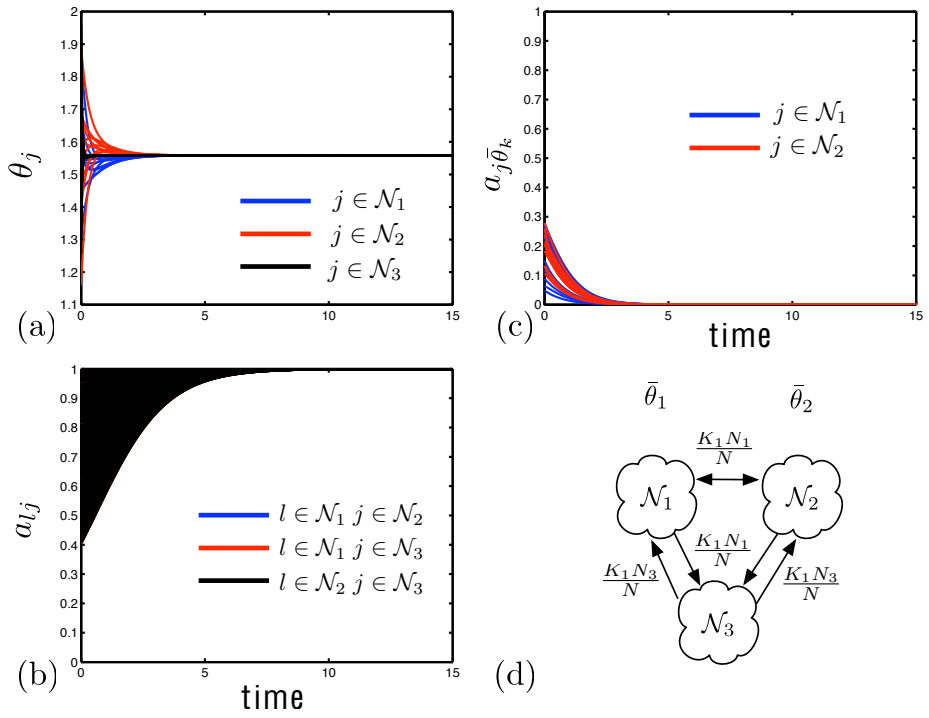

Figure 6.9: Simulation of the model (6.47) with $K_1 = 2,\ K_2 = 7,\ N_1 = N_2 = 10,\ N_3 = 30,\ r = .9, \bar{\theta}_1 = 0$ rad and $\bar{\theta}_2 = \pi$ rad.(a) Phase angle of each individual in the group versus time. Two time-scales in the dynamics can be observed. During a short initial transient time, the heading angles of the individuals in each subgroup synchronize. Then the three average subgroup directions change slowly to their steady states values. We note that at the steady state, the three subgroups are synchronized heading near the average of the preferred directions of the two informed subgroups. (b) Interaction gains for each pair of individuals in different subgroup. The interaction gains between individuals in different subgroups converge to 1 for every pair of individuals between subgroups. (c) Interaction for each informed individuals with its preferred direction. The interaction gains between informed individuals in either informed subgroup and their preferred direction all converge to 0. (d) Diagrams for the interconnection topology between the different subgroups after the fast time scale.

Chapter 7

Conclusions and Future Directions

In this dissertation we present a study of the dynamics and control of multi-agent systems in both the engineered and the natural setting. Focusing first on the engineered setting, in Chapters 2 and 3, we derive provable, distributed control laws for stabilizing and changing the shape of vehicle formations in the plane using dynamic models of tensegrity structures. In Chapters 4, 5 and 6, where we turn our attention to the natural setting, we present and study Lagrangian models to investigate the mechanisms of decision-making and leadership in animal groups. This chapter gives a brief summary of the approaches, results and conclusions presented in this dissertation and suggests possible future lines of research motivated by the presented work.

7.1 Summary

In Chapter 2 we design a control law that drives vehicle formations into arbitrary shapes with forces that can be represented as those internal to tensegrity structures. Tensegrity structures offer important advantages that we seek to translate to vehicle formations, including the ability to maintain shape even in the presence of external forces. It is such dynamics properties of tensegrity structures that led us to choose the tensegrity-based approach as an alternative to approaches based on artificial potentials and edge design. The control law is designed by defining a smooth map that takes any arbitrary planar shape and provides a

planar tensegrity with that shape. We prove stability of the desired shape for the dynamics of the vehicle network that is represented as a tensegrity by using the linearization of the yielded dynamical system. We illustrate the method with examples, one of which we use to investigate how freedom in the choice of the parameter of the control law can be used to affect the resulting interconnection topology of the vehicle network. The smoothness of the mapping between shapes and tensegrities with respect to the shape parameters allows us to extend the method to the transient problem of moving smoothly from one shape to another, while maintaining stability along the way.

This transient problem is worked out formally in Chapter 3, where we use the smooth map between vehicles in a formation and nodes in a tensegrity structure to derive a control law that realizes well-behaved reconfiguration between arbitrary shapes. This control law makes the nodes follow a smooth path in the space of stable tensegrities by smoothly varying the parameters of the control law presented in Chapter 2 for stabilization of planar shapes. Results from the nonlinear systems theory literature are utilized to derive sufficient conditions that guarantee that the trajectory of the formation, in shape space, is close to the prescribed path and that it converges to the desired final shape. Numerical simulations are presented to illustrate the method. These illustrations hint at certain good performance features of the method – specifically, the vehicles do not collide with each other and the distance covered by all the vehicles is minimized during the reconfiguration.

In Chapter 4 we turn our attention to the natural setting and build on the decision-making model of Couzin et al. [19]. We summarize the results from [19] and then focus our attention on the role of naive individuals in the decision-making process. We show that naive individuals help accelerate the process of consensus, unless they are too numerous. In the case that they are too numerous, we show that this "overwhelming" number of naive individuals causes the group to fragment and/or slows down the consensus process. Our analysis, built primarily on simulations, reveals that the model from Couzin et al., although very suggestive, is too complex to be analyzed mathematically. For this reason, proving specific decision-making mechanisms requires the design of simplified, lower-dimensional

models such as the continuous-time models presented in Chapters 5 and 6.

In Chapter 5 we present and analyze a model for the dynamics of leadership and decision-making in animal group motion. The model takes the general form of the Kuramoto model of coupled oscillators with individual preferences; where such preference exist, they are associated with a fixed heading angle. The model is simplified through a time-scale reduction argument to a three-dimensional gradient system of which we study the full phase space dynamics by computing equilibria and proving stability and bifurcations. This model differs from the complex model proposed by Couzin et al. in that it makes several simplifying assumptions, the most important of which are that we assume an all-to-all inter-connecting topology in the group and ignore for the purpose of the analysis the presence of naive individuals in the group. Despite these assumptions, the yielded model captures some important behaviors exhibited in the model presented in Chapter 4, among them that informed individuals tend to compromise toward the average of their preferred directions. This model does not however exhibit full synchronization (i.e., consensus) unless the coupling gain K between individuals is very large, meaning that for small values of K, the group does not fully aggregate and in fact splits. These deviations between the model in Chapter 4 and the model in Chapter 5 motivate the model presented and analyzed in Chapter 6.

In Chapter 6, we derive and study a similar model to the one given in Chapter 5 but relax the two critical simplifying assumption stated above. First we do not assume an all-to-all fixed communication topology but consider instead a time-varying, possibly incomplete, connecting topology. Second, whereas in Chapter 5 we ignore the presence of naive individuals, in Chapter 6 their influence is considered. With those assumptions relaxed, the model yields a much richer behavior with many invariant manifolds; we investigate the attractiveness of eight of these invariant manifolds and study the reduced dynamics on the attractive ones. In contrast to the model from Chapter 5, in which informed individuals always compromise on their preferred directions, we show that with this model it is possible to have informed individuals travel exactly in their preferred direction, but only when the two informed subgroups do not interact with each other. We concluded the chapter with an

interesting extension in which we add a forgetting factor feedback in the form of a dynamic gain on the strength of the attraction that informed individuals feel toward their preferred direction. This extended model is highly suggestive in that it reproduces all the behavior observed with the discrete-time model proposed by Couzin et al.

The work presented in this dissertation may be extended in several directions that may make it possible to better understand how collective behavior emerges in the natural setting and to develop more efficient control strategies for groups of robots emulating natural systems. We list some possible future lines of research motivated by the presented work.

7.2 Future Lines of Research

Modeling collective behavior in animal groups As we noted, with both of the proposed continuous time models from Chapters 5 and 6, the behavior observed both in [19] and in Chapter 4, where the group collectively selects one of the preferred directions, cannot be reproduced unless a forgetting feedback factor is introduced. Moreover, full synchronization of the group cannot occur unless the coupling gain K_1 is very large. This persistent deviation indirectly reveals the importance of a remaining simplifying assumption, namely, that we consider only the dynamics of the phases and not the complete spatial dynamics of the individuals in the group. The lack of explicit consideration of spatial effects is rather critical. For the simulations presented in [19] and in Chapter 4, in the case where the group collectively selects one of the preferred direction, the three subgroups are consistently ordered with the "leading" informed subgroup in the front, the naive individuals just behind, and the other subgroup far to the rear. The spacing between the two informed subgroups created by the intervening presence of naive individuals is critical in that it allows the two informed subgroups to travel in the same direction without directly interacting with each other. This collective decision outcome cannot be reproduced by the phase models proposed in Chapters 5 and 6 (or any other phase model), as interactions between two individuals are solely determined by whether they are traveling in a similar direction or not. In order to reproduce the collective decision-making outcome observed in [19], a challenging (and

necessary) next step for the models proposed in Chapters 5 and 6 would be to define a framework in which the spatial dynamics could be layered on top of the phase dynamics proposed here. This layering of phase and spatial dynamics is not a new idea: Justh and Krishnaprasad developed a motion model in which vehicles travel at constant speed and are controlled by steering their direction of travel [49, 50]. This framework was successfully used by Sepulchre et al. to stabilize circular and parallel collective motion [108]. The challenge in applying such a framework to model animal group motion would be to incorporate a way for individuals/vehicles to have preferences as some do in our models.

Control of a group of robots The work presented in Chapters 2 and 3 in which we designed control laws to stabilize arbitrary shapes and reconfigure a vehicle network between arbitrary shapes can be extended in several ways. We suggest three of them here. First, as we have noted in the examples from Chapter 2, given an arbitrary shape, our mapping often yields a tensegrity structure in which the number of interconnections exceeds the proven lower limit. We showed by means of an example how to manipulate our method so as to reduce the number of interconnections; future work should examine the possibility of making such a modification systematic. Second, the stability results proven in both Chapters 2 and 3 are local; it is of interest to consider proving more global results and exploring the global phase space in view of better leveraging tensegrity structure dynamics. Pais et al. proved global results for one-dimensional tensegrity structures and used the results to prove global stability of planar and three-dimensional structures made up of a set of orthogonal one-dimensional tensegrity structures [89]. Future work extending the method of the present dissertation to three dimensions would provide a compelling alternative for controlling the shape of three-dimensional formations. Finally we have argued using simulations that the control law we have designed for the reconfiguration shows good performance in that vehicles do not collide and the distance covered by all the vehicles is minimized. It would be necessary before implementing our control into any physical system to investigate this issue more rigorously. As our method and simulations imply, the rate of change of the parameters (characterized by τ in our work) plays a crucial role in the robustness issue. As τ gets

larger (i.e., as the network is required to reconfigure at a slower pace), the network remains closer to the prescribed trajectory. Given a path such as the one presented in Chapter 3 where trajectories of distinct vehicles do not collide and where the distance covered by the vehicles is minimized, our control law has good performance. One should realize however that enforcing the restriction of having no intersections in the planned trajectories of the vehicles is more conservative than necessary. It would be sufficient to show that through the path of the reconfiguration no two vehicles are required to be "too close" to each other at any given time; two distinct vehicles could pass through the same location provided they do so at different times.

Appendix A

Technical Proofs for Chapter 5

Proof of lemma 5.2.1: The linearization of (5.20) at each of the two equilibria $\boldsymbol{\psi}_{S1}$ or $\boldsymbol{\psi}_{S2}$ gives the same symmetric Jacobian with eigenvalues $\lambda_1, \lambda_2 \in \mathbb{R}$ satisfying

$$\lambda_1 \lambda_2 = \frac{K^2}{4} \sin^2 \bar{\theta}_2 - 1 < 0 \quad \text{for} \quad \left| \frac{K}{2} \sin \bar{\theta}_2 \right| < 1.$$

For $\bar{\theta}_2 \in [0, \pi]$ the eigenvalues are of opposite sign. This implies that $\boldsymbol{\psi}_{S1}$ and $\boldsymbol{\psi}_{S2}$ are saddle points $\forall K > 0$ and $\forall \bar{\theta}_2 \in [0, \pi]$ if $\frac{K}{2} \sin \bar{\theta}_2 < 1$. In the case $|\frac{K}{2} \sin \bar{\theta}_2| = 1$, $\boldsymbol{\psi}_{S1} = \boldsymbol{\psi}_{S2} = \left(\frac{3\pi}{2}, \frac{\pi}{2} + \bar{\theta}_2\right)$ and the eigenvalues are $\lambda_1 = 0$ and $\lambda_2 = K \cos \bar{\theta}_2 > 0$. Therefore for $\bar{\theta}_2 \in \left(0, \frac{\pi}{2}\right) \cup \left(\frac{\pi}{2}, \pi\right)$, the equilibria $\boldsymbol{\psi}_{S1} = \boldsymbol{\psi}_{S2} = \left(\frac{3\pi}{2}, \frac{\pi}{2} + \bar{\theta}_2\right)$ are unstable with one zero eigenvalue and one strictly positive eigenvalue. In case $\bar{\theta}_2 = \pi/2$ and $K = 2$, $\lambda_1 = \lambda_2 = 0$. □

Proof of lemma 5.2.2: Using $\cos\left(\frac{\bar{\theta}_2}{2} - \psi_2\right) = \rho$ and $\sin\left(\frac{\bar{\theta}_2}{2} - \psi_2\right) = -\sqrt{1-\rho^2}$, the Jacobian at the equilibrium is computed; it is symmetric and the corresponding eigenvalues are

$$\lambda_{1,2} = -\left(\rho \cos \frac{\bar{\theta}_2}{2} + \sqrt{1-\rho^2} \sin \frac{\bar{\theta}_2}{2} + \frac{K}{2}\left(2\rho^2 - 1\right)\right) \pm \frac{K}{2}\left(2\rho^2 - 1\right).$$

We find using (5.30) for all $\left(K, \bar{\theta}_2\right) \in [0, \infty) \times [0, \pi)$ that

$$-\sqrt{1-\rho^2} \sin \frac{\bar{\theta}_2}{2} - K\left(2\rho^2 - 1\right) = -\frac{1}{\rho}\left(1 - \rho^2\right) \cos \frac{\bar{\theta}_2}{2} - K\rho^2 < 0. \tag{A.1}$$

Thus, for all $\left(K, \bar{\theta}_2\right) \in [0, \infty) \times [0, \pi)$, using (A.1) both eigenvalues are real and negative. Hence $\boldsymbol{\psi}_{sync1}$ is a stable node for all $\left(K, \bar{\theta}_2\right) \in [0, \infty) \times [0, \pi)$. □

Proof of lemma 5.2.3: Using $\cos\left(\frac{\bar{\theta}_2}{2} - \psi_2\right) = -\rho$ and $\sin\left(\frac{\bar{\theta}_2}{2} - \psi_2\right) = \sqrt{1-\rho^2}$ the Jacobian evaluated at this equilibrium has eigenvalues

$$\lambda_{1,2} = \rho\cos\frac{\bar{\theta}_2}{2} + \sqrt{1-\rho^2}\sin\frac{\bar{\theta}_2}{2} - \frac{K}{2}\left(2\rho^2-1\right) \pm \frac{K}{2}\left(2\rho^2-1\right).$$

One eigenvalue is equal to $\rho\cos\frac{\bar{\theta}_2}{2} + \sqrt{1-\rho^2}\sin\frac{\bar{\theta}_2}{2} > 0$ for all $\left(K, \bar{\theta}_2\right) \in [0,\infty) \times [0,\pi)$. Hence $\boldsymbol{\psi}_{antisync1}$ is unstable for all $\left(K, \bar{\theta}_2\right) \in [0,\infty) \times [0,\pi)$. $\square$

Proof of lemma 5.2.5: We prove these results by looking at the eigenvalues of the Jacobian. We first look at the case when $\bar{\theta}_2 < \frac{\pi}{2}$ and show that one eigenvalue is real and positive. The eigenvalues of the Jacobian are given by

$$\lambda_{1,2} = \rho\cos\frac{\bar{\theta}_2}{2} - \sqrt{1-\rho^2}\sin\frac{\bar{\theta}_2}{2} - \frac{K}{2}(2\rho^2-1) \pm \frac{K}{2}(2\rho^2-1).$$

For all $K > K_1$, the inequalities in (5.33) yield

$$\lambda_1 > \sqrt{\frac{1}{1+\tan\left(\frac{\bar{\theta}_2}{2}\right)^{\frac{2}{3}}}}\cos\frac{\bar{\theta}_2}{2} - \sqrt{\frac{1}{1+\cot\left(\frac{\bar{\theta}_2}{2}\right)^{\frac{2}{3}}}}\sin\frac{\bar{\theta}_2}{2} > 0 \text{ if } \bar{\theta}_2 < \frac{\pi}{2}, \tag{A.2}$$

proving that for $(K, \bar{\theta}_2) \in [K_1, \infty) \times [0, \frac{\pi}{2})$ the equilibrium $\boldsymbol{\psi}_{sync2}$ is unstable.

We now consider the case when $\bar{\theta}_2 > \frac{\pi}{2}$ and show that for $K \in (K_1, K_0)$, both eigenvalues λ_1, λ_2 are negative and that for $K > K_0$ $\lambda_1 > 0$. When $K = K_1$, equation (5.32) has one solution in $[0,1]$ $\rho_1 = \sqrt{\frac{\cos\left(\frac{\bar{\theta}_2}{2}\right)^{\frac{2}{3}}}{\cos\left(\frac{\bar{\theta}_2}{2}\right)^{\frac{2}{3}} + \sin\left(\frac{\bar{\theta}_2}{2}\right)^{\frac{2}{3}}}}$. The eigenvalues $\lambda_{1,2}$ evaluated at $K = K_1$, $\rho = \rho_1$ are then given by

$$\lambda_1|_{K_1,\rho_1} = \sqrt{\frac{1}{1+\tan\left(\frac{\bar{\theta}_2}{2}\right)^{\frac{2}{3}}}}\cos\frac{\bar{\theta}_2}{2} - \sin\frac{\bar{\theta}_2}{2}\sqrt{\frac{1}{1+\cot\left(\frac{\bar{\theta}_2}{2}\right)^{\frac{2}{3}}}} < 0 \text{ if } \bar{\theta}_2 > \frac{\pi}{2}$$

$$\lambda_2|_{K_1,\rho_1} = 0.$$

The derivative of $\lambda_{1,2}$ with respect to K are given by

$$\frac{\partial\lambda_1}{\partial K} = \left(\cos\frac{\bar{\theta}_2}{2} + \frac{\rho}{\sqrt{1-\rho^2}}\sin\frac{\bar{\theta}_2}{2}\right)\frac{\partial\rho}{\partial K}$$

$$\frac{\partial\lambda_2}{\partial K} = \left(\cos\frac{\bar{\theta}_2}{2} + \frac{\rho}{\sqrt{1-\rho^2}}\sin\frac{\bar{\theta}_2}{2} - 4K\rho\right)\frac{\partial\rho}{\partial K} - (2\rho^2-1).$$

As we noted in the proof of lemma 5.2.4, ρ_{sync2} is an increasing function of K, implying that $\frac{\partial \rho}{\partial K}\Big|_{\psi_{sync2}} > 0$. Using in addition the inequalities (5.33) we get for $\bar{\theta}_2 > \frac{\pi}{2}$

$$\frac{\partial \lambda_1}{\partial K}\bigg|_{\psi_{sync2}} > 0$$

$$\frac{\partial \lambda_2}{\partial K}\bigg|_{\psi_{sync2}} < -2\cos\frac{\bar{\theta}_2}{2} - 3\cos\left(\frac{\bar{\theta}_2}{2}\right)^{\frac{1}{3}}\sin\left(\frac{\bar{\theta}_2}{2}\right)^{\frac{2}{3}} + \frac{\sin\left(\frac{\bar{\theta}_2}{2}\right)^{\frac{2}{3}} - \cos\left(\frac{\bar{\theta}_2}{2}\right)^{\frac{2}{3}}}{\sin\left(\frac{\bar{\theta}_2}{2}\right)^{\frac{2}{3}} + \cos\left(\frac{\bar{\theta}_2}{2}\right)^{\frac{2}{3}}} < 0.$$

$\frac{\partial \lambda_2}{\partial K}\Big|_{\psi_{sync2}} < 0$ implies that $\lambda_2|_{\psi_{sync2}} < 0\ \forall K > K_1$. $\frac{\partial \lambda_1}{\partial K}\Big|_{\psi_{sync2}} > 0$ implies that $\lambda_1|_{\psi_{sync2}}$ is a strictly increasing function of K. Since $\lambda_1|_{K_1,\rho_1} < 0$ it will cross zero only once. When $K = K_0$ the solution of equation (5.32) is $\rho_0 = \sin\frac{\bar{\theta}_2}{2}$. The eigenvalue λ_1 at $K = K_0, \rho_0$ is then $\lambda_1|_{K_0,\rho_0} = 0$. Since λ_1 is an increasing function of K, it will be negative for $K < K_0$ and positive after.

This concludes the proof that The equilibrium $\boldsymbol{\psi}_{sync2}$ is unstable for all $(K, \bar{\theta}_2) \in [K_1, \infty) \times [0, \frac{\pi}{2}) \cup [K_0, \infty) \times (\frac{\pi}{2}, \pi)$ and stable $(K, \bar{\theta}_2) \in [K_1, K_0) \times (\frac{\pi}{2}, \pi)$. □

Proof of lemma 5.2.6: We prove this lemma by showing that $\lambda_2|_{\boldsymbol{\psi}_{antisync2}} > 0$. Since on the branch of equilibria $\boldsymbol{\psi}_{antisync2}$, equation (5.32) is satisfied, taking partial derivative of both sides of (5.32) with respect to K yields

$$\frac{\partial \rho}{\partial K}\left(-\sin\frac{\bar{\theta}_2}{2} + \frac{\rho}{\sqrt{1-\rho^2}}\cos\frac{\bar{\theta}_2}{2} + K\sqrt{1-\rho^2} - \frac{K\rho^2}{\sqrt{1-\rho^2}}\right) + \rho\sqrt{1-\rho^2} = 0,$$

which can be rewritten as

$$\frac{\partial \rho}{\partial K} = \frac{\rho(\rho^2 - 1)}{\lambda_2}. \tag{A.3}$$

Plugging (A.3) in the expression of $\frac{\partial \lambda_2}{\partial K}$ we get

$$\frac{\partial \lambda_2}{\partial K} = \frac{-\rho^3\cos\frac{\bar{\theta}_2}{2} + K - (1-\rho^2)^{\frac{3}{2}}\sin\frac{\bar{\theta}_2}{2}}{\lambda_2}. \tag{A.4}$$

For all $K > K_1, \rho \in [0, 1]$, the numerator of (A.4) is strictly positive. This implies that λ_2 does not change sign as a function of K. On the branch of $\boldsymbol{\psi}_{antisync2}$, when $K = 2$, $\lambda_2 = \cos\bar{\theta}_2 > 0$ implying that for all $K > K_1$, $\lambda_2|_{\boldsymbol{\psi}_{antisync2}} > 0$. this concludes the proof that The equilibrium $\boldsymbol{\psi}_{antisync2}$ is unstable for all $(K, \bar{\theta}_2) \in [K_1, \infty) \times [0, \pi)$.

Appendix B

Technical Proofs for Chapter 6

Proof of lemma 6.3.1: We prove that the equilibria $\boldsymbol{\psi}_{\mathcal{M}_{8,1}}$ and is unstable if $K_1 > \min(\frac{N \sin \frac{\bar{\theta}_2}{2}}{N_1}, \frac{N}{N_3}\sqrt{\frac{1+\cos\bar{\theta}_2}{2}})$ by showing that the showing that there is a change of sign between the coefficients of the characteristic polynomial of the Jacobian of the system (6.27) evaluated at $\boldsymbol{\psi}_{\mathcal{M}_{8,1}}$. The characteristic polynomial of the Jacobian of the system (6.27) evaluated at $\boldsymbol{\psi}_{\mathcal{M}_{8,1}}$ is given by

$$
\begin{aligned}
&-\lambda^3 \\
&+2\lambda^2\frac{(K_1N_1 - N\sin\frac{\bar{\theta}_2}{2})}{N} \\
&+\lambda\frac{(-N^2N_3 + K_1^2N_3^3 - N_1(N^2(1+\cos\bar{\theta}_2) - 2K_1N_3(N\sin\frac{\bar{\theta}_2}{2} + K_1N_3)))}{N^2N_3} \\
&-\frac{\sin\frac{\bar{\theta}_2}{2}N_1(N^2(1+\cos\bar{\theta}_2) - 2K_1^2N_3^2)}{N^2N_3}.
\end{aligned}
$$

The coefficient of the cubic term of the characteristic polynomial is equal to -1 always strictly negative. If $K_1 > \frac{N\sin\frac{\bar{\theta}_2}{2}}{N_1}$ (respectively $K_1 > \frac{N}{N_3}\sqrt{\frac{1+\cos\bar{\theta}_2}{2}}$) the coefficient of the quadratic term (respectively the constant term) of the characteristic polynomial is strictly positive. In either cases (whether one or both inequalities are satisfied) there is at least one change of sign of the coefficient of the characteristic polynomial and Routh stability criterion guarantees that there is at least one unstable eigenvalue. This concludes the proof that the equilibrium $\boldsymbol{\psi}_{\mathcal{M}_{8,1}}$ and is unstable if $K_1 > \min(\frac{N \sin \frac{\bar{\theta}_2}{2}}{N_1}, \frac{N}{N_3}\sqrt{\frac{1+\cos\bar{\theta}_2}{2}})$. The instability of

the equilibrium $\boldsymbol{\psi}_{\mathcal{M}_8,2}$ can be shown in an identical way, and the condition to have change of signs in the coefficient of the characteristic polynomial of the Jacobian remain identical. □

Proof of lemma 6.3.2: The linearization of (6.27) evaluated at the equilibrium $\boldsymbol{\psi}_{\mathcal{M}_8,7}$ can be written as follow:

$$J|_{\boldsymbol{\psi}_{\mathcal{M}_8,7}} = \begin{pmatrix} \alpha & \beta & \delta \\ \beta & \alpha & \delta \\ \gamma & \gamma & -2\gamma \end{pmatrix}, \tag{B.1}$$

where α, β, γ and δ are given by

$$\begin{aligned}
\alpha &= -\hat{\rho}\left(\cos\frac{\bar{\theta}_2}{2} + \frac{K_1 N_3}{N}\right) - \sqrt{1-\hat{\rho}^2}\sin\frac{\bar{\theta}_2}{2} - \frac{K_1 N_1}{N}(2\hat{\rho}^2 - 1) \\
\beta &= \frac{K_1 N_1}{N}(2\hat{\rho}^2 - 1) \\
\gamma &= \hat{\rho}\frac{K_1 N_1}{N} \\
\delta &= \hat{\rho}\frac{K_1 N_3}{N}.
\end{aligned}$$

The eigenvalues of the Jacobian can be calculated as

$$\begin{aligned}
\lambda_1 &= \alpha - \beta \\
\lambda_2 &= \frac{1}{2}\left(\alpha + \beta - 2\gamma - \sqrt{(\alpha+\beta+2\gamma)^2 + 8\gamma\delta}\right) \\
\lambda_3 &= \frac{1}{2}\left(\alpha + \beta - 2\gamma + \sqrt{(\alpha+\beta+2\gamma)^2 + 8\gamma\delta}\right).
\end{aligned}$$

We prove that the equilibrium $\boldsymbol{\psi}_{\mathcal{M}_8,7}$ is stable by showing that all three eigenvalues are strictly negative. Using the expression for α and β we rewrite λ_1 as

$$\lambda_1 = -\frac{N(\hat{\rho}\cos\frac{\bar{\theta}_2}{2} + \sqrt{1-\hat{\rho}^2}\sin\frac{\bar{\theta}_2}{2}) + K_1(N_1(4\hat{\rho}^2 - 2) + \hat{\rho}N_3)}{N} < 0.$$

Also using the expression of α, β and γ we have

$$\alpha + \beta - 2\gamma = -\hat{\rho}\left(\cos\frac{\bar{\theta}_2}{2} + \frac{K_1 N_3}{N}\right) - \sqrt{1-\hat{\rho}^2}\sin\frac{\bar{\theta}_2}{2} - 2\hat{\rho}\frac{K_1 N_1}{N} < 0,$$

implying that $\lambda_2 < 0$. Finally we compute the product of λ_2 and λ_3 as

$$\lambda_2\lambda_3 = \frac{2\hat{\rho}\left(\rho\cos\frac{\bar{\theta}_2}{2} + \sqrt{1-\hat{\rho}^2}\sin\frac{\bar{\theta}_2}{2}\right)K_1 N_1}{N} > 0,$$

implying that $\lambda_3 < 0$. This concludes the proof that all the eigenvalues of J are strictly negative and that the equilibrium $\boldsymbol{\psi}_{\mathcal{M}_8,7}$ is locally exponentially stable. $\square$

Proof of lemma 6.3.3: The linearization of (6.27) evaluated at the equilibrium $\boldsymbol{\psi}_{\mathcal{M}_8,8}$ can be also written as follow:

$$J|_{\boldsymbol{\psi}_{\mathcal{M}_8,8}} = \begin{pmatrix} \alpha & \beta & \delta \\ \beta & \alpha & \delta \\ \gamma & \gamma & -2\gamma \end{pmatrix}, \tag{B.2}$$

where α, β, γ and δ are now given by

$$\begin{aligned} \alpha &= -\hat{\rho}\left(\cos\frac{\bar{\theta}_2}{2} - \frac{K_1 N_3}{N}\right) - \sqrt{1-\hat{\rho}^2}\sin\frac{\bar{\theta}_2}{2} - \frac{K_1 N_1}{N}(2\hat{\rho}^2 - 1) \\ \beta &= \frac{K_1 N_1}{N}(2\hat{\rho}^2 - 1) \\ \gamma &= \hat{\rho}\frac{K_1 N_1}{N} \\ \delta &= \hat{\rho}\frac{K_1 N_3}{N}. \end{aligned}$$

The eigenvalues of the Jacobian can be calculated as

$$\begin{aligned} \lambda_1 &= \alpha - \beta \\ \lambda_2 &= \frac{1}{2}\left(\alpha + \beta + 2\gamma - \sqrt{(\alpha+\beta-2\gamma)^2 + 8\gamma\delta}\right) \\ \lambda_3 &= \frac{1}{2}\left(\alpha + \beta - 2\gamma + \sqrt{(\alpha+\beta-2\gamma)^2 + 8\gamma\delta}\right). \end{aligned}$$

We prove that the equilibrium $\boldsymbol{\psi}_{\mathcal{M}_8,8}$ is unstable by showing that one of the eigenvalues is strictly positive. The product of the eigenvalues λ_2 and λ_3 is given by

$$\lambda_2\lambda_3 = -\frac{2\hat{\rho}\left(\rho\cos\frac{\bar{\theta}_2}{2} + \sqrt{1-\hat{\rho}^2}\sin\frac{\bar{\theta}_2}{2}\right)K_1 N_1}{N} < 0,$$

implying that the two eigenvalues are of opposite sign and that the equilibrium $\boldsymbol{\psi}_{\mathcal{M}_8,8}$ is unstable. $\square$

Proof of lemma 6.3.4: We prove the lemma in two steps showing separately that the equilibria $\boldsymbol{\psi}_{\mathcal{M}_8,9}$ and $\boldsymbol{\psi}_{\mathcal{M}_8,10}$ are both unstable.

The linearization of (6.27) evaluated at the equilibrium $\boldsymbol{\psi}_{\mathcal{M}_{8,9}}$ can be also written as follow:

$$J|_{\boldsymbol{\psi}_{\mathcal{M}_{8,9}}} = \begin{pmatrix} \alpha & \beta & \delta \\ \beta & \alpha & \delta \\ \gamma & \gamma & -2\gamma \end{pmatrix}, \tag{B.3}$$

where α, β, γ and δ are now given by

$$\begin{aligned} \alpha &= \hat{\rho}\left(\cos\frac{\bar{\theta}_2}{2} + \frac{K_1 N_3}{N}\right) + \sqrt{1-\hat{\rho}^2}\sin\frac{\bar{\theta}_2}{2} - \frac{K_1 N_1}{N}(2\hat{\rho}^2 - 1) \\ \beta &= \frac{K_1 N_1}{N}(2\hat{\rho}^2 - 1) \\ \gamma &= -\hat{\rho}\frac{K_1 N_1}{N} \\ \delta &= -\hat{\rho}\frac{K_1 N_3}{N}. \end{aligned}$$

The eigenvalues of the Jacobian can be calculated as

$$\begin{aligned} \lambda_1 &= \alpha - \beta \\ \lambda_2 &= \frac{1}{2}\left(\alpha + \beta - 2\gamma - \sqrt{(\alpha+\beta+2\gamma)^2 + 8\gamma\delta}\right) \\ \lambda_3 &= \frac{1}{2}\left(\alpha + \beta - 2\gamma + \sqrt{(\alpha+\beta+2\gamma)^2 + 8\gamma\delta}\right). \end{aligned}$$

We prove that the equilibrium $\boldsymbol{\psi}_{\mathcal{M}_{8,8}}$ is unstable by showing that at least one of the eigenvalues is strictly positive. The sum of the eigenvalues λ_2 and λ_3 is given by

$$\lambda_2 + \lambda_3 = \hat{\rho}\left(\cos\frac{\bar{\theta}_2}{2} + \frac{K_1 N_3}{N}\right) + \sqrt{1-\hat{\rho}^2}\sin\frac{\bar{\theta}_2}{2} + 2\hat{\rho}\frac{K_1 N_1}{N} > 0,$$

implying that one or both these eigenvalues are strictly positive and that the equilibrium $\boldsymbol{\psi}_{\mathcal{M}_{8,9}}$ is unstable.

The linearization of (6.27) evaluated at the equilibrium $\boldsymbol{\psi}_{\mathcal{M}_{8,10}}$ can be also written as follow:

$$J|_{\boldsymbol{\psi}_{\mathcal{M}_{8,10}}} = \begin{pmatrix} \alpha & \beta & \delta \\ \beta & \alpha & \delta \\ \gamma & \gamma & -2\gamma \end{pmatrix}, \tag{B.4}$$

where α, β, γ and δ are now given by

$$\begin{aligned}
\alpha &= \hat{\rho}\left(\cos\frac{\bar{\theta}_2}{2} - \frac{K_1 N_3}{N}\right) + \sqrt{1-\hat{\rho}^2}\sin\frac{\bar{\theta}_2}{2} - \frac{K_1 N_1}{N}(2\hat{\rho}^2 - 1) \\
\beta &= \frac{K_1 N_1}{N}(2\hat{\rho}^2 - 1) \\
\gamma &= \hat{\rho}\frac{K_1 N_1}{N} \\
\delta &= \hat{\rho}\frac{K_1 N_3}{N}.
\end{aligned}$$

The eigenvalues of the Jacobian can be calculated as

$$\begin{aligned}
\lambda_1 &= \alpha - \beta \\
\lambda_2 &= \frac{1}{2}\left(\alpha + \beta - 2\gamma - \sqrt{(\alpha+\beta+2\gamma)^2 + 8\gamma\delta}\right) \\
\lambda_3 &= \frac{1}{2}\left(\alpha + \beta - 2\gamma + \sqrt{(\alpha+\beta+2\gamma)^2 + 8\gamma\delta}\right).
\end{aligned}$$

We prove that the equilibrium $\boldsymbol{\psi}_{\mathcal{M}_8,8}$ is unstable by showing that one of the eigenvalues is strictly positive. The product of the eigenvalues λ_2 and λ_3 is given by

$$\lambda_2\lambda_3 = -\frac{2\hat{\rho}\left(\rho\cos\frac{\bar{\theta}_2}{2} + \sqrt{1-\hat{\rho}^2}\sin\frac{\bar{\theta}_2}{2}\right)K_1 N_1}{N} < 0,$$

implying that the two eigenvalues are of opposite sign and that the equilibrium $\boldsymbol{\psi}_{\mathcal{M}_8,10}$ is unstable. $\square$

References

[1] J. Acebròns, L. Bonilla, and R. Spigler. The Kuramoto model: A simple paradigm for synchronization phenomena. *Reviews of Modern Physics*, 77:137–185, 2005.

[2] J. Ame, J. Halloy, C. Rivault, C. Detrain, and J. Deneubourg. Collegial decision making based on social amplification leads to optimal group formation. *Proceedings of the National Academy of Science*, 103:5835–5840, 2006.

[3] I. Aoki. An analysis on the schooling mechanism in fish. *Bull. Japanese Society Scientific Fisheries*, 48:1081–1088, 1982.

[4] M. Ballerini, N. Cabibbo, R. Candelelier, A. Cavagna, E. Cisbani, I. Giardina, V. Lecomte, A. Orlandi, G. Parisi, A. Procaccini, M. Viale, and V. Zdravkovic. Interaction ruling animal collective behaviour depends on topological rather than metric distance: Evidence from a field study. *Proceedings of the National Academy of Science*, 105:1232–1237, 2008.

[5] D. Bertsekas and J. Tsitsiklis. *Parallel and Distributed Computation:Numerical Methods*. Prentice-Hall, 1989.

[6] E. Biyik and M. Arcak. Area aggregation and time scale modeling for sparse nonlinear networks. *Proceedings of the 45th IEEE Conference on Decision and Control*, pages 4046–4051, 2006.

[7] R. Bogacz, E. Brown, J. Moehlis, P. Holmes, and J. D. Cohen. The physics of optimal decision making: A formal analysis of models of performance in two-alternative forced choice tasks. *Psychological Review*, 113:700–765, 2006.

[8] B. Bollobas. *Graph Theory: An Introductory Course*. Springer-Verlag, New York, 1979.

[9] E. Burian, D. Yoerger, A. Bradley, and H. Singh. Gradient search with autonomous underwater vehicle using scalar measurments. *Proc. IEEE OES AUV Conf*, 1996.

[10] S. Camazine, J. Deneubourg, N. Franks, J. Sneyd, G. Theraulaz, and E. Bonabeau. *Self-Organization in Biological Systems*. Princeton University Press, Princeton, 2001.

[11] J. Cardy and S. Ostlund. Random symmetry-breaking fields and the xy model. *Phys. Rev. B*, 25:6899–6909, 1982.

[12] R. Connelly. Rigidity and energy. *Invent. Math.*, 66:11–33, 1982.

[13] R. Connelly. Tensegrity structures: why are they stable? *Rigidity theory and applications.*, pages 47–543, 1999.

[14] R. Connelly. Generic global rigidity. *Discrete Comput. Geom.*, 33:549–563, 2005.

[15] R. Connelly and W. Whiteley. Second-order rigidity and prestress stability for tensegrity frameworks. *SIAM J.*, 9, No. 3:453–491, 1996.

[16] J. Cortés, S. Martínez, T. Karatas, and F. Bullo. Coverage control for mobile sensing networks. *IEEE Trans. on Robotics and Automation*, 20:243255, 2004.

[17] I. Couzin. Collective minds. *Nature*, 445:715, 2007.

[18] I. Couzin. Collective cognition in animal groups. *Trends in Cognitive Sciences*, 13, No 1:36–43, 2009.

[19] I. Couzin, J. Krause, N. Franks, and S. Levin. Effective leadership and decision making in animal groups on the move. *Nature*, 434:513–516, 2005.

[20] I. D. Couzin and J. Krause. Self-organization and collective behaviour in vertebrates. *Marine Ecology Progress Series*, 273:239–249, 2004.

[21] J. Deneubourg and S. Goss. Collective patterns and decision-making. *Ethology, Ecology, and Evolution*, 4:295–311, 1989.

[22] J. Deneubourg and S. Goss. Collective patterns and decision-making. *Ethology Ecology and Evolution*, 1:295–311, 1989.

[23] S. Emlen. *Modelling social animal aggregation*, pages 129–219. Avian Biology, Vol. 5, Ed. D.S. Farner and J.R. King and K.C. Parkes. Academic Press, 1975.

[24] D. Emmerich. Self-tensioning spherical structures: Single and double layer spheroids. *International Journal of Space Structures*, 5, No. 3:353–374, 1990.

[25] M. Erdmann and T. Lozano-Perez. On multiple moving objects. *Algorithmica*, 2:477–521, 1987.

[26] T. Eren, P. Belhumeur, and A. Morse. Closing ranks in vehicle formations based on rigidity. In *Decision and Control, 2002, Proceedings of the 41st IEEE Conference on*, volume 3, pages 2959–2964, 2002.

[27] J. Fax and R. Murray. Graph laplacians and stabilization of vehicle formations. In *Proc. 15th IFAC World Congress*, volume 3, pages 283–288, 2002.

[28] J. Fax and R. Murray. Information flow and cooperative control of vehicle formations. *IEEE Trans. on Automatic Control*, 49:1465–1476, 2004.

[29] E. Fiorelli, N. Leonard, P. Bhatta, D. Paley, R. Bachmayer, and D. Fratantoni. Multi-AUV control and adaptive sampling in Monterey Bay. *IEEE Journal of Oceanic Engineering*, 31(4):935–948, 2006.

[30] G. Flierl, D. Grünbaum, S. Levin, and D. Olson. From individuals to aggregations: the interplay between behavior and physics. *J. Theor. Biol*, 196:397–454, 1999.

[31] N. R. Franks, S. C. Pratt, E. B. Mallon, N. F. Britton, and D. J. T. Sumpter. Information flow, opinion polling and collective intelligence in house-hunting social insects. *Philosophical Transactions: Biological Sciences*, 357(1427), 2002.

[32] R. B. Fuller. Tensile-integrity structures, *US Patent 3,063,521*, 1962.

[33] H. Furuya. Concept of deployable tensegrity structures in space application. *International Journal of Space Structures*, 2:143–151, 1992.

[34] V. Gazi and K. Passino. Stability analysis of social foraging swarms: combined effects of attractant/repellent profiles. *Proceedings of the 41st IEEE Conference on Decision and Control*, 3:2848–2853 vol.3, 2002.

[35] G.Grégoire and H. Chaté. Onset of collective and cohesive motion. *Phys. Rev. Lett.*, 92(2):025702, 2004.

[36] G.Grégoire, H. Chaté, and Y. Tu. Moving and staying together without a leader. *Physica D*, 181:157–170, 2003.

[37] D. Grunbam and A. Okubo. *Modelling social animal aggregation*, pages 296–325. Frontiers in Mathematical Biology Ed. S. Levin. Springer, 1994.

[38] D. Grünbaum. Translating stochastic density-dependent individual behavior with sensory constraints to an Eulerian model of animal swarming. *Journal of Mathematical Biology*, 33:139–161, 1994.

[39] D. Grünbaum, S. Viscido, and J. Parrish. Extracting interactive control algorithms from group dynamics of schooling fish. In V. Kumar, N. Leonard, and A. Morse, editors, *Proceeding, Block Island Workshop on Cooperative Control*. Springer-Verlag, 2005.

[40] J. Guckenheimer and P. Holmes. *Nonlinear Oscillations, Dynamical Systems, and Bifurcations of Vector Fields*. Springer-Verlag, New York, 1983.

[41] S. Gueron and S. Levin. Self-organization of front patterns in large wildebeest herds. *J. Theor. Biol*, 165:541–552, 1993.

[42] S. Gueron, S. Levin, and D. Rubenstein. The dynamics of herds: From individuals to aggregations. *J. theor. Biol*, 182:85–98, 1996.

[43] W. Hamilton. Geometry for the selfish herd. *J. Theoretical Biology*, 31:295–311, 1971.

[44] A. Helbig. Genetic basis of inheritance and evolutionary changes of migratory directions in palearctic warblers (aves: Sylviidae). *The Journal of Experimental Biology*, 199:49–55, 1996.

[45] R. Horn and C. Johnson. *Matrix Analysis*. Cambridge University Press, Cambridge, 1985.

[46] T. Inanc, S. Shadden, and J. Marsden. Optimal trajectory generation in ocean flows. In *Proc. American Control Conference*, 2005.

[47] D. Ingber. Cellular tensegrity: defining new rules of biological design that govern the cytoskeleton. *Journal of Cell Science*, 104:613–627, 1993.

[48] A. Jadbabaie, J. Lin, and A. Morse. Coordination of groups of mobile autonomous agents using nearest neighbor rules. *IEEE Trans. Aut. Control,*, 48:988–1001, 2003.

[49] E. Justh and P. Krishnaprasad. Equilibria and steering laws for planar formations. *Systems and Control Letters*, 52:25–38, 2004.

[50] E. Justh and P. S. Krishnaprasad. A simple control law for UAV formation flying. Technical report, University of Maryland, 2002. Institute for Systems Research.

[51] M. Kelemen. A stability property. *IEEE Trans. on Automatic Control*, 31, No. 8, 1986.

[52] H. Khalil and P. Kokotovic. On stability properties of nonlinear systems with slowly varying inputs. *IEEE Transactions on Automatic Control*, 35, No. 7:860–864, 1990.

[53] H. Khalil and P. Kokotovic. On stability properties of nonlinear systems with slowly varying inputs. *IEEE Trans. on Automatic Control*, 36, No. 2, 1991.

[54] H. K. Khalil. *Nonlinear Systems 3rd ed.* Prentice Hall, 2002.

[55] O. Khatib. Real-time obstacle avoidance for manipulators and mobile robots. *Int. J. Rob. Res.*, 5(1):90–98, 1986.

[56] P. Khosla and R. Volpe. Superquadric artificial potentials for obstacle avoidance and approach. *Proceedings., 1988 IEEE International Conference on Robotics and Automation*, pages 1778–1784 vol.3, 1988.

[57] J. Krause and G. D. Ruxton. *Living in Groups.* Oxford Univ. Press, Oxford, 2002.

[58] L. C. V. Kumar and F. M. Campos. A paradigm for dynamic coordination of multiple robots. *Autonomous Robots*, 17:721, 2004.

[59] Y. Kuramoto. Self-entrainment of a population of coupled non-linear oscillators. In *Proc. Int. Symp. Mathematical Problems in Theoretical Physics*, pages 420–422, Kyoto, Japan, 1975.

[60] Y. Kuramoto. *Chemical oscillations, waves, and turbulence.* Springer-Verlag, 1984.

[61] G. Laman. On graphs and rigidity of plane skeletal structures. *Journal of Engineering Mathematics*, 4, No. 4, 1970.

[62] D. Lawrence and W. Rugh. On a stability theorem for nonlinear systems with slowly varying inputs. *IEEE Transactions on Automatic Control*, 36, No. 2:229, 1991.

[63] N. Leonard and E. Fiorelli. Virtual leaders, artificial potentials and coordinated control of groups. *Proceedings of the 40th IEEE Conference on Decision and Control*, 3:2968–2973, 2001.

[64] N. E. Leonard, D. Paley, F. Lekien, R. Sepulchre, D. Fratantoni, and R. Davis. Collective motion, sensor networks and ocean sampling. *Proceedings of the IEEE*, 95, No. 1:48–74, 2007.

[65] W. Levine and M. Athans. On the optimal error regulation of a string of moving vehicles. *IEEE Trans. Automatic Control*, 11, No. 3:355–361, 1966.

[66] M. Lindauer. Communication in swarm-bees searching for a new home. *Nature*, 179:63–67, 1957.

[67] M. Lindhe. A flocking and obstacle avoidance algorithm for mobile robots. Master's thesis, Royal Institute of Technology, Stockhom, Sweden, 2004.

[68] J. Marsden. *Lectures on Mechanics*. Cambridge University Press, 1992.

[69] J. Marsden and T. Ratiu. *Introduction to Mechanics and Symmetry 2nd ed.* Springer-Verlag, 1999.

[70] S. Melzer and B. Kuo. A closed-form solution for the optimal error regulation of a string of moving vehicles. *IEEE Trans. Automatic Control*, 16:50–51, 1971.

[71] R. E. Mirollo and S. H. Strogatz. Jump bifurcation and hysteresis in an infinite-dimensional dynamical system of coupled spins. *SIAM J. Appl. Math.*, 50(1):108–124, 1990.

[72] S. Moon, B. Nabet, N. Leonard, S. Levin, and I. Kevrekidis. Heterogeneous animal group models and their group-level alignment dynamics; an equation-free approach. *Journal of Theoretical Biology*, 246:100–112, 2007.

[73] K. Moored and H. Smith. The analysis of tensegrity structures for the design of morphing wing. *Transactions of the ASME*, 74:668–676, 2007.

[74] L. Moreau. Stability of multiagent systems with time-dependent communication links. *IEEE Transaction on Automatic Control*, 50, No. 2, 2005.

[75] R. Motro. Forms and forces in tensegrity systems. *Third International Conference on Space Structures*, pages 180–185, 1984.

[76] R. Motro, S. Najari, and P. Jouanna. Static and dynamic analysis of tensegrity systems. In *Proc. ASCE Int. Symp. Shells and Spatial Structures, Computational Aspects*, pages 270–279, New York, 1986. Springer.

[77] B. Nabet and N. Leonard. Shape control of a multi-agent system using tensegrity structures. In *Proceedings of the 3rd IFAC Workshop on Lagrangian and Hamiltonian Methods for Nonlinear Control, Nagoya, Japan*, 2006.

[78] B. Nabet and N. Leonard. Tensegrity models and shape control of vehicle formations, 2009. http//arxiv.org/abs/0902.3710v1.

[79] B. Nabet, N. Leonard, I. Couzin, and S. Levin. Leadership in animal group motion: A bifurcation analysis. In *Proceedings of the 17th International Symposium on Mathematical Theory of Networks and Systems, Kyoto, Japan*, 2006.

[80] B. Nabet, N. Leonard, I. Couzin, and S. Levin. Dynamics of decision-making in animal group motion. *Journal of Nonlinear Science*, 19, No 4:399–435, 2009.

[81] O.E.Wilson. *Sociobiology, The New Synthesis*. Harvard University Press, Cambridge, 1975.

[82] P. Ögren, M. Egerstedt, and X. Hu. A control lyapunov function approach to multi-agent coordination. *Proceedings of the 40th IEEE Conference on Decision and Control*, 2:1150–1155 vol.2, 2001.

[83] P. Ögren, E. Fiorelli, and N. Leonard. Cooperative control of mobile sensor networks: Adaptive gradient climbing in a distributed environment. *IEEE Trans. on Automatic Control*, 49, No. 8:1292–1302, 2004.

[84] A. Okubo. *Diffusion and Ecological Problems: Mathematical Models*, volume 10 of *Lecture Notes in Biomathematics*. Springer-Verlag, New York, 1980.

[85] R. Olfati-Saber and R. Murray. Distributed cooperative control of multiple vehicle formations using structural potential functions. In *Proceedings of The 15th IFAC World Congress , Barcelona, Spain*, 2002.

[86] R. Olfati-Saber and R. Murray. Graph rigidity and distributed formation stabilization of multi-vehicle systems. In *Proceedings of the 41st Conference on Decision and Control*, 2002.

[87] R. Olfati-Saber and R. Murray. Consensus problems in networks of agents with switching topology and time-delays. *IEEE Trans. on Automatic Control*, 49(9):1520–1533, 2004.

[88] I. Oppenheim and W. Williams. Vibration and damping in tensegrity structures. *ASCE Journal of Aerospace Engineering*, 14:8591, 2001.

[89] D. Pais, M. Cao, and N. Leonard. Formation shape and orientation control using projected collinear tensegrity structures. In *American Control Conference, St. Louis, MO*, 2009.

[90] D. Paley, F. Zhang, and N. Leonard. Cooperative control for ocean sampling: The glider coordinated control system. *IEEE Trans. on Control Systems Technology*, 16, No. 4:735–744, 2008.

[91] J. Pearson. On controlling a string of moving vehicles. *IEEE Trans. Automatic Control*, 12:328–329, 1967.

[92] A. Perdeck. Two types of orientation in migrating starlings. *Ardea*, 46:1–37, 1958.

[93] T. Poston and I. Stewart. *Catastrophe Theory and its Applications*. Pitman, London, 1978.

[94] S. Pratt, E. Mallon, D. Sumpter, and N. Frank. Quorum sensing, recruitment, and collective decision-making during colony emigration by the ant leptothorax albipennis. *Behavioral Ecology and Sociobiology*, 52:117–127, 2002.

[95] A. Pugh. *An Introduction to Tensegrity.* University of California Press, Berkeley, CA, 1976.

[96] S. Reebs. Can a minority of informed leaders determine the foraging movements of a fish shoal? *Animal Behaviour*, 59:403–409, 2000.

[97] C. Reynolds. Flocks, herds, and schools: A distributed behavioral model. *Computer Graphics*, 21, No 4:25–34, 1987.

[98] E. Rimon and D. Koditschek. Exact robot navigation using artifical potential functions. *IEEE Trans. on Robotic and Automations*, pages 501–518, 1992.

[99] G. Roberts. Why vigilance declines as group size increases. *Animal Behavior*, 51, 1996.

[100] B. Roth and W. Whiteley. Tensegrity frameworks. *Trans. American Math. Soc*, 265, No 2.:419–446, 1981.

[101] S. Sadao. Fuller on tensegrity. *International Journal of Space Structures*, 11, 1996.

[102] A. Savkin. Coordinated collective motion of groups of autonomous mobile robots: Analysis of Viscek's model. *IEEE Trans. on Automatic Control*, 49, No. 6:981–983, 2004.

[103] L. Scardovi, A. Sarlette, and R. Sepulchre. Synchronization and balancing on the N-torus. *Systems and Control Letters*, 56(5):335 – 341, 2007.

[104] T. Seeley and P. Visscher. Quorum sensing during nest-site selection by honeybee swarms. *Behavioral Ecology and Sociobiology*, 56:594–601, 2004.

[105] T. D. Seeley. *Honeybee ecology: a study of adaptation in social life.* Princeton University Press, 1985.

[106] E. Selous. *Thought Transference (or What?) in Birds.* Constable and Company Ltd, London, 1931.

[107] R. Sepulchre, D. Paley, and N. Leonard. Stabilization of planar collective motion with limited communication. *IEEE Trans. Aut. Control*, 53, No. 3:706–719, 2008.

[108] R. Sepulchre, D. Paley, and N. E. Leonard. Stabilization of planar collective motion: All-to-all communication. *IEEE Transactions on Automatic Control*, 52, No.5:811–824, 2007.

[109] R. Skelton and M. de Oliveira. *Tensegrity Systems*. Springer, 2009.

[110] R. Skelton, J. Helton, R. Adhikari, J. Pinaud, and W. Chan. An introduction to the mechanics of tensegrity structures. *The Mechanical Systems Design Handbook: Modeling, Measurement, and Control CRC Press*, 2001.

[111] R. Skelton and C. Sultan. Controllable tensegrity, a new class of smart structures. In *Proc. SPIE 4th Symposium on Smart Structures and Materials*, pages 166–177, 1997.

[112] K. Snelson. Continuous tension, discontinuous compression structures. *U.S. Patent 3,169,611,*, 1965.

[113] H. Sompolinsky, D. Golomb, and D. Kleinfeld. Global processing of visual stimuli in a neural network of coupled oscillators. *Proceedings of the National Academy of Science USA*, 87:7200–7204, 1990.

[114] S. Strogatz. *Nonlinear Dynamics and Chaos*. Perseus, 1994.

[115] S. H. Strogatz. From Kuramoto to Crawford: Exploring the onset of synchronization in populations of coupled oscillators. *Physica D*, 143:1–20, 2000.

[116] C. Sultan. *Modeling, design and control of tensegrity structures with applications*. PhD thesis, Purdue University, School of Aeronautics and Astronautics, 1999.

[117] C. Sultan and R. Skelton. Integrated design of controllable tensegrity structures. In *Proc. ASME Int. Mechanical Engineering Congress and Exposition*, volume 54, pages 27–37, 1997.

[118] D. Sumpter, J. Krause, I. D. Couzin, and A. Ward. Consensus decision making by fish. *Current Biology*, 18:1773–1777, 2008.

[119] W. Swaney, J. Kendal, H. Capon, C. Brown, and K. Laland. Familiarity facilitates social learning of foraging behavour in the guppy. *Animal Behaviour*, 62:591–598, 2001.

[120] P. Tabuada, G. Pappas, and P. Lima. Feasible formations of multi-agent systems. In *Proceedings of the American Control Conference*, volume 1, pages 56–61, 2001.

[121] R. Thom. *Structural Stability and Morphogenesis.* Benjamin, New York, 1972.

[122] A. Tibert. *Deployable Tensegrity Structures for Space Applications.* PhD thesis, Royal Institute of Technology, Sweden, Department of Mechanics, 2002.

[123] A. Tibert and S. Pellegrino. Review of form-finding methods for tensegrity structures. deployable structures lab, university of cambridge. *International Journal of Space Structures*, 18, No. 4:209–223, 2003.

[124] N. Tinbergen. On aims and methods of ethology. *Zeitschrift für Tierpsychologie*, 20, 1986.

[125] J. Toner and Y. Tu. Long-range order in a two-dimensional dynamical xy model: How birds fly together. *Phys. Rev. Lett.*, 75(23):4326–4329, 1995.

[126] J. Toner and Y. Tu. Flocks, herds, and schools: A quantitative theory of flocking. *Phys. Rev. Lett.*, 58(4):4828–4858, 1998.

[127] J. Tsitsiklis. *Problems in decentralized decision making and computation.* PhD thesis, MIT, Department of Electrical Engineering, Cambridge, MA, 1984.

[128] J. Tsitsiklis and D. Bertsekas. Distributed asynchronous deterministic and stochastic gradient optimization algorithms. *IEEE Trans. Autom. Control*, AC-31, No 9:803–812, 1986.

[129] T. Viscek, A. Czirók, E. Ben-Jacob, I. Cohen, O. Shochet, and A. Tenenbaum. Novel type of phase transition in a system of self-driven particles. *Phys. Rev. Lett.*, 75(6):1226–1229, 1995.

[130] S. Viscido, J. Parrish, and D. Grünbaum. Individual behavior and emergent properties of fish schools: a comparison between observation and theory. *Advances in the Study of Behavior*, 32:1–75, 2003.

[131] P. Wang. Interaction dynamics of multiple mobile robots with simple navigation strategies. *Journal of Robotic Systems*, 7:77–101, 1989.

[132] A. Ward, D. Sumpter, I. D. Couzin, P. Hart, and J. Krause. Quorum decision-making facilitates information transfer in fish shoals. *Proceedings of the National Academy of Science*, 105, No.19:6948–6953, 2008.

[133] C. Warren. Multiple robot path coordination using artificial potential fields. *Proceedings of the IEEE International Conference on Robotics and Automation*, pages 500–505 vol.1, 1990.

[134] W. Williams. A primer on the mechanics of tensegrity structures. Technical report, Carnegie Mellon University, 2003. Center for Nonlinear Analysis.

[135] A. Winfree. Biological rhythms and the behavior of populations of coupled oscillators. *Journal of Theoretical Biology*, 16(1):15–42, 1967.

[136] R. Wood, S. Avadhanula, E. Stelz, M. Seeman, J. Entwistle, A. Bachrach, G. Barrows, S. Sanders, and R. Fearing. Enabling technologies and subsystem integration for an autonomous palm-sized glider. *IEEE Robotics and Automation Magazine*, 14, No. 2:82–91, 2007.

[137] G. Zanotti and C. Guerra. Is tensegrity a unifying concept of protein folds? *FEBS Letters*, 534:7–10, 2003.

[138] F. Zhang, M. Goldgeier, and P. S. Krishnaprasad. Control of small formations using shape coordinates. *Proc. 2003 IEEE International Conference on Robotics and Automation*, pages 2510–2515, 2003.

[139] F. Zhang and N. Leonard. Generating contour plots using multiple sensor platforms. *Proc. of 2005 IEEE Symposium on Swarm Intelligence*, pages 309–314, 2005.

[140] F. Zhang and N. Leonard. Cooperative control and filtering for cooperative exploration. *IEEE Transactions on Automatic Control*, 2008. to appear.